Modelling co-seismic drainage effects on liquefaction triggering using SANISAND plasticity



Abhinanda Dilip

University College, University of Oxford

A thesis submitted for the degree of

Doctor of Philosophy

Trinity Term 2025

Acknowledgements

I would like to extend my heartfelt gratitude to Professors Orestis Adamidis and Sinan Acigkoz for allowing me this wonderful opportunity of pursuing a doctoral degree at University of Oxford. The past four years in research have been very enriching and fulfilling and I thank everyone who supported me in my decision to return to academia after spending years in the AEC industry. This thesis is a culmination of the vision of my supervisor Professor Orestis Adamidis, without whose unwavering guidance and support, this work would not have been possible. I consider myself lucky to have had such an encouraging and understanding supervisor.

I would like to thank University College for awarding me the Oxford-Ashton Memorial Graduate Scholarship that provided full financial support during my doctoral studies. I would like to express my gratitude to Alison May for her help in procuring lab items, and to Clive Baker for helping me set up the triaxial device in the soils lab at Jenkin. In this regard, the suggestions on advanced element testing by Dr Mark Qiu is highly appreciated. I also thank Kathy, Rachel, Dim and Ioannis for the fun lab conversations and frequent helping hands with the heavy lifting of the triaxial cell.

I must thank Dr Miad Saberi for his insightful suggestions on constitutive modelling and for sharing his knowledge on numerical analysis. I am also deeply thankful to Adrienne for her kind friendship and support. I would like to thank Yide Wang for providing me with his experimental data on Congleton sand. Finally, I am grateful to Professors Katerina Ziotopoulou and Mahdi Taiebat for providing me with important resources on their constitutive models.

On the personal front, my immense gratitude goes to my loving family, especially Abhinav and Neelakshi for taking care of everything back home and letting me fly. And to my dearest parents, Dilip and Kajal, who I owe everything in my life. Ma, without you I wouldn't have come this far and I dedicate this thesis to you. A special mention to my childhood bestie Snigdha, who is as much family to me, for her immense belief in my potential and for pushing me towards this doctoral journey. Last, but not the least, I am grateful to my loving husband Shivang for his constant motivation. I could not have completed this journey without you.

Abstract

Liquefaction susceptibility assessment procedures used in practice today have led to false predictions due to the evaluation of soil layers in isolation, disregarding any layer interactions. The view of liquefaction as an undrained phenomenon has been challenged by analytical, experimental, and field data that have demonstrated the occurrence of co-seismic drainage. In this thesis, the implications of co-seismic drainage on modelling liquefaction triggering in sands are investigated, at the element and at the deposit level. Particular attention is given to the ability of the SANISAND-family of constitutive models to capture drainage effects, which is examined and improved.

Initially, the focus is on drainage effects during monotonic loading. Monotonic triaxial compression tests are presented, in which constant expansive volumetric to deviatoric strain rates are imposed. It is shown that within the SANISAND framework, a specific instability point on these coupled strain paths corresponds to an a priori known value of the state parameter. Building on this observation, an updated state parameter definition is proposed, consistent with the experimentally identified points of known state parameter. The updated state parameter is shown to markedly improve predictions across the examined stress paths, as compared to the standard SANISAND formulation. This outcome is consequential for modelling liquefaction in sloped, layered deposits, where similar conditions could manifest and enable the triggering of liquefaction at the interface between different permeability layers.

Using the proposed state parameter framework, a method is proposed to infer the critical state line from coupled strain monotonic triaxial paths, which only reach moderate strain and load magnitudes. This is particularly beneficial for highly dilative sands, which cannot reach the critical state under conventional testing due to strain, load and instrumentation constraints. Using Congleton sand as an example, it is shown that an inferred critical state line can be used to successfully calibrate a SANISAND model and to produce realistic predictions of soil behaviour at the element level.

Subsequently, drainage effects during cyclic loading are targeted. SANISAND models are

assessed for their ability to capture such effects as recorded in cyclic triaxial tests from literature, performed under constant rates of volumetric expansion and corresponding to soil at the interface of a liquefiable layer with an overlying low permeability layer. Amendments in the calibration process of SANISAND models are proposed, the most important being the direct calibration of the bulk modulus from experimental isotropic unloading - reloading curves. The proposed calibration significantly increases the reliability of liquefaction triggering predictions at the element level under non-standard drained conditions.

Finally, the implications of the updated calibration for layered deposits are investigated, using the finite element software OpenSees to run non-linear, effective stress, fully hydromechanically coupled soil column simulations. Before simulating layered profiles, a validation exercise versus centrifuge test results for a uniform deposit is performed. The validated simulations confirm that the proposed direct bulk modulus calibration leads to significantly more reliable results when co-seismic drainage is important. Idealised layered deposits, motivated by experiments and case studies known to produce false liquefaction predictions using simplified assessment procedures, are then simulated. The proposed bulk modulus calibration is shown to capture the manifestation or mitigation of liquefaction in the critical layer in a manner that neither simplified assessment procedures nor simulations with a traditional Poisson's ratio calibration can. These findings provide new insight into the role of co-seismic drainage in liquefaction triggering within layered deposits, highlight limitations of current state-of-practice assessment procedures, and identify practical improvements for state-of-the-art numerical simulations.

Contents

Nomenclature **viii**

1 Introduction **1**
1.1 Background and motivation 1
1.1.1 Research gap 5
1.2 Research aims and objectives 6
1.3 Thesis outline 8

2 Literature review **12**
2.1 Introduction 12
2.2 Liquefaction susceptibility 13
2.3 Undrained behaviour of sand under monotonic loading 15
2.4 Undrained behaviour of sand under cyclic loading 17
2.5 State parameter 19
2.6 Fabric 21
2.7 Liquefaction susceptibility assessment 22
2.7.1 Simplified procedures 22
2.7.2 Numerical procedures 24
2.8 Liquefaction and drainage 26
2.8.1 Mechanisms involving drainage 26
2.8.2 System response 28
2.8.3 Non-standard drained behaviour of sands 30

3 Constitutive modelling **33**
3.1 Introduction 33
3.2 Dafalias and Manzari, 2004 (DM04) 35
3.3 SANISAND 2008 38
3.4 SANISAND-MSf 40
3.5 PM4Sand3D 44

4 Experimental testing **48**
4.1 Introduction 48
4.2 Methodology 51
4.2.1 Testing equipment 51
4.2.2 Testing material 52
4.2.3 Sample preparation 52

4.2.4 Testing protocol . . . 53
4.3 Test results . . . 54
4.3.1 Monotonic triaxial test results . . . 54
4.3.2 Coupled strain triaxial test results . . . 57

5 State parameter for coupled shear-volumetric strain paths using a SANISAND model 61
5.1 Introduction . . . 61
5.2 Numerical simulation of monotonic triaxial tests . . . 64
5.2.1 Results for undrained monotonic compression tests . . . 65
5.2.2 Results for coupled strain monotonic compression tests . . . 65
5.3 Instability triggering under coupled strain paths . . . 67
5.3.1 Instability assessment . . . 68
5.3.2 Criterion for instability under coupled strain paths . . . 69
5.3.3 Isolation of state parameter from instability points . . . 71
5.3.4 Applicability of the proposed instability locus . . . 73
5.3.5 Verification of proposed instability line . . . 76
5.3.6 Role of dilatancy . . . 77
5.4 Hostun sand calibration . . . 78
5.4.1 Elastic moduli . . . 79
5.4.2 Critical state parameter . . . 80
5.4.3 Bounding surface parameter . . . 81
5.4.4 Dilatancy surface parameter . . . 82
5.4.5 Stress-dilatancy characteristics . . . 83
5.4.6 Bounding parameters h_0 and c_h . . . 84
5.4.7 Compression parameters . . . 84
5.5 Model performance . . . 85
5.5.1 Undrained and drained simulation results . . . 86
5.5.2 Coupled strain simulation results . . . 87
5.5.3 Updated state parameter definition . . . 91
5.6 Model performance with updated state parameter . . . 98
5.6.1 Model calibration with updated state parameter . . . 99
5.6.2 Simulation of undrained and drained monotonic triaxial tests . . . 99
5.6.3 Simulation of coupled strain monotonic triaxial tests . . . 100
5.7 Conclusions . . . 104

6 Identification of the critical state line of sands using coupled shear-volumetric strain paths 107
6.1 Introduction . . . 107
6.2 Determination of the critical state line . . . 109
6.2.1 Experimental results . . . 110
6.2.2 State parameter form . . . 112
6.2.3 LCSI and CSL functions . . . 117
6.2.4 Validation of the proposed methodology . . . 119
6.2.5 State parameter definition . . . 121

6.3 Model calibration . . . 123
6.3.1 Elastic shear modulus . . . 124
6.3.2 Elastic bulk modulus . . . 125
6.3.3 Bounding surface parameter . . . 126
6.3.4 Dilatancy surface parameter . . . 126
6.3.5 Fitting parameters . . . 128
6.3.6 Compression parameters . . . 129
6.4 Model performance . . . 129
6.4.1 Undrained monotonic triaxial test simulations . . . 130
6.4.2 Coupled strain triaxial compression test simulations . . . 131
6.5 Conclusions . . . 135

7 Assessment and calibration of double surface plasticity models for cyclic loading under volumetric expansion 138
7.1 Introduction . . . 138
7.2 Model calibration . . . 140
7.2.1 DM04 model parameters . . . 141
7.2.2 SANISAND-MSf model parameters . . . 148
7.2.3 PM4Sand3D model parameters . . . 150
7.3 Model performance . . . 153
7.3.1 Undrained monotonic triaxial test simulations . . . 154
7.3.2 Undrained cyclic triaxial test simulations . . . 157
7.3.3 Volumetric expansion cyclic test simulations . . . 163
7.4 Liquefaction resistance curves . . . 169
7.5 Impact of updated SANISAND state parameter on liquefaction resistance . . . 177
7.5.1 State parameter definition . . . 178
7.5.2 Calibration of model parameters . . . 180
7.5.3 Simulation results with updated SANISAND state parameter . . . 180
7.6 Conclusions . . . 185

8 Numerical analysis of liquefaction triggering in layered deposits 192
8.1 Introduction . . . 192
8.2 Verification of element-level behaviour in OpenSees . . . 194
8.2.1 Model setup . . . 194
8.2.2 Analysis parameters . . . 195
8.2.3 Material model . . . 196
8.2.4 Simulation results . . . 197
8.3 Validation versus centrifuge testing data . . . 201
8.3.1 Model setup . . . 202
8.3.2 Analysis parameters . . . 203
8.3.3 Soil properties and material model . . . 205
8.3.4 Simulation results . . . 206
8.3.5 Mechanisms of excess pore pressure accumulation and liquefaction triggering . . . 212
8.3.6 Comparison with traditional calibration of elastic moduli . . . 219

8.4 Effects of layering 221
8.4.1 Parametric cases 222
8.4.2 'False-negative' case: Model setup 224
8.4.3 'False-negative' case: Simulation results 225
8.4.4 'False-positive' case: Model setup 241
8.4.5 'False-positive' case: Simulation results 243
8.5 Conclusions 248

9 Conclusions **251**
9.1 Research conclusions 251
9.1.1 Performance evaluation and model improvements under coupled strain monotonic shearing 252
9.1.2 Performance evaluation and model improvements under water inflow cyclic shearing 257
9.2 Future research 265

References **268**

Nomenclature

CRR	Cyclic Resistance Ratio
CS	Critical State
CSL	Critical State Line
CSR	Cyclic Stress Ratio
CSR_{ss}	CSR in simple shear condition
CSR_{tx}	CSR in triaxial condition
FS_L	Factor of Safety against Liquefaction
$INST$	Instability
$LCSI$	Locus of Constant State parameter Instabilities
$PSRS$	Peak Stress-Ratio State
PTS	Phase Transformation State
α	back stress ratio
α^b, M^b	slope of bounding surface
α^c, M^c	slope of critical surface
α^d, M^d	slope of dilatancy surface
$\ddot{W}$	second-order work
$\Delta U, \bar{u}$	excess pore pressure
$\dot{\varepsilon}_1$	axial strain rate
$\dot{\varepsilon}_q$	deviatoric strain rate
$\dot{\varepsilon}_q{}^e$	elastic deviatoric strain rate
$\dot{\varepsilon}_q{}^p$	plastic deviatoric strain rate

$\dot{\varepsilon}_v$ volumetric strain rate

$\dot{\varepsilon}_v{}^e$ elastic volumetric strain rate

$\dot{\varepsilon}_v{}^p$ plastic volumetric strain rate

$\varepsilon_{1,DA}$ double amplitude of axial strain

η stress ratio ($= q/p'$)

Λ $\dot{\varepsilon}_v/\dot{\varepsilon}_q (= \frac{3\zeta}{3-\zeta})$

ν Poisson's ratio

Ω state parameter form constant

ϕ friction angle

ψ state parameter ($= e - e_{cs}$)

ψ_D updated state parameter definition

ψ_F state parameter form

$\sigma_{v0}, \sigma'_{v0}$ initial total and effective vertical stress, respectively

ξ_R relative state parameter index

ζ inflow rate, $\dot{\varepsilon}_v/\dot{\varepsilon}_1$

A_0, A_d, n^d, k^d, n_g positive dilatancy parameters

a_{max} peak ground acceleration

b exponent in power-fit for CRR curve

c ratio of slope of surfaces in extension to compression

C^e, C^{ep} elastic and elastoplastic compliance matrix, respectively

c_l, x semi-fluidised state parameters

c_r correction factor for CSR

c_v coefficient of consolidation

c_z, z, z_{max} fabric-dilatancy parameters

D dilatancy

D^e, D^{ep} elastic and elastoplastic stiffness matrix, respectively

D_r relative density

e void ratio

e_0, λ, ξ, R, Q critical state line material constants

e_{cs} void ratio at critical state

G, K elastic shear and bulk moduli, respectively

G_0, K_0 elastic moduli model parameters

G_{max} small-strain bender element stiffness

h, b_0, h_0, c_h hardening parameters

H hardening modulus

H_L limiting hardening modulus

h_{po} contraction rate parameter

k permeability constant

K_o earth pressure coefficient at rest

m_v volume compressibility constant

N loading cycles

n^b, k^b positive bounding parameters

$N_{\varepsilon_1}, N_{\varepsilon_{1,DA}}$ cycles to $\varepsilon_{1,DA} = 5\%$

N_{R_u}, N_{ult} cycles to liquefaction

p' mean effective stress

p'_{in}, p'_0 initial mean effective stress, at end of isotropic consolidation

p_{at} atmospheric pressure

q deviatoric stress

r_d stress reduction factor

R_u excess pore pressure ratio

s' mean effective stress in plane strain condition

u, μ_0 memory surface parameters

V_s shear wave velocity

w updated state parameter exponent

γ shear strain

τ_{cyc} cyclic shear stress

Chapter 1

Introduction

1.1 Background and motivation

Liquefaction is a collective term for ground failure phenomena caused by the sudden loss of shear strength in saturated, loose, cohensionless soils subjected to rapid monotonic or cyclic loading, typically due to an earthquake, and potentially followed by large deformations. The earliest mentions of earthquake-induced liquefaction have been interpreted from the flood stories in the Epic of Gilgamesh and the Hebrew Scriptures where the "fountains of the great deep" erupted from "a shattering of the earth" (Krinitzsky, 2005). Compilations of post-earthquake reconnaissance surveys and historical recounts indicate the oldest recorded occurrence of liquefaction in Japan in the year 745 AD in Gifu Prefecture, Honsyu Island induced by a $M_w = 7.9$ earthquake (Wakamatsu, 2000). Paleo-liquefaction studies of sand dikes and sills in the glaciomarine deposits from the 1727 Newbury earthquakes in Massachusetts, USA reveal liquefaction features formed from earthquakes around 2480 BC (Tuttle and Seeber, 1991). Liquefaction-related geologic features similar to the great 1811-1812 earthquakes in New Madrid, USA (Obermeier, 1996) were identified in southern Indiana and Illinois and were detected to have been caused by paleo-earthquakes of magnitudes in excess of $M_w = 7.0$, struck as early as 10,000 BC (Obermeier, 1997).

Early instances of liquefaction from recorded earthquake events include the 1755 Great Lisbon earthquake, where widespread fissures were reported in the city centre, and the 1811-1812 New Madrid earthquakes where subsidence and sand blows were observed in Missouri and nearby states. Significant manifestations of liquefaction were observed in the 1906 San Francisco earthquake followed by the liquefaction-induced failure of Sheffield Dam in the 1925 Santa Barbara earthquake, that prompted U.S. building codes to adopt provisions for earthquake resistance (Kramer, 1996). However, the destructive consequences of liquefaction were only widely brought to attention in the later half of the past century by the earthquakes in Niigata, Japan and Anchorage, Alaska in 1964, see figure 1.1. Buildings with shallow foundations settled and tilted excessively. Underground utility structures were pushed upward to the ground due to buoyancy. Lateral movements of liquefied soil resulted in landslides, fissures and flooding of low-lying areas (Seed and Idriss, 1967). The catastrophic damage caused by liquefaction in two distant locations within the same year sparked intense interest in the phenomenon.



Figure 1.1: Liquefaction-induced failures from the 1964 earthquakes in Niigata, Japan (left) and Anchorage, Alaska (right), photographs courtesy of University of Washington

While casualties caused by liquefaction have been historically rare, it has led to significant financial and infrastructure losses (Abeling et al., 2020; Crowley and Elliott, 2012; Widiyanto et al., 2019). Liquefaction related deformations can result in permanent structural defects in foun-

dations or superstructures that may require entire localities to be displaced along with the need for reconstruction of residential buildings and utility structures. Damages to lifeline networks such as bridges, pipelines, etc. and other infrastructure facilities such as ports can lead to major disruptions and incur indirect losses. According to the National Disaster Mitigation Agency (BNPB) data, physical damages worth $780 million USD were estimated, with most damages in the residential sector due to significant liquefaction, in the recent 2018 Sulawesi earthquake, Indonesia. Such damages take a toll on governments and insurance agencies and can deter the economic growth of nations, especially in developing countries. The 2025 Myanmar earthquake, characterised by severe liquefaction, resulted in $11 billion USD in damages to physical assets, representing 14% of Myanmar's GDP, with $1.3 billion USD attributed to insured losses. The Turkish government estimated $105 billion USD as the cost to rebuild and repair affected areas of the 2023 Kahramanmaraş earthquakes, amounting to 10% of its GDP. Thus, an understanding of the mechanisms driving liquefaction is crucial to introduce necessary amendments in building codes and improve resilience of the built environment against such calamities.

Since the 1964 earthquakes, there has been a greater effort in the scientific community to understand the mechanisms driving liquefaction. In order to limit the hazard from infrastructure damage, the assessment of liquefaction susceptibility at sites supporting existing and future structures, especially in highly seismic zones, is imperative. As such, extensive laboratory tests at element level and field investigations of liquefied sites were conducted that led to the development of methodologies for liquefaction assessment (Kramer, 1996). The most widely used methodology for liquefaction susceptibility assessment is a stress-based simplified framework developed by Seed and Idriss (1971). The method compares the seismic loading to the liquefaction resistance of soil, both expressed as a uniform cyclic stress ratio for a set number of cycles, which has also been correlated to in-situ soil parameters such as SPT and CPT resistance (Boulanger and Idriss, 2014). Alternative energy-based methods comparing the seismic input energy to the dissipated strain energy have also been developed (Berrill and Davis, 1985; Kokusho, 2013).

Furthermore, with advancements in computational methodologies and infrastructure, effective stress-based nonlinear numerical analyses procedures that allow the simulation of fully coupled soil-fluid formulation (Zienkiewicz and Shiomi, 1984) and incorporate advanced constitutive models (Boulanger and Ziotopoulou, 2015; Prévost, 1985) have also been used. Such formulations have been implemented in software for one-dimensional applications such as DEEPSOIL (Hashash et al., 2018) and CYCLIC 1D (Elgamal and Yang, 2000), focusing on a soil column, or have been implemented in finite difference codes, such as FLAC 3D (Itasca, 2011), or finite-element codes, such as OpenSees (McKenna, 2011). Despite major advancements, liquefaction-induced failures continue to cause significant functional and monetary losses to the built environment, even in countries with advanced seismic codes, as for example during the 2010-2011 Christchurch earthquakes in New Zealand and the 2011 Tohoku earthquake in Japan (Bhattacharya et al., 2011; Cubrinovski, 2013; Ishihara et al., 2014).

The simplified stress-based liquefaction evaluation procedure that dominates practice today evaluates each soil layer within a stratified deposit in isolation and is significantly influenced by the undrained assumption. It does not explicitly take into account drainage effects during earthquake shaking and thus ignores the consequences of layer interaction. However, fluid flow-induced pore pressure evolution has been analytically shown to be of significance within the timeframe of an earthquake (Ben-Zeev et al., 2023; Goren et al., 2010; Lakeland et al., 2014). Experimental results confirm that water flow takes place during an earthquake and show that layer interaction can be of importance (Adamidis and Madabhushi, 2018; Kokusho, 1999; Malvick et al., 2008; Sinha et al., 2024), thereby challenging the undrained hypothesis. For instance, a liquefiable layer overlain by a low permeability layer can manifest liquefaction more easily than under undrained conditions. 'False-negative' assessments using the simplified procedure have been reported for sites that liquefied in the 2010-2011 Christchurch earthquakes (Cubrinovski et al., 2019; Tsaparli et al., 2020).

Much uncertainty remains in numerical simulations of liquefaction phenomena, particularly when layer interaction due to co-seismic drainage becomes important. Coupled effective stress

analyses conducted to capture seismic response that is affected by drainage, indicate the need to update dynamic soil properties such as permeability during the liquefaction event (Tsaparli et al., 2020). Updating soil properties is typically done to match recorded settlement and is not necessarily supported by experimental results on fluidisation at the element level (e.g., Haigh et al. (2012)). It is also worth noting that constitutive models used in numerical analyses are typically developed to capture undrained behaviour and are also calibrated with results from undrained element tests. The models' performance under conditions other than undrained is not tested and the same constitutive models typically require a different set of parameters to capture drained tests. As a result, co-seismic drainage can lead to predictions of erroneous stress-strain behaviour. To improve reliability, constitutive models must be assessed at the element level against relevant experimental data and amended where necessary.

1.1.1 Research gap

A growing body of analytical, experimental, and field evidence has demonstrated that co-seismic drainage can significantly influence liquefaction triggering (Adamidis and Anastasopoulos, 2022; Ben-Zeev et al., 2023). Case studies have shown that current simplified assessment procedures can produce false predictions when drainage-related layer interaction becomes important (Cubrinovski et al., 2019). As simplified procedures, starting with Seed and Idriss, 1971, were developed with the implicit assumption of undrained behaviour, a more holistic assessment of stratified deposits is required, that allows for void redistribution and drainage within layers, rather than evaluation of each layer in isolation.

Reliable simulation of such system-level behaviour requires constitutive models capable of reproducing the corresponding element-level response under a wide range of drainage conditions. Nevertheless, existing constitutive models targeting liquefaction behaviour, such as the popular models of the SANISAND family, are typically developed and calibrated using exclusively undrained element tests, particularly for cyclic loading. Therefore, it remains unclear whether they can reliably capture the influence of drainage on liquefaction triggering.

Few experimental studies have examined the influence of drainage on sand behaviour at the element level, under monotonic (Lashkari et al., 2021) or cyclic loading (Adamidis and Anastasopoulos, 2022). These experimental observations have not yet been systematically used to evaluate the performance of advanced constitutive models under representative co-seismic drainage conditions. Only a limited number of such studies exist, focusing on the ability of advanced constitutive models to capture monotonic flow failures in contractive sands and limited-flow failures in dilative sands (Lashkari and Yaghtin, 2018; Lashkari et al., 2021), relevant for static liquefaction failures. However, water inflow-triggered flow failures in dilative sands, a mechanism that may develop in sloping layered deposits, have received little attention. More importantly, advanced constitutive models have not been assessed for their ability to capture liquefaction triggering under 'non-undrained' cyclic loading, limiting the ability of advanced numerical analyses to address the shortcomings of simplified liquefaction assessment procedures for stratified deposits.

Addressing these gaps requires a systematic assessment of constitutive model performance versus element-level experiments under representative drainage conditions and, where necessary, the development and validation of improvements to either model calibration or constitutive definitions. Validated constitutive models can then be employed in boundary-value analyses of deposits which can include different permeability layers, improving the reliability of liquefaction triggering predictions.

1.2 Research aims and objectives

This research aims to evaluate the implications of co-seismic drainage for constitutive modelling of liquefaction triggering at the element level and for numerical analyses of layered deposits at the system level. The study focuses on bounding surface plasticity models of the SANISAND family, which are widely used for liquefaction modelling in both research and engineering practice.

First, SANISAND constitutive models, developed and typically calibrated using undrained element tests, are systematically evaluated against experimental data obtained under non-standard drainage monotonic and cyclic loading. Where limitations are identified, targeted improvements to model calibration and parameter definitions are developed, validated, and assessed. Finally, the updated constitutive models are implemented and validated in boundary-value analyses at the scale of a deposit, to evaluate the improvement in predictions and to reliably investigate the implications of drainage for liquefaction triggering under realistic field conditions.

The key objectives undertaken to accomplish the aforementioned research aims are the following:

1. Generate a database of monotonic triaxial tests under undrained, fully drained, and coupled deviatoric to volumetric strain paths, which are relevant for sloped stratified profiles that include liquefiable layers. The coupled strain paths will focus on volumetric expansion due to water inflow, as this condition is critical for stability.
2. Assess the ability of bounding surface plasticity models of the SANISAND family to reliably capture the experiments of the aforementioned experimental database on monotonic loading, with particular importance given to the coupled strain triaxial tests, which fall outside of the range of experiments typically used for model calibration.
3. Where shortcomings are identified, develop and validate improvements to the SANISAND constitutive framework, examining both constitutive parameter definitions and updated model calibration protocols.
4. Assess the ability of SANISAND models with conventional calibration based on undrained tests to reproduce cyclic triaxial tests under water inflow conditions, relevant for liquefaction triggering in layered deposits.
5. Where necessary, develop and validate improvements of SANISAND models, to better predict cyclic behaviour under conditions of water inflow.
6. Validate the proposed constitutive model developments through fully coupled numerical analyses of a uniform soil column, by comparison to published centrifuge testing data.

7. Numerically investigate the influence of co-seismic drainage and layer interaction on liquefaction triggering in stratified deposits using the validated constitutive models, and evaluate the implications for simplified liquefaction assessment procedures and advanced numerical analyses.

1.3 Thesis outline

The thesis contains nine chapters which are listed below along with a brief description of their contents. The thesis begins with an element-level experimental investigation that includes unconventional drainage conditions, followed by constitutive model assessment and formulation or calibration updates as required, first for monotonic and then for cyclic loading. Finally, the thesis concludes with boundary-value validation and a numerical investigation on the implications of drainage for layered deposits.

1. **Chapter 1**: *Introduction*

   This chapter gives an overview of the phenomenon of liquefaction, its impact on the built environment and explains the methods used in practice to assess liquefaction susceptibility. The shortcomings of these methods are highlighted, the gaps in research are identified and the aim of this thesis is established. Key objectives to achieve the stated aim are briefly enumerated.

2. **Chapter 2**: *Literature review*

   This chapter gives a detailed description of the liquefaction phenomenon and the types of soil failures related to it. Background on undrained monotonic and cyclic behaviour of sands is provided and the basis of simplified procedures used in practice for liquefaction assessment is outlined. Subsequently, experimental, analytical and field evidence for the occurrence of co-seismic drainage is reviewed at the element and the deposit scale. Finally, numerical approaches for analysing liquefaction triggering in layered deposits are discussed.

3. **Chapter 3**: *Constitutive modelling*

   This chapter introduces the SANISAND family of constitutive models employed throughout the thesis in the chronological order of their development. For some models, the constitutive equations were transformed from multiaxial to triaxial space for use in this thesis. Constitutive developments proposed in this thesis are introduced in the relevant chapters where they are developed and validated.

4. **Chapter 4**: *Experimental testing*

   This chapter presents the experimental programme, including the testing methodology, sample preparation and the database of monotonic triaxial tests under undrained, drained and coupled strain conditions conducted by the author. The experimental results provide the basis for the constitutive model assessment and developments presented in the following chapters.

5. **Chapter 5**: *State parameter for coupled shear-volumetric strain paths using a SANISAND model*

   This chapter investigates the ability of the SANISAND family of models to capture monotonic behaviour under undrained, drained and coupled strain conditions. An analytical-cum-numerical framework is developed to relate specific instability points on coupled strain paths to the state parameter, revealing limitations in the conventional state parameter definition. An updated state parameter is proposed and shown to substantially improve predictions of monotonic behaviour under coupled strain paths.

6. **Chapter 6**: *Identification of the critical state line of sands using coupled shear-volumetric strain paths*

   This chapter applies the analytical-cum-numerical framework developed in Chapter 5 to infer the critical state line of highly dilative sands for which conventional triaxial testing cannot reach the critical state because of strain, load, or instrumentation constraints, thus obstructing the typical SANISAND calibration process. An example using coupled strain

paths on Congleton sand is presented, where the critical state line is inferred and used along with an updated state parameter function to calibrate a SANISAND model. The resulting calibration is shown to reproduce the monotonic behaviour of Congleton sand under both undrained and coupled strain conditions.

7. **Chapter 7**: *Assessment and calibration of double surface constitutive models for cyclic loading under volumetric expansion*

   This chapter assesses the ability of three bounding surface plasticity models, namely DM04 (Dafalias et al., 2004), SANISAND-MSf (M. Yang et al., 2022), and PM4Sand3D (Kippen et al., 2026), to reproduce the cyclic response of sands under both undrained and volumetric expansion conditions, as captured in published element tests. Element-level observations hint towards the importance of the bulk modulus in capturing the unconventional drainage experiments. Two calibration schemes for the bulk modulus are undertaken, (a) a typical calibration through the shear modulus and Poisson's ratio, as suggested in literature, and (b) a direct calibration from isotropic unloading-reloading data. Simulations of cyclic triaxial tests under constant volumetric expansion rates are used to generate liquefaction resistance curves and evaluate model performance. The direct calibration of the bulk modulus is shown to significantly improve predictions of liquefaction triggering under volumetric expansion.

8. **Chapter 8**: *Numerical analysis of liquefaction triggering in layered deposits*

   This chapter implements the constitutive developments proposed in Chapter 7 in fully coupled effective stress analyses of one-dimensional soil columns using the finite element code OpenSees. The updated SANISAND-MSf model is first validated against published centrifuge test data for a uniform deposit, demonstrating that the proposed bulk modulus calibration significantly improves predictions when co-seismic drainage becomes important. The validated model is then used to investigate idealised layered deposits inspired by real cases where simplified liquefaction assessment procedures produce 'false-negative' or 'false-positive' predictions. Conclusions are drawn about co-seismic drainage and layer

interaction effects on liquefaction triggering, the range of reliability of current stress-based simplified methodology predictions, and the shortcomings of typical bounding surface plasticity model calibration methods.

9. **Chapter 9**: *Conclusions*

   This chapter condenses the principal findings of the thesis, evaluates the extent to which the research aims have been achieved, discusses the limitations of the work, and identifies priorities for future research.

Chapter 2

Literature review

2.1 Introduction

Liquefaction is a complex phenomenon involving soil stiffness and strength degradation due to increased pore pressures caused by a rapid monotonic or cyclic disturbance, that can lead to permanent soil deformations. The loss of strength and deformations have consistently resulted in catastrophic failures of infrastructure over the past decades, for instance, in the 2010-2011 Christchurch earthquakes (Cubrinovski, 2013), 2011 Tohoku earthquake in Japan (Ishihara et al., 2014) and the 2023 Turkey-Syria earthquakes (Tobita et al., 2024). Liquefaction has been primarily associated with loose saturated cohensionless soils (Kramer, 1996). Upon an external perturbation, the loose soil matrix tends to densify. Due to the rapid nature of the imposed loading, the pore water in the soil matrix is unable to escape to facilitate densification, giving rise to an undrained condition. As a result, pore pressures begin to rise. Eventually, soil grains can loose contact with each other due to the increasing pore pressure and decreasing effective stress (σ'), and reach a liquefied state, see figure 2.1. An excessive build-up of pore pressures that results in $\sigma' = 0$ is known as initial liquefaction (NRC, 1985).

The reduction in effective stress directly impacts the shear strength of soil. When a static shear stress is present, as for instance in a slope, the shear strength of liquefied soil may fall short

of that required to maintain equilibrium under a seismic disturbance. The unbalanced static shear stress triggers sudden large permanent deformations of the soil mass resulting in flow liquefaction or flow failures. Such flow slide failures led to the destruction of the Sheffield Dam in the 1925 Santa Barbara earthquake (Kramer, 1996). When the static shear stress is minimal and the shear strength of liquefied soil remains sufficient, as for instance in a level deposit or in gently sloping ground, cyclic mobility failures are observed. During these failures, large transient ground oscillations of the liquefied soil driven by both cyclic and static shear stresses occur that lead to permanent deformations such as lateral spreading. For level-ground conditions where no static shear stress exists, the dissipation of excess pore pressures, which continues even post shaking, leads to vertical settlement of soil, settlement and rotation of structures, development of sand boils and potential flooding. During the 2010-2011 earthquakes in Christchurch, New Zealand, severe lateral spreading and ground subsidence occurred and critical infrastructure and utility lines were damaged beyond repair (Cubrinovski, 2013).

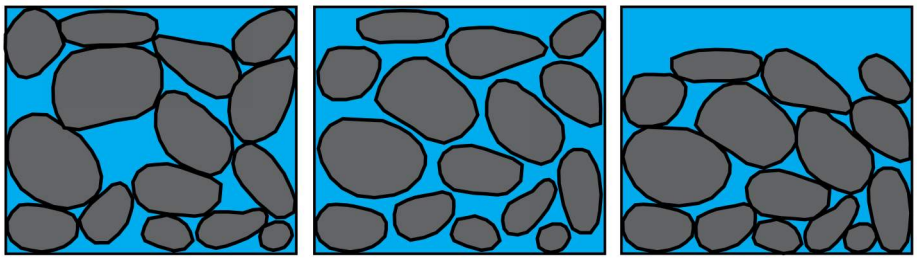

(a) Before earthquake (b) During earthquake (c) Post earthquake

Figure 2.1: Particle arrangement during liquefaction in saturated sand

2.2 Liquefaction susceptibility

A preliminary sense of soil vulnerability to liquefaction can be inferred from the site seismology, geology, composition and the current stress state. Correlations between earthquake intensity and epicentral distance of liquefied sites established from post-earthquake field surveys, provide an indication of areas where liquefaction can be triggered in the future (Galli, 2000). The depth of

the groundwater table plays a significant role in soil saturation, which facilitates liquefaction. Studies on the physical characteristics of liquefiable soil from past events reveal that newly deposited, loose, cohensionless soils with uniform grain size distribution have a higher tendency to liquefy because they have a greater densification potential that facilitates the accumulation of excess pore pressures (Hwang et al., 2003; Kramer, 1996). Well-graded soils with angular grains typically have lower liquefaction susceptibility as their closely packed structure has a lower tendency for volume change. Hence, most recorded liquefaction cases involve sandy soils and therefore extensive laboratory tests simulating liquefaction exist for sands.

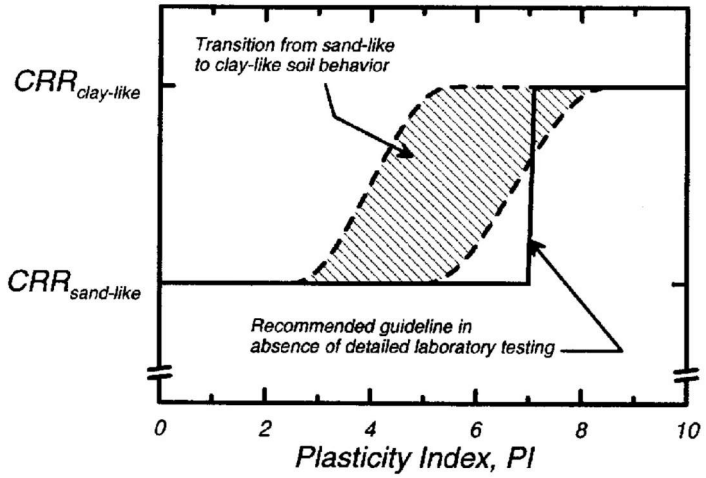

Figure 2.2: Illustration of transition of fine-grained soils from sand-like to clay-like behavior with increasing plasticity index, reproduced from Boulanger and Idriss (2006)

Recent earthquakes have also revealed the propensity of fine-grained soils to liquefy depending on their plasticity characteristics. Liquefaction of low plasticity silts was found to be the primary cause of extensive damage in the 1999 Kocaeli earthquake, Turkey (Bray et al., 2004). Boulanger and Idriss (2006) showed that fine-grained soils exhibit monotonic and cyclic undrained loading behaviour that range from sand-like to clay-like. Depending on the plasticity index (PI), fine-grained soils can undergo liquefaction failure similar to sands, exhibiting high excess pore pressures with diminishing values of the effective confinement pressure, or undergo cyclic softening similar to low plasticity clays, where the excess pore pressures reach a limiting value that does not nullify the effective confinement pressure, but rapidly increases strains, dis-

sipating more energy than sands per loading cycle. Their recommendation on determining soil behaviour based on the plasticity index is shown in figure 2.2, where the vertical axis represents the cyclic strength. Fine-grained soils falling in the clay-like zone with high plasticity index aren't susceptible to liquefaction due to sufficient cohesion. Low plasticity clay-like soils can be evaluated for liquefaction potential based on established field and empirical procedures for monotonic undrained shear strength as it is closely related to the cyclic strength. Low-plasticity fine-grained soils behave fundamentally like sand and are evaluated based on the initial state of stress and density characteristics as discussed in the following sections.

2.3 Undrained behaviour of sand under monotonic loading

The undrained behaviour of sand under monotonic loading has been investigated in laboratory experiments by several researchers (Castro, 1969; Ishihara, 1993; Kramer and Seed, 1988). Soil specimens are isotropically or anisotropically consolidated before undrained shearing. Loose samples show contractive behaviour. Upon reaching the peak deviator stress, a sudden loss of strength with rapid accumulation of strains ensues in stress-controlled tests. A contrasting behaviour is observed for dense samples, where initial contractive behaviour quickly turns to dilative with strength gain until large strains. Medium dense sand initially follows a contractive trend as that of loose samples until a point where excess pore pressure begins to drop and the sample gradually gains strength, similar to a dilating dense sample. The point where the behaviour turns from contractive to dilative is called the point of phase transformation. Castro (1969) concluded that dense soils do not develop flow liquefaction failures under static loading whereas loose sands can reach flow liquefaction conditions after reaching their peak strength. Medium dense sands undergo 'limited' flow liquefaction beyond the peak deviator stress and until the phase transformation point (Ishihara et al., 1975), see figure 2.3.

Sladen et al. (1985) identified the existence of a "collapse surface" in three-dimensional void ratio-shear stress-normal stress space from undrained triaxial tests on sands. When at the

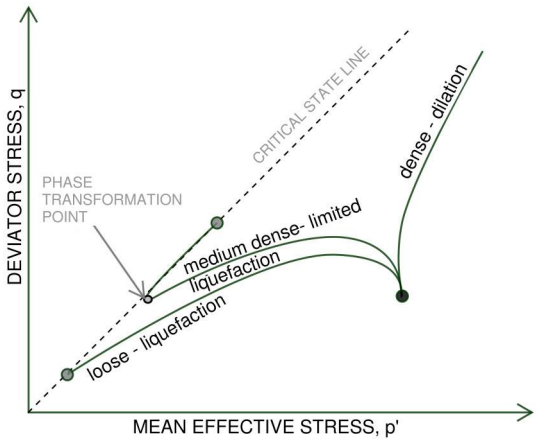

Figure 2.3: Liquefaction susceptibility in dense, medium dense and loose sand under static loading, recreated from Kramer (1996)

surface, an instability is observed with instantaneous build-up of strains until the point of mobilisation of residual strength, i.e. the strength at large strains. The "collapse surface" represents the line joining the peak strengths in $p' - q$ (mean effective stress - deviator stress) space and its slope increases with increasing density. Depending on the initial state, flow liquefaction potential can be assessed by examining whether the soil state approaches the collapse surface when a disturbance generates excess pore pressures. Vaid and Chern (1985) proposed a similar surface to detect initiation of flow liquefaction which was the "collapse surface" truncated at the steady state point in stress space (represents stress ratio at failure, discussed in the following sections), called the flow liquefaction surface (FLS), see figure 2.5. Soil states below the steady state point dilate to reach the failure surface and therefore do not undergo flow failures. Kramer and Seed (1988) also discerned the importance of peak strengths in determining the onset of flow liquefaction. The ratio of peak strength to the incident shear stress from external perturbation was introduced as a measure of the potential for flow liquefaction. Additionally, the severity of liquefaction-induced deformations was related to the normalised difference in peak strength and residual strength at large strains (Ishihara, 1993; Kramer and Seed, 1988). It was further concluded that the potential for flow liquefaction decreases with increasing relative density, increasing confining pressure and decreasing initial shear stress levels.

2.4 Undrained behaviour of sand under cyclic loading

A wealth of publications use experiments to examine the undrained behaviour of sand under cyclic loading, aimed primarily at capturing the behaviour of sand in level deposits (Ishihara et al., 1975; Vaid and Chern, 1983). An isotropically consolidated loose sand subjected to cyclic loading with stress reversals undergoes gradual build-up of pore pressures until initial liquefaction is triggered ($\sigma' = 0$), as shown in figure 2.4. In stress-controlled tests, cyclic axial strains also progressively develop with the loading cycles. Vaid and Chern (1983) deduced from several cyclic triaxial test data that the strain accumulation is significant only after a critical effective stress ratio (q/p') is reached. Flow deformations at this stress ratio may be triggered during the compressional or extensional phase of loading. The effective stress greatly reduces until the phase transformation line is approached. At this point, the sample undergoes dilation, an increase in effective stress and follows the drained failure envelope until a reversal of loading. Unloading leads to the stress path traversing through the transient liquefaction state ($\sigma' = 0$) and following the opposite failure envelope. This back and forth through the transient liquefaction state continues and strain is accumulated in each cycle of loading on both compression and extension sides.

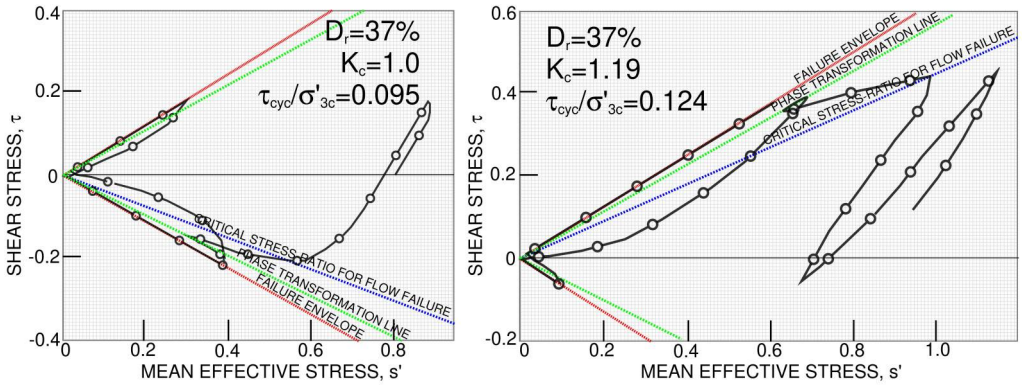

Figure 2.4: Undrained cyclic behaviour of sand under isotropic consolidation (left) and anisotropic consolidation (right), recreated from Vaid and Chern (1983)

Conversely, the cyclic loading response of dense and medium dense sands were found to accrue a lower magnitude of residual strains than loose sands. Initial cycles of loading lead to

gradual increments of pore pressures and strains. Upon reaching the phase transformation point, pore water pressure decreases due to dilation. The increase in pore pressure during unloading pushes the stress state closer to the transient liquefaction state. The stress path remains in a steady loop within the failure envelope similar to the loose sample, accumulating significant strains only beyond the phase transformation point. For anisotropically consolidated samples, i.e. samples with an initial static shear stress, stress reversal may not occur under cyclic loading. Pore pressures increase progressively until a terminal value which is lower than the initial confining pressure ($\sigma' > 0$). If stress reversal occurs, initial liquefaction is triggered ($\sigma' = 0$) as shown in figure 2.4. Kramer (1996) identified zones of initial stress states, for soils isotropically

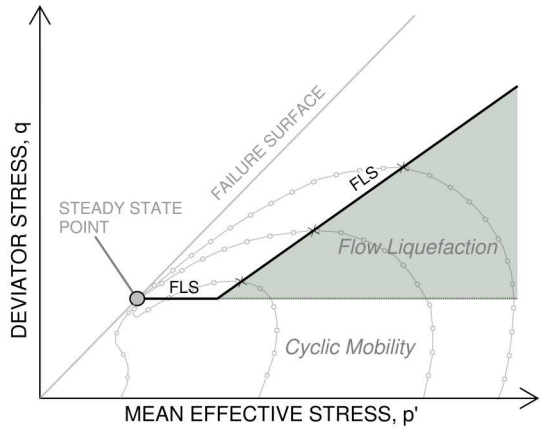

Figure 2.5: Zone of susceptibility to flow liquefaction and cyclic mobility, recreated from Kramer (1996)

consolidated to the same initial void ratio, where flow liquefaction and cyclic mobility could be triggered under cyclic loading. Figure 2.5 shows two distinct zones in stress space bounded by the flow liquefaction surface and the steady state strength. The reader is referred to section 2.5 for the definition of steady state. Initial states in the shaded zone have initial static shear stress greater than the steady state strength and can be pushed towards the flow liquefaction surface (FLS) under an undrained cyclic disturbance, triggering a flow liquefaction failure. Below the shaded zone, the initial static stresses are lower than the steady state strength. Under a cyclic load, the stress path is gradually pushed towards reducing mean effective stress until cyclic mobility failure. For cyclic shear stress not causing stress reversal and where the steady state

strength is not exceeded, the stress path reaches the drained failure envelope and moves along it under continued cyclic loading, accruing significant permanent strains with each loading cycle. If the steady state strength is exceeded, the stress path momentarily crosses the FLS before reaching the failure envelope. Large strains are accumulated at these momentary instabilities as well. For cyclic shear stress causing stress reversal, the rate of excess pore pressure generation increases with stress reversals. The stress path attains a butterfly-loop configuration, attaining $p' = 0$ at each half cycle, referred to as initial liquefaction.

2.5 State parameter

An important feature of soil behaviour was identified upon the execution of monotonic and cyclic experiments by several researchers where the soil upon shearing reached a unique state of stress and density as shear deformations continued. Roscoe et al. (1958) called this the critical state and defined it as the state achieved at large strains, where unlimited deformation can occur with no change in volume, at constant normal and shear stress. The locus of critical state points in void ratio (or density) and effective confining stress space gives the critical void ratio line, also known as critical state line (CSL). Though the framework of Critical State Soil Mechanics (CSSM) by Schofield and Wroth (1968) was initially developed for clays, the CSL is commonly employed in modelling of sand behaviour. Another term, the 'steady state' has also been in use for sands. It is defined by Poulos (1981) as follows: 'The state in which the mass is continuously deforming at constant volume, constant normal effective stress, constant shear stress, and constant velocity. The steady state of deformation is achieved only after all particle orientation has reached a statistically steady state condition and after all particle breakage, if any, is complete so that the shear stress needed to continue deformation and the velocity of deformation remain constant'. The critical and steady state have in practice often been used without distinction (Been et al., 1991). In this thesis, the term critical state has been used and the locus of points reaching this state is referred to as the CSL. This terminology is commonly used within

the context of bounding surface plasticity models, except for some of the fabric considerations of the anisotropic critical state theory (e.g., Li and Dafalias, 2012; Theocharis et al., 2019) that are more aligned with the steady state definition. The critical state line in stress and void ratio space is unique for a given soil. Irrespective of initial conditions and stress path, the soil will attain the same density at critical state under the same effective confining stress (Been et al., 1991; Verdugo and Ishihara, 1996). Nevertheless, the extension and compression critical states are distinct from each other due to anisotropy pertaining to the direction of the major principal stress with reference to the deposition plane of the soil samples.

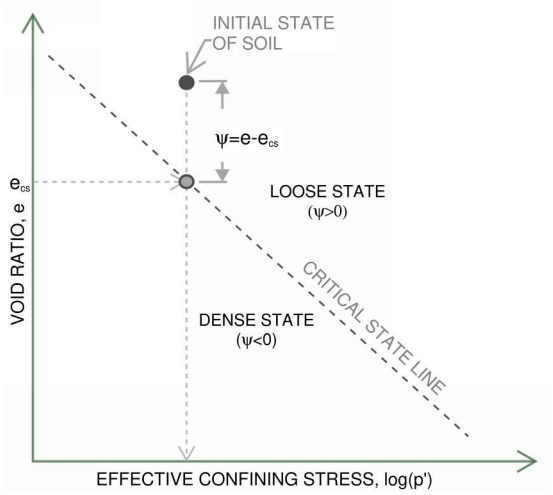

Figure 2.6: State parameter (ψ), after Been and Jefferies (1985)

A generic characterisation of soil is often made by relative density measures regarding its contractive or dilative nature. Looser soil specimens show contractive behaviour when sheared whereas denser soil specimens show dilative behaviour. However, contractive behaviour of dense sand has been identified under high confining pressures, as has dilative behaviour of loose sands under low confining pressures. This ambiguity is resolved by describing the relative position of the initial states from the critical state line. Roscoe (1963) first observed that the behaviour of a sand element can be predicted by its proximity to the CSL in the void ratio - mean effective stress ($e - p'$) space. The concept of the state parameter was introduced by Been and Jefferies (1985) to quantify the relative distance from the critical state line - a positive distance implies contractive soils and a negative distance implies dilative soils, see figure

2.6. The state parameter has since been incorporated into soil constitutive models to define the evolution of important physical properties such as strength and dilatancy (e.g., Boulanger and Ziotopoulou, 2015; Dafalias et al., 2004; Jefferies, 1993; Li and Dafalias, 2000; Li et al., 1999; Liu et al., 2022; Papadimitriou et al., 2001; Taiebat and Dafalias, 2008; M. Yang et al., 2022). Other definitions of the state parameter exist in literature, such as the state pressure index, relative dilatancy index, etc. (e.g., Bolton, 1986; Dafalias et al., 2004; Lashkari, 2009; Wan and Guo, 1998; Z. L. Wang et al., 2002), but the Been and Jefferies (1985) state parameter, ψ, is the most widely used.

2.6 Fabric

Besides the state parameter, another variable that plays a significant role in characterising the behaviour of sand is the fabric. Fabric relates to the arrangement of particle grains in the sand matrix and includes an overall description of particle contacts, direction and distribution of major axis orientation (Been et al., 1991). At large strains, sufficient particle rearrangement occurs for the initial fabric to be completely eliminated (Ishihara, 1993). As a result, it has minimal impact on the location of the critical state line in triaxial compression. However, the trajectory to the critical state, location of critical state line in triaxial extension and the inherent tendency of sands to dilate/contract differs depending on the initial fabric (Z. X. Yang et al., 2008). Numerous studies investigated the micromechanical fabric properties using discrete-element method analyses during undrained and drained monotonic and undrained cyclic shearing of sands (R. Wang et al., 2019; Yimsiri and Soga, 2001; Yimsiri and Soga, 2010). These studies indicated that when soil samples are sheared in the direction of highest degree of contact normals, the soils show stiffer and more dilative behaviour than when sheared in an orthogonal direction to contact normals. The initial fabric evolves with continuous shearing, the fabric anisotropy changing rapidly when transitioning from contractive to dilative behaviour.

The evolution of fabric with dilatancy has been incorporated in the parent SANISAND model

by Dafalias and Manzari (2004). The influence of inherent fabric anisotropy was incorporated using an anisotropic state variable in the definitions of dilatancy (strength) and plastic modulus (stiffness) in critical state based bounding surface plasticity models (Dafalias et al., 2004; Li and Dafalias, 2002). These models capture the effect of different loading manners and directions on soil samples with same initial fabric. Z. X. Yang et al. (2008) developed an image-analysis technique combined with a mathematical approach to measure the initial fabric at micro level under different sample preparation methods. They incorporated the fabric model into the Li and Dafalias (2002) constitutive to calibrate and validate simulated results with laboratory tests.

Li and Dafalias (2012) presented the Anisotropic Critical State Theory (ACST) that accounts for fabric anisotropy at critical state as a constitutive ingredient, which evolves to approach its critical state value, similar to the state parameter. Petalas et al. (2020) incorporated the ACST into the parent SANISAND model (Dafalias and Manzari, 2004) to include the evolution of fabric anisotropy on the mechanical response of sands under various densities, confining pressures and loading directions. A significant dependency of failure mechanisms on evolution of fabric anisotropy has been demonstrated experimentally and numerically (R. Wang et al., 2019; Yu et al., 2013), that could be very consequential for current liquefaction resistance evaluation procedures. Although research on fabric effects is gaining momentum (Garcia et al., 2024; Moller et al., 2024), there is not a conclusive method to accurately quantify and qualitatively assess its implications on cyclic loading response of soils. Therefore, replication of natural deposition methods in laboratory testing is desirable to maximise the applicability of laboratory results in calibration of these constitutive models.

2.7 Liquefaction susceptibility assessment

2.7.1 Simplified procedures

Extensive studies with the underlying assumption of undrained conditions have formed the backbone for empirical and semi-empirical methodologies used to determine liquefaction susceptibil-

ity. Seed and Idriss (1971) proposed the simplified procedure which is a stress-based framework to compare the earthquake time history and the liquefaction resistance of soil, both expressed as an equivalent uniform cyclic shear stress subjected to the same number of loading cycles. The maximum earthquake-induced shear stress (τ_{cyc}) is numerically computed from the peak ground acceleration (a_{max}) and the initial total vertical stress (σ_{v0}), $\tau_{cyc} = 0.65\frac{a_{max}}{g}\sigma_{v0}r_d$. The reduction factor r_d reduces the peak ground acceleration to the acceleration value at a specific depth (Idriss and Boulanger, 2008). The liquefaction resistance is determined from a series of undrained cyclic triaxial tests or simple shear tests. The number of cycles required to generate excess pore pressures equal to the initial confinement pressure ($R_u = 100\%$) are plotted against the normalised cyclic stress amplitude. These graphs constitute the cyclic resistance curves and are unique to soil density, initial confinement and initial shear to normal stress ratio.

The cyclic resistance ratio (CRR) required to initiate liquefaction and the equivalent earthquake-induced cyclic stress ratio (CSR) are compared along the soil depth to identify liquefiable zones. The cyclic stress ratio is computed based on the type of loading used to develop the CRR curves; for simple shear tests, the CSR is defined by the ratio of cyclic shear stress to initial effective vertical stress ($CSR_{ss} = \tau_{cyc}/\sigma'_{v0}$) and for triaxial tests, it is defined by the ratio of maximum cyclic shear stress to initial effective confining stress ($CSR_{tx} = q_{max}/2p'_0$). The two CSR values are related by a correction factor c_r such that $CSR_{ss} = c_r \cdot CSR_{tx}$. The cyclic stress ratios determined by the simplified procedure were computed for level-ground or gentle slopes that require modification for sloped surfaces and high confining pressures. The cyclic stress ratio is modified to incorporate the effects of initial static shear stress and high effective confining pressure by multiplying the cyclic stress ratio values for zero initial static shear stress and initial effective vertical stress of 100 kPa by the K_α and K_σ factors, respectively (Seed, 1983).

In more recent iterations of the simplified method described above, cyclic resistance has been linked to ground investigation values. Initial efforts were based on Standard Penetration Test (SPT) results (Seed et al., 1983; Tokimatsu and Yoshimi, 1983). An archive of ground investigation results and seismic stress ratios at sites with and without history of liquefaction

failures was developed. A critical *N* value (SPT blow counts) signifying the boundary between liquefiable and non-liquefiable soils was then obtained for varying seismic stress ratios. To further extend the use of SPT results, undisturbed samples were obtained by the freezing method and were subjected to cyclic undrained triaxial tests. The cyclic shear stress ratio for a given amplitude of shear strain was empirically related to the SPT resistance values (Idriss and Boulanger, 2010). From this empirical relationship, the CRR at a site could be obtained from the measured SPT blow count value and compared with the CSR. More recently, the Cone Penetration Test (CPT) and shear wave velocity measurements have replaced SPT as ground investigation methods to assess liquefaction potential (Boulanger and Idriss, 2014).

As case histories have been added to the available archive, uncertainties in field data have been better quantified and a probabilistic version of CPT-based liquefaction triggering model has been developed (Boulanger and Idriss, 2016). Alternative energy-based methods for predicting liquefaction potential have also been developed that are founded on the undrained assumption (Berrill and Davis, 1985). In these methods, empirical relationships between excess pore pressure and dissipated energy are derived from extensive undrained cyclic triaxial testing (Green et al., 2000). The seismic input energy obtained from one-dimensional dynamic soil response analyses is then compared with the dissipated strain energy from tests to assess liquefaction potential (Kokusho, 2013). A similar method to the stress-based simplified framework that uses cyclic strains in lieu of cyclic stresses to compute the earthquake loading and liquefaction resistance have also been proposed using data from undrained tests (Dobry et al., 1982). Nevertheless, these simplified procedures based on experimental, theoretical and case history findings fail to capture the possibility of void redistribution as the assessment is confined to each individual soil layer and boundary interactions are not accounted for.

2.7.2 Numerical procedures

Numerical simulations based on effective stress formulations of soil constitutive behaviour that also consider nonlinear site response can be used to evaluate liquefaction potential in soil de-

posits, in lieu of the aforementioned simplified methodologies. For reliable simulations, an approach that couples the deformation of the soil skeleton and the motion of the pore fluid (u-P-U formulation) is required (Zienkiewicz and Shiomi, 1984), where 'u' represents the displacement of the solid phase, 'p' represents the pore pressure due to the fluid phase and 'U' represents the displacement of the fluid phase. An approximation of the general u-P-U formulation, the u-p formulation (Zienkiewicz and Shiomi, 1984), where the displacements (u) of the solid phase, i.e. the soil skeleton and pore pressure evolution (p) due to the fluid phase, i.e. pore-fluid is coupled, neglecting the fluid acceleration terms in the equation of motion for the total system, is used for most earthquake analysis problems (e.g., Kamai, 2011; Seid-Karbasi and Byrne, 2007; Z. Yang and Elgamal, 2002). The motion of the pore-fluid relative to the soil skeleton is driven by a diffusion equation through which pressures are directly computed. Advanced constitutive models that mimic the stress-strain response of soils, capturing nonlinear behaviour under cyclic loading, especially stiffness degradation with increasing excess pore-pressures, are used in these numerical formulations (Boulanger and Ziotopoulou, 2015; Dafalias et al., 2004; Prévost, 1985). Software implementing nonlinear response analyses include one-dimensional, soil column codes, such as DEEPSOIL (Hashash et al., 2018) and Cyclic1D (Elgamal and Yang, 2000), finite difference codes, such as FLAC3D (Itasca, 2011) and three-dimensional finite-element codes, such as OpenSees (McKenna, 2011).

It is worth noting that the reliability of numerical analyses depends on the constitutive models that govern soil behaviour. One-dimensional codes such as DEEPSOIL (Hashash et al., 2018) typically incorporate pore-pressure evolution based on semi-empirical stress, strain or energy-based models of pore pressure generation and any dilative tendency is ignored. CYCLIC 1D (Elgamal and Yang, 2000) can account for the shear-induced dilatancy mechanism through the use of a multi-yield surface plasticity model implemented by Prévost (1985) for frictional cohesionless soils and modified by Parra (1996) and Z. Yang (2000). Most constitutive models are typically not able to simulate the behaviour in the post-triggering, large deformation regime as they are built to capture behaviour up to liquefaction triggering. Bounding surface plas-

ticity models such as SANISAND-MSf (M. Yang et al., 2022) and PM4Sand (Boulanger and Ziotopoulou, 2015) are based on the critical state framework and are fundamentally more adept in simulating post-triggering soil behaviour. However, these models only perform reliably under the loading conditions for which they have been calibrated, i.e. for cyclic loading under undrained conditions. They are not developed or calibrated to capture void redistribution. As such, their performance when void redistribution occurs requires further assessment. Detailed framework of the bounding surface plasticity models assessed in this study is provided in chapter 3.

2.8 Liquefaction and drainage

2.8.1 Mechanisms involving drainage

Whilst liquefaction related phenomena have been extensively studied for saturated, loose cohesionless soils under undrained conditions (Ishihara, 1993; Verdugo and Ishihara, 1996), there is mounting evidence for the importance of drainage. This is especially true for soils within a stratified deposit (NRC, 1985; Seed, 1987). The NRC (1985) report illustrates the different processes through which liquefaction can be triggered, see figure 2.7. The process of liquefaction of loose soils in an undrained condition such that its steady-state strength is lower than the forces required for equilibrium is termed as *Mechanism A*, e.g. undrained shearing of soil with initial states within the flow liquefaction zone in figure 2.5. *Mechanism B* pertains to redistribution of void ratio due to movement of pore pressure in a soil layer confined within a globally undrained boundary. Consequently, a zone of densified soil and a zone of loosened soil is developed, which is now susceptible to liquefaction. *Mechanism C* pertains to outflow of water from a zone of high pore pressure into adjacent non-liquefied layers. The movement of pore pressure is facilitated by the spatial variation of piezometric pressure (Sivathayalan and Logeswaran, 2008) and the resulting fluid inflow leads to loss of strength of the overlying soil.

Experimental tests undertaken to investigate the effect of a low-permeability layer overlying

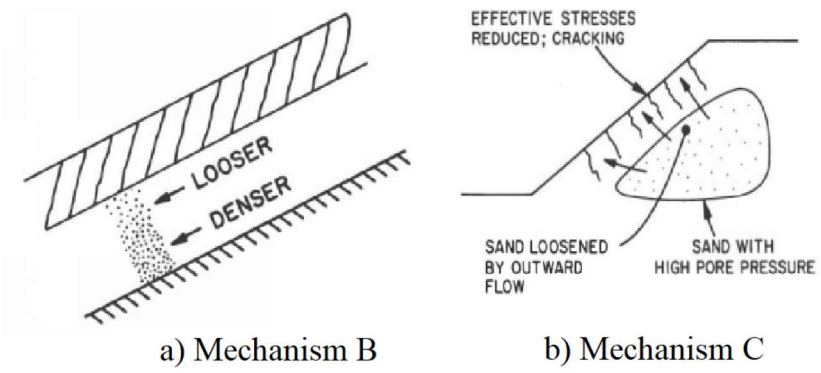

a) Mechanism B b) Mechanism C

Figure 2.7: Potential mechanisms for liquefaction failure through a) local void redistribution and b) global volume changes (NRC, 1985)

a liquefiable layer have confirmed the formation of a water film at the interface of the two layers during earthquake shaking (Kokusho, 1999). As the pore water rises upwards to dissipate the accumulated pressure, it loosens the top portion of the layer. The excess volume of pore-fluid remains trapped below the low-permeability sublayer and can form a thin water film, that can act as a shear failure plane. Adamidis and Madabhushi (2018) conducted dynamic centrifuge tests to investigate the drainage conditions during earthquake-induced liquefaction where they restricted drainage from a part of the soil sample by enclosing it within a flexible chamber. They observed the dissipation of excess pore pressures within the chamber along with the formation of a fluid film at the upper boundary. They concluded that the process of localised fluid flow and void redistribution can take place within the duration of ground shaking. Malvick et al. (2006, 2008) also observed fluid-flow effects in saturated slopes and presented analysis methods to quantify volumetric strains from varying excess pore pressures measured in centrifuge tests. In light of these findings, it can be argued that liquefaction evaluation must not be restricted to undrained studies on isolated layers, especially for stratified deposits. The possibility of pore-fluid movement across soil layers based on hydraulic gradient and permeability, and subsequent void redistribution can have a significant impact on the pore-pressure evolution and liquefaction susceptibility (Goren et al., 2010; Lakeland et al., 2014).

2.8.2 System response

The recent earthquakes at Christchurch, New Zealand in 2010-2011 have resulted in the generation of extensive field and laboratory test data that can be used to confirm the veracity of the available procedures for liquefaction assessment. One such investigation has been conducted by Tsaparli et al. (2020) on a liquefied site in Christchurch. The simplified liquefaction procedures predicted no occurrence of liquefaction at this site though in reality liquefaction did occur. Numerical analyses were performed to understand the cause of liquefaction triggering. The deposit was layered with non-liquefiable clayey silt (PI $\geq$ 10) at the strata and alternately placed with the liquefiable sand layer, underlain by gravel. The liquefiable layer was modelled using a bounding surface plasticity model calibrated from site-specific laboratory data. The non-liquefiable layers were assigned a simpler cyclic nonlinear model based on a modified hyperbolic backbone curve. A fully coupled u-p hydromechanical formulation (Zienkiewicz and Shiomi, 1984) was used in the one-dimensional finite-element analyses. The numerical results managed to predict the occurrence of liquefaction, unlike the simplified assessment made through CPT resistance and liquefaction resistance charts. Liquefaction occurrence was attributed to the existence of a low-permeability silt layer ($k = 1$ x 10^{-7} m/s) above the liquefiable sand layer ($k = 1$ x 10^{-4} m/s). The silt layer impeded the co-seismic upward pore-fluid flux and led to the loosening and subsequent liquefaction of the sand layer, a phenomenon that cannot be captured by simplified assessments. But even for such coupled effective stress analyses to reliably capture the actual response, appropriate modelling of the dynamic soil behaviour and updating of properties such as permeability during the liquefaction event were necessary (Tsaparli et al., 2020).

Cubrinovski et al. (2019) investigated the mechanism of liquefaction triggering in sites with evidence of liquefaction as opposed to sites with no evidence of liquefaction that had the same critical layer (layer most vulnerable to liquefaction in a deposit) characteristics in terms of depth and penetration resistances. The key difference distinguishing the liquefied and non-liquefied sites was the layering of the deposit, see figure 2.8. A critical zone was identified in the liquefied sites which included the critical layer immediately below the water table, along with vertically

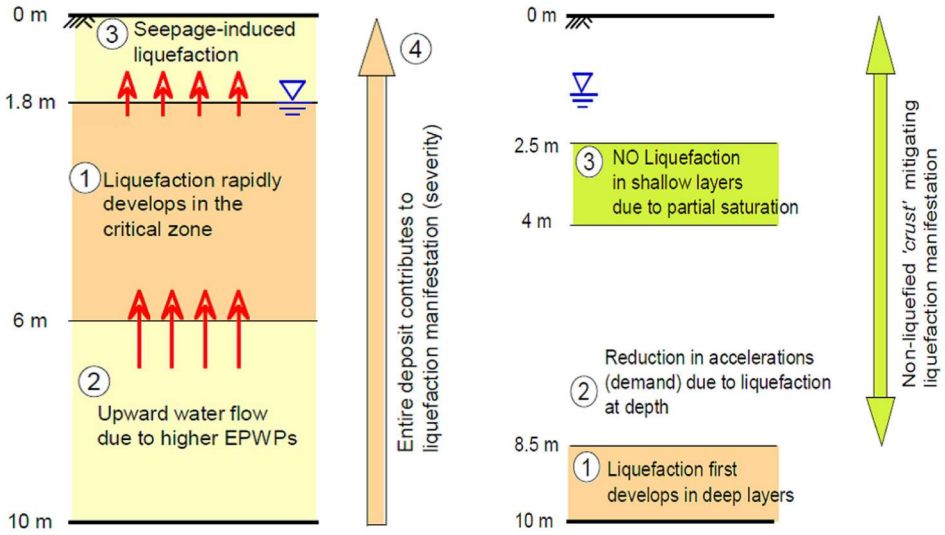

Figure 2.8: Schematic mechanisms of system-response impacting liquefaction manifestation in sites at Christchurch (Cubrinovski et al., 2019)

continuous layers of low liquefaction resistance further down. The crust consisted of liquefiable non-plastic silt. This type of layering worked as a connected unit during liquefaction manifestation, allowing pore-fluid flow and pore pressure redistribution. In addition to the internal void redistribution in the critical zone, higher excess pore pressures in non-liquefiable layers below led to seepage action and inflow of water, further aggravating the fluidisation and instability in the already liquefied zone (Cubrinovski et al., 2019; Ntritsos and Cubrinovski, 2022).

At the non-liquefied sites, vertically disconnected thin liquefiable zones were layered in between non-liquefiable zones and the deposits had a non-liquefiable crust at the top. A shallow critical layer was identified below the crust. However, the liquefiable layers at the bottom liquefied first and softened. This layer acted like a base isolation system, thereby reducing the seismic demand in the upper layers (Ntritsos and Cubrinovski, 2022). Partial saturation of overlying non-liquefiable layer further absorbed any fluid-flow and mitigated the occurrence of liquefaction in the shallow critical layer (Ntritsos and Cubrinovski, 2024). The simplified evaluation procedures underestimated occurrence of liquefaction in half of the liquefied sites and overestimated liquefaction failures in most of the non-liquefied sites. These erroneous predictions are due to the inability of the simplified procedures to account for the system response which results from the

cross-interaction effects between the layers within a deposit (Bullock et al., 2022; Cubrinovski and Ntritsos, 2024; Cubrinovski et al., 2019).

2.8.3 Non-standard drained behaviour of sands

Boundary conditions deviating from the idealised states of fully drained or undrained, where simultaneous generation and dissipation of excess pore pressures take place fall under 'expansive drainage', 'partial drainage' or 'excessive drainage' as shown in figure 2.9. However, strain path tests where "both the volumetric and shear strain rates are varied simultaneously during the tests and restriction on free volume change leads to accumulation of pore-water pressure" (as conducted in Nicot et al. (2013), Sivathayalan and Logeswaran (2008), Vaid and Eliadorani (2000), and Wanatowski et al. (2008)) have also been generally referred to as 'partially drained' tests in literature (Lashkari et al., 2021) for both expansive and contractive volumetric strain rates. Due to the ambiguity in nomenclature, in this study, boundary conditions other than the fully drained and the undrained are referred to as "non-standard drained" conditions. Additionally, non-standard drained tests where the volumetric strain rate is a proportion of the shear strain rate, are referred to as coupled shear-volumetric strain paths. Researchers exploring non-standard drained behaviour in monotonic testing have concluded that the undrained hypothesis may not reflect the worst case scenario for liquefaction susceptibility assessment (Suzuki et al., 2019; Vaid and Eliadorani, 2000; Wanatowski et al., 2008). Coupled shear-volumetric strain paths have been experimentally investigated on loose and dense sands to quantify the significance of conditions other than undrained or fully drained, typically regarding strain-softening and instability triggering (Chu and Leong, 2001; Chu et al., 2015; Jrad et al., 2012; Lancelot et al., 2004; Nicot et al., 2013; Sivathayalan and Logeswaran, 2008; Vaid and Eliadorani, 1998, 2000; Wanatowski and Chu, 2011). Vaid and Eliadorani (2000) conducted triaxial compression tests on saturated sand under fully drained, undrained and non-standard drained conditions using linearly coupled shear-volumetric strain paths, $\dot{\varepsilon}_v/\dot{\varepsilon}_1 = constant$. The tests indicated that the degree of drainage or the strain increment path controlled the effective stress increment, see

figure 2.9. This means that a given soil may be stable under undrained conditions and yet liquefy under non-standard drained conditions. Medium dense sand showing limited liquefaction (refer figure 2.3) under undrained conditions may show spontaneous liquefaction similar to contractive (loose) sands under an inflow condition. The shear stiffness was found to increase in sand layers under compressive volumetric strains and decrease under expansive volumetric strains indicating that an inflow of pore fluid from adjacent layers into the sand layer can potentially induce softening and loss of strength in an otherwise stable, non-liquefiable sand layer that exhibits dilation or limited liquefaction under undrained conditions as shown in figure 2.3.

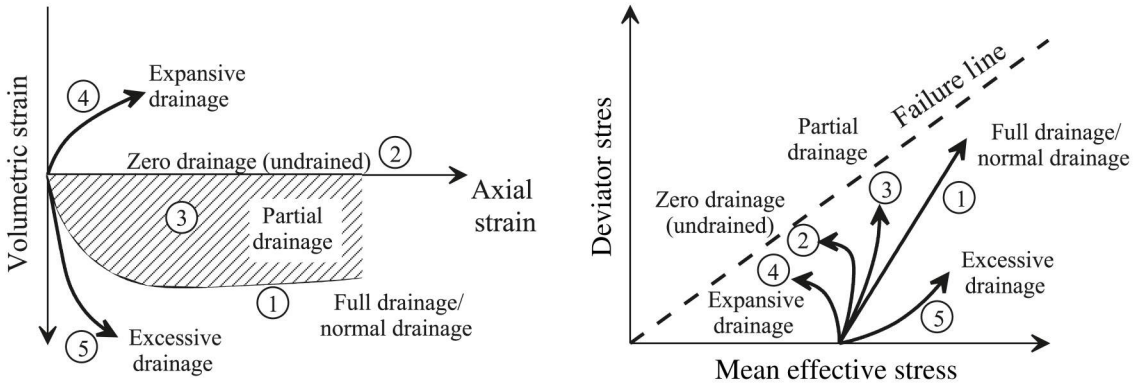

Figure 2.9: Schematic illustration of strain paths and associated stress paths under triaxial compression loading (Sivathayalan and Logeswaran, 2008)

For medium dense sand, Wanatowski et al. (2008) reported strain-hardening behaviour at inflow rates lower than the dilative strain rate at failure of fully drained tests and strain-softening at inflow rates higher than this threshold value. This indicates that instability could be triggered if the inflow strain paths imposed exceeded the sand's inherent capacity to dilate as obtained from drained compression tests. Sivathayalan and Logeswaran (2008) conducted non-standard drained tests using linear and nonlinear coupled strain paths. They observed that the friction angle mobilized at the instant of peak shear strength is dependent on the strain path. The friction angle at peak excess pore pressure and at ultimate failure is independent of the loading path or drainage conditions. Suzuki et al. (2019) inferred from their experimental campaign that under non-standard drained conditions, the soil behaves similarly to undrained conditions at

small strains and closer to fully drained conditions at large strains. In a more recent study by Adamidis and Anastasopoulos (2022), cyclic tests under constant water inflow rates were performed and it was shown that cyclic resistance was severely affected for even small inflow rates. They proposed a simplified methodology of superposition of isotropic unloading and undrained cyclic shearing to estimate cyclic resistance under constant water inflow rates, which is not accounted for in the current simplified procedures.

Thus, the non-standard drained experimental campaigns undertaken highlight even more severe mechanisms of failure than under the undrained condition. Note that these experimental studies were conducted under monotonic and cyclic loading with constant inflow rates. In reality, the volumetric strain evolution at layer interfaces would vary with time. Therefore, the behaviour of sand under time-varying volumetric strains due to a time-varying spatial distribution of pore pressure from seismic loading needs to be further investigated. Temporal changes in pore pressures and volumetric strains at layer boundaries can be computed using fully coupled effective stress analyses of layered deposits with advanced constitutive models equipped to capture non-standard drained behaviour at an element level. The SANISAND family of bounding surface plasticity models have been developed and refined over the years to replicate undrained cyclic behaviour of sand and are extensively used in numerical analyses of liquefaction triggering problems. Their ability to mimic behaviour under a range of drainage conditions needs to be evaluated at the element level so that their implementation at the system level portrays layer interactions appropriately.

Chapter 3

Constitutive modelling

3.1 Introduction

The stress-strain behaviour of soils is highly nonlinear and dependent on fabric anisotropy, stress state and history of loading. Robust constitutive models are essential to simulate such complex material behaviour, preferably with minimal model parameters. Efforts to capture soil response began with mimicking element-level behaviour observed in testing under specific loading conditions through the widely used classical isotropic hardening plasticity formulation. With the development of critical state theory (Roscoe et al., 1958; Schofield and Wroth, 1968), researchers implemented the theory of classical elastoplasticity within the critical state soil mechanics framework (Roscoe and Burland, 1968), which captured well the response of normally consolidated clays and to some extent the response of sands under monotonic loading. However, to adequately capture the cyclic response (excess pore pressure and shear strain accumulation) under short-term loading such as earthquakes, advanced plasticity formulations were adopted such as kinematic hardening, bounding surface plasticity and multiyield surface plasticity; Dafalias and Popov (1975), Mrŏz et al. (1978), and Prévost (1978) constituting some of the seminal works. The multiyield surface plasticity models (e.g., Elgamal and Yang (2000)) consist of a collection of nested yield surfaces, each defining regions of constant plastic moduli, that

can predict complicated stress paths of loading-unloading-reloading, but require larger computational memory. The bounding surface plasticity models eliminate the requirement of all surfaces but two, the inner yield surface or loading surface and the outermost bounding or limit surface and hence are often referred to as two-surface or double surface plasticity models (Prévost, 1982). Hardening rules are applied for both surfaces. The hardening of the yield surface depends on the distance from the current stress state to a projected stress point on the bounding surface, determined using a mapping rule (Dafalias, 1986). Bounding surface plasticity models for sands were further refined with the incorporation of critical state theory ingredients (Bardet, 1986) and the incorporation of the state parameter to control the evolution of surfaces. These changes allowed a single set of model parameters to predict the behaviour of sand at different relative densities.

The SANISAND family of constitutive models began with the work of Manzari and Dafalias (1997), which proposed a bounding surface plasticity model with kinematic hardening, ingrained with the concept of the state parameter within the critical state framework. Since its inception, the model has been incrementally refined to capture increasingly complex aspects of sand behaviour (Dafalias and Manzari, 2004; Dafalias and Taiebat, 2016; Petalas et al., 2019, 2020; Taiebat and Dafalias, 2008; M. Yang et al., 2022). Models within the SANISAND (acronym for 'Simple ANIsotropic SAND', coined by Taiebat and Dafalias (2008)) family are widely adopted for liquefaction modelling in research and to a certain extent in engineering practice, due to their ability to replicate both monotonic and cyclic behaviour with a unique set of model constants across densities and confining pressures.

In this chapter, a brief summary of the constitutive framework for each of the SANISAND plasticity models used in this thesis is presented. For simplicity, the constitutive relations for each model are provided in the triaxial space, either as existing in literature or following derivation from published multiaxial formulations. The following models are outlined: DM04 by Dafalias and Manzari (2004), which forms the basis for subsequent SANISAND models; SANISAND 2008 by Taiebat and Dafalias (2008), which is employed for monotonic investiga-

tions thanks to its relatively simple formulation, that however remains relevant for the monotonic response of more complex SANISAND iterations; SANISAND-MSf by M. Yang et al. (2022), which includes several improvements targeted at cyclic loading; and PM4Sand3D by Kippen et al., 2026, which is a new, three-dimensional generalisation of the plane strain model PM4Sand2D, that is widely used in academia and industry, partly aided by its inclusion in the finite element code PLAXIS2D. The conclusions drawn in the thesis for multiple SANISAND family models can be taken to apply for the wider framework, rather than be tied to model-specific constitutive ingredients.

3.2 Dafalias and Manzari, 2004 (DM04)

The DM04 model by Dafalias and Manzari (2004), also referred to as the ManzariDafalias model, is a refined version of the parent SANISAND model (Manzari and Dafalias, 1997), which incorporates a fabric tensor into the plastic modulus, that is tuned using an internal variable upon dilation. The model was predominantly developed to capture the reduction in stiffness upon dilative plastic volumetric changes in undrained cyclic loading. Like its parent model, it is a stress-ratio ($\eta = q/p'$) controlled bounding surface sand plasticity model built around the critical state soil mechanics framework by associating the state parameter ψ (Been and Jefferies, 1985) with the evolution of its surfaces. In triaxial space, its yield surface (f) is a narrow conical wedge, with the slope of the bisector represented by α (also known as the back stress ratio) and a fixed opening angle, represented by the parameter m, see figure 3.1. Elastic behaviour is restricted to stress states within the wedge for any loading direction and on the arms of the wedge upon a constant stress-ratio loading ($\dot{\eta} = 0$). Under varying stress-ratio loading on the wedge, plastic behaviour is triggered resulting in the rotation of the wedge, captured by the kinematic hardening variable $\dot{\eta}$ ($= \dot{\alpha}$). The constitutive relations are summarised in table 3.1. Dafalias and Manzari (2004) used a power relationship to define the critical state line from Li and Wang (1998). The slope of the phase transformation line, η_{PTS} is denoted by the dilatancy

surface stress ratio, $M^d_{c,e}$ and the peak stress-ratio states, η_{PSRS} are denoted by the bounding surface stress ratio, $M^b_{c,e}$ and both surfaces evolve as functions of the critical surface M^c and the state parameter ψ as noted in table 3.1. In the surface notations, subscript 'c' stands for triaxial compression loading and 'e' stands for triaxial extension loading. Note that in extension, the slope of the critical surface reduces by parameter c. Hence all three surfaces are shallower in extension than in compression in triaxial space.

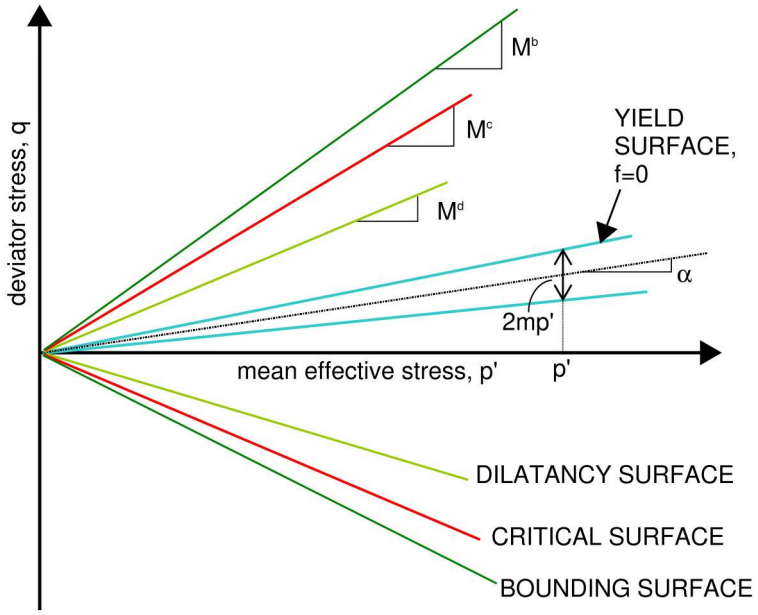

Figure 3.1: Schematic illustration of DM04 model surfaces in triaxial space, recreated from Dafalias and Manzari (2004)

The elastic strain increments, $\dot{\varepsilon}_v{}^e$ and $\dot{\varepsilon}_q{}^e$, and the plastic strain increments, $\dot{\varepsilon}_v{}^p$ and $\dot{\varepsilon}_q{}^p$, are defined by the incremental stress-strain relationships shown in table 3.1. G and K are the elastic shear and bulk moduli, respectively. H represents the plastic hardening modulus and is a function of the distance of the current stress state from the bounding surface. Hardening coefficient h is a function of the shear modulus constant G_0, hardening parameters h_0 and c_h, the stress ratio at the start of a loading process, η_{in} and the current stress state. Note that h can be expressed as either a linear or an exponential function of c_h and void ratio e (Taiebat and Dafalias, 2008). Dilatancy D is based on the distance of the current stress state from the dilatancy surface as shown in table 3.1, where coefficient A_d captures the effect of fabric changes on dilatancy. A_d

captures the fabric changes through the evolution of the macroscopic fabric-dilatancy internal variable 'z', which only changes upon dilation and allows for a highly contractive response upon post-phase transformation stress reversal. This model is used in this study for simulation and assessment of cyclic behaviour in chapter 7.

Equations	**Model Constants**	**Description**
Stress Quantities: $p' = (\sigma'_1 + 2\sigma'_3)/3$ $q = (\sigma'_1 - \sigma'_3)$	$\sigma'_2 = \sigma'_3$	σ'_i : Principal effective stress along i-th axis p' : Effective Confining Stress q : Deviator Stress
Strain Quantities: $\varepsilon_v = (\varepsilon_1 + 2\varepsilon_3)$ $\varepsilon_q = 2(\varepsilon_1 - \varepsilon_3)/3$	$\varepsilon_2 = \varepsilon_3$	ε_i : Principal strain along i-th axis ε_v : Volumetric Strain ε_q : Deviatoric Strain
Critical State Line: $e_{cs} = e_0 - \lambda(p'/p_{at})^{\xi}$	e_0 , λ , ξ	p_{at} : Atmospheric Pressure e_{cs} : Critical Void Ratio
Elasticity: $G = G_0 p_{at} \frac{(2.97-e)^2}{1+e}(p'/p_{at})^{1/2}$ $K = \frac{2(1+\nu)}{3(1-2\nu)}G$	G_0 , ν	e : Current Void Ratio; ν : Poisson's Ratio G : Elastic Shear Modulus K : Elastic Bulk Modulus
Yield Surface: $f = \lvert\eta - \alpha\rvert - m = 0$	m	α : Back Stress Ratio η : Stress Ratio q/p'
Strain Increments: $\dot{\varepsilon_q}^e = \dot{q}/3G$ $\dot{\varepsilon_v}^e = \dot{p'}/K$ $\dot{\varepsilon_q}^p = \dot{\eta}/H$ $\dot{\varepsilon_v}^p = D\lvert\dot{\varepsilon_q}^p\rvert$		$\dot{\varepsilon_q}^e$: Elastic Deviatoric Strain Increment $\dot{\varepsilon_v}^e$: Elastic Volumetric Strain Increment $\dot{\varepsilon_q}^p$: Plastic Deviatoric Strain Increment $\dot{\varepsilon_v}^p$: Plastic Volumetric Strain Increment H : Hardening Modulus; D : Dilatancy
Hardening Rule: $H = h(M^b_{c,e} \mp \eta)$ $h = b_0/\lvert\eta - \eta_{in}\rvert$ $b_0 = G_0 h_0 (1 - c_h e)(p'/p_{at})^{-1/2}$ or; $b_0 = G_0 h_0 exp(-c_h e)(p'/p_{at})^{-1/2}$	h_0 , c_h	$M^b_{c,e}$: Bounding Surface Stress Ratio h : Positive Hardening Parameter η_{in} : Stress Ratio at Loading Initiation Linear evolution of b_0 Exponential evolution of b_0
Dilatancy: $D = A_d(M^d_{c,e} \mp \eta)$ $A_d = A_0(1 + <sz>)$ $\dot{z} = -c_z < -\dot{\varepsilon}_v^p > (sz_{max} + z)$ $s = (\eta - \alpha)/\lvert\eta - \alpha\rvert$	A_0, c_z, z_{max}	$M^d_{c,e}$: Dilatancy Surface A_d : Dilatancy Coefficient s: $+1$ for compression, -1 for extension <> : Macauley Brackets $< x >= x$ if $x > 0$; $< x >= 0$ if $x \leq 0$
Surface Evolution Laws: $M^b_c = M^c exp(-n^b \psi)$ $M^b_e = cM^c exp(-n^b \psi)$ $M^d_c = M^c exp(n^d \psi)$ $M^d_e = cM^c exp(n^d \psi)$	M^c, n^b , n^d , c	$M^{b,d}_c$: Surfaces in Compression $M^{b,d}_e$: Surfaces in Extension M^c : Critical Surface Stress Ratio cM^c : Critical Surface in Extension ψ: State Parameter ($= e - e_{cs}$)

Table 3.1: Triaxial formulation of the DM04 model (Dafalias and Manzari, 2004)

3.3 SANISAND 2008

The SANISAND 2008 model by Taiebat and Dafalias (2008) is a modified version of its predecessor, DM04 (Dafalias and Manzari, 2004), refined with a p'-controlling cap to capture plastic deformations from grain crushing mechanisms at very high confining pressures. This enables the model to accumulate plastic strains under constant stress-ratio loading paths, a feature absent in the DM04 model. This model further abandons the need to store initial values of internal variables, such as η_{in} and z, which makes it computationally more efficient. The yield surface in triaxial space is very similar to the DM04 model, with the addition of a closed cap at the end of the conical wedge, see figure 3.2. The closed cap at the end of the wedge is activated under constant stress-ratio loading, $\dot{\eta} = 0$ to capture plastic deformations at high confining pressures. The location of the end cap, represented by P_0' in figure 3.2, thus, represents the isotropic hardening variable. As before, any stress state, represented by the stress ratio, η, lying within the wedge remains elastic and plastic deformations are accumulated only when the stress state falls on the arms of the wedge. The rotational hardening variable is represented by the back stress ratio, α and $\dot{\alpha}$ simulates the evolution of anisotropy under a varying stress ratio, $\dot{\eta} \neq 0$, unlike the DM04 model where stress ratio η controlled the kinematic hardening. The plastic volumetric and shearing strains are accumulated in two portions, contributed by a varying stress ratio and a constant stress ratio. Table 3.2 shows constitutive relations for the SANISAND 2008 model. The constitutive relations presented are for plastic deformations accrued only under varying stress-ratio loading. This simplification is appropriate for this thesis, as liquefaction studies are conducted at low confining pressure range, where particle crushing is typically not considered (e.g. Andrianopoulos et al., 2010; Kassas et al., 2021; Petalas et al., 2019; Taiebat et al., 2010; M. Yang et al., 2022). As liquefaction is triggered through gradual reduction in effective stresses, p' remains $<< P_0'$ and particle crushing does not contribute significantly to the plastic strains and strength characteristics. So the end cap of the yield surface that captures crushing related plastic strains at high confining pressures, remains inactivated throughout the numerical simulations conducted in this study. Additionally, in this thesis, the SANISAND 2008 model

(Taiebat and Dafalias, 2008) has been exclusively used for monotonic triaxial test simulation and assessment in chapters 5 and 6, due to its simpler formulation owing to the elimination of discrete memory variables, as exemplified in the later chapters.

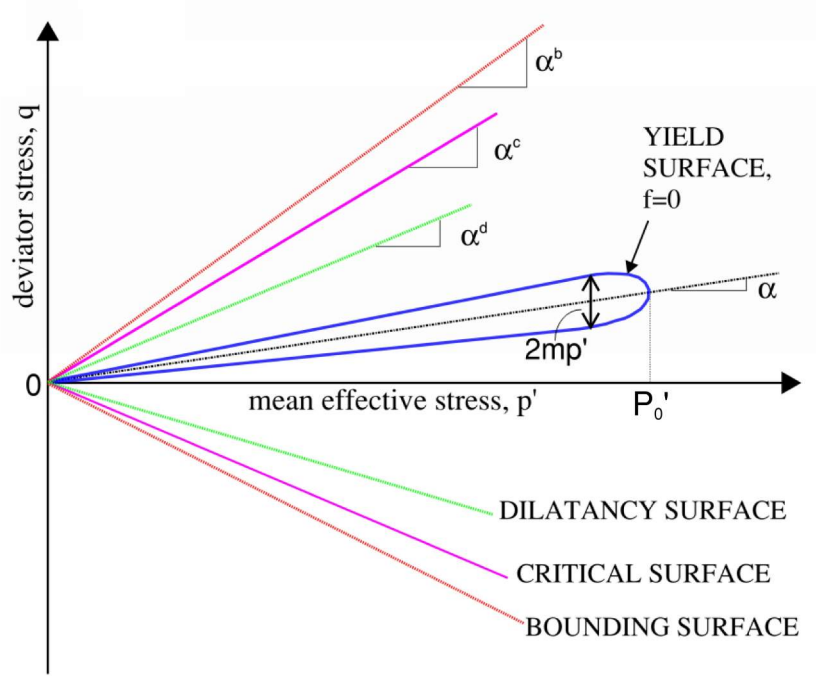

Figure 3.2: Schematic illustration of SANISAND 2008 model surfaces in triaxial space, recreated from Taiebat and Dafalias (2008)

The surfaces are represented by the back stress ratios; bounding surface by α^b and dilatancy surface by α^d, as shown in figure 3.2. The two surfaces evolve based on the critical surface, α^c and the state parameter, ψ, similar to the DM04 model. Alternate expressions for the evolution of surfaces based on a linear dependency on the state parameter have also been used (Manzari and Dafalias, 1997), as shown in table 3.2. At the critical state, the bounding and dilatancy surfaces collapse on the critical surface with $\psi \to 0$. The elastic response follows the hypo-elastic assumption, similar to the DM04 model. Although, an independent expression for the bulk modulus as a function of the current soil state has been proposed in this model, see table 3.2. Alternately, one modulus could be derived from the other using a constant Poisson's ratio, ν, which is the case for deriving the bulk modulus in the DM04 model, see table 3.1. The positive hardening parameter h no longer includes the internal variable η_{in} as in the DM04 model

but includes a new term b_{ref} that represents the diameter of the bounding surface, as noted in table 3.2. Similarly, the dilatancy coefficient A_d is no longer a function of the internal variable for fabric evolution z, but represents a model constant. For the full constitutive formulation in triaxial space including conditions where $p' > P'_0$, the reader is directed to Taiebat and Dafalias (2008). Using the model equations, the elastic stiffness matrix (D^e) and the elastoplastic stiffness matrix (D^{ep}) are obtained for $p' << P'_0$, see equation 3.1. The elastic and elastoplastic compliance matrices, C^e and C^{ep}, respectively are shown in equation 3.2. These matrices are used for concepts developed in the later chapters.

$$D^e = \begin{bmatrix} K & 0 \\ 0 & 3G \end{bmatrix}; \quad D^{ep} = \begin{bmatrix} \frac{p'HK+3GKs}{p'H+3Gs-DK\eta} & \frac{-3GKD}{p'H+3Gs-DK\eta} \\ \frac{3GK\eta s}{p'H+3Gs-DK\eta} & \frac{3Gp'H-3GKD\eta}{p'H+3Gs-DK\eta} \end{bmatrix} \tag{3.1}$$

$$C^e = \begin{bmatrix} 1/K & 0 \\ 0 & 1/3G \end{bmatrix}; \quad C^{ep} = \begin{bmatrix} \frac{1}{K} - \frac{D\eta}{p'H} & \frac{D}{p'H} \\ \frac{-\eta s}{p'H} & \frac{1}{3G} + \frac{s}{p'H} \end{bmatrix} \tag{3.2}$$

3.4 SANISAND-MSf

M. Yang et al. (2022) recently presented a new constitutive model, SANISAND-MSf, to better capture the cyclic behaviour in pre- and post-liquefaction stages by incorporating two additional constitutive ingredients, 'memory surface' denoted by 'M' and 'semifluidised state' denoted by 'Sf' to the reference two surface plasticity model DM04 by Dafalias and Manzari (2004). Therefore, this model is also used in this study for simulation and assessment of cyclic behaviour in chapter 7. The concept of memory surface has been added to bounding surface plasticity model for sands by Corti et al. (2016), and specifically to DM04 by Liu et al. (2019). However, the memory surface used in the SANISAND-MSf model differs in its way of application from the previous models (M. Yang et al., 2022). The DM04 model hardening modulus, H (refer table 3.1) calibrated by fitting monotonic undrained behaviour has been shown to qualitatively capture the response under cyclic loading but over-estimate the pore pressure and shear strain accumulation in the pre-liquefaction stage. To mitigate this inadequacy, in the SANISAND-MSf model

Equations	Model Constants	Description
Stress Quantities: $p' = (\sigma'_1 + 2\sigma'_3)/3$ $q = (\sigma'_1 - \sigma'_3)$	$\sigma'_2 = \sigma'_3$	σ'_i : Principal effective stress along i-th axis p' : Effective Confining Stress q : Deviator Stress
Strain Quantities: $\varepsilon_v = (\varepsilon_1 + 2\varepsilon_3)$ $\varepsilon_q = 2(\varepsilon_1 - \varepsilon_3)/3$	$\varepsilon_2 = \varepsilon_3$	ε_i : Principal strain along i-th axis ε_v : Volumetric Strain ε_q : Deviatoric Strain
Critical State Line: $e_{cs} = e_0 - \lambda(p'/p_{at})^{\xi}$	e_0 , λ , ξ	p_{at} : Atmospheric Pressure e_{cs} : Critical Void Ratio
Elasticity: $G = G_0 p_{at} \frac{(2.97-e)^2}{1+e}(p'/p_{at})^{1/2}$ $K = K_0 p_{at} \frac{(1+e)}{e}(p'/p_{at})^{2/3}$ Alternately, $G = \frac{3(1-2\nu)}{2(1+\nu)}K$	G_0 , ν , K_0	e : Current Void Ratio ν : Poisson's Ratio G : Elastic Shear Modulus K : Elastic Bulk Modulus
Yield Surface: $f = \lvert\eta - \alpha\rvert - m = 0$	m	α : Back Stress Ratio η : Stress Ratio q/p'
Strain Increments: $\dot{\varepsilon_q}^e = \dot{q}/3G$ $\dot{\varepsilon_v}^e = \dot{p'}/K$ $\dot{\varepsilon_q}^p = \dot{\alpha}s/H$ $\dot{\varepsilon_v}^p = D\lvert\dot{\varepsilon_q}^p\rvert$ $s = (\eta - \alpha)/\lvert\eta - \alpha\rvert$		$\dot{\varepsilon_q}^e$: Elastic Deviatoric Strain Increment $\dot{\varepsilon_v}^e$: Elastic Volumetric Strain Increment $\dot{\varepsilon_q}^p$: Plastic Deviatoric Strain Increment $\dot{\varepsilon_v}^p$: Plastic Volumetric Strain Increment H : Hardening Modulus; D : Dilatancy s: $+1$ for compression, -1 for extension
Hardening Rule: $H = h(\alpha^b - \alpha)$ $h = b_0/[b_{ref} - s(\alpha^b - \alpha)]^2$ $b_{ref} = \lvert\alpha_c^b\rvert + \lvert\alpha_e^b\rvert$ $b_0 = G_0 h_0 (1 - c_h e)(p'/p_{at})^{-1/2}$ or; $b_0 = G_0 h_0 exp(-c_h e)(p'/p_{at})^{-1/2}$	h_0 , c_h	α^b : Bounding Surface Back Stress Ratio h : Positive Hardening Parameter α_c^b : Bounding Surface in Compression α_e^b : Bounding Surface in Extension Linear evolution of b_0 Exponential evolution of b_0
Dilatancy: $D = sA_d(\alpha^d - \alpha)$	A_d	α^d : Dilatancy Surface Back Stress Ratio
Surface Evolution Laws: $\alpha_{c,e}^b = s\alpha_{c,e}^c exp(-n^b\psi)$ or; $\alpha_{c,e}^b = s(\alpha_{c,e}^c - k^b\psi)$ $\alpha_{c,e}^d = s\alpha_{c,e}^c exp(n^d\psi)$ or; $\alpha_{c,e}^d = s(\alpha_{c,e}^c + k^d\psi)$ $\alpha_c^c = \alpha^c$; $\alpha_e^c = c\alpha^c$	α^c , c , n^b , k^b , n^d , k^d	α_c^d : Dilatancy Surface in Compression α_e^d : Dilatancy Surface in Extension $\alpha_{c,e}^c$: Critical Surface Stress Ratio α_c^c : Critical Surface in Compression α_e^c : Critical Surface in Extension ψ: State Parameter ($= e - e_{cs}$)

Table 3.2: Triaxial formulation of the SANISAND 2008 model (Taiebat and Dafalias, 2008)

a 'memory surface' is added that stores the history of the stress-ratio range and acts as an auxiliary bounding surface. It increases the hardening modulus H for stress states within the memory surface but keeps it unaltered for stress states on the memory surface, such as for monotonic loading. The effect of the memory surface fades away upon dilation. In the post-liquefaction stage, the DM04 model has been found to stabilise the undrained cyclic stress path in the form

of butterfly loops, which is desirable, but it also stabilises the stress-strain loop at a fixed shear strain amplitude, which contradicts experimental observations of increasing shear strain amplitude with increasing cycles post-liquefaction until a point of saturation. To overcome this limitation in the post-liquefaction stage, the SANISAND-MSf model progressively decreases the hardening modulus H to increase the shear strain amplitude with each cycle, accumulating more plastic deviatoric strain ($\dot{\varepsilon_q}^p$). Simultaneously, it decreases dilatancy D by the same factor such that the plastic volumetric strain ($\dot{\varepsilon_v}^p$) remains unaffected and the stabilised butterfly loops are maintained. This reduction in hardening modulus and dilatancy in the post-liquefaction stage is controlled by a new internal degradation variable called the 'strain liquefaction factor' (SLF) that is activated only at very low mean effective stress, signifying the 'semifluidised state'. This factor was originally introduced and embedded in the SANISAND's hardening and dilatancy rules by Barrero et al. (2020). The SLF increases progressively to a limiting value of unity upon undrained cyclic loading, while it decreases progressively upon drainage.

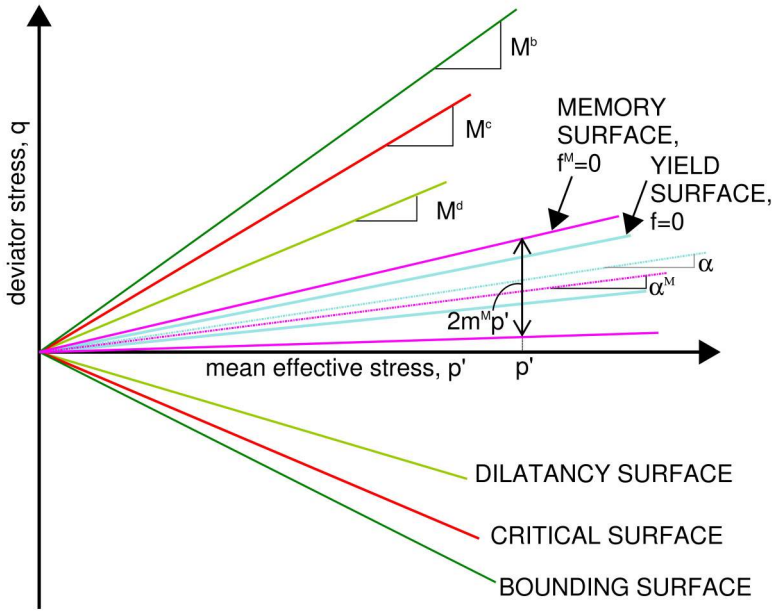

Figure 3.3: Schematic illustration of SANISAND-MSf model surfaces in triaxial space, recreated from M. Yang et al. (2022)

In triaxial space, the constitutive equations of the DM04 model for the state parameter ψ, critical state line, yield surface, dilatancy surface, bounding surface, elastic strain rates, plastic

Equations	Model Constants	Description
Stress Quantities:		Refer table 3.1
Strain Quantities:		Refer table 3.1
Critical State Line:		Refer table 3.1
Elasticity:		Refer table 3.1
Yield Surface:		Refer table 3.1
Strain Increments:		Refer table 3.1
Surface Evolution Laws:		Refer table 3.1
Dilatancy: $D = A_d g^{-n_g}(M^d_{c,e} \mp \eta)$	n_g	$g = 1$ in compression, $g = c$ in extension; Refer table 3.1
Memory surface: $f^M = \lvert\eta^M - \alpha^M\rvert - m^M = 0$		α^M : Back Stress Ratio m^M : Size
Hardening Rule: $\dot{\alpha}^M = H^M \cdot \dot{\varepsilon_q}^p$ $H^M = h^M(M^b_{c,e} - m \mp \eta^M)$ $h^M = \frac{h + \frac{m^M}{\varsigma} sgn(M^b_{c,e} - m \mp \eta^M)\langle -\sqrt{\frac{2}{3}}D\rangle}{1 + c_c \mathscr{H}[M^b_{c,e} - m \mp \eta^M]}$ $h = \frac{b_0}{\lvert\eta - \eta_{in}\rvert} \cdot exp\left[\frac{\mu_0}{\lvert\sqrt{\frac{2}{3}}\alpha_{in}\rvert^u + \varepsilon}\left(\frac{\lvert\eta^M - \alpha\rvert}{\lvert {M_c}^b + {M_e}^b - 2m\rvert}\right)^w\right]$ $b_0 = G_0 h_0 g^{-n_g}(1 - c_h e)(p'/p_{at})^{-1/2}$ or; $b_0 = G_0 h_0 g^{-n_g} exp(-c_h e)(p'/p_{at})^{-1/2}$ $H = h(M^b_{c,e} \mp \eta)$ $\dot{m}^M = \pm\left[c_c h^M \langle {M_{c,e}}^b - m \mp \eta^M\rangle - \frac{m^M}{\varsigma}\left\lvert {M_{c,e}}^b - m \mp \eta^M\right\rvert \langle -\sqrt{\frac{2}{3}}D\rangle\right]\dot{\varepsilon_q}^p$	μ_0, u, h_0 , c_h $\varsigma = 0.00001$ $c_c = 1$ $\varepsilon = 0.01$ $w = 2$	$\mathscr{H}$: Heaviside function; $\mathscr{H}[x] = 1$ if $x \geq 0$; $\mathscr{H}[x] = 0$ if $x < 0$ h : Positive Hardening Parameter α_{in}: Back Stress Ratio & η_{in}: Stress Ratio at Load Initiation Linear evolution of b_0 Exponential evolution of b_0 Refer table 3.1
Semifluidised SLF Rate: $\dot{l} = \sqrt{\frac{3}{2}}\lvert\dot{\varepsilon_q}^p\rvert[c_l\langle 1 - p_r\rangle(1-l)^{n_l}]$ $p_r = p'/p_{th}$ $h_0 = {h_0}'\left[(1 - \langle 1 - p_r\rangle)^{x \cdot l} + f_l\right]$ $A_0 = {A_0}'\left[(1 - \langle 1 - p_r\rangle)^{x \cdot l} + f_l\right]$	c_l , x $n_l = 8$ $p_{th} = 10$ kPa $f_l = 0.01$	l : Strain Liquefaction Factor p_{th} : Threshold Mean Effective Stress ${h_0}'$: h_0 and ${A_0}'$: A_0 in DM04 model, Refer table 3.1

Table 3.3: Triaxial formulation of the SANISAND-MSf model (M. Yang et al., 2022)

strain rates and elastic moduli (refer table 3.1) are valid for the SANISAND-MSf model. The governing equations in triaxial space have been derived from the multiaxial formulation of M. Yang et al. (2022) by the author and only the amended equations from the parent DM04 model are listed in table 3.3. The memory surface is denoted by f^M, and is expressed similarly to the yield surface, with α^M as the centre of the surface and m^M its size, see figure 3.3. The kinematic hardening of the memory surface is given by the rotation of its centre α^M, controlled by the memory surface hardening modulus, H^M. The hardening modulus H is proportional

to the distance between the current stress ratio and the bounding surface, same as the DM04 model. However, the positive hardening parameter h, now incorporates the memory surface with an updated expression for parameter b_0. Note that α_{in} is the back stress ratio at the start of a loading process, similar to the concept of η_{in} in DM04 model, refer section 3.2. The isotropic hardening or softening of the memory surface is captured by the change in size of m^M. Note that the hardening parameter b_0 is divided by a component g^{n_g}, where $g = c$ in triaxial extension and $g = 1$ in triaxial compression. A similar reduction in the dilatancy D, is incorporated to maintain the same plastic volumetric strain rate ($\dot{\varepsilon}_v{}^p$) such that the pore pressure and stress paths remain unaltered. This factor controls the shifting of the stress-strain loops in cyclic triaxial loading, balancing the asymmetrical strain accumulation and impacts the stress-strain curve in extension only. The fabric-dilatancy variable and the dilatancy constant follow the DM04 model formulations, refer table 3.1. The semifluidised state is triggered when the mean effective stress falls below the threshold mean effective stress p_{th}. The strain liquefaction factor is denoted by l that causes stiffness to degrade within the semifluidised state and evolves as shown in table 3.3. The SLF decreases the stiffness and dilatancy, thereby only impacting the accumulation of plastic deviatoric strain ($\dot{\varepsilon}_q{}^p$). The $h_0{}'$ is the hardening constant h_0 and $A_0{}'$ is the dilatancy constant A_0 of the reference DM04 model that now has the SLF embedded per table 3.3. For states outside the semifluidised region, $p_r = \frac{p'}{p_{th}} > 1$ and for a small default value of f_l, parameters h_0 and A_0 remain approximately equal to the original values.

3.5 PM4Sand3D

The PM4Sand3D (Kippen et al., 2026) is a three-dimensional version of the two-dimensional PM4Sand2D v3.2 model (Boulanger and Ziotopoulou, 2022) that was built on the constitutive framework of the DM04 (Dafalias and Manzari, 2004) bounding surface plasticity model. It is a stress-ratio controlled, critical state compatible model which has been revised through the years to match the experimental and case history based trends of sand behaviour under earthquake

loading. The model has been calibrated at the equation level on the basis of extensive laboratory and in-situ based empirical correlations and as such it requires only three primary input parameters. The constitutive equations have been derived for the triaxial space by the author from the multiaxial formulation provided in Kippen et al. (2026). The equations in triaxial space are summarised in table 3.4. For stress, strain and yield surface definitions, the reader is referred to table 3.1. The major modification from the reference DM04 model is in the evolution of fabric as a function of the plastic shear strain increment ($\dot{\varepsilon_q}^p$) in lieu of the plastic volumetric strain increment ($\dot{\varepsilon_v}^p$), used in the parent model (table 3.1). Additionally, the fabric history and cumulative fabric terms are tracked and are included in the plastic modulus and dilatancy relationships. Dilatancy during volumetric expansion is constrained to fit Bolton's dilatancy relationship (Bolton, 1986). The elastic modulus is modified to depend on stress ratio and fabric history. The logic for tracking of back stress ratios is updated to include loading history effects. The critical state framework is incorporated through a relative state parameter, ξ_R in lieu of the state parameter, ψ of Been and Jefferies (1985). Finally, like the SANISAND-MSf model (M. Yang et al., 2022), modelling of shear strain accumulation in the post-liquefaction regime has been improved.

The relative state parameter, ξ_R is defined in terms of relative density, D_r as shown in table 3.4 where relative density at critical state, $D_{r,cs}$ is defined based on Bolton's dilatancy relationship (Bolton, 1986). In triaxial space, the elastic and plastic strain increments are defined similarly to the DM04 model (refer table 3.1). The elastic moduli include additional terms for fabric and stress-ratio history as shown in table 3.4. The yield surface is the same as in the DM04 model and the dilatancy and bounding surfaces are similar to DM04 model, expressed as functions of the relative state parameter, ξ_R instead of ψ as shown in table 3.4. The parameter c for determining the critical state stress ratio in extension is expressed as a function of the critical surface stress ratio M^c, see table 3.4. The hardening modulus H, is allowed to take positive values for stress-ratio states within the bounding surface. Once the stress ratio crosses the bounding surface, the hardening modulus diminishes to zero and the stress ratio is corrected such that it falls on the bounding surface. Parameter p_{zp} in table 3.4 is initialized as a small percentage of

the mean effective stress ($= p'_{in}/100$) at initialisation and is updated to the current mean effective stress each time the product of the current mean effective stress p' and the fabric-dilatancy variable z exceeds the previous product.

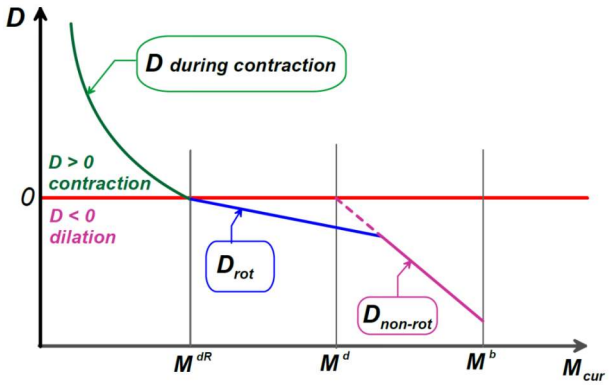

Figure 3.4: Schematic illustration of dilatancy D calculation based on current stress ratio M_{cur} relative to the rotated dilatancy M^{dR}, dilatancy M^d and bounding M^b surfaces for stress path traversing from contraction to dilation, following Kippen et al. (2026)

In the development of PM4Sand3D, the expression for dilatancy D used in the DM04 model (refer table 3.1) was found to greatly overestimate the slope of liquefaction resistance curves, as also shown in later chapters of this thesis. Hence, the expression for dilatancy was modified to include additional controlling parameters that allowed better prediction of cycles to liquefaction. More detailed effects of fabric and fabric history were incorporated into the dilatancy. A rotated dilatancy surface that evolves with the fabric history was added, with slope M^{dR} as a function of the dilatancy surface M^d. During dilation, i.e. $M^{dR}_{c,e} \mp \eta < 0$, the dilatancy D is expressed as functions of D_{rot} or D_{nonrot} depending on where the current stress ratio η falls between M^{dR}, M^d and M^b, see figure 3.4. Additional constraint is added to D during dilation for low effective stresses ($p_{min} < p' \leq 2p_{min}$) as noted in table 3.4. The dilatancy coefficient A_d is embedded with additional parameters and uses separate expressions during dilation and contraction. During contraction, i.e. $M^{dR}_{c,e} \mp \eta > 0$, dilatancy D has a different expression than during dilation. The fabric-dilatancy internal variable and its history is updated when $M^d_{c,e} \mp \eta < 0$, see table 3.4. In addition to the DM04 and the SANISAND-MSf models, the PM4Sand3D model is used in this study for simulation and assessment of cyclic behaviour in chapter 7.

Equations	Constants & Definitions	Description
Critical State Line: $D_{r,cs} = \frac{R}{Q-ln(100p'/p_{at})}$; $\xi_R = D_{r,cs} - D_r$	e_{max} , e_{min} , R , Q $D_r = \frac{e_{max}-e}{e_{max}-e_{min}}$	$D_{r,cs}$: Relative Density at Critical State ξ_R : Relative State Parameter
Elasticity: $G = G_0 p_{at} \left(\frac{p'}{p_{at}}\right)^{1/2} C_{SR} \left(\frac{1+\frac{z_{cum}}{z_{max}}}{1+\frac{z_{cum}}{z_{max}} C_{GD}}\right)$ $C_{SR} = \frac{1-C_{SR,o}\cdot\left(\frac{\lvert\eta\rvert}{M^{b*}}\right)^{m_{SR}}}{\left[1-C_{SR,o}\cdot\left(\frac{\lvert\eta\rvert}{M^{b*}}\right)^{m_{SR}}\right]_{initial}} \leq 1$ $M^{b*} = M_c^b$ if $\eta \geq 0$; $M^{b*} = M_e^b$ if $\eta < 0$	G_0 , $C_{SR,o} = 0.5$ $z_{max} = 0.7exp(-6.1\xi_{Ro}) \leq 20$, $m_{SR} = 4$, $C_{GD} = 2$ $c = 0.9 - 0.15M^c \geq 0.64$	G : Elastic Shear Modulus; K : Refer table 3.1 ξ_{Ro} : Initial Relative State Parameter M^c : Critical Surface Stress Ratio, Refer table 3.1
Hardening Rule: $H = \frac{3Gh_o g^{-n_g} C_{rev}}{2p'} \cdot \frac{\left[\sqrt{\frac{2}{3}}(M_{c,e}{}^b \mp \eta)\right]^{0.5}}{\left[exp(\sqrt{\frac{2}{3}}s(\alpha-\alpha_{in}))-1\right]+C_{\gamma 1}} \cdot \frac{C_{K\alpha}}{1+C_{K_p}\left(\frac{z_{peak}}{z_{max}}\right)\langle\sqrt{\frac{2}{3}}(M_{c,e}{}^b \mp \eta)\rangle\sqrt{1-C_{zpk2}}}$ $C_{K\alpha} = 1 + \frac{C_{K\alpha f}}{1+\left(2.5\langle\sqrt{\frac{2}{3}}s(\alpha-\alpha_{in})\right)^2} \cdot C_{pzp2} \cdot C_{zpk1}$ $C_{pzp2} = \frac{-\langle-(p_{zp}-p')\rangle}{-\langle-(p_{zp}-p')\rangle+p_{min}}$ $C_{zpk1} = \frac{z_{peak}}{z_{cum}+\frac{z_{max}}{5}}$; $C_{zpk2} = \frac{z_{peak}}{z_{cum}+\frac{z_{max}}{100}}$	$C_{rev} = 1$, $C_{\gamma 1} = \frac{h_o}{200}$ $h_o = 0.25 + \frac{D_r}{2} \geq 0.3$; $C_{Kp} = \sqrt{2}$ $C_{K\alpha f} = 1 + 600(D_{ro} - 0.37)^3 \in [3;50]$ $n_g = 0.5(2.35 - D_{ro}) \leq 1$ $z_{peak} = max(\sqrt{z^2}, z_{peak})$; $dz_{cum} = dz$	$M_{c,e}^b$: Refer table 3.1, replace ψ with ξ_R for $\psi \leq 0$ and replace ψ with $\xi_R/4$ for $\psi > 0$ D_{ro} : Initial Relative Density <> : Macauley Brackets, Refer table 3.1 g , α_{in}: Refer table 3.3, s : Refer table 3.1, p_{min} : $\frac{p'_{in}}{200}$
Dilatancy: If dilating, $M_{c,e}^{dR} \mp \eta \leq 0$ $M_{c,e}^{dR} = \frac{M_{c,e}^d}{C_{rot1}}$; $C_{rot1} = 1 + \frac{\sqrt{2}\langle-sz\rangle}{z_{max}} \cdot (1-C_{zin1}) \geq 1$ $D = D_{nonrot} - \langle D_{nonrot} - D_{rot}\rangle \cdot \frac{\langle M_{c,e}^b - \eta\rangle}{\langle M_{c,e}^b - \eta + 0.01\rangle}$; $D_{rot} = A_d \cdot \frac{\langle-sz\rangle}{z_{max}} \cdot \frac{(M_{c,e}{}^{dR} \mp \eta)}{C_{DR}}$ $D_{nonrot} = \sqrt{\frac{3}{2}} A_d \left(-\left\langle-\sqrt{\frac{2}{3}}(M_{c,e}{}^d \mp \eta)\right\rangle\right)$ $D \geq -\sqrt{\frac{3}{2}} \cdot 3.5 \cdot A_{do} \langle M_{c,e}^b - M_{c,e}^d\rangle \frac{2p_{min}-p'}{p_{min}}$ $A_d = \frac{A_{do} \cdot g^{-n_g} \cdot C_{zin2}}{\frac{z_{cum}{}^2}{2z_{max}}\left(1-\frac{\langle-sz\rangle}{z_{peak}}\right)^3 (C_\varepsilon)^2 (C_{pzp})(C_{pmin})(C_{zin1})+1}$ $A_{do} = 3.125 \frac{\left[\sin^{-1}\left(\frac{3M^b}{6+M^b}\right) - \sin^{-1}\left(\frac{3M^c}{6+M^c}\right)\right]}{(M^b - M^d)}$	$C_{DR} = 5 + 25(D_{ro} - 0.35) \leq 10$ $C_{zin1} = \left\langle 1 - exp\left(-2\left\lvert\frac{sz_{in}-sz}{z_{max}}\right\rvert\right)\right\rangle$ $C_{zin2} = \frac{1+C_{zin1}\frac{z_{cum}-z_{peak}}{3z_{max}}}{1+3C_{zin1}\frac{z_{cum}-z_{peak}}{3z_{max}}}$ $C_{pzp} = \frac{1}{1+\left(\frac{2.5p'}{p_{zp}}\right)^5}$ $C_{pmin} = \frac{1}{1+\left(\frac{p_{min2}}{p'}\right)^2}$ $C_\varepsilon = 50exp[-11.5(D_{ro} - 0.35)] \geq 0.3$	$M_{c,e}^d$: Refer table 3.1, replace ψ with ξ_R for $\psi \leq 0$ and replace ψ with $4\xi_R$ for $\psi > 0$
Dilatancy: If contracting, $M_{c,e}^{dR} \mp \eta > 0$ $D = A_{dc}\left[\sqrt{\frac{2}{3}}s(\alpha-\alpha_{in}) + C_{in}\right]^2 \cdot \frac{(M_{c,e}{}^d \mp \eta)}{\sqrt{\frac{2}{3}}(M_{c,e}{}^d \mp \eta)+C_D} C_{pmin2}$; $C_{rot2} = 1 - \frac{z_{peak}}{z_{cum}+\frac{z_{max}}{100}}$ $D \leq 1.5A_{do}\frac{(M_{c,e}{}^d \mp \eta)}{\sqrt{\frac{2}{3}}(M_{c,e}{}^d \mp \eta)+C_D}$ $A_{dc} = \frac{A_{do}\left(g^{-n_g}\right)(1+\langle sz\rangle)}{h_p C_{dz}}$; $C_{dz} = \left(1 - C_{rot2}\cdot\frac{z_{peak}}{z_{max}}\right)\left(\frac{z_{max}}{z_{max}+C_{rot2}\cdot z_{cum}}\right) \geq \frac{1}{1+\frac{z_{max}}{2}}$	$C_{in} = \frac{\sqrt{2}\langle sz\rangle}{z_{max}}$, $C_D = 0.1$ $h_p = h_{po} \cdot exp(0.9 + 6.1\langle 0.5 - \xi_R\rangle^{2.1})$, h_{po} $C_{pmin2} = \frac{\langle p'-2p_{min}\rangle}{16p_{min}} \leq 1$ $dz = -\frac{c_z}{1+\langle\frac{z_{cum}}{2\sqrt{2}z_{max}}-1\rangle} \cdot \frac{\langle-\dot{\varepsilon}_v{}^p\rangle}{D}(sz_{max}+z)$	h_{po} : Contraction Rate Parameter p_{min2} : $\frac{p_{in}{}'}{20}$ c_z : $100 + 750(D_{ro} - 0.35) \in [100;400]$

Table 3.4: Triaxial formulation of the PM4Sand3D model (Kippen et al., 2026)

Chapter 4

Experimental testing

4.1 Introduction

In order to conduct the performance assessment of constitutive models of the SANISAND family presented in chapter 3, a series of experimental tests at the element-level addressing both monotonic and cyclic behaviour of sand under undrained and non-standard drained conditions were required. A programme of element tests on Hostun HN31 sand under different drainage conditions were conducted by Prof Orestis Adamidis at ETH Zurich, from which the cyclic tests were published in Adamidis and Anastasopoulos (2022). Upon investigation of the monotonic test data, it was found that the coupled shear-volumetric strain paths were incomplete or insufficient to draw reliable conclusions for constitutive model assessment. Therefore, the author of this thesis conducted an experimental campaign on Hostun HN31 sand to characterise the monotonic behaviour under triaxial coupled shear-volumetric strain paths.

Hostun HN31 sand is a widely used sand for liquefaction investigations, including for element and centrifuge modelling across testing facilities in Europe (Adamidis and Madabhushi, 2018; Azeiteiro et al., 2017). This sand is provided by a single company, Sibelco France. The tests conducted at ETH Zurich by Prof Orestis Adamidis were performed on a batch of Hostun HN31 purchased in 2017 (referred to as batch 1 in this study). The tests presented in this chapter

were performed by the author on a batch of Hostun sand previously used for physical modelling at the University of Cambridge (referred to as batch 2 in this study). A third batch was purchased in 2022 for further element testing at the University of Oxford. Upon physical characterisation of the different batches of Hostun HN31 sand, it was found that the particle size distribution and the maximum and minimum densities varied across the different batches. A detailed investigation on sand batch variability of Hostun HN31 provided by the same manufacturer, Sibelco France, has been carried out by Adrienne Eckstein at the University of Oxford and can be found in chapter 4 of her doctoral thesis (Eckstein, 2026). The investigation concluded that physical characterisation data on a sand from literature should be used with caution. The discrepancies in properties observed across batches contest the assumption that constitutive model calibration parameters obtained for one batch will apply for another and highlight the importance of characterising the specific batch of sand being used. As a result, mixing experiments from different batches during calibration should be undertaken with caution. For the constitutive model assessments conducted in this thesis, it was decided that the cyclic performance would be assessed using the tests on batch 1 of Hostun HN31 conducted by Prof Orestis Adamidis at ETH Zurich. On the other hand, given the need for additional coupled-strain monotonic compression data, it was decided that the monotonic performance would be assessed using the test results on batch 2 of Hostun HN31, conducted by the author at the University of Oxford. Additional undrained and fully drained monotonic tests were performed on batch 2 by the author to fully characterise the sand.

All experimental tests conducted by the author of this thesis from here on will be reported as tests conducted by 'AD'. The experimental tests from Prof Orestis Adamidis will be reported as tests by 'OA' and are presented in this thesis with permission. The tests on Hostun HN31 sand presented in this thesis were either conducted at the University of Oxford by 'AD' on batch 2 or at ETH Zurich by 'OA' on batch 1 and were used for the constitutive model assessments. Test data on a third sand - Congleton HST-95 sand conducted by researcher Yide Wang at the University of Oxford are also used in chapter 6 of this thesis. These tests will be reported as

Material	Tests conducted by	Institution	Loading	Use in thesis
Hostun HN31, batch 1	OA	ETH Zurich	Monotonic and cyclic	Cyclic constitutive assessment, Chapters 7–8
Hostun HN31, batch 2	AD	Oxford	Monotonic	Monotonic assessment, Chapters 4–5
Congleton HST-95	YW	Oxford	Monotonic	Application of Chapter 5 framework in Chapter 6
Toyoura sand	Published data (Taiebat and Dafalias, 2008)	Literature	Monotonic	Benchmark for framework development, Chapter 5

Table 4.1: Datasets used in the thesis

tests conducted by 'YW' and are presented in this thesis with permission. Note that the tests on Congleton sand have not been used to conduct the performance assessment of the constitutive models. Rather, they have been used in chapter 6 to present an application of the analytical framework developed in chapter 5 for the monotonic performance assessment of constitutive models. Table 4.1 presents all the datasets used in the thesis.

In this chapter, only the tests conducted by the author, i.e. 'AD' are presented. These tests include monotonic triaxial compression tests under undrained, fully drained and non-standard drained boundary conditions on batch 2 of Hostun HN31 sand. Undrained or fully drained tests from this experimental campaign and from literature that reached the critical state were used to establish the critical state line for Hostun HN31 sand, using relative density as the parameter in lieu of void ratio due to the batch variability of maximum and minimum void ratio. The coupled strain tests were conducted under three constant ratios of volumetric to axial strain rates. Moreover, these coupled strain tests were specifically scrutinised for instability triggering using Hill's stability criterion (Hill, 1958). These instability points using Hill's criterion will be used to verify the analytical framework developed in chapter 5 for the monotonic performance assessment of constitutive models. The following sections describe the laboratory testing program in detail.

4.2 Methodology

This section presents the testing equipment, testing material, sample preparation method and testing protocol adopted for the monotonic triaxial compression tests conducted in this study.

4.2.1 Testing equipment

The experiments were performed using a GDS advanced dynamic triaxial testing device at the University of Oxford. The device can perform stress- or strain-controlled tests under monotonic, cyclic, and dynamic loading. The tests presented in this chapter were conducted under strain controlled monotonic compression loading. A sketch of the testing device is given in figure 4.1. For the tests presented in this chapter, the dynamic cell pressure actuator was used to control the radial pressure. The back pressure controller was used to control back pressure and volume flow into and out of the sample. The back pressure controller was filled with de-aired water and the water lines into the base of the sample, including the pore pressure line, were flushed with de-aired water to remove any air bubbles prior to sample preparation.

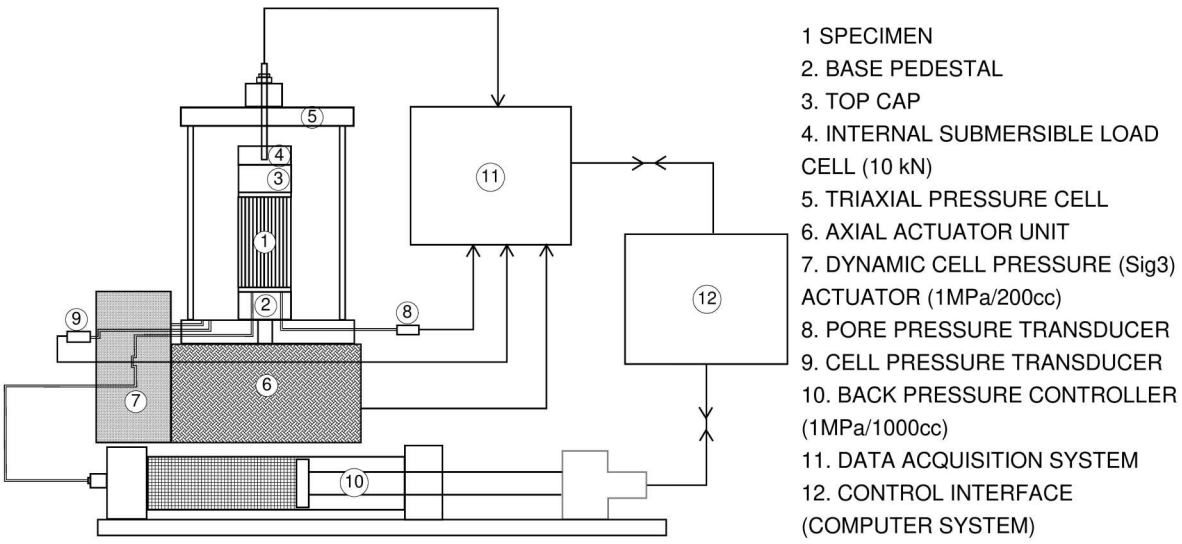

Figure 4.1: Diagram of GDS advanced dynamic triaxial testing device at University of Oxford

4.2.2 Testing material

As mentioned in section 4.1, all tests were performed on batch 2 of Hostun HN31, a widely used sand for liquefaction-related studies in Europe. It is a uniformly graded fine sand comprising sub-angular to angular siliceous particles. The sand properties obtained from physical characterisation tests conducted at the University of Oxford are listed in table 4.2. The limiting void ratios were measured through the Norwegian Geotechnical Institute (NGI) method based on DIN-18126 (1996). The properties obtained for the sand differ from the values reported by Adamidis and Anastasopoulos (2022) for batch 1. However, they fall within the range reported from various testing facilities as listed by Azeiteiro et al. (2017).

e_{max}	e_{min}	d_{50}	C_u	C_c	G_s
0.993	0.647	$355\mu m$	1.79	0.99	2.65

e_{max} = maximum void ratio; e_{min} = minimum void ratio;
d_x = particle size for which (x)% of the material is finer;
$C_u = d_{60}/d_{10}$ coefficient of uniformity;
$C_c = {d_{30}}^2/(d_{10} \cdot d_{60})$ coefficient of curvature;
G_s = specific gravity of solids.

Table 4.2: Properties of batch 2 of Hostun Sand

4.2.3 Sample preparation

The specimens were prepared using the water (wet) pluviation technique as this method is able to closely replicate the deposition of sand layers through natural sedimentation. Oven dried sand was first saturated with de-aired water under vacuum. The saturated sand was also vibrated under vacuum to ensure release of any entrapped air. A cylindrical split mould of 70 mm diameter and 140 mm height was lined with a latex membrane using suction and filled entirely with de-aired water. The fully saturated sand was then pluviated into the mould. The mould was gently tapped from all around and along its height to densify the sample to the required void ratio. A back pressure of -10 kPa was applied and maintained during dismantling of the split mould and filling of the triaxial cell. Figure 4.2 shows the stages involved in specimen preparation.

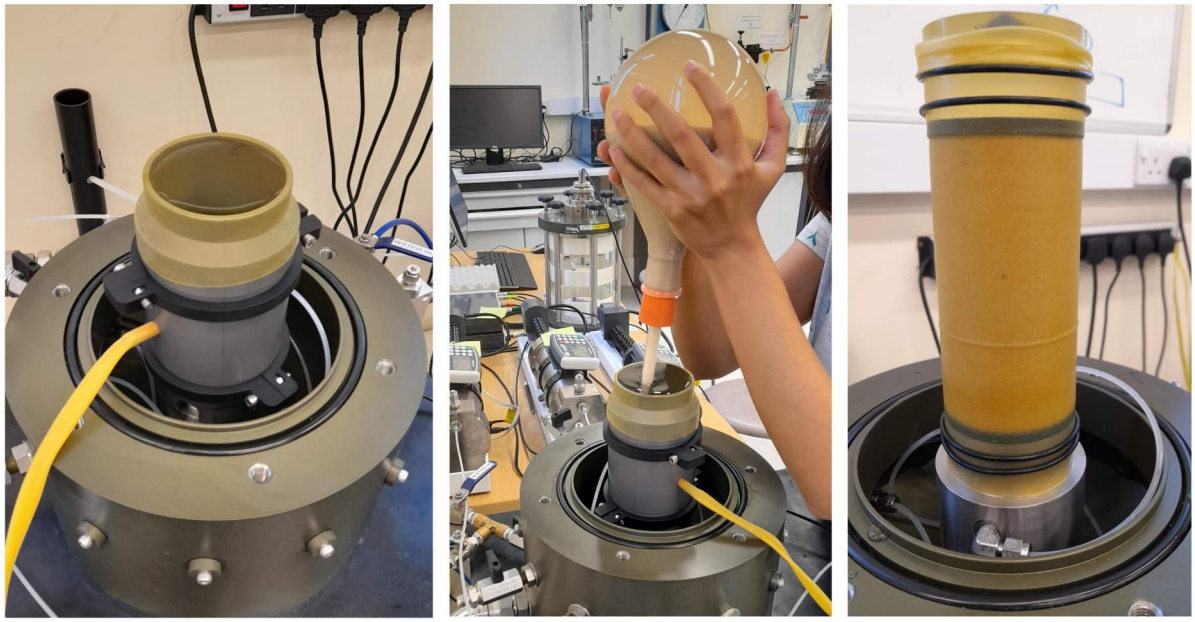

(a) Split mould lined with membrane and filled with de-aired water

(b) Saturated sand pluviated into split mould

(c) Prepared specimen prior to testing

Figure 4.2: Specimen preparation stages prior to testing

4.2.4 Testing protocol

The testing protocol was based on ASTM D4767-11R20 for undrained tests and ASTM D7181-20 for drained tests. After the triaxial cell was filled, the back pressure was increased to 500 kPa for undrained and coupled strain tests to avoid cavitation in case the specimen dilation was high enough to reduce pore pressures to sufficiently negative values. For the fully drained tests, the minimum back pressure applied was 200 kPa. The B-values for all tests were greater than 96%. The specimens were isotropically consolidated to the required mean effective stress, p'_{in}. Any minor volume changes prior to the consolidation stage were not accounted for as it was assumed that any trapped air bubbles would get dissolved as back pressure increased. A rate of 100 kPa every 3 hrs was applied for the consolidation stage. Strain controlled monotonic compression was imposed with axial displacement rates of 6 mm/hr for undrained tests and 3 mm/hr for fully drained tests, up to a maximum of 35% axial strain. The coupled strain triaxial tests were conducted by imposing an axial strain of 35% at 6 mm/hr and calculating the volumetric strain as a ratio of the axial strain. The calculated volumetric strain rate was applied through the back

pressure controller using its volume control mode. Membrane correction during both consolidation and shearing stages, and parabolic barreling during the shearing stage were considered according to Lade (2016). Membrane penetration effects calculated based on Lade (2016) were found to be negligible due to low effective cell pressures (cell pressure - pore pressure $\leq$ 300 kPa) and small particle size.

4.3 Test results

The results of the undrained, fully drained and coupled strain tests conducted on batch 2 of Hostun HN31 sand by AD are presented in this section. The undrained and fully drained tests were considered for the critical state line, and compared with published results in literature.

4.3.1 Monotonic triaxial test results

Table 4.3 summarises the monotonic tests performed under undrained and fully drained conditions. Figure 4.3 includes all tests of table 4.3, plotted in red in $e - p'$ space, along with a proposed critical state line (CSL). As seen in the figure, none of the fully drained tests were able to reach the critical state line whereas 4 out of 7 undrained tests attained critical state. A test was deemed to have reached critical state based on the flattening of the excess pore pressure versus axial strain curve for undrained tests and the flattening of the volumetric strain versus axial strain curve for the fully drained tests. Phase transformation states (PTS) were detected when the mean effective stress p' was minimised in undrained tests. Peak stress-ratio states (PSRS) were obtained at the maximum stress-ratio η point in fully drained and undrained tests. Detailed results of undrained test U3 and fully drained test D1 are presented in figures 4.4 and 4.5, respectively.

The proposed expression for the CSL was based on the tests listed in table 4.3 and shown in red paths in figure 4.3. Undrained and fully drained monotonic compression tests conducted on batch 1 of Hostun HN31 by OA at ETH Zurich, reproduced with permission and published in

Test ID[a]	e_{in}^{b}	$p'^{\,b}_{in}$	e_{end}	p'_{end}	η^{c}_{PTS}	ϕ^{c}_{PTS}	η^{d}_{PSRS}	ϕ^{d}_{PSRS}	η_{end}	ϕ_{end}
ICUMC/0.832/100 (U1)	0.832	100	0.832	302.8	1.24	30.9°	1.36	33.6°	1.31	32.5°
ICUMC/0.828/300 (U2)	0.828	300	0.828	974.9	1.14	28.6°	1.31	32.6°	1.13[e]	28.5°
ICUMC/0.874/300 (U3)	0.874	300	0.874	499.9	1.27	31.5°	1.34	33.2°	1.17[e]	29.3°
ICUMC/0.736/300 (U4)	0.736	300	0.736	1331.9	1.22	30.4°	1.43	35.3°	1.40[f]	34.6°
ICUMC/0.718/300 (U5)	0.718	300	0.718	1583.1	1.25	31.2°	1.44	35.4°	1.39[e]	34.4°
ICUMC/0.790/300 (U6)	0.790	300	0.790	1114.3	1.20	29.9°	1.36	33.7°	1.09[e]	27.4°
ICUMC/0.896/10 (U7)	0.896	10	0.896	215.04	1.28	31.9°	1.47	36.1°	1.10	27.7°
ICDMC/0.784/300 (D1)	0.784	300	0.830	504.7	–	–	1.43	35.4°	1.19	29.7°
ICDMC/0.821/100 (D2)	0.821	100	0.884	177.2	–	–	1.47	36.1°	1.22	30.4°
ICDMC/0.827/200 (D3)	0.827	200	0.845	331.8	–	–	1.37	33.9°	1.15	28.8°
ICDMC/0.842/100 (D4)	0.842	100	0.885	170.8	–	–	1.42	35.0°	1.14	28.7°
ICDMC/0.869/20 (D5)	0.869	20	0.909	39.8	–	–	1.45	35.8°	1.11	27.8°
ICDMC/0.812/20 (D6)	0.812	20	0.881	36.7	–	–	1.44	35.5°	0.98	25.0°
ICDMC/0.874/12 (D7)	0.874	12	0.913	24.2	–	–	1.46	35.8°	0.91	23.3°
ICDMC/0.865/150 (D8)	0.865	150	0.872	241.4	–	–	1.35	33.4°	1.09	27.4°

[a](1) type of consolidation: IC for isotropic consolidation; (2) type of drainage: D for fully drained and U for undrained; (3) type of loading: MC for monotonic compression; (4)void ratio immediately after consolidation; and (5) mean effective stress immediately after consolidation [kPa]. [b]Post consolidation values; [c]PTS: Phase transformation state; [d]PSRS: Peak stress-ratio state; [e]The test reached critical state; [f]Load cell maximum capacity attained just before critical state.

Table 4.3: Results of monotonic triaxial tests performed on batch 2 of Hostun sand by AD, also published in Dilip and Adamidis (2024a)

Dilip and Adamidis (2024b), are also shown in grey (see Adamidis and Anastasopoulos (2022) for information on experimental methods for these tests). Previous tests reaching the CSL using Hostun HN31 are included, as published by Azeiteiro et al. (2017) and Konrad (1993). Though all tests were performed on nominally the same sand, different batches were used each time. To account for variability in maximum and minimum void ratios, relative density D_r is used in figure 4.3. The proposed CSL for Hostun sand, given in equation 4.1 and shown in purple in figure 4.3, follows the form proposed by Bolton (1986), with p' in kPa. This CSL is steeper at high levels of p' compared to the one proposed by Azeiteiro et al. (2017) and included in green in figure 4.3.

$$D_{r,cs} = \frac{R}{Q - ln(p')} \therefore e_{cs} = e_{max} - \frac{(e_{max} - e_{min})R}{Q - ln(p')} \tag{4.1}$$

where $D_{r,cs}$ relative density at critical state, $e_{cs} =$ void ratio at critical state, $R = 0.73$, and

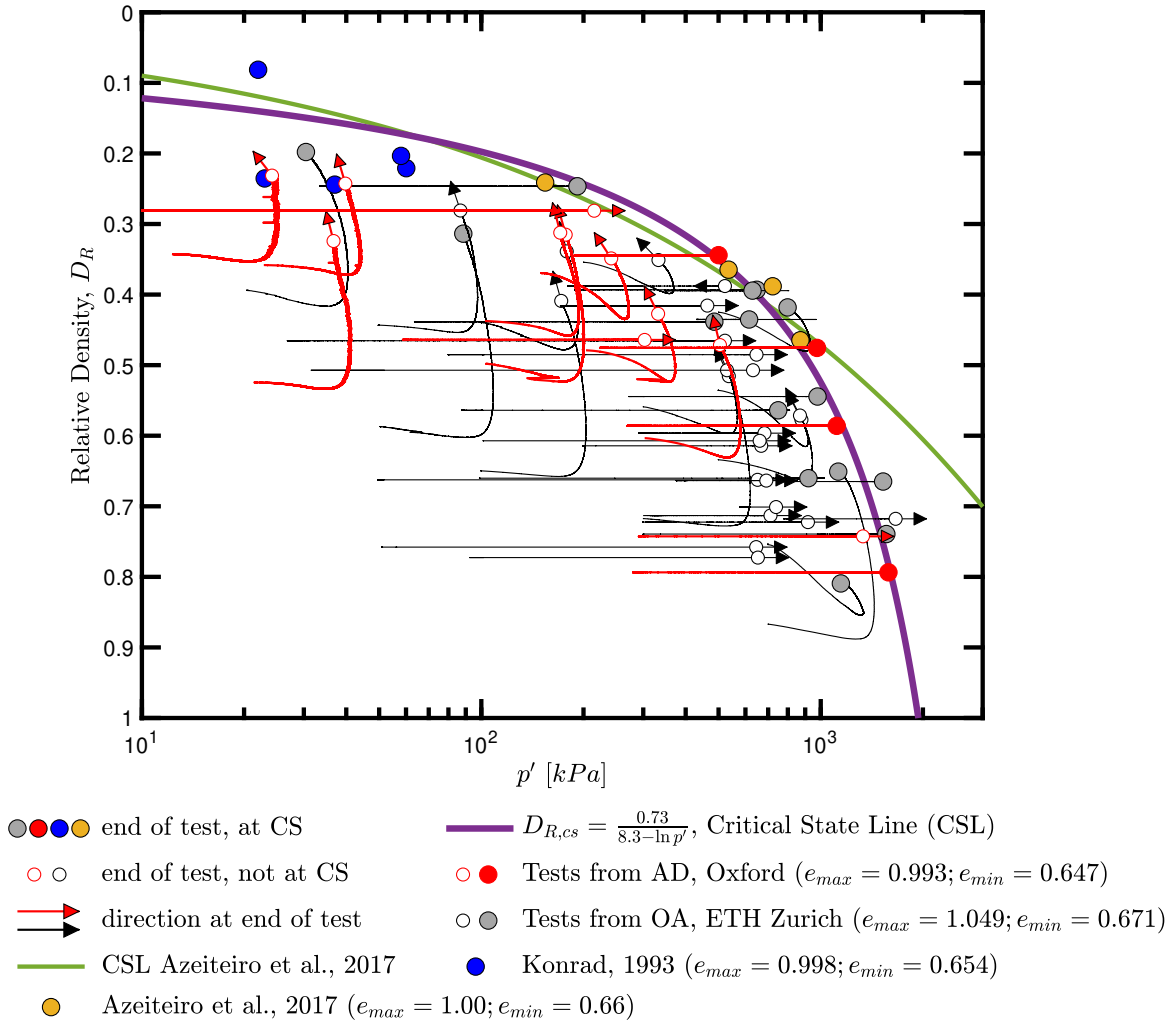

Figure 4.3: Critical state line for Hostun sand

$Q = 8.3$.

Note that equation 4.1 is applicable for critical void ratios $\geq e_{min}$. To account for critical void ratios $< e_{min}$, breakage related broadening of the particle size gradation needs to be considered through additional testing to locate the CSL appropriately at higher confining pressures. Increased particle crushing upon continued shearing at higher confining pressures results in lowering of the CSL, the evolution of which has been incorporated in constitutive models in literature, using a grading state index or by considering a dynamic reference line (e.g. Kikumoto et al., 2010; Yao et al., 2019). The current study is aimed at numerical modelling of liquefaction

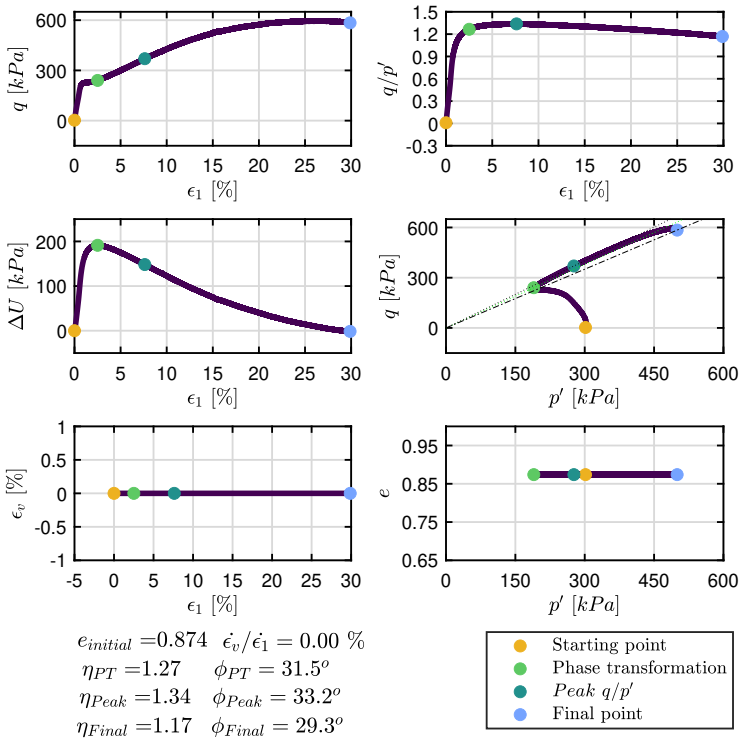

Figure 4.4: Result from undrained test U3, Test ID: ICUMC/0.874/300

triggering phenomena for silica sands, which occur at low confining pressures and where particle crushing is typically not considered (e.g. Andrianopoulos et al., 2010; Kassas et al., 2021; Petalas et al., 2019; Taiebat et al., 2010; M. Yang et al., 2022). As such, the effect of particle breakage at higher confining pressures has not been taken into account.

4.3.2 Coupled strain triaxial test results

Table 4.4 summarises the initial states and results of the coupled strain monotonic triaxial compression experiments. Three constant ratios of expansive volumetric strain rate to axial strain rate, $\zeta = \dot{\varepsilon}_v/\dot{\varepsilon}_1$ were used. Unlike for the undrained tests, and similarly to fully drained tests, the phase transformation point cannot be accurately determined for the coupled strain tests as $\dot{p'} \neq 0$ at the phase transformation state.

As explained in the following chapter, instability points were identified by examining when Hill's stability criterion (Hill, 1958), $\ddot{W} = \dot{p'}\dot{\varepsilon}_v + \dot{q}\dot{\varepsilon}_q > 0$ in triaxial space, was violated. The

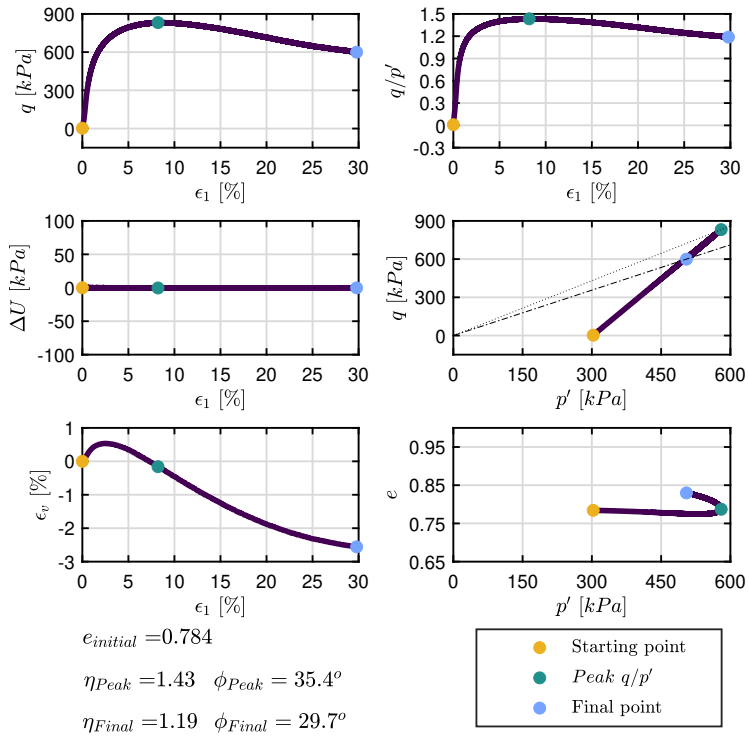

Figure 4.5: Result from fully drained test D1, Test ID: ICDMC/0.784/300

rationale behind identifying instability points is explained in detail in the next chapter. Note that the instability being pursued arises purely from material behaviour rather than geometrical effects, such as necking in extension tests. Hence, the strain-controlled tests remained controllable during the entire shearing stage.

Detailed data from one coupled strain test, P6, are presented in figures 4.6 and 4.7. For P6, an instability triggering point is identified, when Hill's stability criterion is violated. That point occurs after the peak stress-ratio state, as seen in figure 4.6. The phase transformation state can be qualitatively identified from the fact that the incremental change in excess pore pressure ΔU goes from positive to negative, indicating dilation. Hence, the instability point at P6, identified using $\ddot{W} = 0$, is a post-phase transformation and post-peak stress-ratio state instability. This observation is pertinent for the verification of the framework developed in the next chapter.

Test ID[a]	e^b_{in}	$p'^{\,b}_{in}$	e^c_{INST}	$p'^{\,c}_{INST}$	η^d_{PSRS}	ϕ^d_{PSRS}	η^e_{end}	ϕ^e_{end}
ICPDMC/0.758/300/-5 (P1)	0.758	300	0.774	963.9	1.40	34.5°	1.16	29.2°
ICPDMC/0.800/100/-5 (P2)	0.800	100	0.819	459	1.39	34.4°	1.17	29.2°
ICPDMC/0.825/60/-5 (P3)	0.825	60	0.846	297	1.42	35.1°	1.14	28.7°
ICPDMC/0.842/20/-5 (P4)	0.842	20	0.861	191.4	1.42	35.0°	1.12	28.1°
ICPDMC/0.722/300/-10 (P5)	0.722	300	0.744	1015.9	1.44	35.4°	1.18	29.6°
ICPDMC/0.748/250/-10 (P6)	0.748	250	0.773	738.3	1.43	35.3°	1.18	29.5°
ICPDMC/0.818/80/-10 (P7)	0.818	80	0.840	105.7	1.39	34.5°	0.99	25.1°
ICPDMC/0.828/30/-10 (P8)	0.828	30	0.853	78.4	1.44	35.4°	1.01	25.6°
ICPDMC/0.714/300/-15 (P9)	0.714	300	0.742	927.6	1.48	36.4°	1.19	29.8°
ICPDMC/0.737/250/-15 (P10)	0.737	250	0.768	635.7	1.46	35.9°	1.17	29.2°
ICPDMC/0.763/100/-15 (P11)	0.763	100	0.793	385.4	1.45	35.8°	1.12	28.1°
ICPDMC/0.804/50/-15 (P12)	0.804	50	0.829	81.2	1.41	34.9°	0.52	13.8°

[a](1) type of consolidation: IC for isotropic consolidation; (2) type of drainage: PD for coupled strain conditions; (3) type of loading: MC for monotonic compression; (4) void ratio immediately after consolidation; (5) mean effective stress immediately after consolidation [kPa]; and (6) coupled strain ratio at shearing stage, $\zeta = \dot{\varepsilon}_v/\dot{\varepsilon}_1$ in percentage. [b]Post consolidation values; [c]INST: Instability Point; [d]PSRS: Peak stress-ratio state; [e]End of test.

Table 4.4: Results of coupled strain monotonic triaxial tests performed on batch 2 of Hostun sand by AD under three different values of $\zeta(=\dot{\varepsilon}_v/\dot{\varepsilon}_1)$, also published in Dilip and Adamidis (2024a)

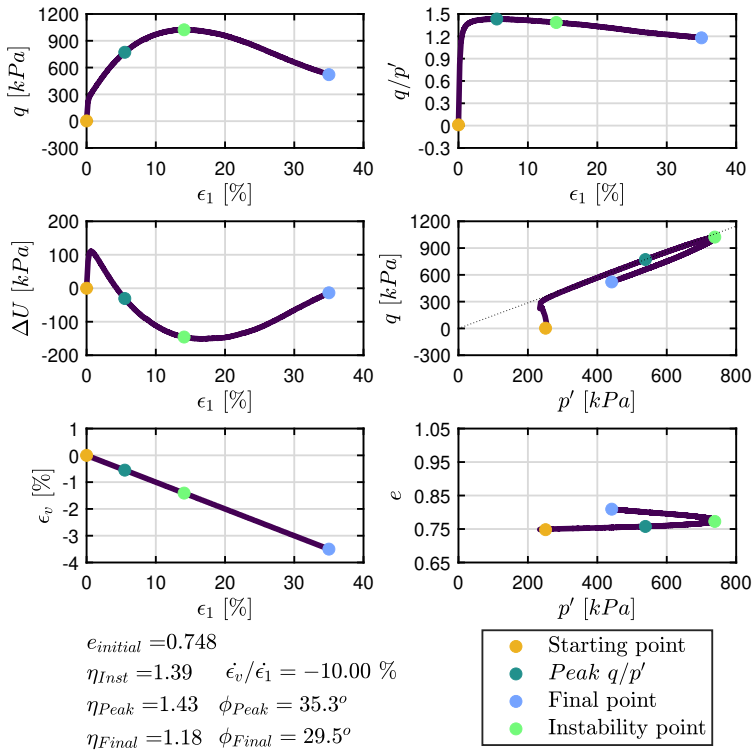

Figure 4.6: Result from coupled strain test P6, Test ID: ICPDMC/0.748/250/-10

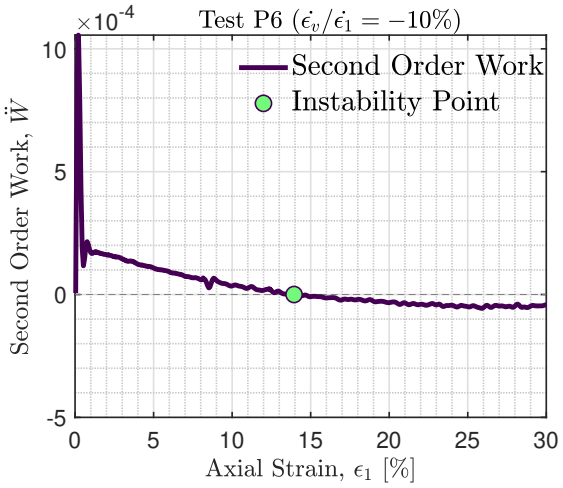

Figure 4.7: Instability point for coupled strain test P6, Test ID: ICPDMC/0.748/250/-10

Chapter 5

State parameter for coupled shear-volumetric strain paths using a SANISAND model

5.1 Introduction

In this chapter, the performance assessment of the SANISAND family of constitutive models is conducted for non-standard drained monotonic behaviour. Drainage effects related to water flow and consequent local volumetric expansion control the triggering of instability failures under monotonic shearing, such as the seismic and post-seismic triggering of flow failures in slopes studied using centrifuge experiments by Malvick et al. (2006, 2008) and element tests by Chu et al. (2015). Reliably modelling such instabilities caused by non-standard drained monotonic soil behaviour has been receiving increasing attention. State-dependent bounding surface plasticity models, such as the SANISAND family and other derivative models, have shown promise in capturing monotonic behaviour with coupled volumetric and shear strains. Kamai and Boulanger (2012) conducted a numerical study on the behaviour of medium to dense sands in plane strain conditions using the PM4Sand model (Boulanger and Ziotopoulou, 2022), where

a constant volumetric to shear strain ratio was imposed. Their numerical results qualitatively captured experimental data. Lashkari and Yaghtin (2018) and Lashkari et al. (2021) presented an extension of the state-dependent plasticity model of Li and Dafalias (2000) to study instability in sands, that exhibited fully contractive or limited-flow type behaviour under direct simple shear and triaxial compression paths, using linear, bilinear, and non-linear correlations between volumetric and shear strain. They concluded that state-dependent plasticity models better predicted coupled strain behaviour than pressure-dependent models.

Motivated by the observation of Kamai and Boulanger (2012) in 2D space (plane strain), that simulated coupled shear-volume softening paths in $e - p'$ relate to a constant state parameter, the existence of such constant state lines under simulated and experimental coupled shear-volume softening paths in triaxial space is examined here, with the additional aim of using them to assess the state parameter definition incorporated in SANISAND models. The state parameter is an important ingredient in the SANISAND models as it controls the evolution of bounding and dilatancy surfaces up to the critical state. The state parameter proposed by Been and Jefferies (1985) is used in such models and is arguably the most popular representation of state, though other equivalent parameters have been used in literature (e.g., Bolton, 1986; Dafalias and Manzari, 2004; Lashkari, 2009; Wan and Guo, 1998; Z. L. Wang et al., 2002). Despite the state parameter being central during the calibration process of SANISAND models, its definition, that ultimately drives the evolution of surfaces, is not directly scrutinised. This chapter, therefore, focuses on the importance, the definition, and the calibration of the state parameter when modelling coupled volumetric to shear strain paths within the SANISAND family of bounding surface plasticity models, specifically using SANISAND 2008 (Taiebat and Dafalias, 2008).

First, the SANISAND 2008 model (Taiebat and Dafalias, 2008), chosen here for its relatively simple formulation, is implemented in MATLAB and the implementation is verified against the numerical simulation results on Toyoura sand provided in the paper that introduced the model, Taiebat and Dafalias (2008). Next, the constant state parameter curves in $e - p'$ space under coupled shear-volume softening paths simulated by Kamai and Boulanger (2012) in 2D space on

Toyoura sand are replicated in triaxial space using the verified implementation of SANISAND 2008 in MATLAB. It is then analytically demonstrated using Hill's criterion (Hill, 1958) that actually, only instability points triggered post-phase transformation and post-peak stress ratio correspond to a state parameter that can be linked to the imposed volumetric to shear strain ratio. It should be pointed out that these instability points differ from the pre-phase transformation triggering points for flow liquefaction under volumetric expansion, as studied by Lashkari and Yaghtin (2018) and Lashkari et al. (2021). Using the locus of post-phase transformation and post-peak stress-ratio instability points for a given strain coupling ratio, it is shown that one can recreate a constant state parameter curve. The state parameter is related to the strain coupling ratio using an analytical expression derived from the constitutive model equations. This fundamental investigation is performed using benchmark data for Toyoura sand, to facilitate verification and comparison to literature.

The analytical-cum-numerical framework established, that relates specific instability points under a given strain coupling ratio in triaxial space to a constant state parameter, is evaluated against, and subsequently calibrated using, the coupled strain triaxial compression experiments on Hostun HN31 sand presented in chapter 4. The SANISAND 2008 model is calibrated for Hostun sand based on undrained and fully drained monotonic compression tests of chapter 4 and the coupled shear-volumetric experiments of chapter 4 are subsequently simulated. Comparing the numerical and experimental instability loci, it is demonstrated that an update to the state parameter is required for SANISAND 2008 to capture the experimental results.

Two modelling strategies may be adopted in updating the mapping of state. The conventional state parameter may be retained while the bounding and dilatancy surface evolution laws are reformulated, or the established evolution laws may be retained while the state variable is altered. These approaches are mathematically equivalent if the same functional mapping and calibration are adopted. The latter approach is adopted here because it isolates the influence of state mapping to the state parameter definition, it facilitates the calibration of the parameters introduced, and it preserves continuity with the existing SANISAND framework, which from its

conception allowed for different state mapping rules.

An updated definition for the state parameter is proposed for Hostun HN31, which allows better modelling of not only the identified instability points, but of the overall behaviour throughout the coupled strain paths.

The novel contribution of this chapter is twofold: first, it demonstrates a procedure for direct assessment of the relative state mapping within SANISAND models against experimental data; second, it demonstrates that updating the relative state mapping based on coupled-strain experimental data substantially improves the prediction of such paths.

5.2 Numerical simulation of monotonic triaxial tests

This study employs the SANISAND 2008 (Taiebat and Dafalias, 2008) model to replicate sand behaviour in the triaxial stress space. The model formulation is described in detail in section 3.3 and the constitutive equations are listed in table 3.2. The model was numerically implemented in MATLAB using the forward Euler method for integration of strain-controlled loading steps. The model parameters for Toyoura sand, adopted from Taiebat and Dafalias (2008), are shown in table 5.1. Additionally, default values of $m = 0.05 \cdot \alpha^c$ and $p_{at} = 98.06$ kPa were used. The purpose of using Toyoura sand calibration parameters was to verify that the current implementation performs in congruence with the published simulation results in Taiebat and Dafalias (2008). Following the validation of the constitutive model implementation in MATLAB, coupled strain tests were numerically simulated in triaxial space on Toyoura sand similar to Kamai and Boulanger (2012), who simulated two-dimensional (direct simple shear) coupled strain paths on Toyoura sand using the PM4Sand model (Boulanger and Ziotopoulou, 2022). Constant ratios of volumetric strain increment ($\dot{\varepsilon}_v$) to axial strain increment ($\dot{\varepsilon}_1$) were imposed, following the constant volumetric-to-shear-strain ratios of Kamai and Boulanger (2012), with positive volumetric strain indicating contraction.

Parameter		Parameter		Parameter		Parameter	
G_0	125	e_0	0.934	A_d	0.4	$h_0{}^{(1)}$	36.96
K_0	150	λ	0.019	n^d	2.1	$c_h{}^{(1)}$	0.987
α^c	1.2	ξ	0.7	n^b	1.25	c	0.712

$^{(1)}$Linear evolution of b_0, refer table 3.2 for parameter definitions.

Table 5.1: SANISAND 2008 model parameters for Toyoura sand (Taiebat and Dafalias, 2008)

5.2.1 Results for undrained monotonic compression tests

Undrained monotonic tests were simulated for a range of void ratios and initial effective confining pressures ($p' << P'_0$), following the experimental and numerical data presented in Taiebat and Dafalias (2008). The simulation results are presented in figure 5.1 and show good agreement with the published results.

5.2.2 Results for coupled strain monotonic compression tests

Indicative results for a specimen of Toyoura sand with $D_r = 37.9\%$ and for a range of coupling strain ratios, including the undrained condition, are shown in figure 5.2. Researchers have previously experimentally explored sand response under coupled strain loading paths as discussed in section 2.8.3. Numerical simulations of coupled strain path tests have also been presented in literature, using critical state compatible models in plane strain space (Kamai and Boulanger, 2012; Lashkari et al., 2021) and in triaxial space (Lashkari and Yaghtin, 2018). Experimental findings and simulation results match well with the paths shown in figure 5.2.

The undrained path of figure 5.2 undergoes strain-hardening. Under water outflow conditions ($\dot{\varepsilon}_v/\dot{\varepsilon}_1 > 0$), more significant strain-hardening is observed, bringing q to higher values than under undrained loading. The combined effect of dilation and water outflow, increase p', leading the path beyond the CSL in $e - p'$ space. Note that the imposed coupled strain conditions do not allow critical state to ever be reached. Under water inflow conditions ($\dot{\varepsilon}_v/\dot{\varepsilon}_1 < 0$), initial strain hardening is followed by post-peak strain softening down to $q = 0$, a behaviour indicative of a flow liquefaction failure. The path in $e - p'$ space never reaches the CSL. Dur-

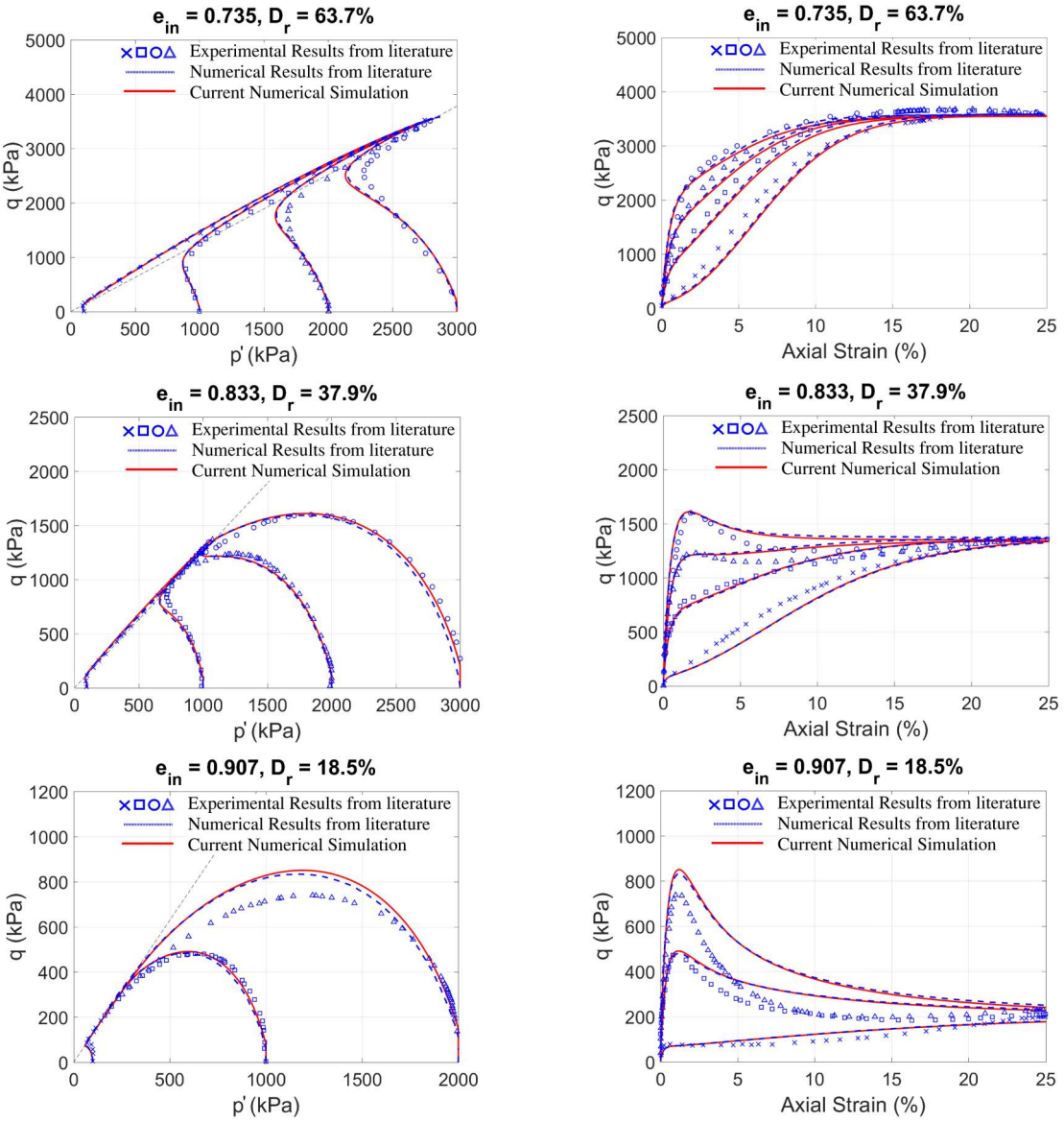

Figure 5.1: Comparison of experimental/simulation data from Taiebat and Dafalias (2008) and simulations from the MATLAB implementation in this study for undrained triaxial compression tests on isotropically consolidated samples of Toyoura sand

ing the strain-softening response, the effect of water inflow can no longer be counteracted by dilation, signifying that instability triggering and flow liquefaction are possible under water inflow conditions, even for soils that display a stable response under undrained conditions. For loose-of-critical specimens subjected to water inflow, strain softening becomes even more pronounced than under undrained conditions (refer figure 5.4), whereas, water outflow can prevent

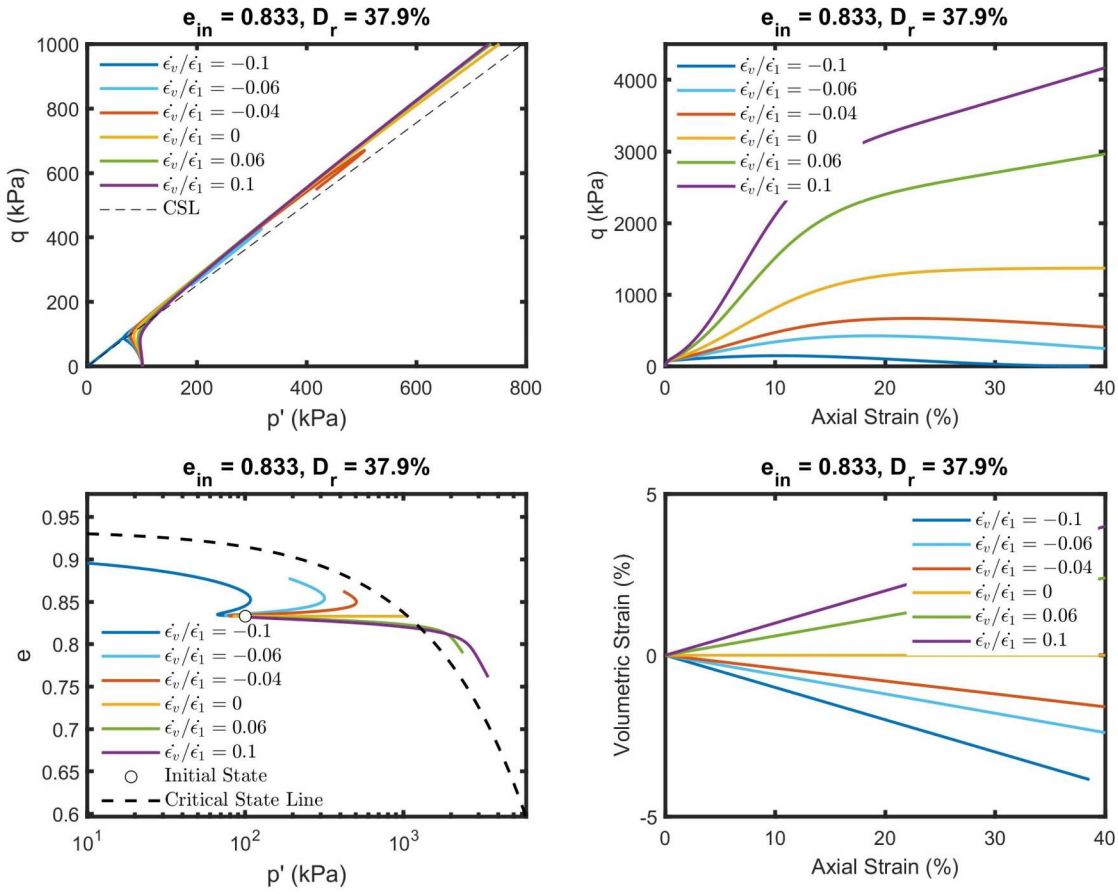

Figure 5.2: Simulations for coupled strain paths on isotropically consolidated samples of Toyoura sand in triaxial space ($p'_{in} = 100$ kPa) for varying strain ratios $\dot{\varepsilon}_v/\dot{\varepsilon}_1$

liquefaction manifestation.

5.3 Instability triggering under coupled strain paths

In this section, the process of using coupled strain paths to analytically isolate and examine the state parameter function embedded within the SANISAND family of constitutive models is presented. This analysis was motivated by the coupled strain 2D numerical results of Kamai and Boulanger (2012) using the PM4SAND model (Boulanger and Ziotopoulou, 2015). Kamai and Boulanger (2012) simulated dilative specimens under water inflow conditions and found that the resulting strain softening branch in $e - p'$ space relates to a constant state parameter. In the following section, we investigate the existence of such a constant state parameter curve in triaxial

space analytically and demonstrate that it corresponds to the locus of post-phase transformation and post-peak stress-ratio instability triggering points, obtained under the same strain coupling ratio. A maximum of one such point can be identified for each coupled strain path. The reader is directed to refer SANISAND 2008 model (Taiebat and Dafalias, 2008) equations and definitions listed in table 3.2.

5.3.1 Instability assessment

Instability triggering is associated with a loss of uniqueness of the incremental response under a particular loading programme. A unique incremental response under a loading programme can be ensured as long as the matrix relating the responding variables to the controlled variables remains invertible. For example, in a purely strain-controlled triaxial test, a non-unique incremental response is expected when the determinant of the elastoplastic compliance matrix (equation 3.2) becomes zero: $det[C^{ep}] = 0$. Imposing this condition on the SANISAND 2008 constitutive model (Taiebat and Dafalias, 2008), the modulus of critical softening H_c (Imposimato and Nova, 1998) can be obtained where $H_c = (3Gs - DK\eta)/p'$ such that when the hardening modulus $H = -H_c$, an instability is triggered. Such an instability under a purely strain-controlled condition is rarely encountered in physical testing (Imposimato and Nova, 1998). Indeed, H remains greater than $-H_c$ throughout the strain-controlled tests simulated and examined here.

In reality, multiple loss-of-uniqueness loci exist in the deviatoric plane, some of which can be physically discerned by a loss of test controllability (Imposimato and Nova, 1998). The loss of uniqueness for purely stress-controlled loading was called the 'limit locus' where the stiffness matrix, as shown in equation 3.1, no longer remains invertible ($det[D^{ep}] = 0$). For the SANISAND 2008 constitutive model (Taiebat and Dafalias, 2008) under a pure stress-controlled loading, the hardening modulus vanishes at the 'limit locus' ($det[D^{ep}] = 3GKH/(H + H_c)$). Imposimato and Nova (1998) concluded that the positive definiteness of the second-order work (Hill, 1958) is a necessary and sufficient condition to ensure a unique material response under any combination of mixed stress-strain control loading programmes.

The findings of Imposimato and Nova (1998) were supported by Andrade (2009) and Andrade et al. (2013), who numerically simulated undrained behaviour under monotonic compression in triaxial space, using the Nor-Sand model (Jefferies, 1993) and the Dafalias and Manzari (2004) predecessor of the SANISAND family, respectively. They imposed a loss of uniqueness condition and Hill's stability criterion (Hill, 1958) to detect the onset of instability under a deviatoric stress rate ($\dot{q}$) in undrained compression tests and proved the coincidence of the two approaches. Using Hill's condition, Andrade et al. (2013) further related the slope of the instability line in stress ($q - p'$) space to a limiting hardening modulus that was found to be a function of the soil state. The onset of instability under coupled strain path simulations has been similarly evaluated using Hill's criterion (Lashkari and Yaghtin, 2018; Lashkari et al., 2021).

Here, the instability point being pursued pertains to a hypothetical mixed stress-strain controlled loading programme, where the deviatoric stress increment ($\dot{q}$) and the volumetric strain increment ($\dot{\varepsilon}_v$) are controlled with a condition that the ratio of the volumetric to deviatoric strain increment remains a constant ($\dot{\varepsilon}_v/\dot{\varepsilon}_q = \Lambda$). Imposing a loss of uniqueness criterion to the SANISAND 2008 constitutive model (Taiebat and Dafalias, 2008), an expression for the hardening modulus was derived such that when the condition of equation 5.1 is achieved, an instability is triggered. One possible point of instability satisfying equation 5.1 is attained when the dilatancy $D = s\Lambda$ and the hardening modulus $H = 0$. It should be pointed out that the numerical simulations performed in this paper were fully strain-controlled and as such are expected to remain stable at the mixed control instability of equation 5.1.

$$H = (D - s\Lambda)\eta K / p' \tag{5.1}$$

5.3.2 Criterion for instability under coupled strain paths

Following the conclusion of Imposimato and Nova (1998), Hill's stability criterion (Hill, 1958) was implemented in this study to detect the onset of instability under coupled strain paths in triaxial space. Andrade et al. (2013) deduced the second-order work, $\ddot{W}$ in triaxial space as a

function of the increments of mean effective stress ($\dot{p'}$), deviator stress ($\dot{q}$) and strains ($\dot{\varepsilon}_v$ and $\dot{\varepsilon}_q$) and imposed Hill's condition to obtain equation 5.2, which is a condition for stability under any loading programme.

$$\ddot{W} = \dot{p'}\dot{\varepsilon}_v + \dot{q}\dot{\varepsilon}_q > 0 \tag{5.2}$$

When applied to the undrained case under strain-controlled monotonic compression loading, $\dot{q} \leq 0$ at instability. Hence, the onset of instability in loose sand specimens under undrained conditions occurs at the peak of the stress path in $q - p'$ space, when $\dot{q} = 0$. This instability can be physically detected under a mixed stress-strain controlled experiment where $\dot{\varepsilon}_v = 0$ and $\dot{q} > 0$ are imposed. There may be temporary instability for dense and medium dense sands under undrained loading, where $\dot{q} \leq 0$ and the soil undergoes limited flow liquefaction, until the phase transformation stress ratio is reached. After phase transformation, the sand dilates with $\dot{q} > 0$ until the critical state, where $\dot{q} = 0$, indicating the final instability point.

An expression for the second-order of work from Hill's stability criterion in triaxial space, shown in equation 5.2, was obtained under a condition of $\dot{\varepsilon}_v/\dot{\varepsilon}_q = \Lambda$, using the elastoplastic constitutive relation of SANISAND 2008 (equation 3.1). Instability was detected when the second-order of work changed from positive to negative or vanished at large strains. Alternatively, a limiting hardening modulus (H_L) determining the onset of instability can be derived, generalising the undrained loading relation obtained by Andrade et al. (2013), so that it applies for any ratio of volumetric strain increment to axial strain increment ($\zeta = \dot{\varepsilon}_v/\dot{\varepsilon}_1$):

$$H_L = \frac{3GK(D - s\Lambda)(\eta + \Lambda)}{p'(K\Lambda^2 + 3G)} \tag{5.3}$$

$$\Lambda = \frac{\dot{\varepsilon}_v}{\dot{\varepsilon}_q} = \frac{3\zeta}{3 - \zeta} \tag{5.4}$$

Figure 5.3 shows the instability points detected using Hill's condition (equation 5.2) for three element-level simulations of medium dense - dense Toyoura sand under initial mean effective stress, $p'_{in} = 100$ kPa and $\zeta = -10\%$. The second-order of work instability, as shown in figure

5.3(d), coincides with the point where the limiting hardening modulus first exceeds the hardening modulus, $H_L \geq H$, as shown in figure 5.3(e). Note that equation 5.3 reduces to equation 5.1 for $|\eta| \gg \Lambda$ and $3G \gg K\Lambda^2$.

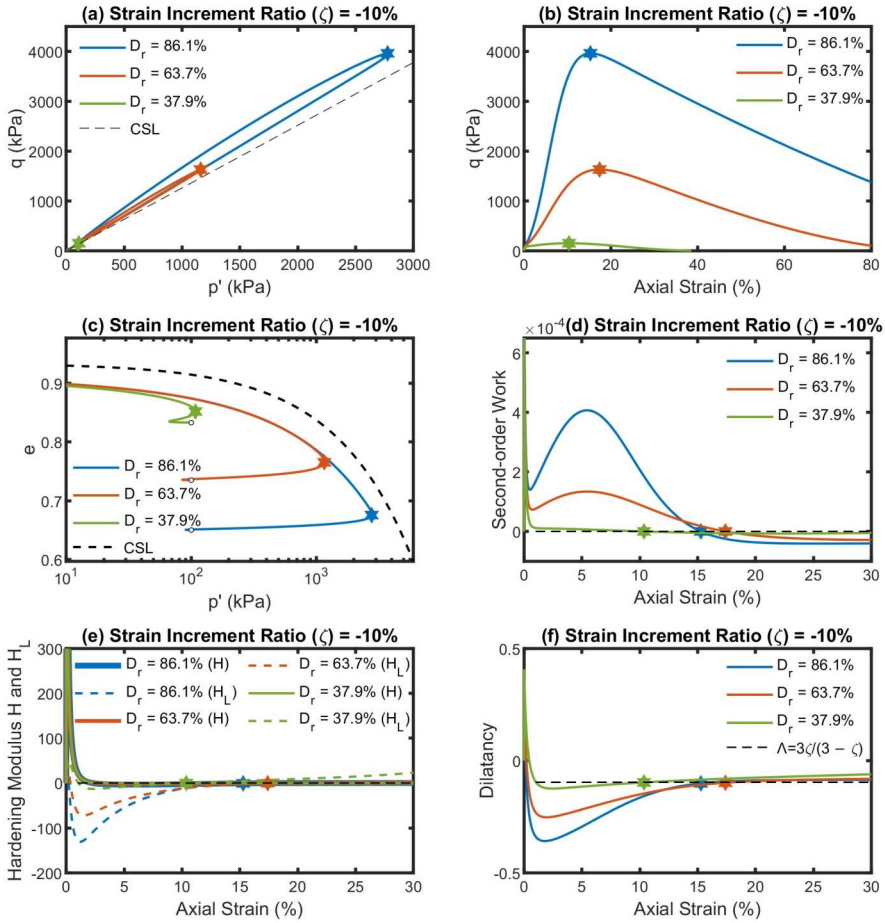

Note: Instability points are shown in star markers.

Figure 5.3: Simulations for coupled strain paths on isotropically consolidated samples of Toyoura sand in triaxial space for $\zeta = -10\%$ and $p'_{in} = 100$ kPa

5.3.3 Isolation of state parameter from instability points

It is worth noting that in figure 5.3(e), the limiting hardening modulus, $H_L \approx 0$ and the hardening modulus, $H \approx 0$ at the instability points. From equation 5.3, it can be deduced that for this to happen, either the dilatancy, $D \approx \Lambda$ (as $s = +1$ for monotonic compression) or the stress ratio,

$\eta \approx -\Lambda$. As seen from the $q - p'$ plots of figure 5.3(a), η is close to or greater than unity at the detected instability points. Hence, it is dilatancy, D that must become equal to Λ. Indeed, this is demonstrated in figure 5.3(f), where the curves depicting the evolution of dilatancy intersect a dashed, constant Λ line at the points of instability.

Drawing from these observations, using definitions for bounding surface, dilatancy surface, hardening modulus H and dilatancy D from SANISAND 2008 model listed in table 3.2, equations 5.3-5.4, and taking $s = +1$ for monotonic compression, the following can be concluded at the identified instability points:

$$H_L \approx 0 \Rightarrow D - s\Lambda \approx 0 \Rightarrow D \approx \Lambda \tag{5.5}$$

$$H \approx 0 \Rightarrow h(\alpha^b - \alpha) \approx 0 \Rightarrow \alpha^b \approx \alpha \tag{5.6}$$

$$D \approx \Lambda \Rightarrow sA_d(\alpha^d - \alpha) \approx \Lambda \Rightarrow A_d(\alpha^d - \alpha^b) \approx \Lambda \tag{5.7}$$

$$\Rightarrow A_d \alpha^c (e^{n^d \psi} - e^{-n^b \psi}) \approx \frac{3\zeta}{3 - \zeta} \tag{5.8}$$

If linear expressions are used for the bounding and dilatancy back stress ratios as functions of ψ (refer table 3.2), equation 5.8 becomes equation 5.9, which is preferential in terms of parameter calibration under coupled strain conditions and is used in this study.

$$A_d(k^d \psi + k^b \psi) \approx \frac{3\zeta}{3 - \zeta} \tag{5.9}$$

Equation 5.9 represents the locus of identified instability triggering points under a constant strain increment ratio, ζ. In equation 5.9, the only variable on the left hand side is the state parameter, ψ, which must have a specific value for a given strain coupling ratio ζ on the right hand side. Consequently, for a given ζ, the locus of the identified instability points corresponds to a constant ψ curve.

5.3.4 Applicability of the proposed instability locus

Though all instability triggering points of figure 5.3 corresponded to the same state parameter, this is not true for instability triggering points in general. The following two conditions must be met for instability triggering points under a given coupling ratio ζ to correspond to a specific state parameter ψ:

$$Condition\ 1:\ H = H_L\ with\ \dot{H}_L \geq \dot{H} \tag{5.10}$$

This condition is a direct consequence of the Hill's stability criterion (equation 5.2). At the onset of instability, $H = H_L$. Loss of stability implies that H_L exceeds H, hence the rate inequality above, indicating a point of instability triggering, rather than the transition from an unstable to a stable region.

$$Condition\ 2:\ H \approx 0\ and\ H_L \approx 0 \tag{5.11}$$

Condition 1 indicates instability triggering, but Condition 2 is also required to derive equation 5.9 that allows the isolation of the state parameter. If both conditions apply for a coupled strain compression test, the point located triggers a final instability, rather than a temporary one. The locus of all such instability points for a particular coupled strain ratio satisfying Conditions 1 and 2 is therefore named the Locus of Constant State parameter Instabilities (LCSI).

As aids to this section, simulations of monotonic triaxial compression tests for a range of initial densities under a strain coupling ratio, $\zeta = -2.5\%$ are presented in figure 5.4, using the parameters of table 5.1. Instability points were obtained using Hill's condition (equation 5.2), as shown in figure 5.4(b). The instability points that satisfy Condition 1 are shown with filled circles and the instability points satisfying both Conditions 1 and 2 are shown with filled stars.

If both Conditions 1 and 2 are met, equation 5.5 holds. As the strain increment ratio ζ (or Λ) < 0 for water inflow conditions, the dilatancy parameter $D \approx \Lambda < 0$ at the instability point, as seen for the two denser soils of figure 5.4(d). This implies that the soil must undergo

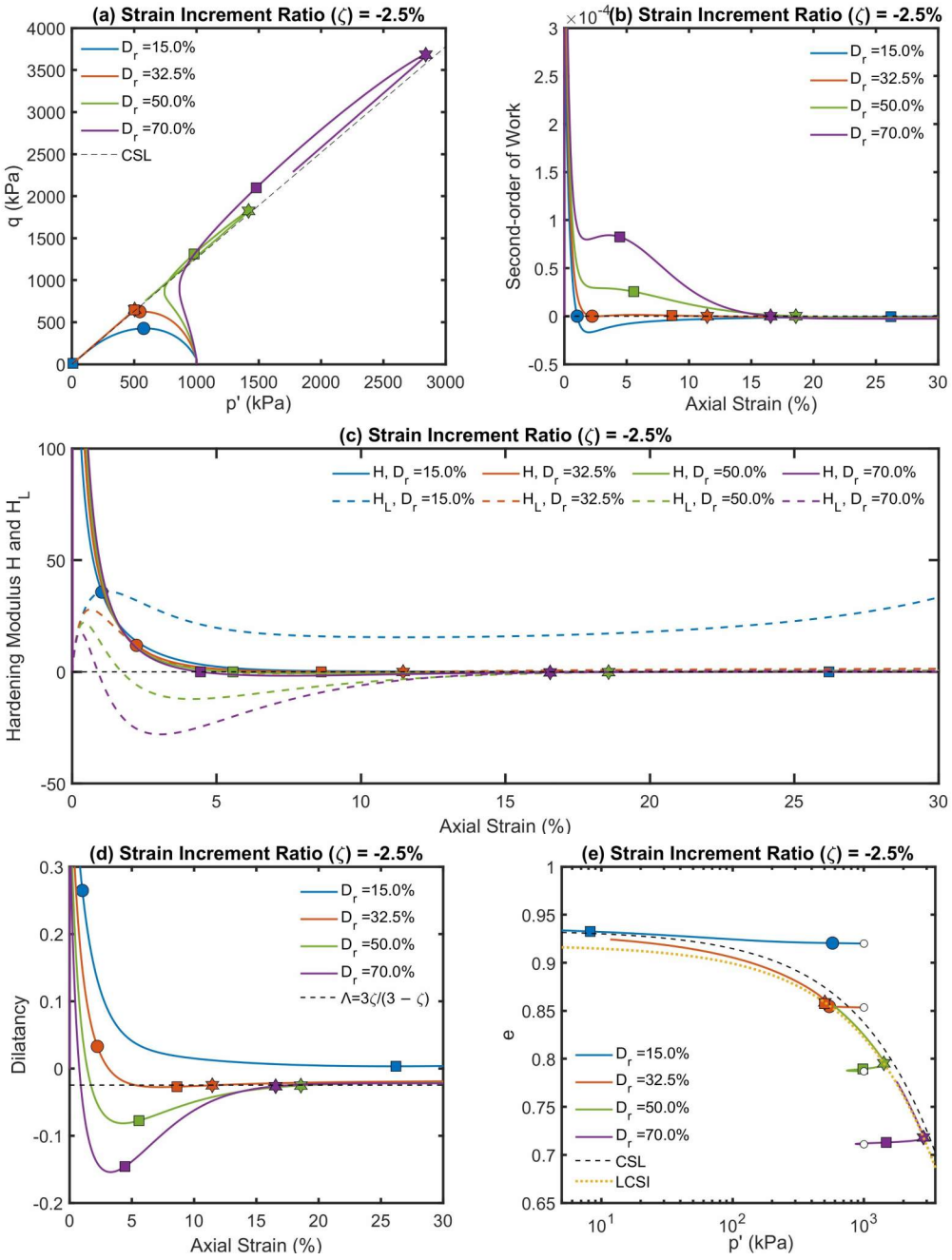

Note: Initial states are shown in white circles, instability points satisfying Condition 1 are shown in solid filled circles, peak stress-ratio points are shown in solid filled squares and instability points satisfying Conditions 1 and 2 are shown in solid filled star markers.

Figure 5.4: Simulations for triaxial compression tests on isotropically consolidated samples of Toyoura sand under $\zeta = -2.5\%$

phase transformation, i.e., the back stress ratio α must cross the dilatancy surface α^d prior to attaining instability (refer equation for dilatancy D in table 3.2). For the undrained case, the dilatancy parameter $D \approx \Lambda \approx 0$ at the instability point. The two specified conditions cannot be satisfied by contractive soils, where $D > 0$. This is confirmed from figure 5.4(d) for the soil with initial $D_r = 15.0\%$. Thus, the locus of the instability points we are pursuing here cannot be attained for soils that only show contractive behaviour under the imposed coupled strain path. For soils undergoing phase transformation, the peak stress-ratio state ($H = 0$), shown in solid filled squares, is reached post-phase transformation and post the maximum magnitude negative dilatancy point, as seen in figures 5.4(c) and 5.4(d). Thus, the hardening modulus $H > 0$ at the phase transformation point, indicating that the back stress ratio α is yet to cross the bounding surface α^b (refer equation for hardening modulus H in table 3.2).

From equation 5.3, it can be inferred that under an inflow condition, the limiting hardening modulus H_L becomes negative when $D < \Lambda$ and remains negative at the peak stress ratio. H_L achieves a minimum negative value at the maximum magnitude negative dilatancy point, see figure 5.4(c). Overall, at the phase transformation point, $H > 0$ and $H_L = 0$ under an undrained condition, while $H > 0$ and H_L is greater than but close to 0 under an inflow condition. In both cases, $H > H_L$. At the peak stress ratio, $H = 0$ and $H_L < 0$, so that still $H > H_L$. Thus, the instability points that satisfy the conditions outlined at the beginning of this section are expected to occur post-phase transformation and post-peak stress ratio. If a specimen fails before these conditions, then it is not possible for it to attain the instability necessary to isolate a state parameter value. Table 5.2 summarises the evolution of the hardening modulus, the limiting hardening modulus and the dilatancy parameter under coupled strain paths for dilative soils.

For the undrained case, the LCSI is represented by the CSL, where $\psi = 0$ (equation 5.8), while for water inflow conditions, the LCSI is represented by a constant $\psi < 0$ curve as shown in figure 5.4(e). For the fully contractive or loose soil state ($D_r = 15.0\%$), the instability points satisfy only Condition 1 and do not fall on the LCSI. As seen in figure 5.4(a) and figure 5.4(e), for the soil states undergoing phase transformation, the instability points satisfying both Conditions

Test Stage	H	H_L	D	Remarks
Before Phase Transformation	'+' ve	'+' ve	'+' ve	$H > H_L$
At Phase Transformation	'+' ve	0 or $\rightarrow 0$	0	$H_L = 0$ for undrained; $H > H_L$
PTS to Peak stress ratio	'+' ve	'-' ve	'-' ve	$H > H_L$
At Peak stress ratio	0	'-' ve	'-' ve	H_L and D are near minimum '-' ve value
Post-Peak stress ratio	'-' ve	'-' ve	'-' ve	H_L and D increase towards 0
At Instability	$\rightarrow 0$	$\rightarrow 0$	'-' ve	$H = H_L \approx 0$; $D \approx \Lambda$

Table 5.2: Sign transition of hardening modulus, H, limiting hardening modulus, H_L and dilatancy, D under incremental coupled strain monotonic compression tests for medium dense to dense sands

1 and 2 occur after the peak stress-ratio state, and fall on the LCSI. A temporary instability point satisfying only Condition 1 but with $H > 0$ and $D > 0$ may be encountered for medium dense initial states prior to undergoing phase transformation. Such a point represents the onset of a limited liquefaction behaviour and does not lie on the LCSI. Post-phase transformation, a second instability point that satisfies both conditions and lies on the LCSI can be achieved for such tests, as in the case of $D_r = 32.5\%$ in figure 5.4. Finally, for the dense specimens, $D_r = 50.0\%$ and 70.0%, both conditions are met at the instability point since $H = H_L \approx 0$ (figure 5.4(c)). Consequently, the instability point lies on the LCSI in figure 5.4(e).

5.3.5 Verification of proposed instability line

Having established the applicability of the LCSI in section 5.3.4, equation 5.8 is plotted for Toyoura sand in the $e - p'$ space in figure 5.5 for three strain coupling ratios. Simulated paths from a range of initial states under the imposed coupling ratios are plotted and the instability points derived from equation 5.2 and satisfying Conditions 1 (equation 5.10) and 2 (equation 5.11) are added as star markers. As seen from figure 5.5, equation 5.8 defines the instability points accurately across a range of initial conditions and ζ values. This theoretical exercise shows that triaxial compression tests performed under a given strain coupling ratio ζ can be used to determine the locus of constant state instability points (LCSI), which for a bounding surface plasticity model of the SANISAND family lie on a constant state parameter ψ curve (equation 5.8 or 5.9).

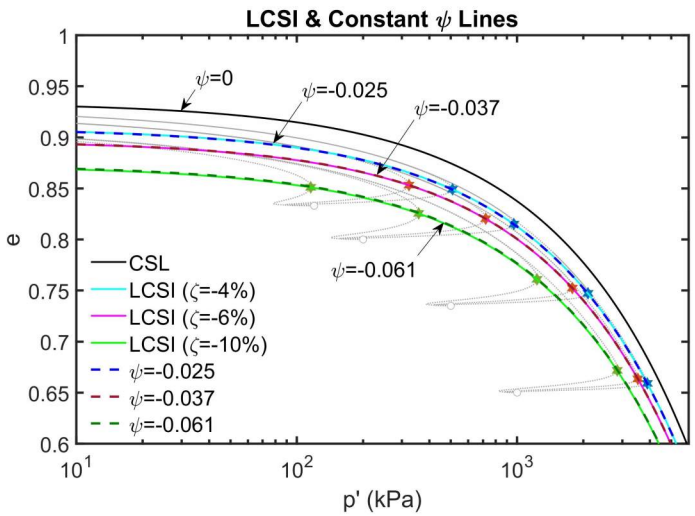

Figure 5.5: Locus of Constant State Parameter Instability points (LCSI) or Constant ψ Lines for simulated coupled strain paths in triaxial space on Toyoura sand under $\zeta = -4\%$, -6% and -10%

5.3.6 Role of dilatancy

The role of dilatancy (D) on the soil response can be understood from the $e - p'$ plot (figures 5.3(c) and 5.4(e)). Initially the sand is contractive ($D > 0$, figures 5.3(f) and 5.4(d)), so it develops positive plastic volumetric strain rates ($\dot{\varepsilon_v}^p > 0$). To ensure the overall response is dilative for an inflow strain increment ($\dot{\varepsilon_v} < 0$), the elastic portion of the volumetric strain rate has to be negative ($\dot{\varepsilon_v}^e < 0$) and a reduction in the effective stress ($\dot{p'} < 0$) can be noted. Upon reaching the phase transformation point, the inherent nature transitions to dilation ($D < 0$) and increasing negative plastic volumetric strain ($\dot{\varepsilon_v}^p < 0$) is accumulated. To combat the excess dilation, the elastic portion of the volumetric strain rate positively increases ($\ddot{\varepsilon_v}^e > 0$) with a positive increase in the effective stress increment ($\ddot{p'} > 0$). Subsequently, as the dilatancy attains increasing negative values, the mean effective stress increases ($\dot{p'} > 0$). As the dilatancy reaches its maximum negative value, the rate of increment of p' also peaks ($\ddot{p'} = 0$). As dilatancy starts to drop (increases positively), the rate of increment of p' follows ($\ddot{p'} < 0$) and at the instability point the dilatancy value matches the imposed strain increment ratio ($D = \Lambda$), figures 5.3(f) and 5.4(d). Note that the volumetric and deviatoric elastic strain increments are not diminished at the instability points, but the ratio of the volumetric and deviatoric plastic strain increments ($= D$

per table 3.2) equals the ratio of total volumetric and deviatoric strain increments. The elastic volumetric strain rate is still positive at this point ($\dot{\varepsilon_v}^e > 0$) but very diminished. Shortly after, there is a momentary stagnation of p' ($\dot{p'} = 0$) where the plastic volumetric strain rate suffices to match the imposed inflow rate ($\dot{\varepsilon_v}^p = \dot{\varepsilon_v}$). The deviator stress attains a peak value ($\dot{q} = 0$) just prior to the instability point which indicates that at the instability point, the elastic shear strain increment attains a very small negative value ($\dot{q} < 0$). Beyond the instability point, the soil loses its ability to dilate due to continued loosening (reduction in state parameter, ψ) and p' has to reduce to keep the elastic volumetric strains negative until failure. Thus, the instability points occur prior to the point of transition from hardening to softening behaviour in $e - p'$ space, see figures 5.3(c) and 5.4(e), and after the peak deviator stress point in the $q - p'$ stress space, see figure 5.3(b).

5.4 Hostun sand calibration

With the analytical framework set up for co-relating the state parameter with specific instability points under coupled strain paths, experimentally obtaining LCSI curves was pursued using the coupled strain triaxial compression tests on batch 2 of Hostun HN31 sand, as presented in chapter 4. As the goal of the study is to assess the performance of the SANISAND models in replicating coupled strain paths through the LCSI curves, an initial calibration of the SANISAND 2008 constitutive model (Taiebat and Dafalias, 2008) was conducted using the undrained and fully drained tests on batch 2 of Hostun HN31 sand from chapter 4 and the state parameter of Been and Jefferies (1985). This initial calibration is essential for the assessment of the currently used definition of the state parameter in replicating the experimentally obtained LCSI curves from the coupled strain monotonic paths, as will be illustrated in the following sections. The critical state line was already established in the previous chapter, and is defined by equation 4.1. The calibration methodology and calibrated parameters are presented in this section.

5.4.1 Elastic moduli

The small-strain shear modulus, G_{max} as obtained by Azeiteiro et al. (2017) using bender element tests on air-pluviated triaxial samples of Hostun sand, is shown in equation 5.12 and follows the form proposed by Hardin (1978). This expression was obtained from specimens at two different initial densities and a unique mean effective stress level.

$$G_{max} = G_0 \, p_{at} \frac{(2.97-e)^2}{1+e} \left(\frac{p'}{p_{at}} \right)^{0.49} \qquad where \quad G_0 = 293 \tag{5.12}$$

At ETH Zurich, bender element tests on wet-pluviated triaxial specimens of Hostun HN31 sand (batch 1) were conducted at four initial densities, each isotropically consolidated to five different levels of confining stress. Equation 5.12 was found to match the stiffness results for three densities (Kassas et al., 2021) but underestimated the value for the densest specimen. An expression for G_{max} resulting from the bender element tests was proposed as shown in equation 5.13 which has been used in this study. Note that bender element test results on batch 2 of Hostun sand were not available to the author at the time of this study. Additionally, due to the different functions used for density dependence, the G_0 values of expressions 5.12 and 5.13 are not directly comparable.

$$G_{max} = G_0 \, p_{at} e^{-1.8} \left(\frac{p'}{p_{at}} \right)^{0.5} \qquad where \quad G_0 = 530 \tag{5.13}$$

The value of G_{max} captured by small-strain measurements has been observed to be 2-4 times higher than that required to adequately model the initial stages of monotonic shearing with bounding surface plasticity models (Andrianopoulos et al., 2010; Papadimitriou et al., 2001, 2023). Taiebat and Dafalias (2008) estimated the value of the small-strain shear modulus coefficient G_0 when calibrating SANISAND 2008 (refer table 3.2), by using the initial stages of stress-strain curves from drained monotonic compression tests (selecting the secant modulus at strain levels $\sim 3 \times 10^{-4}$, from observation). A similar approach was followed here as it yielded improved results in terms of capturing the monotonic experiments. Along with the fully drained

monotonic tests described in section 4.3.1, slopes corresponding to G_0, $G_0/2$ and $G_0/3$ of equation 5.13 are shown in figure 5.6. It was found that the average secant modulus at strain levels $\sim 3 \times 10^{-4}$ is $G_0/3$. The following expression was thus used for the shear modulus:

$$G = G_0 \, p_{at} e^{-1.8} \left(\frac{p'}{p_{at}} \right)^{0.5} \qquad where \qquad G_0 = 176.67 \tag{5.14}$$

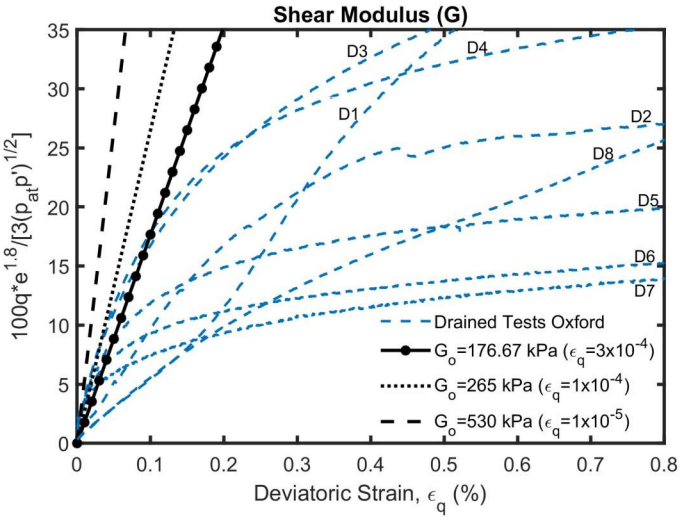

Figure 5.6: Calibration of G_0 using data of fully drained triaxial compression tests on isotropically consolidated Hostun sand (batch 2) presented in chapter 4

Taiebat and Dafalias (2008) propose that the elastic bulk modulus, K (refer table 3.2) is also a function of the confining pressure p' and current void ratio e and can be obtained from the elastic shear modulus G or from isotropic unloading data. Equation 5.15 is proposed for the incremental bulk modulus in isotropic unloading from triaxial experiments on batch 2 of Hostun HN31 sand conducted at the University of Oxford by Grey and Adamidis (2024).

$$K = K_0 \, p_{at} e^{-2} \left(\frac{p'}{p_{at}} \right)^{0.65} \qquad where \qquad K_0 = 225 \tag{5.15}$$

5.4.2 Critical state parameter

The critical state line was described in section 4.3.1. The state parameter definition by Been and Jefferies (1985) was used for this initial calibration, as noted in table 3.2. The stress ratio η at

critical state in triaxial compression, M^c was determined as shown in figure 5.7. An $M^c = 1.251$ yields a critical state friction angle $\phi_{cs} = 31.2°$, which is very close to $\phi_{cs} = 31.5°$ concluded by Azeiteiro et al. (2017). The value of m was chosen as 0.05 (Taiebat and Dafalias, 2008), which resolves the back stress ratio at critical state, $\alpha^c = 1.201$, following the yield surface equation shown in table 3.2. The critical state stress ratio in extension to that of compression was taken as $c = 0.71$ based on results presented by Azeiteiro et al. (2017). This yields a critical state friction angle $\phi_{cs} = 22.8°$ in extension.

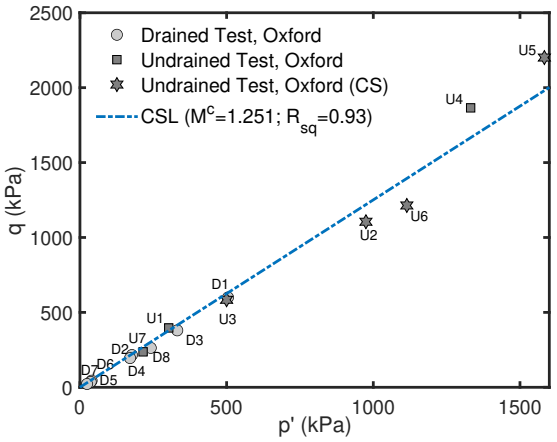

Figure 5.7: Critical state strength of Hostun sand (batch 2) in compression

5.4.3 Bounding surface parameter

The bounding surface parameter, n^b was obtained from surface evolution laws in table 3.2. The bounding surface, α^b was obtained from peak stress-ratio states (PSRS), $\eta_{PSRS} - m$ from drained and undrained tests using the yield surface equation. For an exponential bounding evolution, $ln(\alpha^c/\alpha^b)$ and for a linear bounding evolution, $(\alpha^c - \alpha^b)$ were plotted against the corresponding state parameter, ψ. The slope of the fitted line gives the n^b and k^b values, as shown in figure 5.8(a) and 5.8(b), respectively. Undrained tests were prioritised in calibration, since as volume controlled they are closer to the coupled strain tests that we aim to simulate.

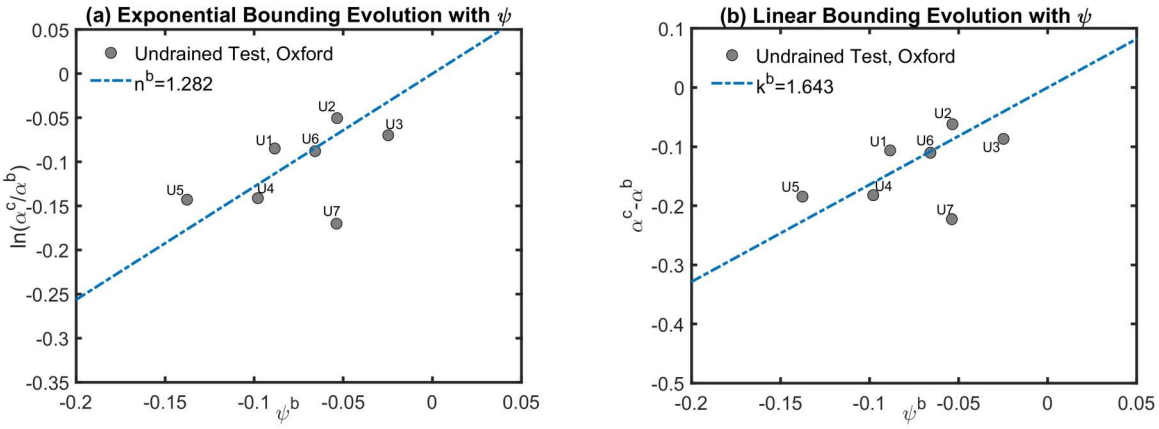

Figure 5.8: Calibration of constants (a) n^b and (b) k^b (refer table 3.2) for Hostun sand (batch 2) using the results of undrained monotonic compression tests presented in chapter 4

5.4.4 Dilatancy surface parameter

The dilatancy surface parameter, n^d was selected based on surface evolution laws in table 3.2. The dilatancy surface, α^d was obtained from the stress ratio at phase transformation state (PTS), so that $\alpha^d = \eta_{PTS} - m$ from undrained tests. For an exponential evolution, $ln(\alpha^d/\alpha^c)$ and for a linear evolution, $(\alpha^d - \alpha^c)$ were plotted against the corresponding state parameter, ψ. The slope of the fitted line gives the n^d and k^d value, respectively (figures 5.9(a) and 5.9(b)).

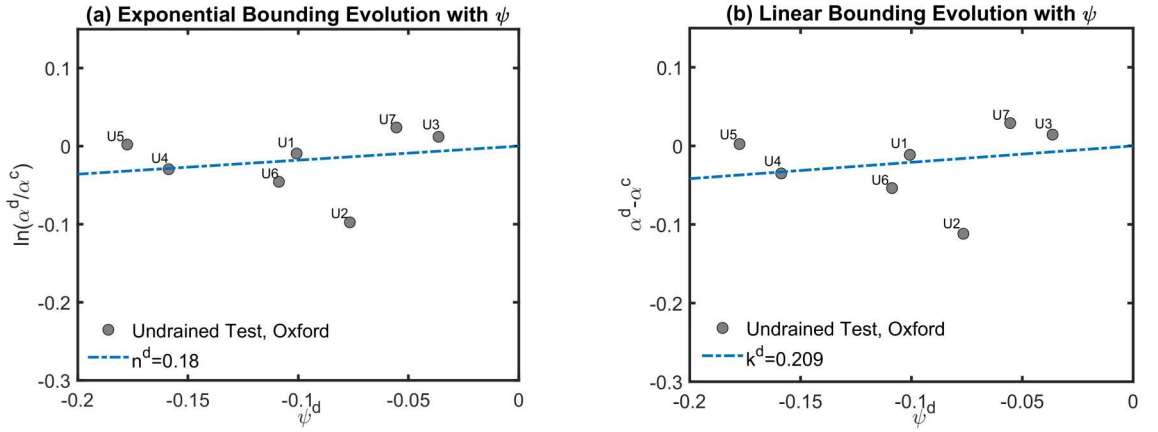

Figure 5.9: Calibration of constants (a) n^d and (b) k^d (refer table 3.2) for Hostun sand (batch 2) using the results of undrained monotonic compression tests presented in chapter 4

5.4.5 Stress-dilatancy characteristics

The dilatancy parameter, A_d was determined from stress-dilatancy curves obtained from drained tests using dilatancy equation in table 3.2, where the dilatancy parameter D is expressed as a function of the difference between the slope of the dilatancy surface, α^d and the current back stress ratio α. The dilatancy D is a ratio of the plastic volumetric to the plastic deviatoric strain increment, so that $D = \dot{\varepsilon}_v{}^p / \dot{\varepsilon}_q{}^p$ for monotonic compression tests, where $\dot{\varepsilon}_q{}^p > 0$. In order to obtain plastic strain increments, the elastic strain increments must be subtracted from the total strain increments. The elastic strain increments can be computed from the stress increments and elastic moduli per elasticity equations in table 3.2, where the tangent elastic moduli are taken from equations 5.14 and 5.15. This approach has been used before by Azeiteiro et al. (2017) for drained tests. The data was plotted for axial strains ranging from 1% to peak stress ratio in figure 5.10(a). The slope of the stress-dilatancy curves gives the A_d value.

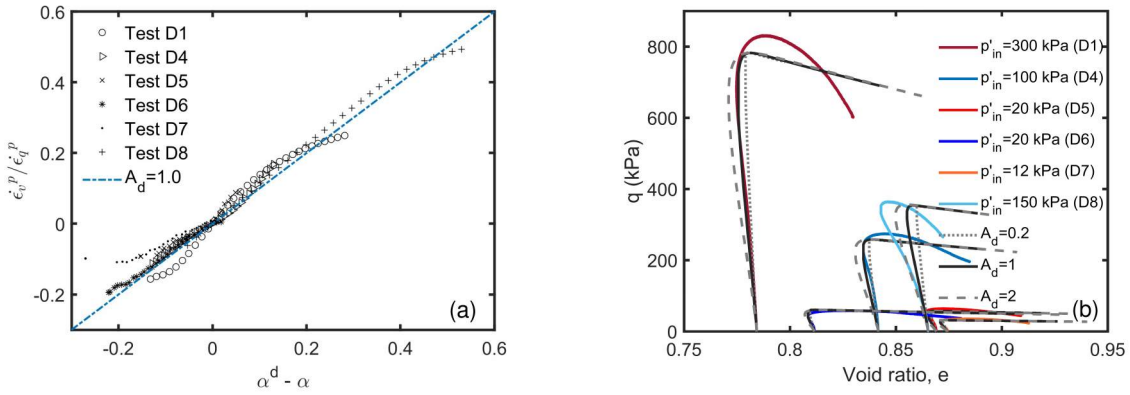

Figure 5.10: Calibration of constant A_d (refer table 3.2) for Hostun sand (batch 2) using the results of fully drained monotonic compression tests presented in chapter 4

Taiebat et al. (2010) estimated the A_0 parameter in DM04 model (Dafalias and Manzari, 2004) by plotting the deviatoric stress, q against void ratio, e from drained experiments and taking the value of A_0 that gives the best-fit simulation, following a trial and error approach. A similar process, depicted in figure 5.10(b), verifies the value of $A_d = 1$ from figure 5.10(a).

5.4.6 Bounding parameters h_0 and c_h

The bounding parameters h_0 and c_h pertain to the distance from the bounding surface and according to Taiebat and Dafalias (2008) are to be determined using trial and error. The undrained test data were used to calibrate these parameters by fitting simulation results to the experimental curves of deviatoric stress, q versus axial strain, ε_1, varying the function of h_0 and c_h, and aiming to capture the response at low strains, as in Taiebat et al. (2010). The exponential function of h_0 and c_h as noted in table 3.2 provided a better overall fit for all tests. Figure 5.11 shows this calibration process, including two examples of undrained tests.

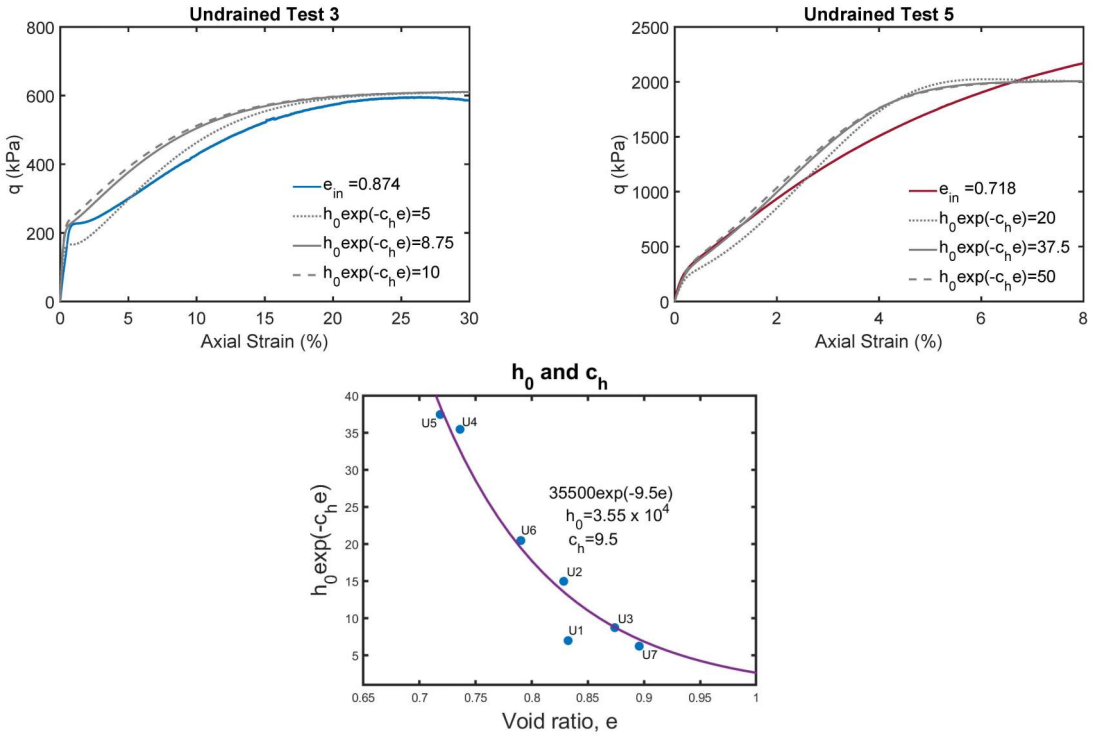

Figure 5.11: Calibration of h_0 and c_h for Hostun sand (batch 2) using the results of undrained monotonic compression tests presented in chapter 4

5.4.7 Compression parameters

The compression parameters are applicable for loading at high-confining pressures related to the limiting compression curve regime, which is around $p' = 10 - 50$ MPa for siliceous sands

(Taiebat and Dafalias, 2008). Liquefaction related studies are conducted at low confining pressure range as the phenomenon involves a gradual reduction in effective confining stress to failure. Particle crushing does not contribute significantly to the plastic strains and strength characteristics in liquefaction triggering, which is why the compression properties of Hostun sand were not probed in this study, as in other liquefaction studies (e.g. Andrianopoulos et al., 2010; Kassas et al., 2021; Petalas et al., 2019; Taiebat et al., 2010). In fact, the model used here (Taiebat and Dafalias, 2008) is an exception within the SANISAND family, whose models generally do not allow for consideration of the compression property. Nevertheless, the compression property could further improve simulation of behaviour at higher stresses (Taiebat et al., 2010), especially for crushable sands, such as calcareous sands (McDowell and Bolton, 1998).

5.5 Model performance

A summary of the calibrated model parameters are listed in table 5.3. p_{at} is taken as 100 kPa. Some characteristic simulations of the experimental tests from chapter 4 are presented in this section. The model was found to perform in a similar way under either a linear or an exponential evolution assumption of the bounding and dilatancy surfaces with the state parameter (refer surface evolution laws in table 3.2). Here, a linear evolution was used, as it was found to be advantageous for the coupled strain path investigation presented in the later sections. A summary of the SANISAND 2008 constitutive model equations chosen/modified for the simulations presented here are listed in table 5.4. For the remaining equations refer to table 3.2.

Parameter		**Parameter**		**Parameter**		**Parameter**	
$G_0{}^{(1)}$	176.67	$e_{max}{}^{(3)}$	0.993	n^b	1.282	n^d	0.18
$K_0{}^{(2)}$	225	$e_{min}{}^{(3)}$	0.647	k^b	1.643	k^d	0.209
α^c	1.201	$R^{(3)}$	0.73	$h_0{}^{(4)}$	3.55×10^4	A_d	1
c	0.71	$Q^{(3)}$	8.3	$c_h{}^{(4)}$	9.5	m	0.05

$^{(1)}$Implemented in equation 5.14; $^{(2)}$Implemented in equation 5.15; $^{(3)}$Implemented in CSL equation 4.1; $^{(4)}$Exponential function used, see section 5.4.6; refer table 5.4 for model equations.

Table 5.3: SANISAND 2008 model parameters for Hostun sand (batch 2)

Equations	Model Constants	Description
Critical State Line: $e_{cs} = e_{max} - \frac{(e_{max}-e_{min})R}{Q-ln(p')}$	e_{max} , e_{min} , Q , R	Equation 4.1
Elasticity: $G = G_0\ p_{at} e^{-1.8}(\frac{p'}{p_{at}})^{0.5}$ $K = K_0\ p_{at} e^{-2}(\frac{p'}{p_{at}})^{0.65}$	G_0 , K_0	p_{at} : 100 kPa Equation 5.14 Equation 5.15
Hardening Rule: $b_0 = G_0 h_0 exp(-c_h e)(p'/p_{at})^{-1/2}$	h_0 , c_h	Exponential evolution of b_0
Surface Evolution Laws: $\alpha^b_{c,e} = s(\alpha^c_{c,e} - k^b \psi)$ $\alpha^d_{c,e} = s(\alpha^c_{c,e} + k^d \psi)$	k^b , k^d	Linear Surface Evolution ψ: State Parameter ($= e - e_{cs}$)

Table 5.4: Selected/modified equations for SANISAND 2008 model to be used in conjunction with model parameters of table 5.3, refer table 3.2 for remaining equations

5.5.1 Undrained and drained simulation results

Figure 5.12 shows a comparison between the numerical simulations and the experimental data for undrained tests, while figure 5.13 shows a comparison for fully drained tests. The numerical simulations were able to capture the behaviour sufficiently well across a range of densities.

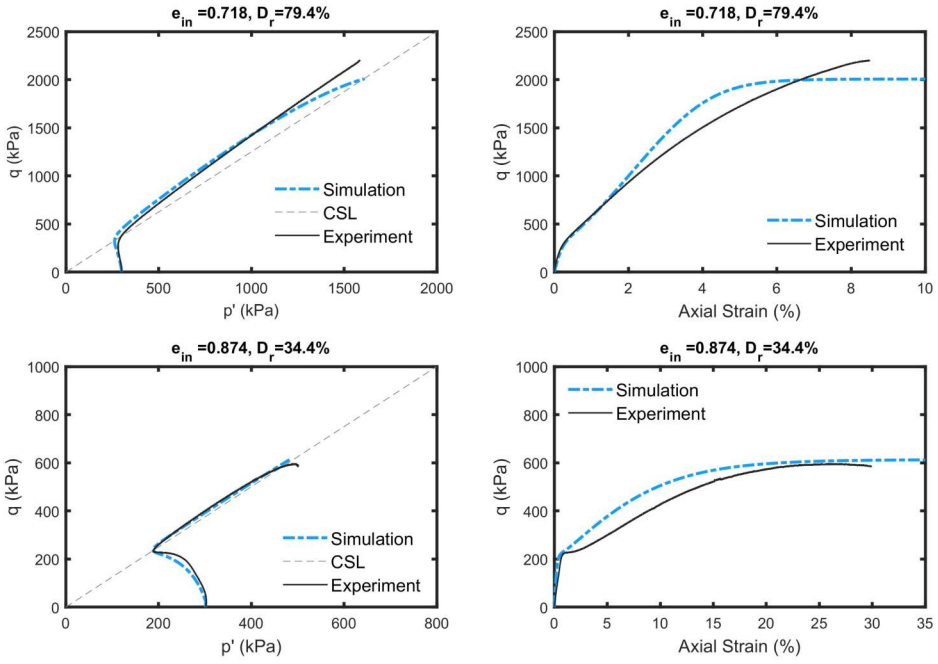

Figure 5.12: Simulations of undrained monotonic triaxial compression tests on isotropically consolidated samples of Hostun sand (batch 2) and comparison with experimental test data (top-bottom: Tests U5 and U3 from section 4.3.1)

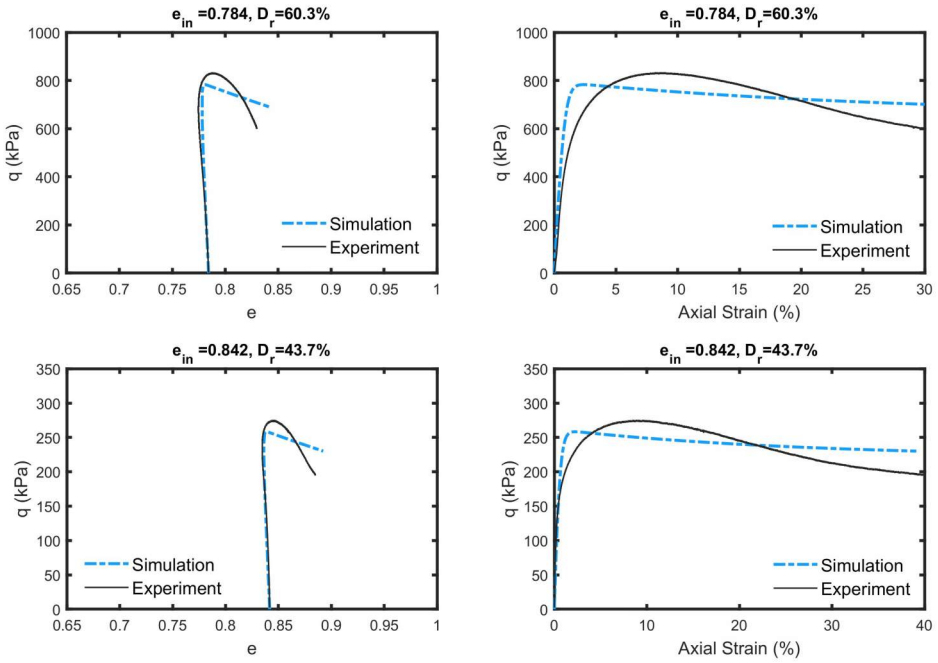

Figure 5.13: Simulations of fully drained monotonic triaxial compression tests on isotropically consolidated samples of Hostun sand (batch 2) and comparison with experimental test data (top-bottom: Tests D1 and D4 from section 4.3.1)

5.5.2 Coupled strain simulation results

Using the calibration parameters from table 5.3 and model equations from table 5.4, the coupled strain triaxial tests of section 4.3.2 were numerically simulated using SANISAND 2008 model (Taiebat and Dafalias, 2008) by imposing a volumetric strain rate as a function of the imposed axial strain rate. Figures 5.14 - 5.16 show the comparison of experimental and numerical results for each coupling ratio at the highest and lowest densities obtained during testing. The instability points are shown in square markers for the simulation and star markers for the experimental data. The comparison reveals that the calibration performs better for the denser specimens across all strain coupling ratios, ζ. For the looser specimens, the comparison is poor. The simulated stress paths in $q - p'$ space only capture the experimental response before dilation commences. The peak deviator stresses predicted are much higher than the observed ones. Across all densities, the instability point is detected at axial strains close to the observed values. Given that the performance of the model in simulating coupled strain behaviour notably varies

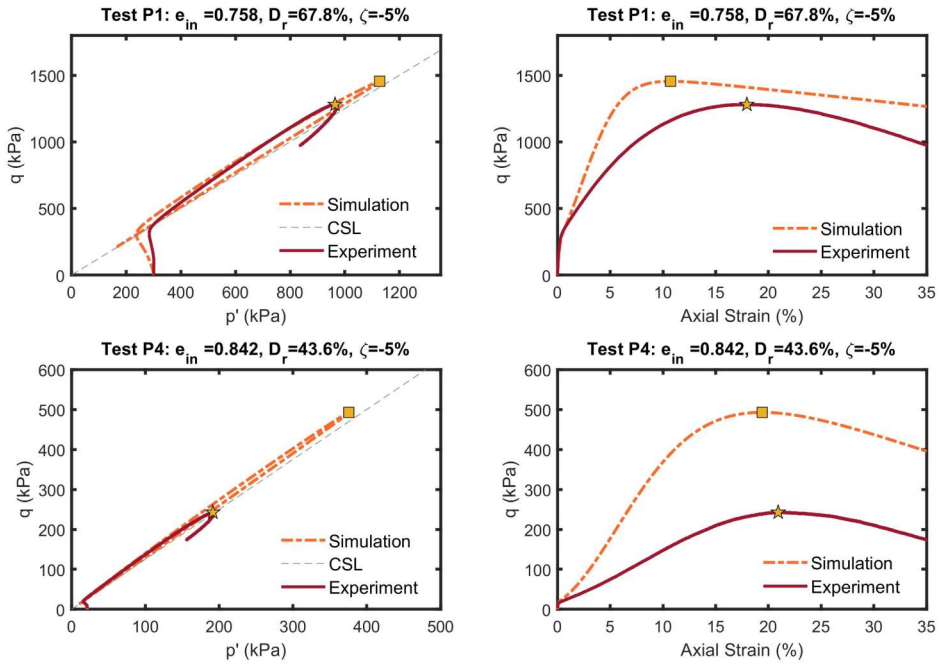

Figure 5.14: Simulations of coupled strain monotonic triaxial compression tests under $\zeta = -5\%$ on isotropically consolidated samples of Hostun sand (batch 2) and comparison with experimental test data from section 4.3.2

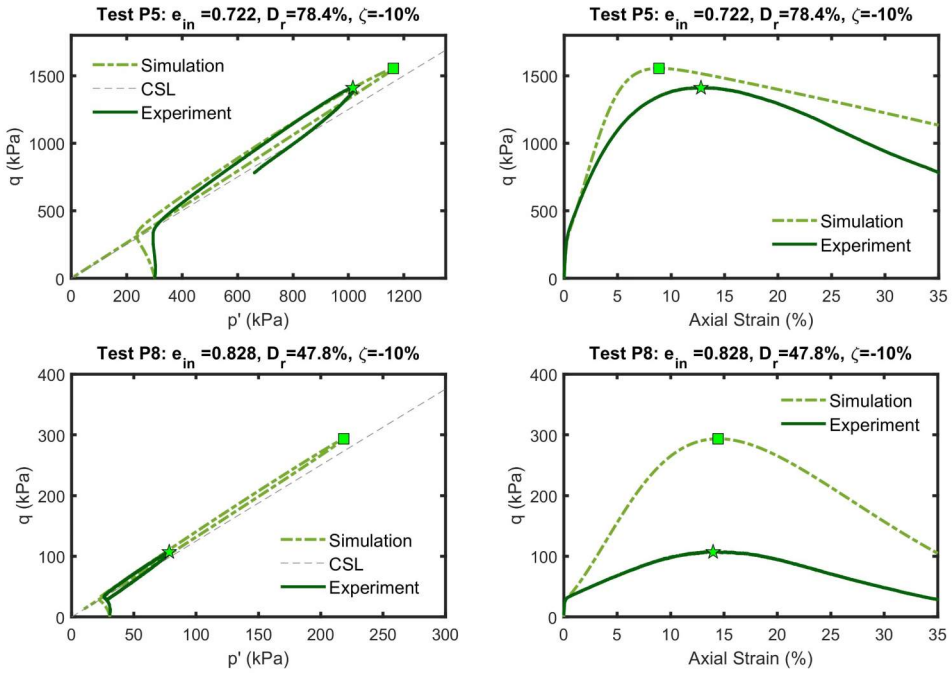

Figure 5.15: Simulations of coupled strain monotonic triaxial compression tests under $\zeta = -10\%$ on isotropically consolidated samples of Hostun sand (batch 2) and comparison with experimental test data from section 4.3.2

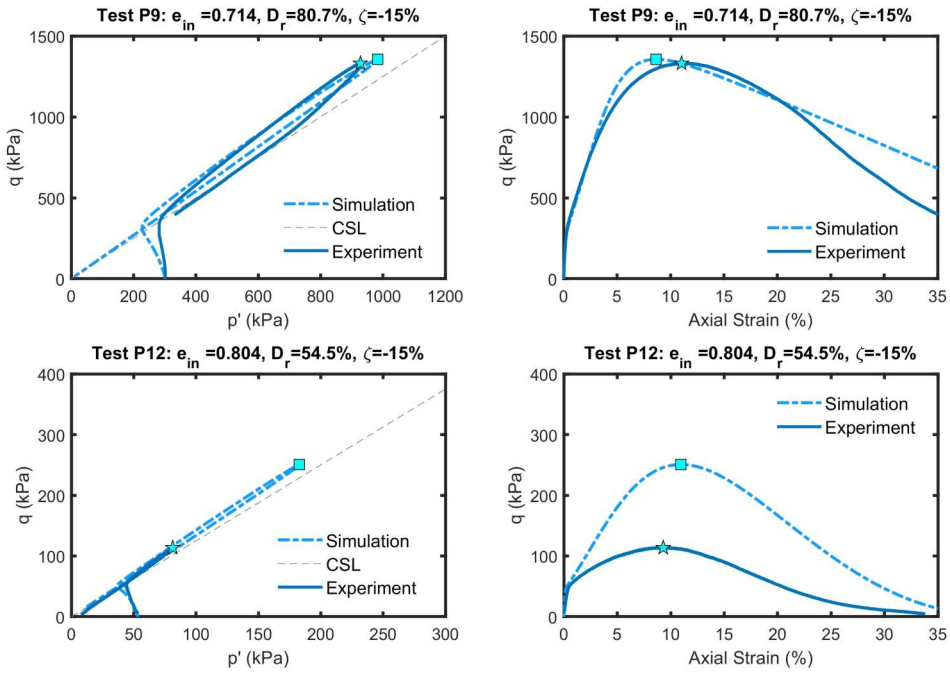

Figure 5.16: Simulations of coupled strain monotonic triaxial compression tests under $\zeta = -15\%$ on isotropically consolidated samples of Hostun sand (batch 2) and comparison with experimental test data from section 4.3.2

with the initial density, the results are plotted in $e - p'$ space in figure 5.17 and compared against the experimental data.

Note that the instability points obtained in table 4.4 occur post-phase transformation states and post-peak stress-ratio states. Thus, they satisfy both Condition 1 (equation 5.10) and Condition 2 (equation 5.11) required to isolate a single state parameter. Constant ψ lines were plotted as dotted lines in figure 5.17, using equation 5.9, and are shown to represent well the locus of the numerically obtained instability points (numerical LCSI curve). However, the experimental LCSI points do not fall on the same curve. As the stress paths of the densest specimens (Tests P1, P5 and P9) are captured better by the constitutive model under coupled strain ratios, a constant ψ curve is drawn through each of the densest experimental instability points, represented in a dashed line in figure 5.17. It is evident that the LCSI points from the remaining three experiments for each coupling strain ratio do not fall on the same constant ψ curve. However, since LCSI points under the same strain coupling ratio must satisfy the condition of a constant ψ (equation 5.9) when modelled with the selected SANISAND model (Taiebat and Dafalias,

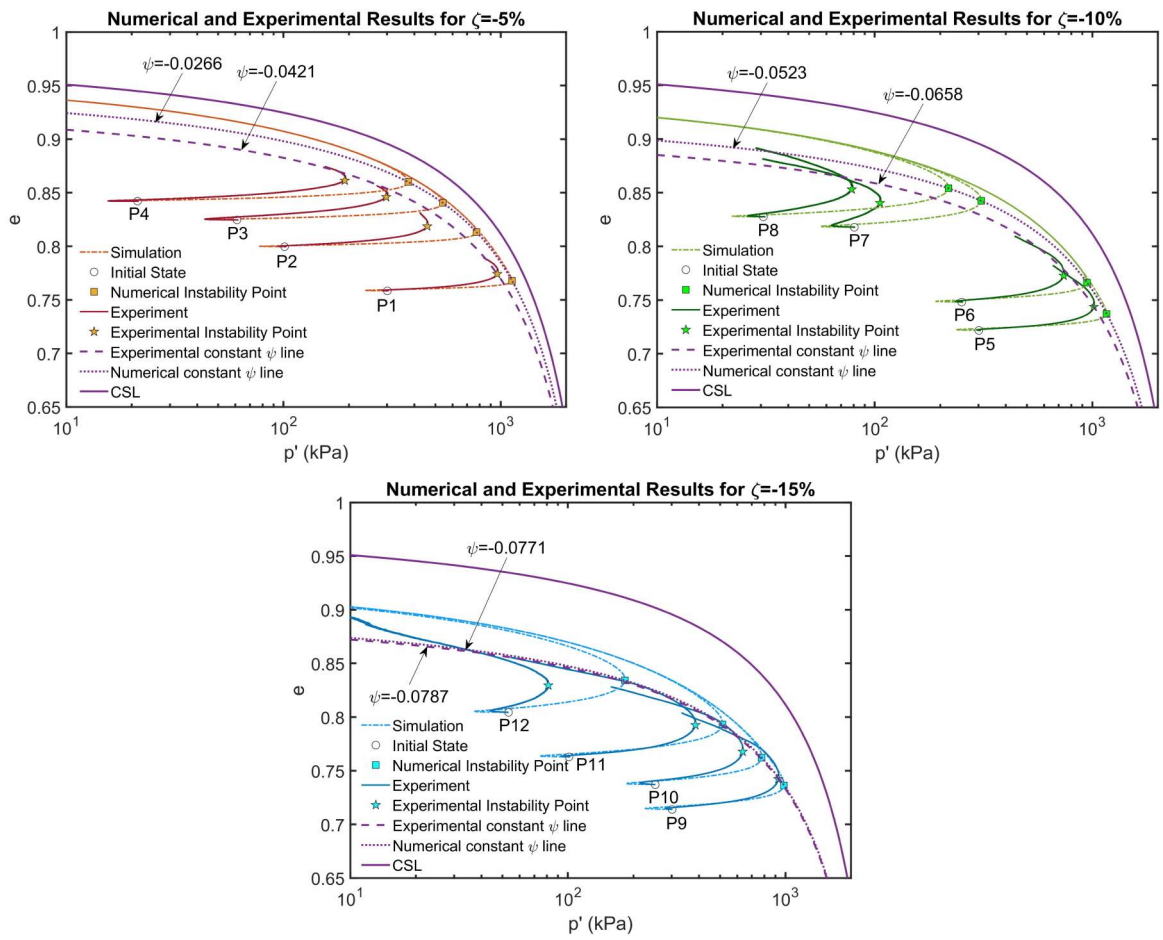

Figure 5.17: Simulations of coupled strain monotonic triaxial compression tests under $\zeta = -5\%$, -10% and -15% in $e - p'$ space and comparison with experimental test data from section 4.3.2

2008), the definition of the state parameter, ψ, used in the constitutive model must be updated so that a constant ψ curve coincides with the experimentally observed LCSI. Alternatively, the bounding and dilatancy surface evolution laws could be reformulated, while the existing state parameter definition is retained. However, this approach is not pursued here, to isolate the influence of state mapping to the state parameter, and to preserve continuity with the existing SANISAND framework.

5.5.3 Updated state parameter definition

Different state parameter definitions have been proposed in literature, such as the commonly used relative distance $e - e_{cs}$ (Been and Jefferies, 1985), state pressure index $I_p = p'/p'_{cs}$ (Z. L. Wang et al., 2002), distance ratio e/e_{cs} (Wan and Guo, 1998), and others noted in Bolton (1986), Dafalias et al. (2004), and Lashkari (2009). These definitions were explored to obtain a better fit to the experimental LCSI points. The best fit was obtained for the distance ratio e/e_{cs} index, across all strain coupling ratios $\zeta(=\dot{\varepsilon}_v/\dot{\varepsilon}_1)$, as seen in figure 5.18.

The Been and Jefferies (1985) state parameter definition, $e - e_{cs}$, diminishes to 0 at the CSL, yields negative values for states below the CSL and positive values for states above the CSL. This ensures a logical evolution of bounding and dilatancy surfaces depending on the soil state, that ultimately collapse on the critical surface at critical state when the state parameter value reduces to 0, see table 5.4. This attribute of the state parameter definition is important for the way the equations of the SANISAND 2008 (Taiebat and Dafalias, 2008) and in general of the SANISAND family of models are cast and is an attribute that an updated state parameter definition needs to retain. To preserve these properties for the distance ratio index e/e_{cs}, a function of its natural logarithm $ln(e/e_{cs})$ is proposed.

The second attribute that a state parameter definition must satisfy, and which was deduced from the analytical framework developed for the LCSI curves, is the fulfillment of equations 5.8 or 5.9 at the LCSI points under each strain coupling ratio ζ.

To facilitate the investigation for a state parameter that satisfies the two attributes listed above, the state parameter is restructured into two constituent parts:

1. The first part is referred to as the state parameter form and is denoted by $\psi_F = f(p', e)$. It is selected to describe the shape of the experimentally identified LCSI curves. The state parameter form must satisfy the first attribute defined above, namely $\psi_F > 0$ for loose-of-critical states, $\psi_F < 0$ for dense-of-critical states, and $\psi_F = 0$ at the critical state. It must also remain constant along the LCSI associated with a given strain coupling ratio ζ. At this stage ψ_F is not required to satisfy equations 5.8 or 5.9 consistently across the full

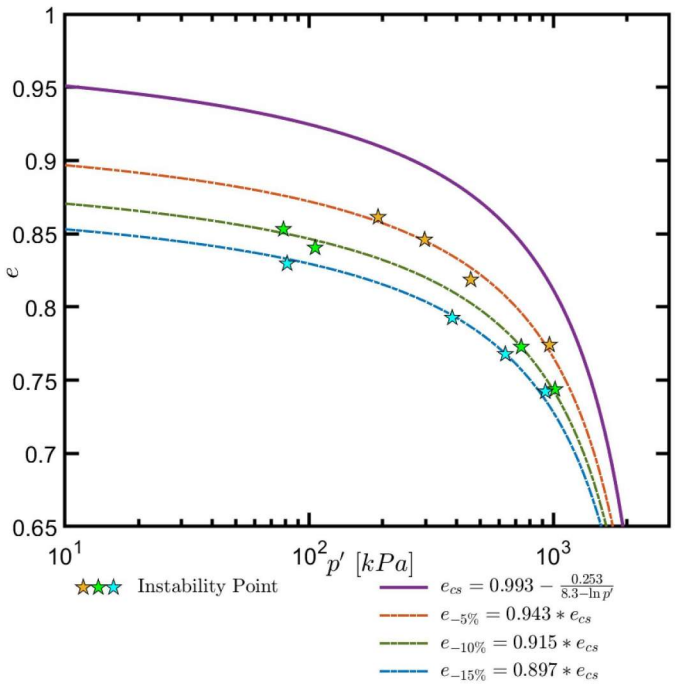

Figure 5.18: Experimental instability points from coupled strain monotonic triaxial tests under strain coupling ratio, $\zeta = -5\%$, -10% and -15% from table 4.4 and corresponding constant state parameter instability lines

range of ζ values for a single set of calibrated surface-evolution parameters. Thus, ψ_F describes the shape and directionality of the relative soil state, but does not necessarily provide the constitutive mapping required by the SANISAND surface-evolution laws. For example, figure 5.18 indicates that $\psi_F = \ln(e/e_{cs})$ adequately represents the shape of the LCSI curves, retains the correct directionality relative to the critical state line, and remains constant along the LCSI corresponding to each value of ζ.

2. The second part is referred to as the state parameter definition and is denoted by ψ_D, where $\psi_D = g(\psi_F)$. The function g maps the state parameter form into the state variable used by the bounding- and dilatancy-surface evolution laws. The state parameter definition is selected so that the second attribute is satisfied consistently: a single function ψ_D must satisfy equation 5.8 or 5.9 for all experimentally identified LCSI curves across the examined range of ζ. Like ψ_F, ψ_D remains constant along the LCSI corresponding to a given ζ. The transformation must also preserve the directionality of the relative state

represented by ψ_F. For example, under water-inflow conditions, $\zeta < 0$ and equations 5.8 or 5.9 require $\psi_D < 0$. The corresponding value of ψ_F must therefore also be negative, consistent with the LCSI curves lying below the CSL in $e - p'$ space.

Considering the state parameter form ψ_F before the full definition ψ_D, allows for a process in which the shape of the LCSI curves is considered first through ψ_F, before the calibration of sand-specific parameters contained in ψ_D to ensure that equation 5.8 or 5.9 is numerically satisfied for all experimental data. Therefore, ψ_F and ψ_D need not be the same. A general function for the state parameter definition ψ_D is proposed in equation 5.16, with x and w positive calibration parameters. Note that $\psi_D = \psi_F$ only when $x = 1$ and $w = 1$. In this study, for batch 2 of Hostun HN31 sand, it was concluded from figure 5.18 that the state parameter form $\psi_F = ln(e/e_{cs})$ in lieu of $\psi_F = e - e_{cs}$, is more appropriate.

$$\psi_D = x \cdot sign(\psi_F) |\psi_F|^w \tag{5.16}$$

The parameters x and w in equation 5.16 must be chosen so that equation 5.9 is satisfied at the LCSI points under each strain coupling ratio ζ. Also, with increasing rates of inflow or increasing magnitudes of ζ, ψ_D increases in magnitude monotonically. The experimental LCSI curves (figure 5.18) indicate that as ζ increases in magnitude, so do the selected forms ψ_F, indicating that a positive exponent w in equation 5.16 is needed to produce the required linear dependency of ψ_D on ζ (or Λ). The benefit of a linear bounding surface evolution over an exponential evolution definition (refer to the surface evolution laws in table 3.2) is that by using it, one can analytically solve equation 5.9 for ψ_D, given the ζ and the relevant model constants appearing in the equation. Parameter k^b of equation 5.9 is determined from equation 5.17, using the equation for the bounding surface at the peak stress-ratio state (PSRS) and parameter k^d is determined from equation 5.18, using the equation for the dilatancy surface at the phase transformation state (PTS). The denominators of equation 5.17 and 5.18 include the coefficient x of equation 5.16. In equation 5.9, $(k^b + k^d)$ is multiplied by the ψ_D value at the LCSI points, which also includes the coefficient x. Since parameter x appears in both the numerator and

denominator of equation 5.9, it suffices to take x as equal to 1, for the sake of simplicity.

$$k^b = \frac{\alpha^c - \alpha_{PSRS}}{\psi_{D,PSRS}} \tag{5.17}$$

$$k^d = \frac{\alpha_{PTS} - \alpha^c}{\psi_{D,PTS}} \tag{5.18}$$

It is shown from equations 5.17 and 5.18 that k^b and k^d are dependent on the state parameter definition, and thereby depend on the parameter w. The numerators of equations 5.17 and 5.18 remain constant. Parameter A_d was obtained from drained monotonic compression tests using the equation for dilatancy in table 3.2, which can be expanded using the definition of dilatancy D and equation 5.18 and expressed as equation 5.19. The left-hand side of equation 5.19 is derived from the experimental data and is independent of the state parameter definition chosen. The right-hand side is a function of the ratio $\psi_D/\psi_{D,PTS}$ and thus dependent on parameter w. The other parameters included in the right-hand side are derived directly from experimental data and remain unaffected by w.

$$\frac{\dot{\varepsilon_v}^p}{\dot{\varepsilon_q}^p} = A_d \left(\alpha^c + \left(\frac{\alpha_{PTS} - \alpha^c}{\psi_{D,PTS}} \right) \psi_D - \alpha \right) \tag{5.19}$$

As all parameters on the left-hand side of equation 5.9 are dependent on the state parameter definition ψ_D chosen, which in this case depends on parameter w, a range of values between 0.2 and 4 were examined to determine the exponent w. Parameters k^b, k^d and A_d corresponding to the new exponent were determined for each value of w through the calibration procedure discussed in section 5.4. These parameters along with the constant state parameter value ψ_D corresponding to the LCSI at each strain coupling ratio ζ were then used to calculate the left-hand side of equation 5.9. The result was compared to the right-hand side of equation 5.9 and the coefficient of determination (R^2) was computed, across all strain coupling ratios examined. The value of w corresponding to the maximum R^2 was taken as the overall best-fit value for the exponent. The outcome of this process is shown in figure 5.19. The calibrated values of k^b and

k^d with each variation of exponent w are shown in figure 5.20. The parameter A_d is shown in figure 5.21 at each value of exponent w. The variation in A_d with w is insignificant, and thus the initially obtained value was maintained across iterations.

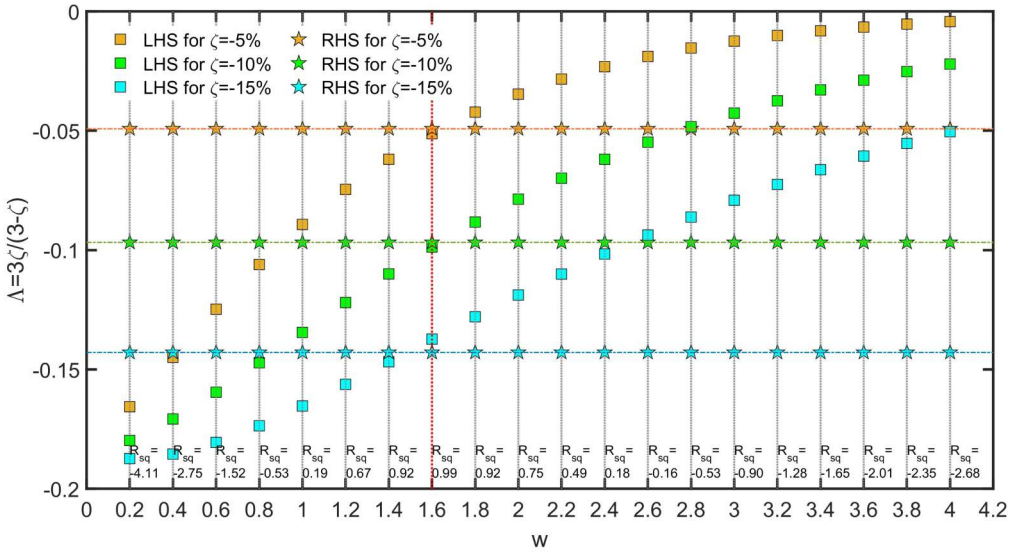

Figure 5.19: Variation of left-hand side (LHS) of equation 5.9 with exponent w using updated state parameter definition ψ_D (equation 5.16, where $\psi_F = ln(e/e_{cs})$ and $x = 1$) and comparison with right-hand side (RHS) for convergence

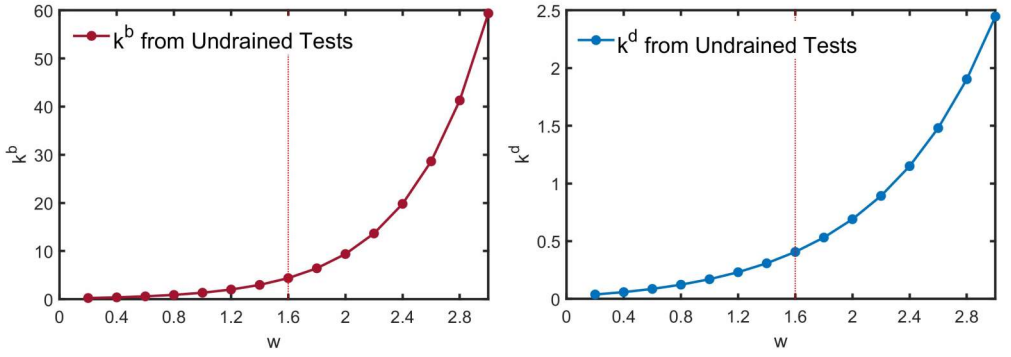

Figure 5.20: Calibration of constants k^b and k^d (refer surface evolution laws in table 5.4) for batch 2 of Hostun sand with updated state parameter definition ψ_D (equation 5.16, where $\psi_F = ln(e/e_{cs})$ and $x = 1$)

In figure 5.19, a maximum overall R^2 value is attained at $w = 1.6$. The updated SANISAND state parameter for batch 2 of Hostun HN31 sand can thus be fully defined by equation 5.20. This updated state parameter definition should be able to capture the locus of the experimentally

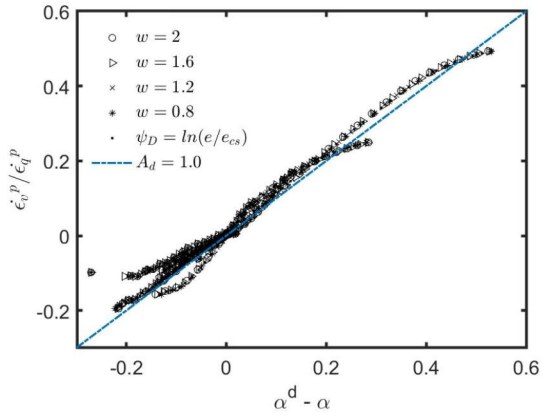

Figure 5.21: Calibration of constant A_d (refer dilatancy equation in table 3.2) for batch 2 of Hostun sand with updated state parameter definition ψ_D (equation 5.16, where $\psi_F = ln(e/e_{cs})$ and $x = 1$)

observed constant state instability points (LCSI) using the SANISAND 2008 model (Taiebat and Dafalias, 2008), as derived in equation 5.9.

$$\psi_D = sign\left[ln\left(\frac{e}{e_{cs}}\right)\right]\left|ln\left(\frac{e}{e_{cs}}\right)\right|^{1.6} \tag{5.20}$$

From the monotonically increasing values of k^b and k^d with w (figure 5.20), as well as from the results of figure 5.19, one can observe that an iterative procedure for the determination of w would converge. Figure 5.22 shows the results from an iterative procedure of determining the exponent w. For each iteration, k^b and k^d values were obtained from calibration using the state parameter definition of equation 5.16 with $\psi_F = ln(e/e_{cs})$ and $x = 1$, with a starting value of $w = 1$. These k^b and k^d values were incorporated in equation 5.9 and the equation was solved at each strain coupling ratio for a new best-fit value of the state parameter exponent w_i, to be used for the i-th iteration. This process was repeated until w, k^b and k^d converged. The values converged within 1% after 15 iterations. Thus, an iterative procedure, as illustrated in figure 5.23, is recommended to determine the exponent in a computationally efficient manner.

The approach outlined here produces a sand-specific relative state mapping rule, which might be viewed as a departure from traditional state parameter definitions. However, it is worth pointing out that calibration of sand-specific parameters is always required to map the state relative to

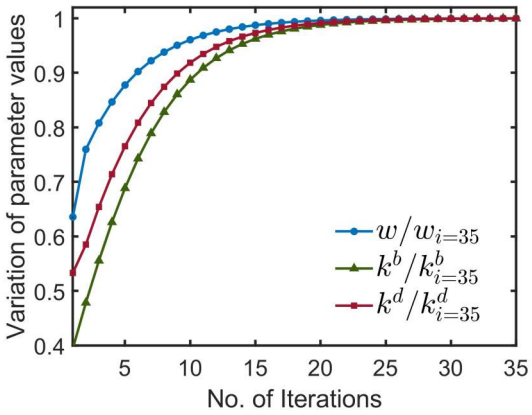

Figure 5.22: Variation of parameter values with each iteration using updated state parameter definition ψ_D (equation 5.16, where $\psi_F = ln(e/e_{cs})$ and $x = 1$)

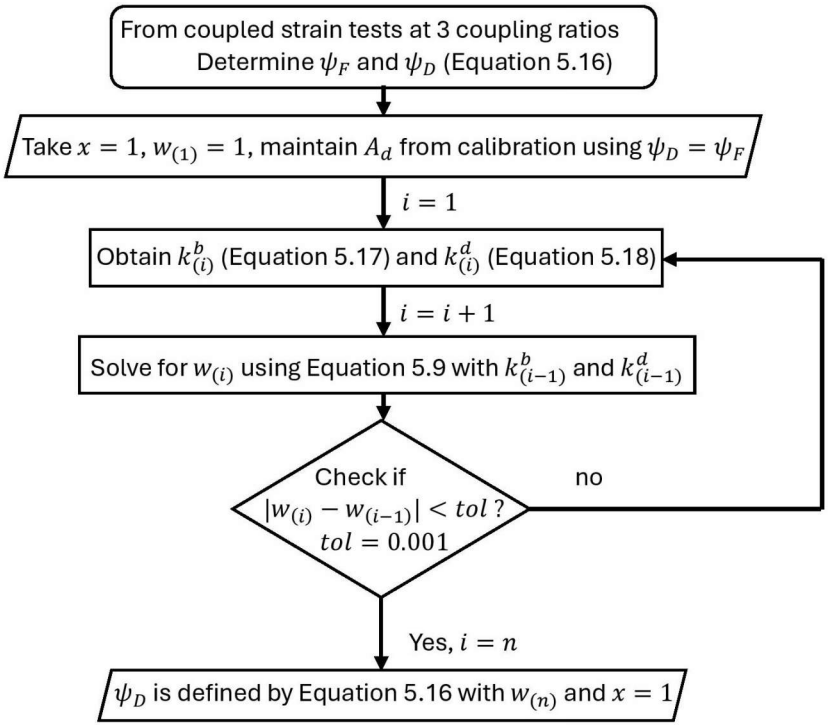

Figure 5.23: Flowchart showing steps to determine updated state parameter definition, ψ_D

critical. At a minimum, the sand-specific critical state line in $e - p'$ space must be defined (e.g. Been and Jefferies, 1985). Often, additional parameters such as e_{min} and e_{max} are incorporated in quantifying the 'distance' from critical state (e.g. Bolton, 1986). In the proposed approach, in addition to the sand-specific critical state line, the quantification of 'distance' captured by ψ_D becomes sand-specific and requires calibration of exponent w versus experimental LCSI curves.

In exchange for making the state parameter definition ψ_D sand-specific, the SANISAND evolution laws for the bounding and dilatancy surfaces are left unaltered and their calibration process is left untouched. By isolating updates to ψ_D, the rest of the SANISAND models can thus operate as usual.

An alternative approach would be to take the state parameter form ψ_F as the quantification of relative state mapping, and incorporate the proposed state parameter definition function $\psi_D = g(\psi_F)$ within the evolution laws for the bounding and dilatancy surfaces. The benefit is that no calibration is required for the state parameter, beyond the definition of a critical state line – though some level of comparison to experimental data would still be needed to decide which state parameter form ψ_F is appropriate. In reality, the complexity is transferred to the calibration of the parameters for the bounding and dilatancy surfaces, which would need to be calibrated versus an unknown function of the state parameter form $g(\psi_F)$. That unknown function would in essence be ψ_D. Direct calibration of all surface evolution parameters would require simultaneous calibration of existing SANISAND parameters for the bounding (n^b or k^b) and the dilatancy (n^d or k^d) surfaces, along with the new parameter w within ψ_D. That would require an optimisation process which could be similar to the one proposed here. Conceptually, it would be convenient to define ψ_D as a function of ψ_F, likely under a different name, and use it for the calibration of existing SANISAND bounding and dilatancy surface parameters (n^b and n^d or k^b and k^d) in the usual way, within the optimisation process. Overall, the equations and the calibration process produced by this approach would remain equivalent to the process proposed in this chapter, with the only potential difference in the naming of ψ_D and hence the perception of its function: either as quantification of relative state mapping or as a component of constitutive surface evolution.

5.6 Model performance with updated state parameter

The SANISAND 2008 model was re-calibrated using the updated state parameter definition and the experimental tests were numerically simulated. The updated calibration parameters and

simulation results of undrained, fully drained and coupled strain monotonic compression tests are presented in this section.

5.6.1 Model calibration with updated state parameter

In this section, the model parameters for the SANISAND 2008 model are presented, corresponding to the updated state parameter definition given in equation 5.20. Note that the elastic moduli and critical state parameters remain unchanged as they do not have a dependence on the state parameter and are directly obtained from experimental data. The calibration of bounding parameter k^b and dilatancy parameter k^d for $w = 1.6$ is determined in figure 5.20. Parameter A_d was shown to remain unchanged in figure 5.21. Finally, the bounding parameters h_0 and c_h were calibrated, as described in section 5.4.6, and were also found to closely match the values determined with the original definition of ψ ($= e - e_{cs}$). Table 5.5 summarises the model parameters corresponding to the updated state parameter ψ_D (equation 5.20) and table 5.6 shows the modified equations used from table 3.2.

Parameter		**Parameter**		**Parameter**		**Parameter**	
${G_0}^{(1)}$	176.67	${e_{max}}^{(3)}$	0.993	k^b	4.39	k^d	0.407
${K_0}^{(2)}$	225	${e_{min}}^{(3)}$	0.647	${h_0}^{(4)}$	3.55×10^4	A_d	1
α^c	1.201	$R^{(3)}$	0.73	${c_h}^{(4)}$	9.5	m	0.05
c	0.71	$Q^{(3)}$	8.3				

$^{(1)}$Implemented in equation 5.14; $^{(2)}$Implemented in equation 5.15; $^{(3)}$Implemented in CSL equation 4.1; $^{(4)}$Exponential function used, see section 5.4.6; refer table 5.6 for model equations.

Table 5.5: SANISAND model parameters for Hostun sand with updated state parameter definition ψ_D (equation 5.20)

5.6.2 Simulation of undrained and drained monotonic triaxial tests

Figure 5.24 shows a comparison of the numerical simulation results and experimental data of undrained tests on Hostun sand while figure 5.25 shows a comparison for fully drained tests. In both figures, the numerical simulations with the updated state parameter definition adequately capture the experimentally observed behaviour. Comparing the undrained test simulations with

Equations	Model Constants	Description
Critical State Line: $e_{cs} = e_{max} - \frac{(e_{max}-e_{min})R}{Q-ln(p')}$	e_{max} , e_{min} , Q , R	Equation 4.1
Elasticity: $G = G_0\ p_{at} e^{-1.8}(\frac{p'}{p_{at}})^{0.5}$ $K = K_0\ p_{at} e^{-2}(\frac{p'}{p_{at}})^{0.65}$	G_0 , K_0	p_{at} : 100 kPa Equation 5.14 Equation 5.15
Hardening Rule: $b_0 = G_0 h_0 exp(-c_h e)(p'/p_{at})^{-1/2}$	h_0 , c_h	Exponential evolution of b_0
Surface Evolution Laws: $\alpha^b_{c,e} = s(\alpha^c_{c,e} - k^b \psi_D)$ $\alpha^d_{c,e} = s(\alpha^c_{c,e} + k^d \psi_D)$	k^b , k^d	Linear Surface Evolution ψ_D: State Parameter $(= sign[ln(\frac{e}{e_{cs}})]\|ln(\frac{e}{e_{cs}})\|^{1.6})$

Table 5.6: Selected/modified equations for SANISAND 2008 model to be used in conjunction with model parameters of table 5.5, refer table 3.2 for remaining equations

those of figure 5.12, it is observed that the critical state is attained at larger strains with the updated state parameter definition. This is because the state parameter value now is smaller in magnitude than with the original definition (Been and Jefferies, 1985), which indicates an increased proximity of the initial state to the CSL. As these specimens are dense of critical, with negative state parameter values, the bounding surface in stress space is lower with the updated state parameter ψ_D, resulting in a reduction of the hardening modulus H (refer table 3.2) and a slower progression towards the critical state. The maximum deviatoric stresses attained under both undrained and drained condition are slightly lower than the values obtained with the original state parameter definition, which is also because of the reduction in the bounding surface stress ratio (α^b).

5.6.3 Simulation of coupled strain monotonic triaxial tests

The coupled strain triaxial tests of section 4.3.2 were numerically simulated in SANISAND 2008 using the updated state parameter definition ψ_D. Comparisons of the numerical and experimental data for each strain coupling ratio are shown in figures 5.26 - 5.28 at the initial states corresponding to highest and lowest densities obtained during testing. The LCSI points are shown in square markers for the simulation and star markers for the experimental data.

The comparison shows remarkable improvement in the performance of the model across

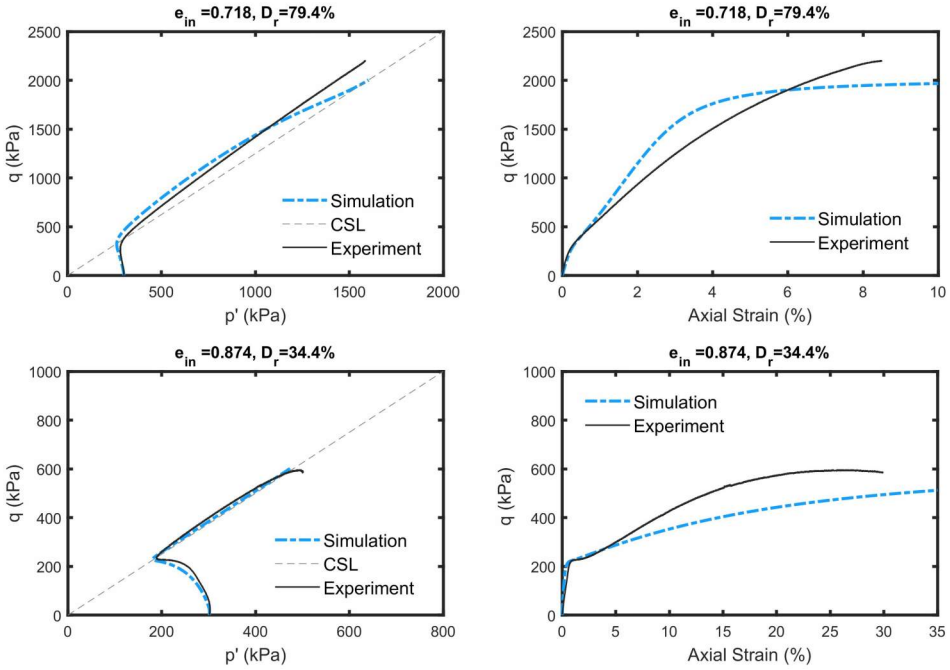

Figure 5.24: Simulations of undrained monotonic triaxial compression tests on isotropically consolidated samples of Hostun sand using updated ψ_D (equation 5.20) and comparison with experimental test data (top-bottom: Tests U5 and U3 from section 4.3.1)

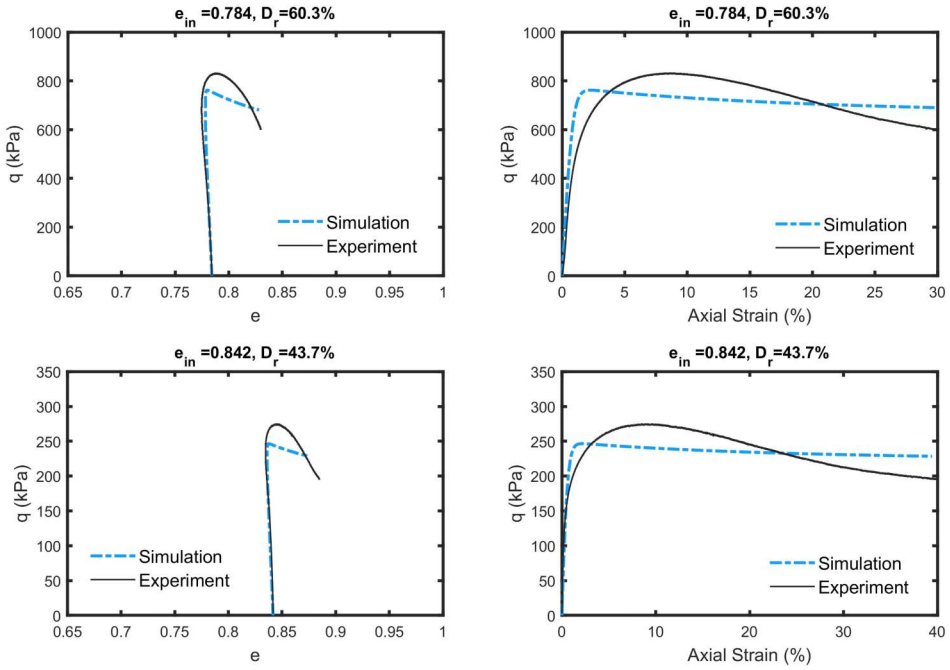

Figure 5.25: Simulations of fully drained monotonic triaxial compression tests on isotropically consolidated samples of Hostun sand using updated ψ_D (equation 5.20) and comparison with experimental test data (top-bottom: Tests D1 and D4 from section 4.3.1)

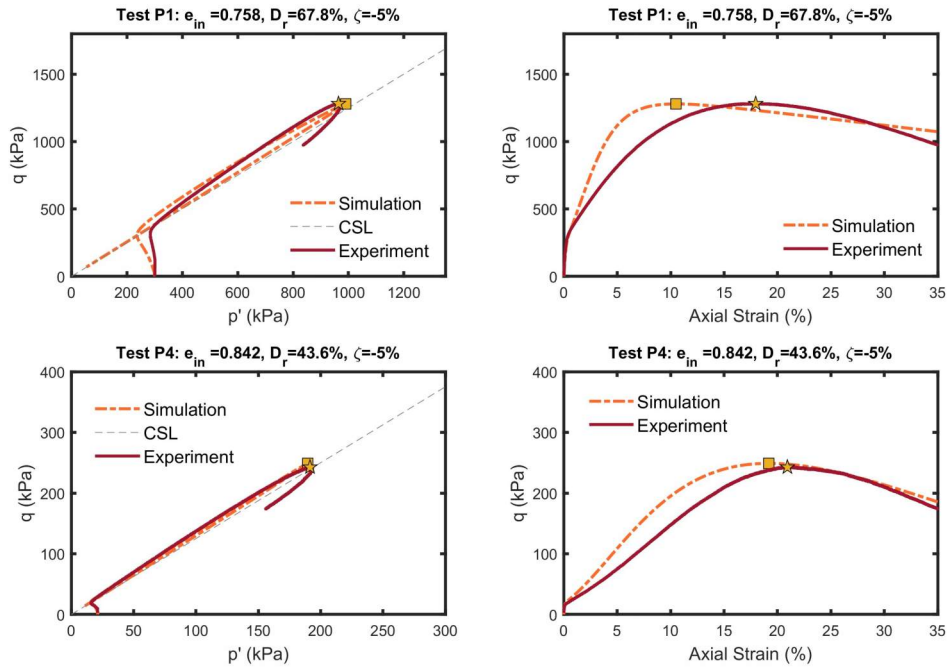

Figure 5.26: Simulations of coupled strain monotonic triaxial compression tests under $\zeta = -5\%$ on isotropically consolidated samples of Hostun sand using updated ψ_D (equation 5.20) and comparison with experimental test data from section 4.3.2

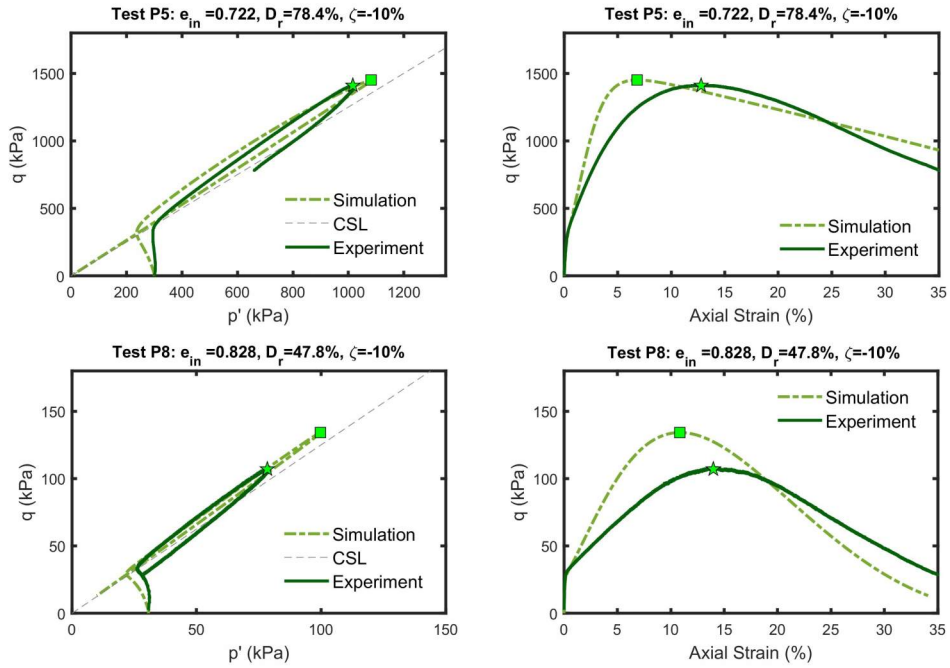

Figure 5.27: Simulations of coupled strain monotonic triaxial compression tests under $\zeta = -10\%$ on isotropically consolidated samples of Hostun sand using updated ψ_D (equation 5.20) and comparison with experimental test data from section 4.3.2

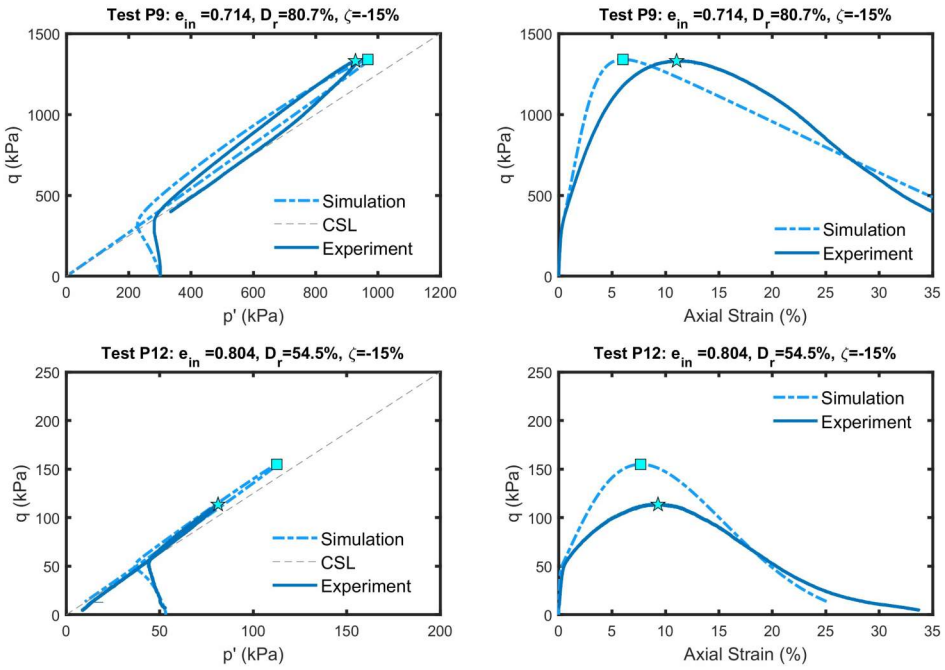

Figure 5.28: Simulations of coupled strain monotonic triaxial compression tests under $\zeta = -15\%$ on isotropically consolidated samples of Hostun sand using updated ψ_D (equation 5.20) and comparison with experimental test data from section 4.3.2

all densities and strain coupling ratios, ζ. The peak deviator stresses predicted for the looser specimens under strain coupling ratios, $\zeta = -10\%$ and $\zeta = -15\%$, are now much closer to the experimentally observed values, as compared to those obtained with the previous calibration using the original state parameter ψ definition ($= e - e_{cs}$). The instability points are detected at axial strains close to the observed values. Comparing the numerical simulation and experimental data in $e - p'$ space in figure 5.29, the experimental instability points forming the LCSI curve now fall on the numerically obtained LCSI, both at a constant updated state parameter ψ_D, as shown in dotted lines.

These results confirm that the proposed updated state parameter definition, ψ_D (equation 5.20) in SANISAND models, significantly improves the performance of the constitutive model for the coupled strain experiments examined in this investigation. The locus of constant state parameter instability points obtained using equation 5.9 accurately represents all experimentally observed instability points. In addition, this investigation shows that an updated state parameter definition allows the constitutive model to better capture soil response across a range of drainage

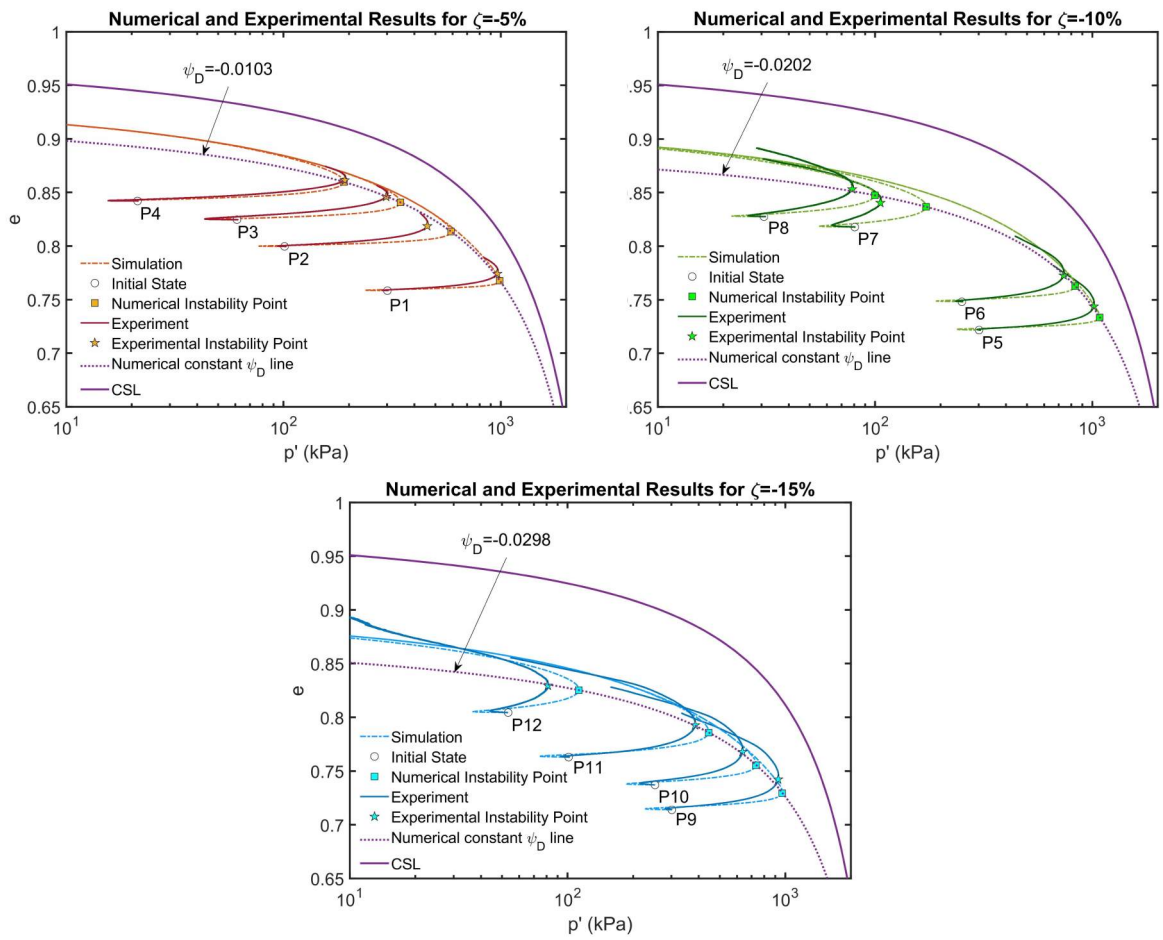

Figure 5.29: Simulations of coupled strain monotonic triaxial compression tests under $\zeta = -5\%$, -10% and -15% using updated ψ_D (equation 5.20) in $e - p'$ space and comparison with experimental test data from section 4.3.2

conditions.

5.7 Conclusions

In this chapter, the capability of SANISAND 2008 to replicate element-level behaviour under coupled strain triaxial monotonic loading was assessed. These models incorporate the state parameter in the expressions of the bounding and dilatancy surfaces, to make them critical-state compatible, where the state parameter controls the evolution of the surfaces. The state parameter (ψ) by Been and Jefferies, 1985, which is the vertical distance between the current soil state

and the critical state line (CSL) in $e - p'$ space, is the commonly embedded state parameter definition in SANISAND models, although other definitions have been used to capture evolution of surfaces.

SANISAND 2008 (Taiebat and Dafalias, 2008), which also uses the Been and Jefferies, 1985 state parameter ψ, was evaluated against strain-controlled, coupled-strain compression tests, where the ratio of volumetric strain rate to axial strain rate was kept constant. Such tests reproduce element-level strain paths that can develop during pore-fluid redistribution in sloping layered deposits. Here, they were used as a way to isolate the state parameter and assess its importance in modelling non-standard drainage conditions. It was analytically demonstrated that for the used constitutive model and a given strain coupling ratio, instability triggering points that violate Hill's stability criterion post-phase transformation and post-peak stress ratio share the same state parameter value ψ. Consequently, the locus of such instability points (LCSI) represents a curve of constant ψ, whose value depends on the strain coupling ratio.

Based on this framework, three LCSI curves were experimentally obtained by identifying the post-phase transformation and post-peak stress-ratio instability points of the coupled strain monotonic compression tests described in chapter 4, with each LCSI curve corresponding to a different strain coupling ratio. Following a typical calibration using undrained and fully drained element tests, SANISAND 2008 was used to numerically simulate the coupled strain triaxial experiments. It was shown that the locus of numerical post-phase transformation and post-peak stress-ratio instability points in $e - p'$ space, which lies at a constant value of the state parameter ψ, does not coincide with the locus of experimentally observed instability points.

To improve the performance of SANISAND 2008 in replicating coupled strain paths, an updated state parameter definition (ψ_D) was proposed, which can consistently capture all three experimentally observed LCSI curves, while maintaining its functionality within the SANISAND framework. After a re-calibration of the SANISAND 2008 model using ψ_D, a substantial improvement was achieved when modelling the coupled strain experiments, without compromising performance for the fully drained and undrained experiments.

As the experimental coupled-strain data were used to calibrate the revised relative state mapping, the results of the updated state parameter definition demonstrate improved calibration performance rather than independent validation. The calibrated mapping is specific to the Hostun batch examined, and is not expected to apply for other sands. Indeed, this work shows that ψ_D requires sand-specific calibration.

The methodology presented here demonstrates how the state parameter definition used within SANISAND 2008 can be isolated and directly assessed versus experimental data, by using coupled strain monotonic tests. Additionally, this chapter shows that an appropriately updated state parameter definition can significantly improve the capability to model monotonic coupled strain behaviour across a range of initial states. While SANISAND 2008 was used throughout this chapter, the framework developed is transferable to other SANISAND-family models, which typically follow the same state-dependent bounding- and dilatancy-surface evolution laws for monotonic paths.

Chapter 6

Identification of the critical state line of sands using coupled shear-volumetric strain paths

6.1 Introduction

This chapter presents an application of the Locus of Constant State parameter Instability (LCSI) framework developed in chapter 5. The LCSI framework is employed to determine the critical state line (CSL) of Congleton sand for which the critical state could not be reached using traditional undrained/ fully drained monotonic triaxial tests.

The CSL of a sand can be experimentally determined as a locus of points in $e - p'$ space, obtained by shearing specimens to large strains, until the critical state is reached. The critical state concept and the CSL are described in detail in section 2.5. These critical state points can be very challenging to obtain for many sands. Triaxial compression to critical state often requires large axial strains ($> 20\%$) that can result in excessive deformations or localised disturbances. Such strains are beyond what most standards allow (e.g., ASTM D7181-20, ASTM D4767-11R20 and ASTM 2850-24) and can render the interpretation of 'element' behaviour challenging, not

least because of area correction requirements. In addition, for critical state points at high mean effective stresses, the load limits of available testing equipment or instrumentation might be triggered prior to the attainment of the critical state. Finally, very dilative sands can lead to negative pore water pressures during undrained compression and potential cavitation, which also prevents a specimen from reaching the critical state, unless a high back pressure can be applied. For instance, Verdugo and Ishihara (1996) designed a high pressure triaxial cell with maximum pressure of 5 MPa to avoid cavitation in highly dilative soil specimens of Toyoura sand. Due to these impediments, researchers often have to rely on a fraction of conducted tests to define the CSL. Azeiteiro et al. (2017) report 4 triaxial compression tests out of 14 as having reached the critical state for Hostun sand, while in chapter 4 for the same sand 4 out of 15 triaxial compression tests reached the critical state. To overcome these physical limitations, in this chapter an alternative method of determining the CSL is proposed, through the novel, analytically based experimental approach using coupled shear-volumetric strain paths developed in chapter 5. Note that within the context of this investigation, a unique CSL assumption is made, which is expected to be valid for the levels of stress used in most geotechnical engineering applications, where the effects of particle breakage are negligible and particle rearrangement remains the predominant mechanism for shear deformation (Bandini and Coop, 2011).

In chapter 5, it was demonstrated using experiments and the SANISAND 2008 constitutive model (Taiebat and Dafalias, 2008) that the locus of post-phase transformation and post-peak stress-ratio instability points obtained from coupled shear-volumetric strain triaxial compression tests represents a constant state parameter curve in $e - p'$ space, with the value of the state parameter definition linked to the strain coupling ratio. The Locus of Constant State parameter Instability (LCSI) curves were found to be optimally represented for Hostun sand using an updated state parameter definition ψ_D, which was incorporated in the selected SANISAND model and was shown to significantly improve simulations of coupled strain triaxial compression tests.

In this study, the LCSI framework is used to indirectly evaluate the CSL in $e - p'$ space for Congleton sand, a sand for which CSL points could not be directly obtained through undrained

triaxial compression tests due to the physical limitations discussed before. First, LCSI curves are experimentally obtained in $e - p'$ space from triaxial compression tests conducted under three strain coupling ratios, ζ ($= \dot{\varepsilon}_v/\dot{\varepsilon}_1$), with specimens sheared to no more than 15% axial strain. These experiments on Congleton sand were conducted by Yide Wang at the University of Oxford. The data were post-processed by the author and are reproduced in this thesis with permission. The LCSI curves obtained experimentally for each strain coupling ratio are then used to back-calculate the CSL and the ψ_D function. This methodology is validated by comparing the predicted CSL of Hostun sand with the known (experimentally determined) CSL of Hostun sand from chapter 4. Further use of the coupled strain experiments to calibrate the SANISAND 2008 model (Taiebat and Dafalias, 2008), described in section 3.3, is also explored. It is found that coupled strain compression tests under three coupling ratios can be used to obtain not only the CSL in $e - p'$ space and the ψ_D, but also the critical and the bounding surface stress ratios. The calibrated constitutive model is subsequently shown to adequately capture both undrained and coupled strain experiments.

Thus, the contribution of this chapter is threefold: first, it proposes an alternative analytical based experimental approach using coupled strain triaxial compression tests to estimate the CSL for sands where directly obtaining it is not possible; second, it demonstrates the extent to which the coupled strain triaxial compression tests required to derive the CSL can be further used to calibrate SANISAND models; and third, it provides calibration parameters for Congleton sand within the SANISAND framework.

6.2 Determination of the critical state line

In this section, the series of coupled shear-volumetric strain triaxial compression experiments conducted on Congleton sand by Yide Wang (YW) at University of Oxford are post-processed and presented with permission, where instability points triggered post-phase transformation and post-peak stress ratio are highlighted. Based on the concept of LCSI explained in chapter 5, each

coupling ratio ζ corresponds to a different LCSI curve (figure 5.5). Further, each LCSI curve is related to the CSL through a constant state parameter value, following equation 5.9. The reader is directed to section 3.3 for a full list of the constitutive equations of the SANISAND 2008 model (Taiebat and Dafalias, 2008) and section 5.3 for equations that are pertinent to this study. The experimental methods used to perform coupled shear-volumetric strain triaxial compression tests on Congleton sand were similar to the ones performed on Hostun sand as detailed in chapter 4 and documented in Dilip et al. (2026).

In order to determine the CSL using the experimentally obtained LCSI curves, a method consisting of the following steps is proposed:

1. An appropriate state parameter form ψ_F must be identified, which preserves the direction of state relative to the CSL and remains constant along each experimentally identified LCSI curve.
2. The available LCSI curves must be described as a function of the chosen state parameter form and an anticipated expression for the CSL (e.g., following Bolton (1986)).
3. The CSL can finally be determined by setting the state parameter form equal to zero within the produced LCSI function.

This process is described in detail below, using as an example the experimental results for Congleton sand presented in the following sections. The process of locating the CSL is also validated using Hostun sand by comparing the predicted CSL with the known CSL from chapter 4.

6.2.1 Experimental results

Table 6.1 lists the triaxial compression tests performed under coupled volumetric and shear strains on Congleton sand by YW (presented with permission). Constant ratios of expansive volumetric strain rate to axial strain rate, $\zeta = \dot{\varepsilon}_v/\dot{\varepsilon}_1$ were imposed and the LCSI points were determined using equation 5.2 and selecting points post-phase transformation and post-peak

Test ID[a]	$e_{in}{}^{b}$	$p'_{in}{}^{b}$	$e_{INST}{}^{c}$	$p'_{INST}{}^{c}$	$\eta_{PSRS}{}^{d}$	$\phi_{PSRS}{}^{d}$	$\eta_{end}{}^{e}$	$\phi_{end}{}^{e}$
ICPDMC/0.655/150/-10 (P1)	0.655	150	–	–	1.35	33.3°	1.32	32.7°
ICPDMC/0.633/150/-10 (P2)	0.633	150	–	–	1.36	33.8°	1.34	33.2°
ICPDMC/0.641/150/-20 (P3)	0.641	150	0.677	616.4	1.38	34.1°	1.19	29.9°
ICPDMC/0.587/150/-20 (P4)	0.587	150	–	–	1.45	35.8°	1.39	34.4°
ICPDMC/0.701/100/-20 (P5)	0.701	100	–	–	1.28	31.7°	0.79	20.5°
ICPDMC/0.615/300/-20 (P6)	0.615	300	–	–	1.40	34.7°	1.32	32.7°
ICPDMC/0.640/150/-30 (P7)	0.640	150	0.669	74.8	1.41	34.8°	1.13	28.4°
ICPDMC/0.657/100/-20 (P8)	0.657	100	0.688	127.4	1.36	33.7°	0.69	18.0°
ICPDMC/0.626/300/-30 (P9)	0.626	300	0.655	142.9	1.41	34.9°	1.14	28.7°
ICPDMC/0.662/30/-20 (P11)	0.662	30	0.698	154.5	1.39	34.3°	1.25	31.1°
ICPDMC/0.670/20/-20 (P12)	0.670	20	0.696	55.7	1.38	34.1°	0.88	22.6°
ICPDMC/0.595/500/-30 (P13)	0.595	500	0.635	1319.1	1.45	35.7°	0.67	17.6°
ICPDMC/0.590/300/-30 (P14)	0.590	300	0.633	1197.3	1.48	36.4°	1.12	28.2°
ICPDMC/0.680/10/-20 (P15)	0.680	10	0.705	35.7	1.54	37.7°	0.46	12.4°
ICPDMC/0.602/100/-40 (P16)	0.602	100	0.635	79.3	1.50	36.9°	1.35	33.3°
ICPDMC/0.582/300/-40 (P17)	0.582	300	0.624	702.1	1.50	36.9°	0.21	5.9°
ICPDMC/0.622/500/-30 (P19)	0.622	500	0.655	367.8	1.43	35.2°	0.78	20.3°
ICPDMC/0.581/200/-40 (P20)	0.581	200	0.621	490.5	1.52	37.4°	1.22	30.4°
ICPDMC/0.632/300/-20 (P21)	0.632	300	0.668	713.8	1.39	34.3°	1.19	29.7°
ICPDMC/0.610/30/-40 (P22)	0.610	30	0.639	34.2	1.60	39.2°	1.50	36.9°
ICPDMC/0.598/150/-40 (P24)	0.598	150	0.631	299.0	1.51	37.1°	1.31	32.4°
ICPDMC/0.636/100/-30 (P26)	0.636	100	0.663	55.7	1.44	35.6°	1.28	31.8°
ICPDMC/0.637/300/-30 (P27)	0.637	300	0.659	230.2	1.40	34.6°	0.76	19.6°
ICPDMC/0.611/200/-40 (P28)	0.611	200	0.643	168.7	1.48	36.4°	0.86	22.0°

[a](1) type of consolidation: IC for isotropic consolidation; (2) type of drainage: PD for coupled strain conditions; (3)type of loading: MC for monotonic compression; (4) void ratio after consolidation; (5) mean effective stress after consolidation; and (6) coupled strain ratio during the shearing stage, $\zeta = \dot{\varepsilon}_v/\dot{\varepsilon}_1$, in percentage. [b]Post consolidation values; [c]INST: Instability Point; [d]PSRS: Peak Stress-Ratio State; [e]End of test.

Table 6.1: Results of coupled strain monotonic triaxial tests performed under different values of $\zeta(=\dot{\varepsilon}_v/\dot{\varepsilon}_1)$ on Congleton sand by YW at University of Oxford (reproduced with permission)

stress ratio. Peak stress ratios are also listed in table 6.1. All coupled strain experimental results are shown in $e-p'$ space in figure 6.1. Note that the pore pressures approached cavitation prior to triggering of instability for tests $P1$ and $P2$ under $\zeta=-10\%$, and the testing equipment reached its load limit prior to instability triggering for tests $P4$ and $P6$ under $\zeta=-20\%$. For test $P5$, the instability point obtained using Hill's criterion did not satisfy the LCSI curve conditions of being post-phase transformation and post-peak stress ratio (equations 5.10-5.11) and was therefore discarded.

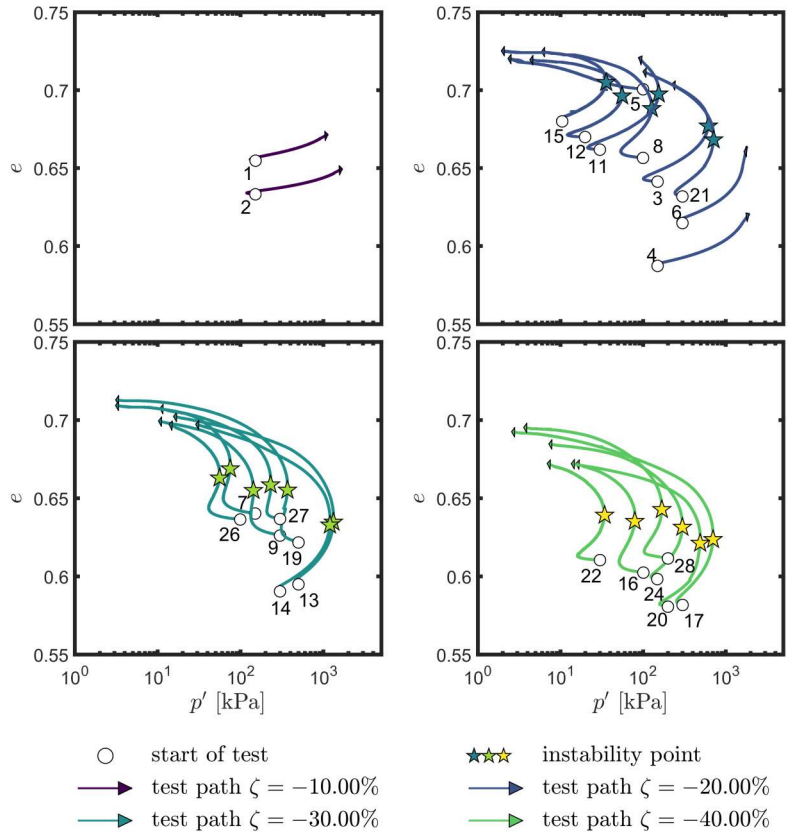

Figure 6.1: Coupled strain tests on Congleton sand from table 6.1 with LCSI points under strain coupling ratio $\zeta(=\dot{\varepsilon}_v/\dot{\varepsilon}_1)$

6.2.2 State parameter form

The state parameter form $\psi_F = f(p',e)$, as introduced in chapter 5, must be contained within the state parameter definition $\psi_D = g(f(p',e))$, where ψ_F and ψ_D need not be the same. For instance, equation 6.1 presents the state parameter definition ψ_D, that was shown to be necessary to ensure compliance with equation 5.9 for Hostun sand in chapter 5, presented as a function of a state parameter form $\psi_F = ln(e/e_{cs})$ and $w = 1.6$. It is possible to determine the CSL through an appropriately selected ψ_F, without fully defining ψ_D, i.e. without knowing parameter w in equation 6.1. This is because at the CSL, $\psi_D = 0$ and $\zeta = 0$ (equation 5.9) or $\Lambda = 0$ (equation 5.4). Nevertheless, ψ_D needs to be defined in a way that satisfies equation 5.9 for $\zeta \neq 0$, if the

constitutive model is to be used.

$$\psi_D = sign(\psi_F)\,|\psi_F|^w \implies \psi_F = sign(\psi_D)\,|\psi_D|^{1/w} \tag{6.1}$$

Important conclusions regarding the nature of ψ_D and ψ_F determined in chapter 5 from equation 5.9 are re-iterated below:

1. At each LCSI curve, ψ_D must hold a constant value, which implies that ψ_F must hold a constant value (e.g., equation 6.1). An appropriate ψ_F is chosen such that the contour of all experimentally captured LCSI curves are optimally captured. For instance, if each LCSI curve is a vertical translation of another in $e-p'$ space, then the $\psi_F = e - e_{cs}$ of Been and Jefferies (1985) can be deemed appropriate.
2. The state parameter definition ψ_D must be linearly related to ζ or Λ for the linear surface evolution laws employed here and thus take a zero value for points on the CSL, which in $e-p'$ space coincides with the LCSI under undrained conditions ($\zeta = 0 \iff \Lambda = 0$). Note that as long as this criterion is satisfied, the CSL can be determined based on ψ_F, without fully defining ψ_D.

Considering the above conditions, an investigation on a state parameter form ψ_F for the Congleton sand results of figure 6.1 was undertaken. First, possible state parameter forms were assessed for their ability to consistently describe the shape of the LCSI curves. Different state parameter forms could be appropriate (e.g., Been and Jefferies, 1985; Bolton, 1986; Dafalias and Manzari, 2004; Lashkari, 2009; Wan and Guo, 1998; Z. L. Wang et al., 2002). Here, the vertical distance in $e-p'$ space, $\psi_{F1} = e - e_{cs}$ (Been and Jefferies, 1985) and the ratio of current void ratio to critical state void ratio $\psi_{F2} = e/e_{cs}$ (Wan and Guo, 1998) were examined.

Taking any two LCSI curves under strain coupling ratios ζ_i and ζ_j respectively, for each of the two ψ_F considered (ψ_{F1} and ψ_{F2}), a constant (Ω) can be derived that links the two LCSI curves. These constants are given in equations 6.2 and 6.3, where void ratios e_ζ and e_{cs} correspond to the same (random) value of mean effective stress p'. Form 1 implies a constant

vertical distance between the two LCSI curves in $e - p'$ space, while form 2 implies a constant ratio between the two LCSI curves.

$$\begin{aligned} &Form\ 1 : \psi_{F1,\zeta} = e_\zeta - e_{cs} \\ &\implies e_{\zeta_i} - e_{\zeta_j} = \psi_{F1,\zeta_i} - \psi_{F1,\zeta_j} = \Omega_1 \end{aligned} \tag{6.2}$$

$$\begin{aligned} &Form\ 2 : \psi_{F2,\zeta} = \frac{e_\zeta}{e_{cs}} \\ &\implies \frac{e_{\zeta_i}}{e_{\zeta_j}} = \frac{\psi_{F2,\zeta_i}}{\psi_{F2,\zeta_j}} = \Omega_2 \end{aligned} \tag{6.3}$$

To avoid the assumption of analytical expressions for the experimental LCSI curves, the assessment for the Ω constants discussed above was based directly on the available data points. This was achieved by selecting one of the LCSI sets of points as a reference and translating the other two LCSI sets of points to the reference through an appropriate Ω constant. As shown in figure 6.2, the LCSI point set corresponding to $\zeta = -20\%$ was selected as reference. For form 1 (equation 6.2 and figure 6.2(a)), an $\Omega_{1,i|j}$ was used to vertically translate each LCSI set corresponding to coupling ratio $'j'$ ($\zeta = -30\%$ and -40%) in $e - p'$ space to the reference set $'i'$ ($\zeta = -20\%$). For form 2 (equation 6.3 and figure 6.2(b)) an $\Omega_{2,i|j}$ was used as a void ratio multiplication constant to move each $'j'$ ($\zeta = -30\%$ and -40%) LCSI set to the reference $'i'$ ($\zeta = -20\%$) in $e - p'$ space. The numerical values of the chosen Ω constants were selected to minimise the overall scatter of all data in $e - p'$ space, including the reference LCSI set ($\zeta = -20\%$) and the two translated sets ($\zeta = -30\%$ and $\zeta = -40\%$). The overall scatter was quantified by the mean of the moving standard deviation of e across the examined range of p'.

Figure 6.3 illustrates the selection process of Ω constants for both ψ_F considered (equations 6.2 and 6.3). A range of values was scanned for each Ω constant. The moving standard deviation in void ratio was calculated as the standard deviation about the moving average across five adjacent points. The mean of the moving standard deviation is the value plotted on the vertical axis of figure 6.3, with its minimum value corresponding to the selected Ω constants as given in table 6.2. Figure 6.2 shows all the obtained LCSI data points translated to the reference

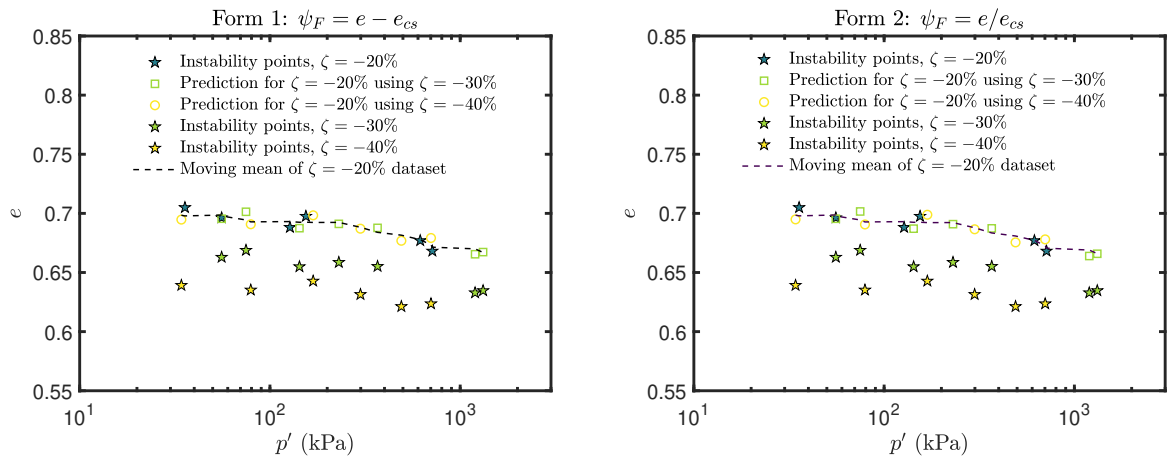

Figure 6.2: Assessment of state parameter forms, (a) Form 1: $\psi_{F1,\zeta} = e_\zeta - e_{cs}$ and (b) Form 2: $\psi_{F2,\zeta} = \frac{e_\zeta}{e_{cs}}$, through transferring LCSI points for $\zeta = -30\%$ and -40% to the $\zeta = -20\%$ LCSI curve

$\zeta = -20\%$ set using the constants of table 6.2. Both state parameter forms explored (equation 6.2 and 6.3) could be considered appropriate for the examined data, as both resulted in a mean of the moving standard deviation of e (~ 0.006), which was similar to the inherent scatter in the dataset of just the reference $\zeta = -20\%$ set.

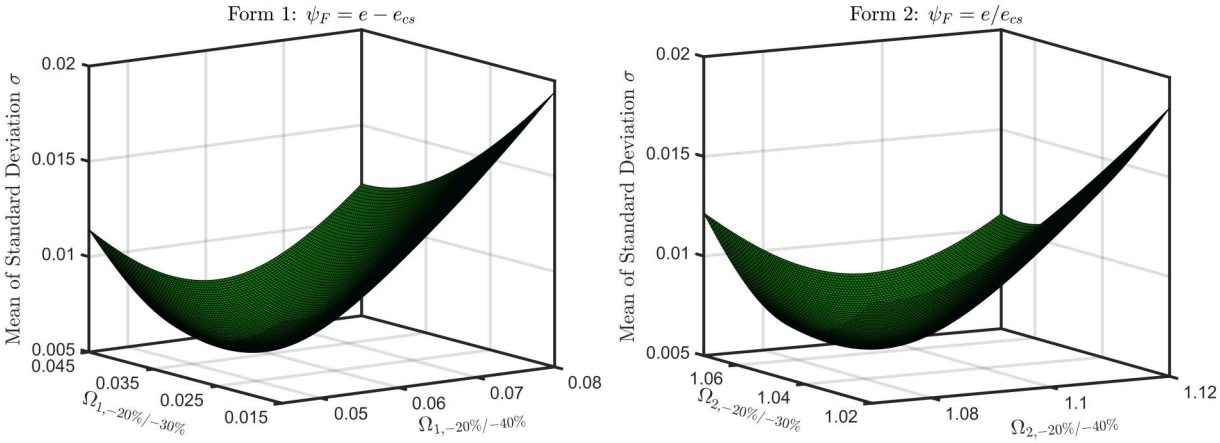

Figure 6.3: Mean of moving (5 point) standard deviation of all experimentally obtained points translated to the reference $\zeta = -20\%$ LCSI curve based on state parameter forms (a) Form 1: $\psi_{F1,\zeta} = e_\zeta - e_{cs}$ and (b) Form 2: $\psi_{F2,\zeta} = \frac{e_\zeta}{e_{cs}}$

A difference between the two definitions could become more prominent at higher mean ef-

Reference set	Constant	Definition	Value
$\zeta = -20\%$	$\Omega_{1,-20\%\|-30\%}$	$e_{-20\%} - e_{-30\%}$	0.0326
$\zeta = -20\%$	$\Omega_{1,-20\%\|-40\%}$	$e_{-20\%} - e_{-40\%}$	0.0556
		Mean of moving σ	0.0058
$\zeta = -20\%$	$\Omega_{2,-20\%\|-30\%}$	$e_{-20\%}/e_{-30\%}$	1.0493
$\zeta = -20\%$	$\Omega_{2,-20\%\|-40\%}$	$e_{-20\%}/e_{-40\%}$	1.0877
		Mean of moving σ	0.0060

Table 6.2: Values for Constants Ω_1 (based on state parameter form of equation 6.2) and Ω_2 (based on state parameter form of equation 6.3) resulting in the minimum mean of moving standard deviation

fective stresses, when the slope of the CSL in $e - p'$ space becomes steeper, producing LCSI curves of different shape depending on the state parameter form assumed. Such a distinction could be made for the Hostun sand results of chapter 5, where ψ_{F2} was deemed more appropriate. However, the steeper part of the CSL for Congleton sand is not expected to fall within the range of mean effective stresses examined here (up to 1 MPa). As a result, both $\psi_{F1} = e - e_{cs}$ and $\psi_{F2} = e/e_{cs}$ can be considered as having adequately satisfied the criterion of describing the shape of the obtained LCSI experimental data.

The next step is to ensure that a state parameter definition ψ_D based on a selected form ψ_F can be found, that becomes zero for points on the CSL. If equation 6.1 applies, only the first form considered ($\psi_{F1} = e - e_{cs}$) produces a ψ_D that satisfies this criterion. The second form ($\psi_{F2} = e/e_{cs}$) produces a ψ_D that becomes unity at critical state. However, it is possible to recast it in a way that preserves the observation of the above investigation, that a constant ratio between LCSI curves can adequately maintain their shape. The form ψ_{F3} used in chapter 5 and shown in equation 6.4 produces a definition ψ_D based on equation 6.1 that satisfies the criterion of being zero at critical state, while it is positive for $e > e_{cs}$ and negative for $e < e_{cs}$.

$$\psi_{F3} = ln\left(\frac{e}{e_{cs}}\right) \tag{6.4}$$

Additionally, it maintains a constant ratio between two LCSI curves, at ζ_i and ζ_j, as demonstrated in equation 6.5 ($\Omega_3 = \Omega_2$) and is thus satisfactory in terms of describing the shape of the

captured LCSI data points based on the previous investigation.

$$\begin{aligned} &Form\ \ 3 : \psi_{F3,\zeta} = ln\left(\frac{e_\zeta}{e_{cs}}\right) \\ &\implies \frac{e_{\zeta_i}}{e_{\zeta_j}} = exp\left(\psi_{F3,\zeta_i} - \psi_{F3,\zeta_j}\right) = \Omega_3 = \Omega_2 \end{aligned} \tag{6.5}$$

Alternatively, the state parameter form $\psi_{F2} = e/e_{cs}$ could have been kept if a different definition ψ_{D2} was used, which results in $\psi_{D2} = 0$ at the critical state as shown in equation 6.6. Equation 6.6 is obviously equivalent to Equation 6.1 with state parameter form $\psi_{F3} = ln(e/e_{cs})$ and as such only the form ψ_{F3} is taken forward in the following sections.

$$\psi_{D2} = sign\left(\ln(\psi_{F2})\right)\left|\ln(\psi_{F2})\right|^w \tag{6.6}$$

6.2.3 LCSI and CSL functions

This section outlines how the functions that describe the available LCSI curves and the CSL were produced. Each LCSI curve was linked to the CSL through a plausible state parameter form, $\psi_{F1} = e - e_{cs}$ or $\psi_{F3} = ln\left(\frac{e}{e_{cs}}\right)$. The function proposed by Bolton (1986) and given in equation 6.7 was chosen to describe the CSL in $e - p'$ space, with $e_{max} = 0.782$ and $e_{min} = 0.538$ for the Congleton sand used (Dilip et al., 2026) and parameters Q and R left to be defined. Using equation 6.7 ensured that the proposed CSL would remain below e_{max}. Each LCSI curve was then expressed using the CSL function and the selected state parameter form (equation 6.8 or 6.9). Note that the experimental data give known pairs of (p', e_ζ).

$$e_{cs} = e_{max} - \frac{(e_{max} - e_{min})R}{Q - ln(p')} \tag{6.7}$$

$$\begin{aligned} &Form\ \ 1 : \\ &e_\zeta = \psi_{F1,\zeta} + \left[e_{max} - \frac{(e_{max} - e_{min})R}{Q - ln(p')}\right] \\ &= sign\left(\psi_{D1,\zeta}\right)\left|\psi_{D1,\zeta}\right|^{1/w} + e_{cs} \end{aligned} \tag{6.8}$$

$$
\begin{aligned}
&Form\ 3: \\
&e_\zeta = exp(\psi_{F3,\zeta}) \cdot \left[e_{max} - \frac{(e_{max} - e_{min})R}{Q - ln(p')} \right] \\
&= exp(sign\left(\psi_{D3,\zeta}\right) \left|\psi_{D3,\zeta}\right|^{1/w}) \cdot e_{cs}
\end{aligned}
\tag{6.9}
$$

Taking the (p', e_ζ) points of the reference $\zeta = -20\%$ set and the $\zeta = -30\%$ and $\zeta = -40\%$ sets translated to the reference through the Ω constants of table 6.2, a curve fitting exercise for equation 6.8 ($\psi_{F1} = e - e_{cs}$) gave the values of $Q = 9.885$, $R = 0.685$ and $\psi_{F1,-20\%} = -0.0577$. Equivalently, using equation 6.9 ($\psi_{F3} = ln\left(\frac{e}{e_{cs}}\right)$) gave $Q = 9.727$, $R = 0.707$ and $\psi_{F3,-20\%} = -0.0744$. A high value of parameter Q (~ 10) is indicative of the sand's mineralogy and according to Bolton (1986) suggests a high silica content, as is indeed the case for Congleton sand. The value of R is typically around 1 for clean sands, with $R < 1$ reported before for silica sands, e.g. Kamai and Boulanger (2012) and Kassas et al. (2021).

Thus expressions were produced to describe the CSL and the LCSI for $\zeta = -20\%$. The remaining LCSI curves were obtained using the constant Ω values of table 6.2. The curves and their corresponding expressions are given in figure 6.4(a) for $\psi_{F1} = e - e_{cs}$ and figure 6.4(b) for $\psi_{F3} = ln\left(\frac{e}{e_{cs}}\right)$. The values of $\psi_{F,\zeta}$ for each state parameter form are shown in table 6.3.

Inflow Rate	Form 1	$\psi_{F1,\zeta}$ Value	Form 3	$\psi_{F3,\zeta}$ Value
$\zeta = -20\%$	$\psi_{F1,-20\%} = e_{-20\%} - e_{cs}$	-0.0577	$\psi_{F3,-20\%} = ln(e_{-20\%}/e_{cs})$	-0.0744
$\zeta = -30\%$	$\psi_{F1,-30\%} = e_{-30\%} - e_{cs}$	-0.0903	$\psi_{F3,-30\%} = ln(e_{-30\%}/e_{cs})$	-0.1225
$\zeta = -40\%$	$\psi_{F1,-40\%} = e_{-40\%} - e_{cs}$	-0.1133	$\psi_{F3,-40\%} = ln(e_{-40\%}/e_{cs})$	-0.1584

Table 6.3: Values for state parameter forms $\psi_{F,\zeta}$ for equation 6.2 and equation 6.5, corresponding to each inflow rate ζ

The two produced expressions for CSL are very similar until about $p' = 3000$ kPa, after which the curve corresponding to $\psi_{F3} = ln\left(\frac{e}{e_{cs}}\right)$ becomes steeper. As mentioned before, a clearer distinction between the two state parameter forms could be made if LCSI points for each coupling ratio were obtained for the higher stresses where the curves become steeper. For the Congleton sand used here it would lead to mean effective stresses beyond the limits of the equipment and instrumentation used, and beyond the range of interest for most geotechnical applications.

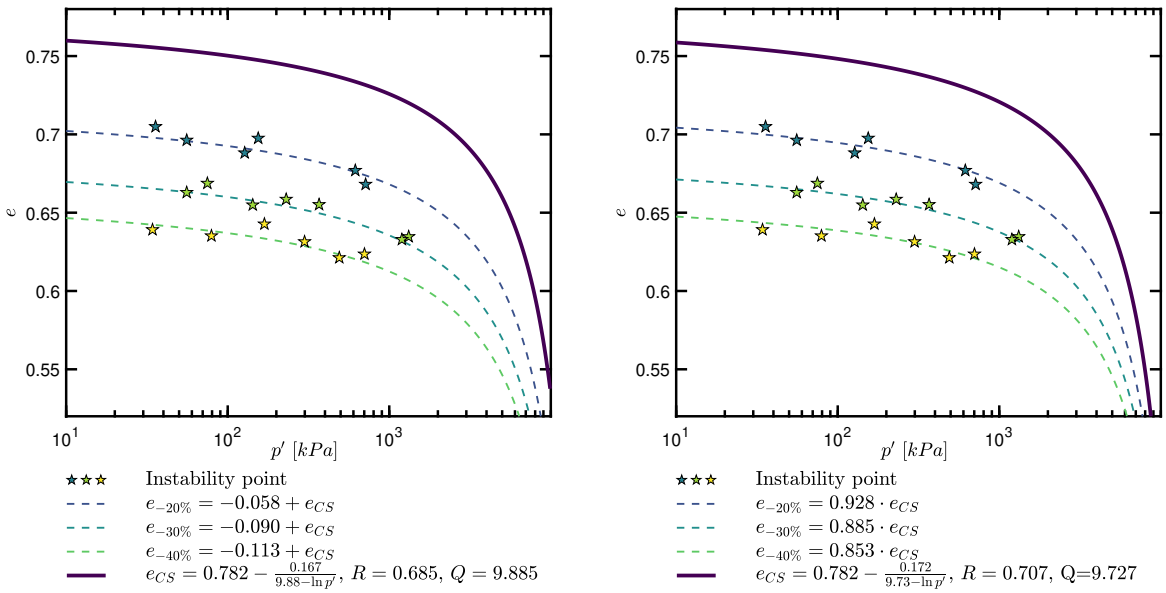

Figure 6.4: Critical state line for Congleton sand for state parameter form (a)$\psi_{F1} = e - e_{cs}$ (left) and (b)$\psi_{F3} = ln\left(\frac{e}{e_{cs}}\right)$ (right)

6.2.4 Validation of the proposed methodology

In this section a validation exercise of the proposed methodology to determine the CSL is presented using results on Hostun sand from chapter 4. The coupled shear-volumetric strain monotonic compression tests conducted in section 4.3.2 were used to predict the CSL following the steps outlined in the previous sections. The relevant LCSI sets of points (post-phase transformation and post-peak stress ratio), determined using Hill's criterion (Hill, 1958) were listed in table 4.4. State parameter forms ψ_{F1} (equation 6.2 and corresponding to state parameter definition of equation 6.1) and ψ_{F2} (equation 6.3 and corresponding to state parameter definition of equation 6.6) were examined following section 6.2.2.

The assessment for the Ω constants for the two state parameter forms was conducted by selecting the LCSI point set corresponding to $\zeta = -15\%$ as the reference and translating the other two LCSI sets of points to the reference. Figure 6.5(a) shows the vertically translated points for form 1 of each LCSI set $'j'$ ($\zeta = -5\%$ and -10%) in $e - p'$ space to the reference set $'i'$ ($\zeta = -15\%$) using $\Omega_{1,i|j}$ (equation 6.2). Similarly, figure 6.5(b) shows the LCSI point sets for $'j'$ ($\zeta = -5\%$ and -10%) moved to the reference $'i'$ ($\zeta = -15\%$) in $e - p'$ space by a void

ratio multiplication constant $\Omega_{2,i|j}$ (equation 6.3) for form 2. The Ω constants listed in table 6.4 minimize the scatter of data points in $e - p'$ space, computed through the mean of the moving standard deviation of e across p', as illustrated in figure 6.6.

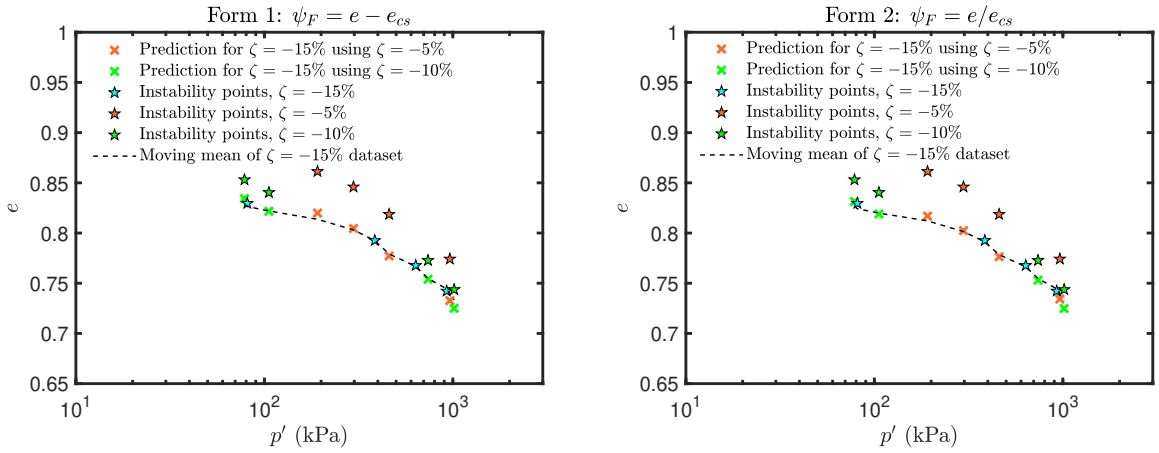

Figure 6.5: Assessment of state parameter forms, (a) Form 1: $\psi_{F1,\zeta} = e_\zeta - e_{cs}$ and (b) Form 2: $\psi_{F2,\zeta} = \frac{e_\zeta}{e_{cs}}$, through transferring LCSI points for $\zeta = -5\%$ and -10% to the $\zeta = -15\%$ LCSI curve for Hostun sand.

Reference set	Constant	Definition	Value
$\zeta = -15\%$	$\Omega_{1,-15\%\|-5\%}$	$e_{-15\%} - e_{-5\%}$	-0.0414
$\zeta = -15\%$	$\Omega_{1,-15\%\|-10\%}$	$e_{-15\%} - e_{-10\%}$	-0.0187
		Mean of moving σ	0.0176
$\zeta = -15\%$	$\Omega_{2,-15\%\|-5\%}$	$e_{-15\%}/e_{-5\%}$	0.9485
$\zeta = -15\%$	$\Omega_{2,-15\%\|-10\%}$	$e_{-15\%}/e_{-10\%}$	0.9745
		Mean of moving σ	0.0171

Table 6.4: Values for Constants Ω_1 (based on state parameter form of equation 6.2) and Ω_2 (based on state parameter form of equation 6.3) resulting in the minimum mean of moving standard deviation for Hostun sand.

The state parameter form 2 (equation 6.3) was considered appropriate for the examined data, as it resulted in the minimum mean of the moving standard deviation of e (table 6.4). Using the state parameter form 2 (e/e_{cs}), the parameters of Bolton's CSL equation were determined, using the instability points for $\zeta = -15\%$ and the translated instability points for $\zeta = -5\%$ and $\zeta = -10\%$, as shown in figure 6.5(b). The best-fit with $R^2 = 0.99$ was obtained using $Q = 8.5$, $R = 0.83$ and $e_{-15\%}/e_{cs} = 0.898$. The obtained Q and R parameters for the critical state can be

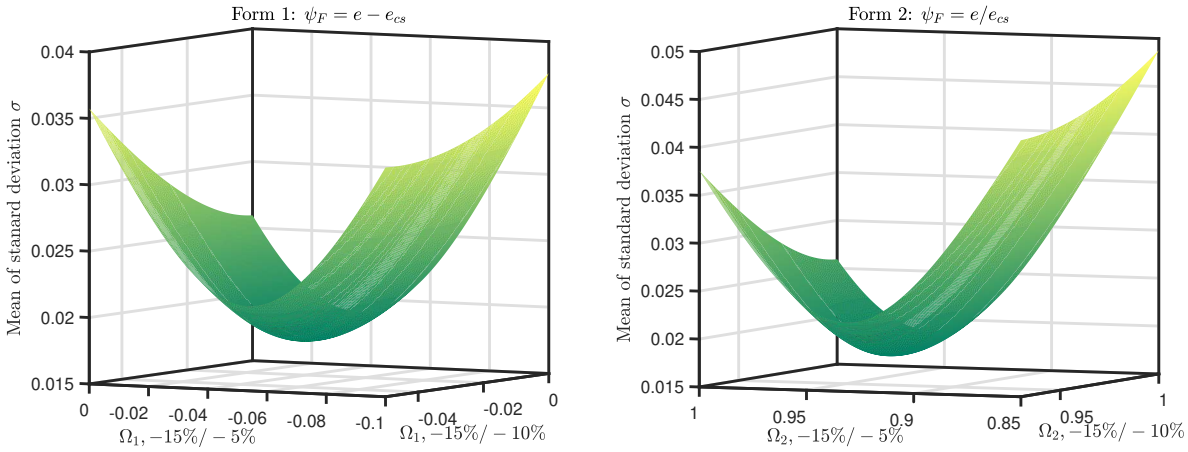

Figure 6.6: Mean of moving (5 point) standard deviation of all experimentally obtained points translated to the reference $\zeta = -15\%$ LCSI curve based on state parameter forms (a) Form 1: $\psi_{F1,\zeta} = e_\zeta - e_{cs}$ and (b) Form 2: $\psi_{F2,\zeta} = \frac{e_\zeta}{e_{cs}}$ for Hostun sand.

compared to the those determined directly, using undrained and drained monotonic compression tests in section 4.3.1: $Q = 8.3$ and $R = 0.73$. For $\zeta = -15\%$ and with a known CSL, a value of $e_{-15\%}/e_{cs} = 0.897$ was calculated. The back-calculated and the directly obtained CSL for Hostun sand are shown in figure 6.7. As seen from the figure, the proposed methodology using proportional strain paths can accurately locate the CSL in $e - p'$ space.

6.2.5 State parameter definition

The investigation up to the previous section is sufficient to derive an expression for the CSL through coupled strain compression tests. Though at this point appropriate state parameter forms ψ_F have been identified, a definition of the state parameter ψ_D that satisfies equation 5.9 numerically for all experimentally obtained LCSI curves remains unknown. If the use of a SANISAND model is intended, then the final step in the CSL determination, necessary for model calibration, is the selection of a state parameter definition ψ_D. Here, the proposed definition in equation 6.1 is investigated for the two state parameter forms considered in the previous section, $\psi_{F1} = e - e_{cs}$ and $\psi_{F3} = ln\left(\frac{e}{e_{cs}}\right)$. As previously noted, following equation 5.9 and 5.4, ψ_D must be linearly related to $\Lambda = \frac{3\zeta}{3-\zeta}$. With increasing magnitudes of Λ, ψ_D increases in

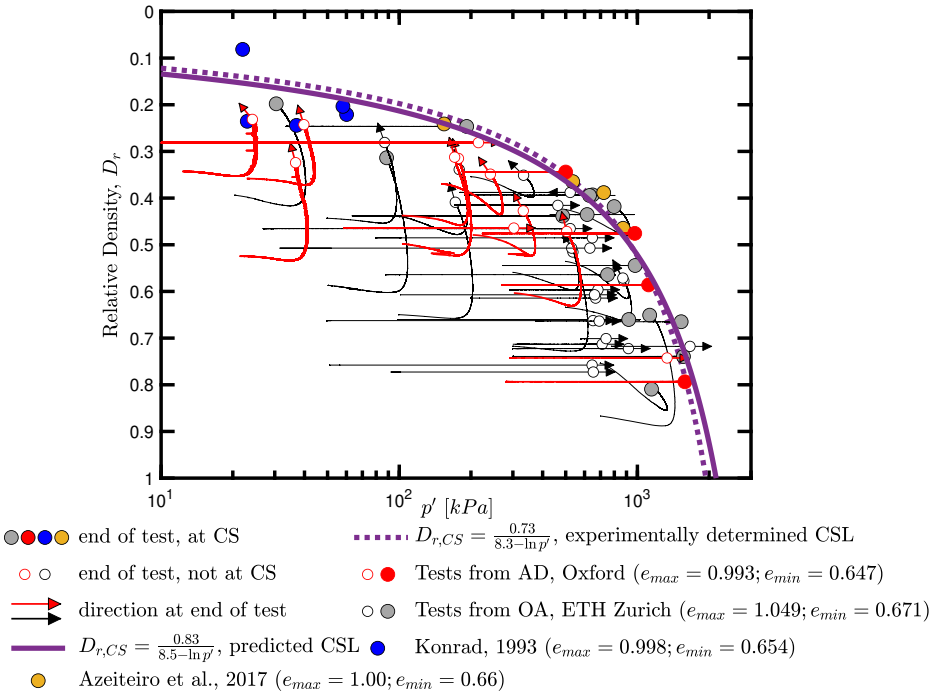

Figure 6.7: Experimentally determined CSL of Hostun sand from section 4.3.1 in $e - p'$ and predicted CSL for Hostun sand determined using the methodology in this chapter.

magnitude monotonically, requiring a positive value for exponent w.

The values of the state parameter forms ψ_{F1} and ψ_{F3} listed in table 6.3 were used for the state parameter definition ψ_D of equation 6.1 and the produced ψ_D values were substituted in equation 5.9, to obtain the following relation for $C = A_d(k^d + k^b)$ at each strain coupling ratio:

$$\begin{aligned} &At\ \ \zeta_i,\ \ C \cdot \psi_{D,\zeta_i} = \frac{3\zeta_i}{3-\zeta_i} = \Lambda_i \\ \Longrightarrow\ &Form\ \ 1 : C \cdot (-\psi_{F1,\zeta_i})^w = -\Lambda_i \\ \Longrightarrow\ &Form\ \ 3 : C \cdot (-\psi_{F3,\zeta_i})^w = -\Lambda_i \end{aligned} \tag{6.10}$$

For each state parameter form ψ_F, a positive coefficient C and a positive exponent w were obtained through curve fitting of equation 6.10 using the three available points of $(\psi_{F,\zeta_i}, \Lambda_i)$, corresponding to the three strain coupling ratios examined. Figure 6.8 depicts this process of relating Λ to the available ψ_F values and gives the calculated C and w values for the two state parameter forms considered. For both forms ψ_F examined, the coefficient of determination for

the fitted ψ_D was 0.993. The more experimentally obtained LCSI curves become available, the more points can be added to the graphs of figure 6.8, allowing further scrutiny on the definition of ψ_D. For equation 6.1 assumed to apply here, further points would lead to a more accurate exponent w.

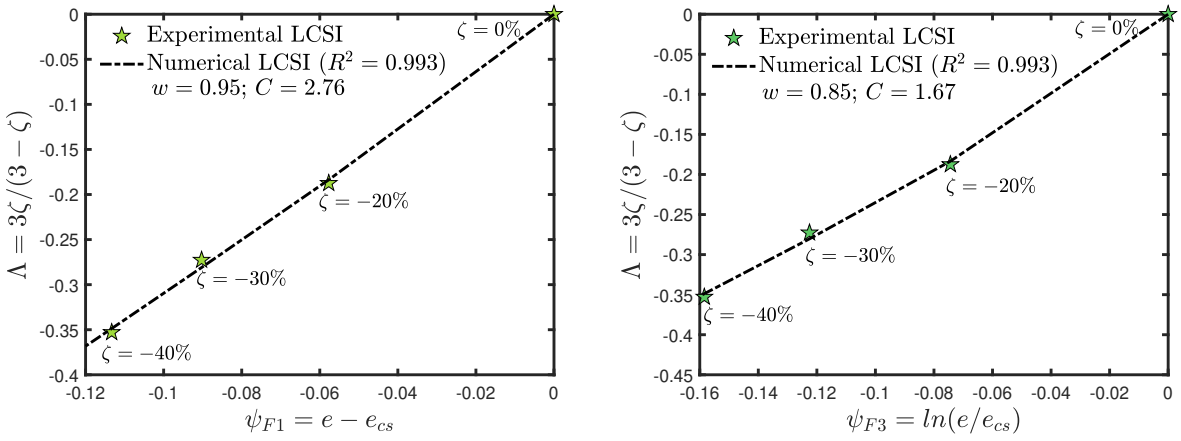

Figure 6.8: Determination of parameters w and $C = A_d(k^d + k^b)$ using (a) Form 1: $\psi_{F1,\zeta} = e_\zeta - e_{cs}$ (left) and (b) Form 3: $\psi_{F3,\zeta} = ln(e_\zeta/e_{cs})$ (right)

Thus, the state parameter definition needed for the constitutive model formulation and calibration (equation 6.1) was fully defined for both state parameter forms. At the end of this investigation, two state parameter definitions $\psi_{D1} = sign(e - e_{cs}) \cdot |(e - e_{cs})|^{0.95}$ and $\psi_{D3} = sign(ln\left(\frac{e}{e_{cs}}\right)) \cdot |ln\left(\frac{e}{e_{cs}}\right)|^{0.85}$ were deemed equally appropriate for the available experimental data. In the sequel ψ_{D3} was selected to be taken forward, to maintain consistency with the conclusions of chapter 5.

6.3 Model calibration

This section examines the possibility of using the coupled strain tests noted in table 6.1 to determine additional SANISAND 2008 model parameters (Taiebat and Dafalias, 2008). However, not all calibration parameters can be directly derived from these tests. Additional experiments are presented below, as required to achieve a model calibration for Congleton sand that can be

used to numerically capture triaxial compression experiments.

6.3.1 Elastic shear modulus

The small-strain shear modulus, G_{max}, is one of the two elasticity parameters required for calibration. As it cannot be directly obtained from the coupled strain tests presented up to now, additional bender element tests were conducted by YW at University of Oxford that was post-processed and presented here with permission. The sample preparation process remained as described for the coupled strain tests (refer chapter 4 and Dilip et al. (2026)). Specimens were prepared at three void ratio values and each was isotropically consolidated in steps, to six levels of mean effective stress, with measurements on shear wave velocity made at each step. The travel time for the shear wave was determined using the peak-to-peak method between input and output signal. A summary of the bender element test results is presented in table 6.5. The corresponding expression for G_{max} is noted in equation 6.11 and shown in figure 6.9.

$$G_{max} = G_0\, p_{at}\, \frac{(2.97-e)^2}{1+e} \left(\frac{p'}{p_{at}}\right)^{0.5} \quad where \quad G_0 = 260 \tag{6.11}$$

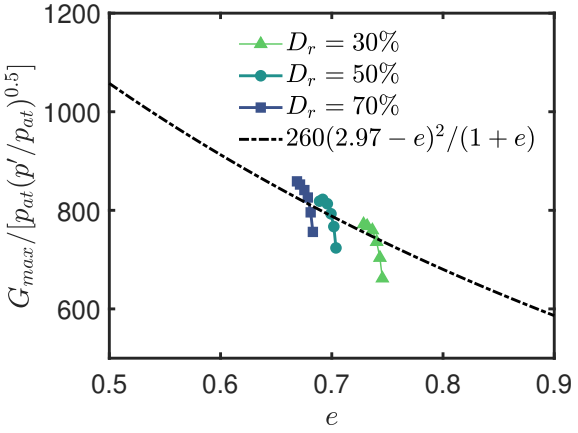

Figure 6.9: Calibration of G_{max} using bender element tests on isotropically consolidated Congleton sand

The value of the small-strain shear modulus G_{max} as obtained from bender element tests has been reported in literature to overestimate by a factor of 2 to 4 the shear modulus required within

Initial D_r [a]	p' [a]	e [a]	t [b]	V_s [b]	G_{max} [b]
30%	24.7	0.745	1.000	130.4	32.9
30%	49.5	0.743	0.828	160	49.5
30%	99.7	0.740	0.680	194.8	73.5
30%	199.7	0.737	0.562	235.3	107.3
30%	399.8	0.732	0.470	281.3	153.6
30%	599.6	0.729	0.423	311.9	189.0
50%	24.6	0.704	0.981	135.5	35.9
50%	49.4	0.702	0.801	165.9	53.9
50%	99.7	0.699	0.661	201.0	79.2
50%	199.7	0.696	0.548	242.1	114.9
50%	399.6	0.692	0.458	289.3	164.4
50%	599.9	0.689	0.415	319.4	200.5
70%	24.2	0.683	0.972	137.4	37.2
70%	49.3	0.681	0.792	168.5	55.9
70%	99.3	0.678	0.653	204.3	82.3
70%	199.2	0.675	0.543	245.3	118.7
70%	399.4	0.671	0.453	293.7	170.3
70%	599.5	0.669	0.408	326.1	210.3

[a]Post consolidation values. [b](1)t: travel time using first peak in ms; (2)V_s: shear wave velocity in m/s; (3)G_{max}: elastic shear modulus in MPa.

Table 6.5: Results of bender element tests on Congleton sand conducted by YW at University of Oxford (reproduced with permission)

bounding surface plasticity models of the SANISAND family in order to adequately capture triaxial compression tests at low to medium strain levels (Andrianopoulos et al., 2010; Papadimitriou et al., 2001, 2023). In chapter 5 a value of $G_{max}/3$ was used to calibrate the SANISAND 2008 model in order to obtain good agreement with triaxial compression experiments for Hostun sand. A factor of two was applied here for Congleton sand, with the final expression adopted for the shear modulus used within SANISAND 2008 shown in equation 6.12.

$$G = G_0\, p_{at}\, \frac{(2.97-e)^2}{1+e} \left(\frac{p'}{p_{at}}\right)^{0.5} \quad where \quad G_0 = 130 \tag{6.12}$$

6.3.2 Elastic bulk modulus

The elastic bulk modulus, K can be obtained either directly from isotropic unloading experiments or indirectly from the elastic shear modulus and Poisson's ratio (Taiebat and Dafalias,

2008). In this study, K was obtained from the elastic shear modulus G (equation 6.12) and Poisson's ratio ν, as shown in equation 6.13. A value of $\nu = 0.05$ was used based on Dafalias and Manzari (2004).

$$K = \frac{2(1+\nu)}{3(1-2\nu)}G \tag{6.13}$$

6.3.3 Bounding surface parameter

The bounding surface parameter can either be defined following an exponential or a linear evolution of the bounding stress ratio, M^b, with the state parameter, ψ_D. Parameter n^b in equation 6.14 corresponds to an exponential evolution, whereas parameter k^b corresponds to a linear evolution. The latter is selected in this study as it produces a linear LCSI equation (equation 5.9) which facilitates calculations. Values for M^b can be obtained experimentally from peak stress-ratio states (PSRS), η_{PSRS}. Such values from the coupled strain tests listed in table 6.1 are plotted against their corresponding state parameter, ψ_D^b in figure 6.10. The slope of the fitted line gives the k^b value, while the ordinate of the fitted line at $\psi_D = 0$ can be used to infer the critical state stress ratio, M^c.

$$M^b = M^c exp(-n^b \psi_D) \quad or \quad M^b = M^c - k^b \psi_D \tag{6.14}$$

6.3.4 Dilatancy surface parameter

To obtain the dilatancy surface parameter, the phase transformation state (PTS), i.e., the point of transition from contraction to dilation ($D = 0$) must be detected. This can be easily done in undrained tests, where $D = 0$ when $\dot{p'} = 0$. However, coupled strain tests impose non-zero volumetric strain increments, $\dot{\varepsilon}_v \neq 0$, so that the point of $\dot{\varepsilon_v}^p = 0$ cannot be directly deduced from the vanishing of $\dot{\varepsilon_v}^e$. Instead, the elastic parameters must be known to locate the PTS, which introduces uncertainty. Thus, a series of undrained monotonic compression tests were conducted

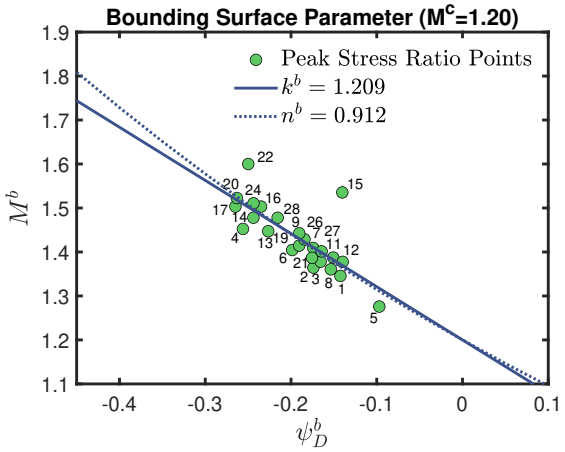

Figure 6.10: Calibration of constants k^b and n^b (equation 6.14) for Congleton sand using the results of coupled strain monotonic compression tests from table 6.1

to capture phase transformation points, summarised in table 6.6, by YW at the University of Oxford (post-processed and presented with permission). The dilatancy surface parameter can

Test ID[a]	${e_{PTS}}^b$	${p'_{PTS}}^b$	${\eta_{PTS}}^b$
ICUMC/0.586/100 (U1)	0.586	105.7	1.14
ICUMC/0.596/200 (U2)	0.596	199.0	1.13
ICUMC/0.636/300 (U3)	0.636	260.6	1.14
ICUMC/0.642/300 (U4)	0.642	297.1	1.11
ICUMC/0.645/100 (U5)	0.645	91.5	1.08
ICUMC/0.658/100 (U6)	0.658	94.1	1.06
ICUMC/0.674/100 (U7)	0.674	91.7	1.06
ICUMC/0.690/50 (U8)	0.690	41.3	1.08

[a](1)type of consolidation: IC for isotropic consolidation; (2)type of drainage: U for undrained; (3)type of loading: MC for monotonic compression; (4)void ratio immediately after consolidation; (5)mean effective stress immediately after consolidation. [b]PTS: Phase Transformation State.

Table 6.6: Results of undrained monotonic triaxial tests on Congleton sand conducted by YW at University of Oxford (reproduced with permission)

either be defined as n^d following an exponential evolution of the dilatancy surface stress ratio, M^d, with ψ_D, or as k^d if a linear evolution is preferred (equation 6.15). Here, a linear evolution was chosen, to match the assumption made for the bounding surface. Values of M^d obtained from the undrained compression tests at the phase transformation stress ratio, η_{PTS}, are plotted against their corresponding state parameter, ψ_D^d, in figure 6.11. With the value of M^c calculated

as described in the previous section, the slope of the best-fit line gives the k^d value. It is worth noting that despite using undrained compression tests, scatter is still present in the data.

$$M^d = M^c exp(n^d \psi_D) \quad or \quad M^d = M^c + k^d \psi_D \tag{6.15}$$

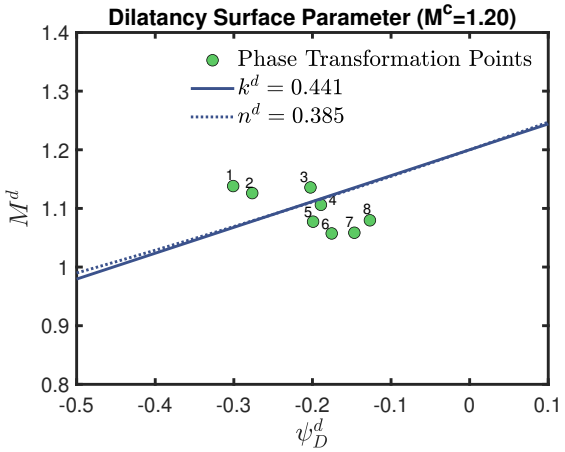

Figure 6.11: Calibration of constants k^d and n^d (equation 6.15) for Congleton sand using undrained monotonic compression tests from table 6.6

6.3.5 Fitting parameters

The dilatancy constant A_d (refer table 3.2) is typically determined from stress-dilatancy curves of drained tests (Taiebat and Dafalias, 2008) as illustrated for Hostun sand in section 5.4.5. However, in this case, equation 5.9 was used to evaluate parameter A_d, eliminating the need for additional experiments. Figure 6.8(b) shows a plot of the right-hand side of equation 5.9, varying with the state parameter, ψ_D ($\psi_D = f(\psi_F)$ per equation 6.1 with $w = 0.85$). The slope of the best-fit gives the value of the coefficient $C = A_d(k^d + k^b) = 1.67$. With parameters $k^b = 1.209$ and $k^d = 0.441$ as calculated earlier, a value of the dilatancy parameter, $A_d = 1.012$ was determined. Parameters h_0 and c_h were selected following trial-and-error in figure 6.12, by fitting undrained triaxial test simulation results to experiments in $q - \varepsilon_1$ space at low to medium strains, as in Taiebat et al. (2010). An exponential dependence on the void ratio (refer table 3.2) ensures

positive values for h in the equation for hardening modulus H across the range of void ratios of Congleton sand.

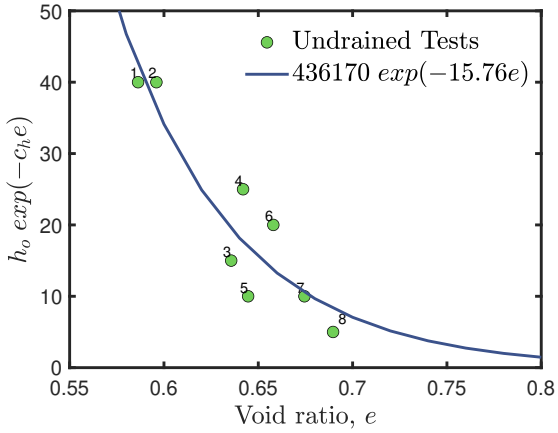

Figure 6.12: Calibration of h_0 and c_h for Congleton sand using undrained monotonic compression tests from table 6.6

6.3.6 Compression parameters

The compression parameters are not included here as they are only applicable for a high confining pressure range (refer section 5.4.7), which is beyond the range of interest of this study.

6.4 Model performance

A summary of the selected SANISAND 2008 model parameters for Congleton sand are listed in table 6.7. Parameter c, the ratio of the slope of the critical surface in triaxial extension to compression and parameter m, controlling the size of the elastic wedge, were taken from Dafalias and Manzari (2004). As discussed above, the shear modulus G was based on a reduced value of that measured through bender element tests and the traditional value of Poisson's ratio ν was used. Parameters M^c, R, Q, n^b or k^b, and A_d were directly obtained from the coupled strain compression tests used to infer the CSL. Parameters n^d or k^d, h_0, and c_h were obtained from undrained tests. This section includes the simulation results for the undrained and the coupled

strain experimental tests on Congleton sand. The selected/modified SANISAND 2008 model equations used for the simulations are listed in table 6.8.

Parameter	Values	Parameter	Values	Parameter	Values
G_0 [(1)]	130	e_{max} [(3)]	0.782	n^b	0.912
ν [(2)]	0.05	e_{min} [(3)]	0.538	k^b	1.209
M^c	1.20	R [(3)]	0.707	h_0 [(4)]	436170
α^c	1.19	Q [(3)]	9.727	c_h [(4)]	15.76
m	0.01	n^d	0.385	A_d	1.012
c	0.71	k^d	0.441	p_{at} (kPa)	100

[(1)]Implemented in equation 6.12; [(2)]Implemented in equation 6.13; [(3)]Implemented in CSL equation 6.7; [(4)]Exponential function used, see section 6.3.5; refer table 6.8 for model equations.

Table 6.7: SANISAND 2008 model parameters for Congleton sand

Equations	Model Constants	Description
Critical State Line: $e_{cs} = e_{max} - \frac{(e_{max}-e_{min})R}{Q-ln(p')}$	e_{max} , e_{min} , Q , R	Equation 6.7
Elasticity: $G = G_0\ p_{at}\frac{(2.97-e)^2}{1+e}(\frac{p'}{p_{at}})^{0.5}$ $K = \frac{2(1+\nu)}{3(1-2\nu)}G$	G_0 , ν	p_{at} : 100 kPa Equation 6.12 Equation 6.13
Hardening Rule: $b_0 = G_0 h_0 exp(-c_h e)(p'/p_{at})^{-1/2}$	h_0 , c_h	Exponential evolution of b_0
Surface Evolution Laws: $\alpha^b_{c,e} = s(\alpha^c_{c,e} - k^b\psi_D)$ $\alpha^d_{c,e} = s(\alpha^c_{c,e} + k^d\psi_D)$	k^b , k^d	Linear Surface Evolution ψ_D: State Parameter $(= sign(ln\left(\frac{e}{e_{cs}}\right))\lvert ln\left(\frac{e}{e_{cs}}\right)\rvert^{0.85})$

Table 6.8: Selected/modified equations for SANISAND 2008 model to be used in conjunction with model parameters of table 6.7, refer table 3.2 for remaining equations

6.4.1 Undrained monotonic triaxial test simulations

A comparison between the numerical simulations and the experimental data for the undrained tests of table 6.6 is shown in figure 6.13. The simulations adequately captured the undrained behaviour across the range of examined densities, both in terms of stress paths in $q-p'$ space and in terms of stress-strain behaviour.

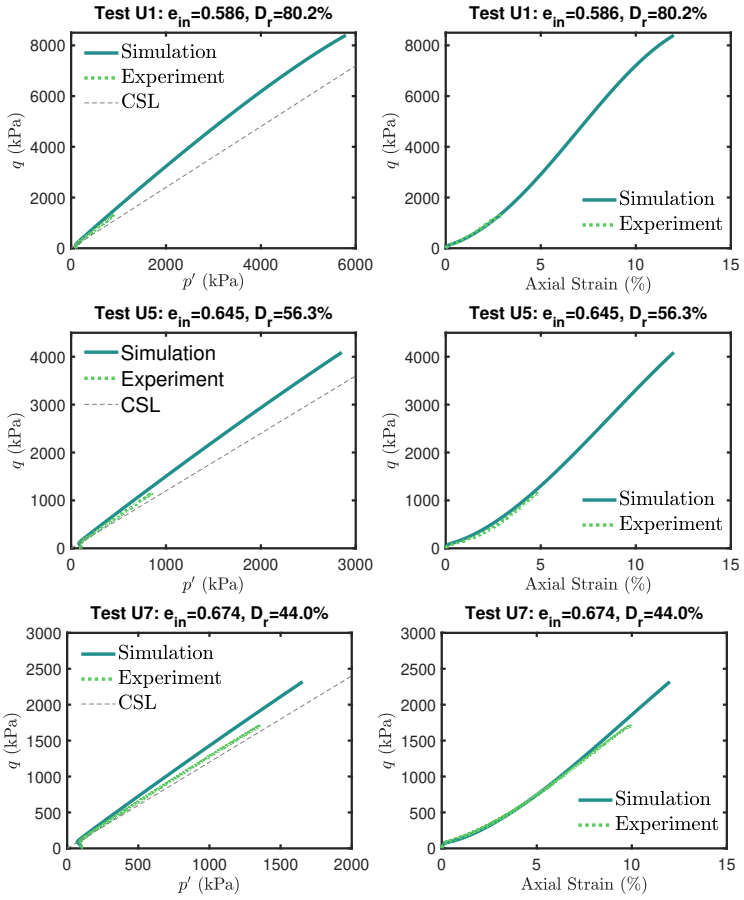

Figure 6.13: Simulations of undrained monotonic triaxial compression tests on isotropically consolidated samples of Congleton sand and comparison with experimental data from table 6.6

6.4.2 Coupled strain triaxial compression test simulations

Using the calibration parameters for a linear evolution of bounding and dilatancy surfaces from table 6.7 and model equations from table 6.8), the coupled strain triaxial tests of table 6.1 were numerically simulated using SANISAND 2008 (Taiebat and Dafalias, 2008). The comparisons between simulation and experiments are shown in figures 6.14 - 6.16. The LCSI instability points of the simulations were detected using Hill's criterion (equation 5.2), similarly to the experimental data. Instability points are depicted in square markers for the numerical simulations and star markers for the experimental data. The experimental and simulated coupled strain paths were also plotted in $e - p'$ space in figure 6.17.

Overall, the calibrated parameters allowed the model to capture the observed behaviour well,

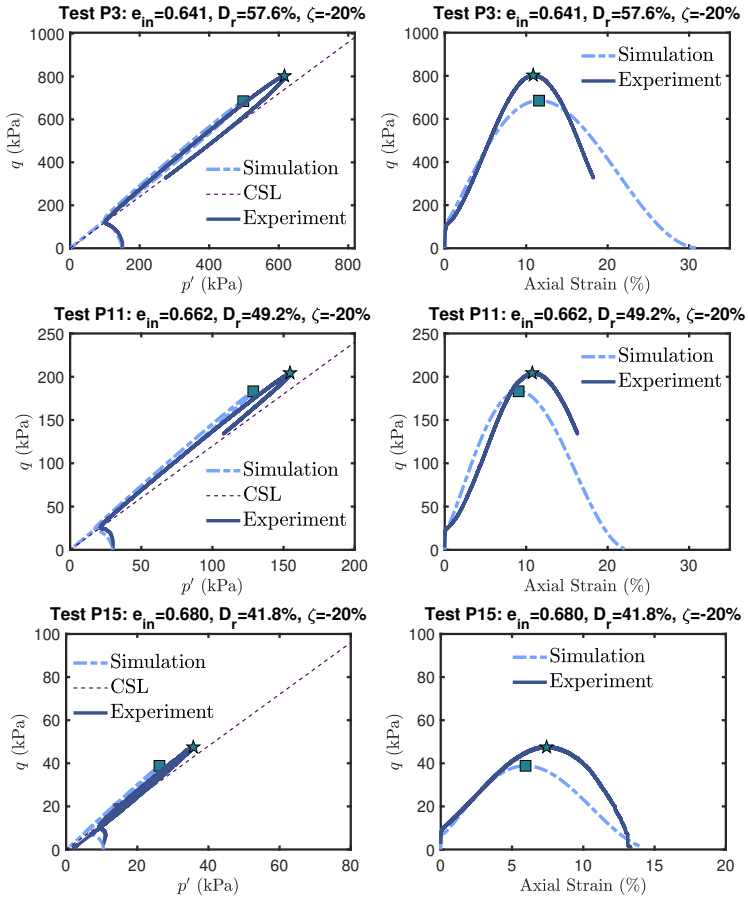

Figure 6.14: Simulations of coupled strain monotonic triaxial compression tests under $\zeta = -20\%$ on isotropically consolidated samples of Congleton sand and comparison with experimental data from table 6.1

across all strain coupling ratios examined. Although the numerical instability points do not exactly match the experimental instability points, the stress paths in $q - p'$ space were adequately replicated. The effective stresses follow a similar path to undrained tests for medium-dense/dense sands, but before the CSL can be reached a reversal towards diminishing p' and q is observed. Initially, the soil accommodates the expansive volumetric strains. After the dilatancy has reached its minimum negative value and has increased to match the imposed strain coupling ratio ($D = \Lambda < 0$), the soil is no longer able to sustain the continuous expansive volumetric strain and unloading takes place (reduction in p' and q). A drastic increase in void ratio and shear strain follows. In the $q - \varepsilon_1$ plots, the peak deviator stresses and the instability points were detected at axial strains similar to the corresponding experimental values. The magnitude of the

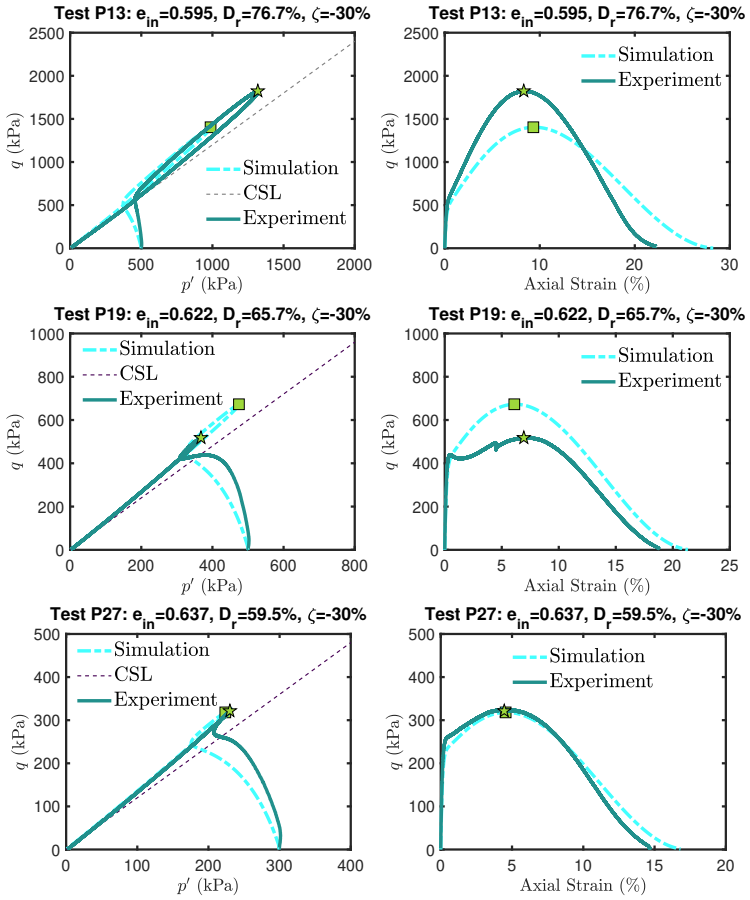

Figure 6.15: Simulations of coupled strain monotonic triaxial compression tests under $\zeta = -30\%$ on isotropically consolidated samples of Congleton sand and comparison with experimental data from table 6.1

peak deviator stress was also overall captured well. An exception was the last experiment of figure 6.16, where larger than experimentally observed values of p' and q were reached. This is because for $\zeta = -40\%$ and to a lesser extent for $\zeta = -30\%$, experiments with low initial mean effective stress were less dilative than predicted by the simulations (figure 6.17).

Figure 6.17 presents results in $e - p'$ space and confirms that the numerically calculated and the experimentally observed LCSI curves (constant ψ_F or ψ_D) practically coincide. For instance, for $\zeta = -30\%$, the experimental constant ψ_D line is located at $e_{-30\%} = 0.885 e_{cs}$ (figure 6.4(b)), while as shown in figure 6.8(b) the power fit used in equation 5.9 predicts the constant ψ_D line at $e_{-30\%} = 0.888 e_{cs}$. For the other two strain coupling ratios, the predicted numerical LCSI is even closer to the experimental LCSI in figure 6.17, as also depicted in figure 6.8(b). Across

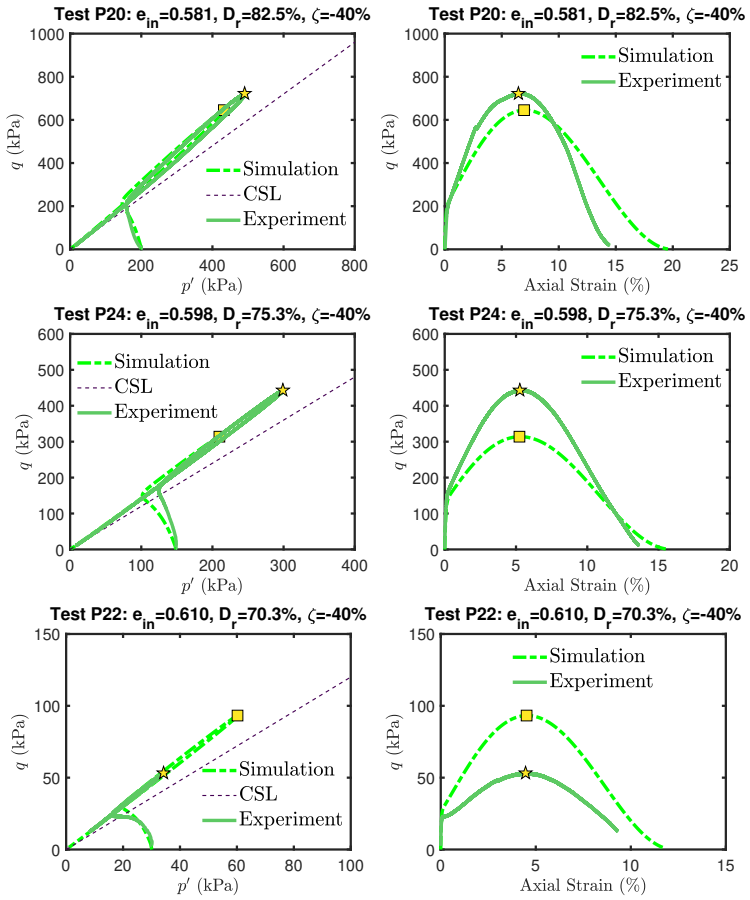

Figure 6.16: Simulations of coupled strain monotonic triaxial compression tests under $\zeta = -40\%$ on isotropically consolidated samples of Congleton sand and comparison with experimental data from table 6.1

all coupling ratios, as already stated, experiments with $p' < 100$ kPa and $e < 0.65$ were less dilative than their corresponding simulations. On the contrary, simulations captured very well experiments with initial mean effective stress of $p' > 100$ kPa or $p' < 100$ kPa with $e > 0.65$. It is worth noting that the dilatancy surface parameter k^d was calibrated from undrained tests in table 6.6, where all but one undrained tests had $p' > 100$ kPa, while the test capturing $p' < 100$ kPa was at a void ratio $e > 0.65$. Therefore, the calibration process of parameter k^d in figure 6.11 did not directly capture cases where phase transformation occurs at $p' < 100$ kPa and $e < 0.65$.

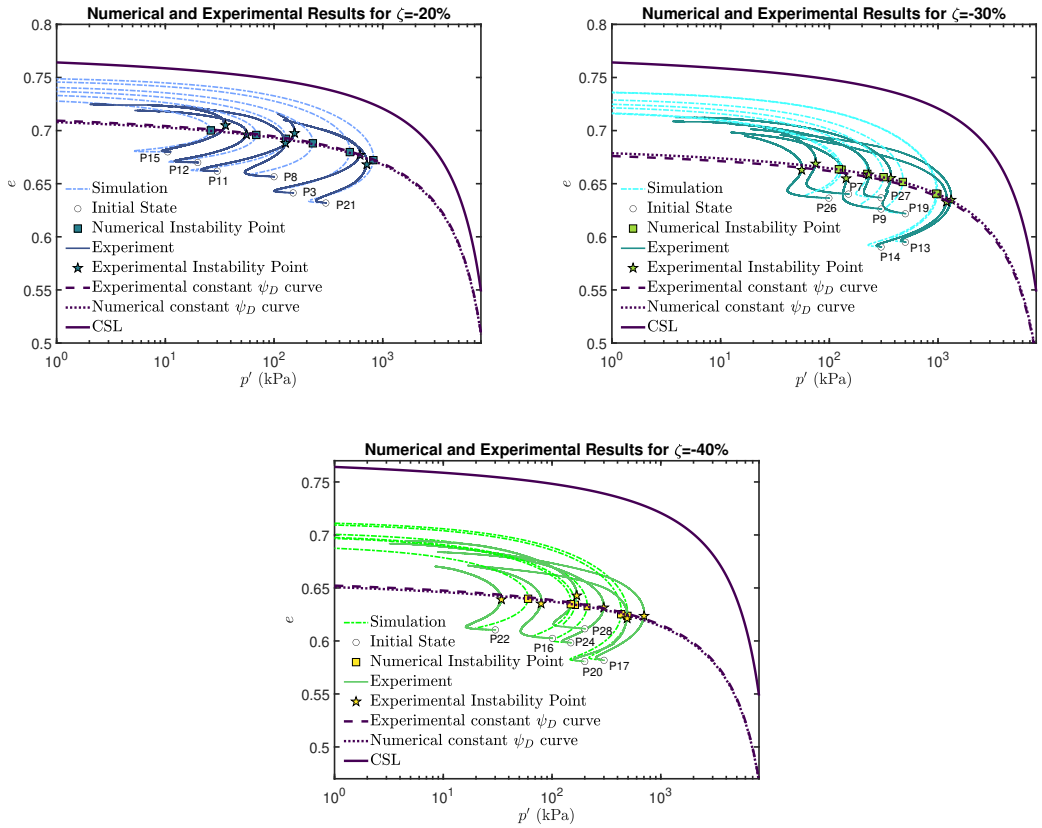

Figure 6.17: Simulations of coupled strain monotonic triaxial compression tests on Congleton sand under $\zeta = -20\%$, -30% and -40% in $e - p'$ space and comparison with experimental data from table 6.1

6.5 Conclusions

Locating the critical state line (CSL) through element tests can be a challenging or impossible task for some sands. This is often due to the excessive strains required to reach the critical state, which can be beyond what testing protocols allow, and which necessitate significant corrections that render result interpretation challenging. In addition, dense sands might require the application of loads that are beyond the limits of typical equipment or instrumentation, especially when considering high initial confining stresses. Further, undrained compression tests for dense sands that undergo dilation can quickly lead to negative pore water pressure and potential cavitation, which prohibits the specimen from reaching the critical state. Finally, scanning the entire density range with experiments is not possible for many sample preparation methods.

In this chapter, an alternative experimental approach to estimate the CSL is proposed, using coupled shear-volumetric strain triaxial compression experiments. These experiments do not require axial strains beyond the generally accepted threshold of 15%. The CSL is indirectly identified through the concept of the Locus of Constant State parameter Instability points (LCSI), as described within the context of bounding surface plasticity models of the SANISAND family in chapter 5. The proposed method requires non-standard drained triaxial compression tests where an expansive volumetric strain increment is applied as a constant fraction of the axial strain increment, conducted under different strain coupling ratios (ζ). Post-phase transformation and post-peak stress-ratio instability points identified using Hill's criterion are first used to establish the LCSI for each ζ. The LCSI curves are then compared to identify an appropriate state parameter form. Using this form, equations for the LCSI and the CSL curves, and the corresponding state parameter definition can be derived. While three coupling ratios ζ are sufficient to estimate the CSL, as shown here, more values of ζ could provide increased reliability regarding the identified state parameter definition and the proposed CSL.

The coupled strain triaxial compression tests performed to identify the CSL can further aid in the calibration of a SANISAND model. Here, the bounding surface parameters and the critical surface stress ratio were directly obtained through the peak stress-ratio points captured in these tests. However, determining the dilatancy surface parameters by identifying points of phase transformation state (PTS) was less straightforward, as due to the imposed volumetric strain rate, $\dot{p}' \neq 0$ at PTS. Instead, additional undrained tests sheared to low strain levels were conducted to obtain phase transformation points. For the elastic shear modulus, bender element tests were used. The elastic bulk modulus was estimated based on the elastic shear modulus and a value for Poisson's ratio used commonly in the SANISAND models. Finally, no drained tests were required to determine the dilatancy constant A_d, which was calculated from the coupled strain tests using the equation of the LCSI. The hardening constants were calibrated using iterations, based on the undrained compression results at low to medium strain. Overall, the use of the coupled strain triaxial compression tests eliminated the need for drained stress-dilatancy data

and in general the need for any experiment that reaches large strains.

A set of calibration parameters for monotonic modelling of Congleton sand within the SANISAND framework was consequently produced. The critical state could not be reached for Congleton sand through conventional testing. With the derived CSL and the remaining SANISAND calibration parameters, a good replication of the experimental test paths was obtained for both the undrained and the coupled strain conditions. It is worth noting that the method proposed to estimate the CSL, which is an inherent soil property, is based on the LCSI curve framework that was derived for SANISAND models. While no soil is bound to follow the SANISAND set of equations, the data of chapter 5 show that the (known) CSL of Hostun sand can be accurately predicted through this method, while the data of this chapter show that the estimated CSL for Congleton sand, when incorporated in numerical simulations, results in good predictions of observed behaviour.

Chapter 7

Assessment and calibration of double surface plasticity models for cyclic loading under volumetric expansion

7.1 Introduction

Pore water flow during the timeframe of an earthquake can significantly influence the evolution of pore water pressure and hence liquefaction triggering, especially in stratified deposits (see section 2.8). Such effects are largely unaccounted for in simplified liquefaction assessment procedures (see section 2.7.1), potentially leading to false predictions. To consider the effects of co-seismic drainage, nonlinear numerical analyses based on effective stress, that allow the use of a coupled soil-fluid formulation (Zienkiewicz and Shiomi, 1984) can be used, where the soil behaviour is captured by advanced constitutive models as detailed in sections 2.7.2 and 2.8.2. However, constitutive parameters calibrated at the element level often have to be updated to match larger scale experimental results in such analyses. For instance, soil permeability is increased as a function of excess pore pressure ratio to capture the experimentally recorded settlement of a deposit (e.g., Shahir et al., 2012). Such practice contradicts element-level ob-

servations on permeability, both regarding the magnitude of increase as well as the range of excess pore pressure ratios that are affected (Haigh et al., 2012). To increase the reliability of numerical simulations of liquefaction triggering in boundary value problems where co-seismic drainage is important, advanced constitutive models that are typically developed to replicate cyclic undrained element tests must be tested for their ability to capture non-standard drained cyclic behaviour.

Bounding surface plasticity models based on the SANISAND framework, discussed in chapter 3, have been popular for the simulation of liquefaction problems as they allow modelling across a wide range of initial densities and confining pressures with the same calibration. In this chapter, three such plasticity models are assessed for their ability to simulate the cyclic response of sand under undrained and non-standard drained conditions: DM04 by Dafalias and Manzari (2004), on which more recent versions of SANISAND are based, SANISAND-MSf by M. Yang et al. (2022), which represents a recent version of SANISAND, and PM4Sand3D by Kippen et al. (2026), which represents a different evolution branch of double surface plasticity. The models are first calibrated using undrained monotonic and cyclic tests conducted on Hostun sand, as would be typical. Next, non-standard element tests on Hostun sand are simulated, where cyclic deviatoric loading is imposed under constant water inflow rates. Tests with water inflow leading to volumetric expansion are chosen for this study as critical for liquefaction triggering. Such a condition can manifest at the interface of a liquefiable layer with an overlying layer of lower permeability and facilitate the onset of liquefaction, as compared to the undrained case. The assessment is done by generating liquefaction resistance curves for three densities under a range of inflow rates, including zero (undrained), and comparing them with the corresponding experiments.

Cyclic resistance under constant water inflow rates was experimentally shown to approximately be a superposition of isotropic unloading and undrained cyclic shearing (Adamidis and Anastasopoulos, 2022). This observation led to the suggestion of direct calibration of the bulk modulus using isotropic unloading data, as opposed to indirect calibration through the shear

modulus and a typically assumed Poisson's ratio. The significance of the direct bulk modulus calibration in obtaining accurate predictions of cycles to liquefaction under volumetric inflow rates is evaluated in this chapter and the overall reliability of the examined constitutive models in simulating cyclic non-standard drained paths is discussed. Finally, the impact of the updated SANISAND state parameter definition, from chapter 5, on cyclic performance is assessed.

The novel contributions of this chapter are twofold. Firstly, three conventionally calibrated constitutive models of the double surface plasticity framework are assessed for their ability to reproduce experimentally obtained cyclic liquefaction resistance curves under volumetric expansion conditions. This comparison illustrates the reliability of the examined constitutive models when simulating the cyclic behaviour of sands within water inflow zones, that can manifest in boundary value problems but for which the models have not been specifically developed or calibrated. Secondly, finding model performance using a conventional calibration lacking, this study proposes an updated process, which involves direct calibration of the bulk modulus using isotropic unloading data. For the Hostun sand dataset examined, this approach remarkably improves the prediction of element-level behaviour under non-standard drained conditions, a prerequisite for reliable performance at the boundary value problem scale.

7.2 Model calibration

As noted in chapter 4, experimental results only on batch 1 of Hostun HN31 sand are used for the assessment of cyclic model response. This is to maintain consistency in model calibration due to observed variability in physical characteristics across different batches of Hostun sand. The models were calibrated in triaxial space using monotonic compression tests and undrained cyclic tests on batch 1 of Hostun sand conducted by OA at ETH Zurich, published in Dilip and Adamidis (2024b) and reproduced here with permission. Information on sand physical characterisation and experimental methods for these tests are provided in Adamidis and Anastasopoulos (2022). Monotonic triaxial compression tests conducted under undrained (U) and

fully drained (D) conditions used for model calibration are listed in table 7.1, and the undrained cyclic triaxial tests can be found in Adamidis and Anastasopoulos (2022).

7.2.1 DM04 model parameters

The DM04 model by Dafalias and Manzari (2004) is described in detail in section 3.2 and the governing equations are listed in table 3.1.

Surface parameters

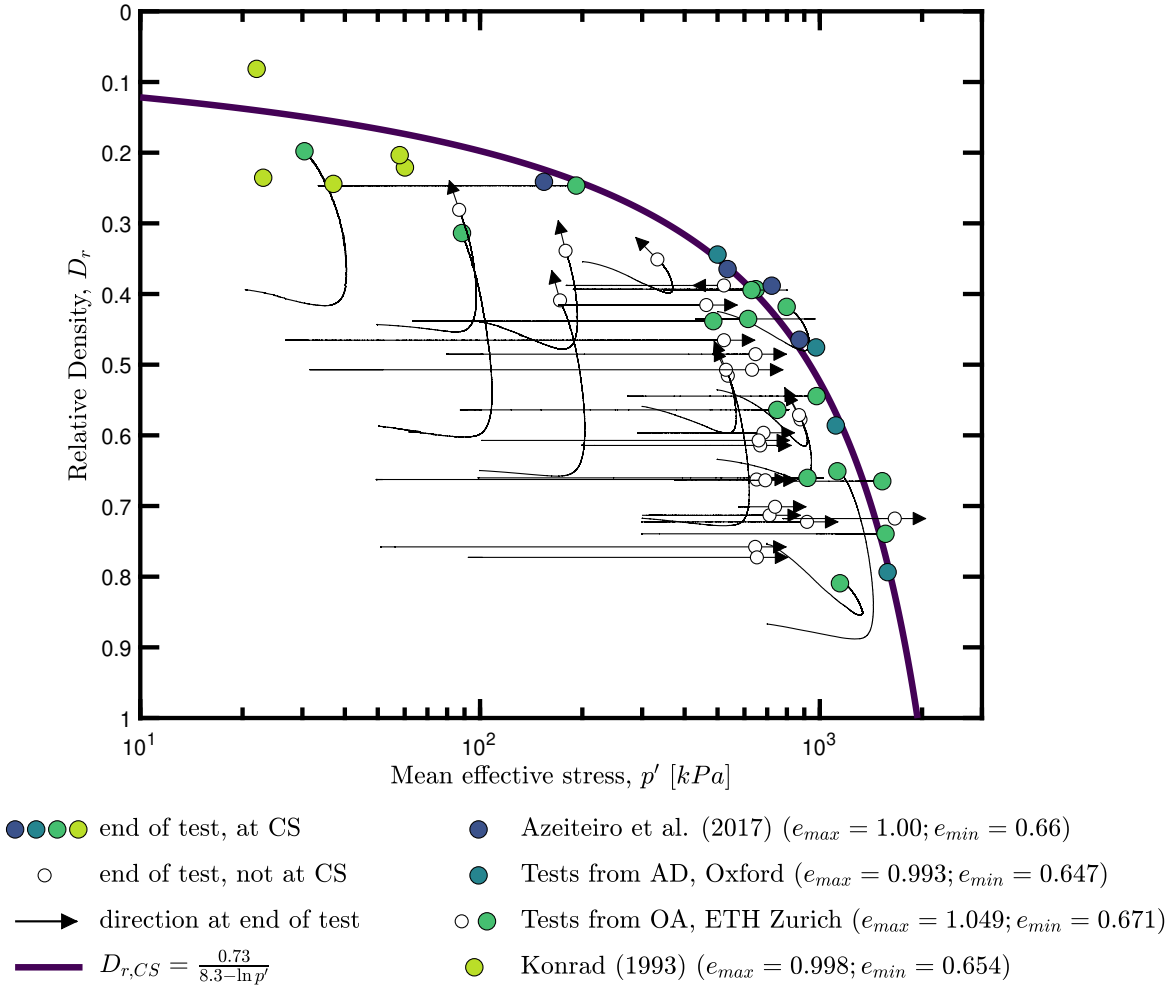

Figure 7.1: Critical state line for Hostun sand, recreated from chapter 4

The critical state line (CSL) was proposed in terms of relative density D_r, denoted by $D_{r,cs}$

Test ID[a]	e_{in}[b]	p'_{in}[b]	e_{end}	p'_{end}	η_{PTS}[c]	η_{PSRS}[d]	η_{end}	ϕ_{end}
ICUMC/0.770/300 (U1)	0.770	300	0.770	1561	1.28	1.45	1.38	34.0°
ICUMC/0.843/300 (U2)	0.843	300	0.843	978	1.24	1.38	1.28	31.9°
ICUMC/0.900/300 (U3)	0.900	300	0.900	648	1.26	1.36	1.14	28.5°
ICUMC/0.884/900 (U4)	0.884	900	0.884	615	1.34	1.36	1.17	29.3°
ICUMC/0.956/100 (U5)	0.956	100	0.956	192	1.30	1.36	1.12	28.2°
ICUMC/0.900/800 (U6)	0.900	800	0.900	630	1.30	1.34	1.22	30.6°
ICUMC/0.798/800 (U7)	0.798	800	0.798	1527	1.32	1.43	1.23	30.8°
ICUMC/0.883/100 (U8)	0.883	100	0.883	486	1.23	1.40	1.24	31.0°
ICUMC/0.836/100 (U9)	0.836	100	0.836	749	1.24	1.46	1.20	29.9°
ICUMC/0.799/99 (U10)	0.799	99	0.799	920	1.23	1.47	1.20	30.0°
ICUMC/0.857/52 (U11)	0.857	52	0.857	632	1.16	1.43	1.42	35.0°
ICUMC/0.824/300 (U12)	0.824	300	0.824	683	1.26	1.40	1.39	34.4°
ICUMC/0.779/300 (U13)	0.779	300	0.779	711	1.27	1.45	1.45	35.8°
ICUMC/0.776/300 (U14)	0.776	300	0.776	917	1.26	1.45	1.45	35.8°
ICUMC/0.902/300 (U15)	0.902	300	0.902	552	1.27	1.35	1.25	31.2°
ICUMC/0.892/300 (U16)	0.892	300	0.892	463	1.28	1.36	1.31	32.5°
ICUMC/0.799/50 (U17)	0.799	50	0.799	651	1.09	1.47	1.46	35.9°
ICUMC/0.817/200 (U18)	0.817	200	0.817	668	1.21	1.40	1.39	34.4°
ICUMC/0.798/400 (U19)	0.798	400	0.798	691	1.25	1.39	1.38	34.2°
ICUMC/0.784/600 (U20)	0.784	600	0.784	738	1.21	1.37	1.37	33.8°
ICUMC/0.873/29 (U21)	0.873	29	0.873	522	1.39	1.48	1.25	31.1°
ICUMC/0.778/800 (U22)	0.778	800	0.778	1662	1.30	1.43	1.37	34.0°
ICUMC/0.866/101 (U23)	0.866	101	0.866	647	1.15	1.42	1.41	34.9°
ICUMC/0.819/102 (U24)	0.819	102	0.819	661	1.21	1.45	1.45	35.8°
ICUMC/0.763/51 (U25)	0.763	51	0.763	645	1.19	1.53	1.53	37.6°
ICUMC/0.757/102 (U26)	0.757	102	0.757	653	1.27	1.55	1.54	37.7°
ICDMC/0.765/700 (D1)	0.765	700	0.743	1146	1.40	1.43	1.17	29.2°
ICDMC/0.888/500 (D2)	0.888	500	0.891	799	1.34	1.39	1.12	28.2°
ICDMC/0.721/701 (D3)	0.721	701	0.803	1126	1.34	1.54	1.14	28.5°
ICDMC/0.900/20 (D4)	0.900	20	0.974	30	1.27	1.48	0.99	25.2°
ICDMC/0.827/50 (D5)	0.827	50	0.930	89	1.36	1.60	1.29	32.0°
ICDMC/0.882/50 (D6)	0.882	50	0.943	87	1.25	1.47	1.28	31.8°
ICDMC/0.883/100 (D7)	0.883	100	0.921	179	1.27	1.42	1.31	32.6°
ICDMC/0.838/300 (D8)	0.838	300	0.854	536	1.30	1.39	1.32	32.7°
ICDMC/0.847/500 (D9)	0.847	500	0.831	877	1.34	1.31	1.29	32.1°
ICDMC/0.803/100 (D10)	0.803	100	0.894	172	1.23	1.53	1.26	31.4°
ICDMC/0.778/301 (D11)	0.778	301	0.857	529	1.29	1.55	1.30	32.2°
ICDMC/0.809/500 (D12)	0.809	500	0.833	869	1.30	1.40	1.27	31.7°
ICDMC/0.915/200 (D13)	0.915	200	0.916	333	1.32	1.37	1.19	29.9°

[a](1)IC for isotropic consolidation; (2)D for fully drained and U for undrained; (3)MC for monotonic compression; (4)e and (5)p' after consolidation. [b]Post consolidation values; [c]Phase transformation state; [d]Peak stress-ratio state.

Table 7.1: Monotonic triaxial compression tests on batch 1 of Hostun sand conducted by OA at ETH Zurich (reproduced with permission)

in chapter 4 using triaxial monotonic compression tests on different batches of Hostun sand, including batch 1 as shown in figure 7.1. For the tests presented in table 7.1, critical state (CS) was detected from the flattening of excess pore pressure (ΔU) in undrained tests; Tests U1 - U10 reached CS, and flattening of the volumetric strain (ε_v) in drained tests; Tests D1 - D5 reached CS. Equation 7.1 represents the CSL for batch 1 of Hostun sand in terms of void ratio. This form of CSL given in equation 7.1 replaces the power form of CSL proposed by Dafalias and Manzari (2004) (table 3.1) as it better captures the critical state points of Hostun sand.

$$e_{cs} = e_{max} - \frac{(e_{max} - e_{min})R}{Q - ln(p')} \tag{7.1}$$

where e_{cs} = void ratio at critical state; $e_{max} = 1.049$; $e_{min} = 0.671$; $R = 0.73$ and $Q = 8.30$

The critical surface stress ratio in compression, M^c shown in figure 7.2, was determined from the final stress state of the undrained monotonic tests reaching the critical state, Tests U1-U10 in table 7.1. The critical surface strength in extension was obtained using $M_e^c = cM^c$, taking M^c from figure 7.2 and $c = 0.71$ from Azeiteiro et al. (2017).

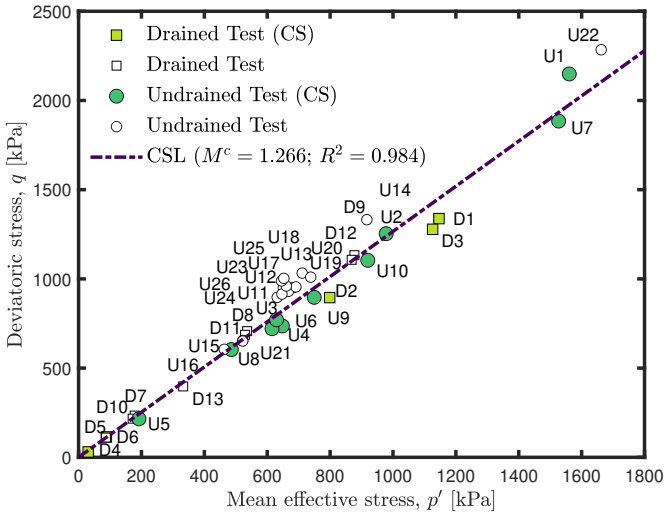

Figure 7.2: Critical surface stress ratio M^c for batch 1 of Hostun sand, refer to table 7.1 for test details

The bounding surface stress ratio, M_c^b in compression and the corresponding state parameter, ψ^b were obtained from the peak stress-ratio states (PSRS) identified at $\eta_{PSRS} = max(q/p')$ of

the undrained monotonic tests in table 7.1. The dilatancy surface stress ratio, M_c^d in compression and the corresponding state parameter, ψ^d were obtained from the phase transformation states (PTS) identified at minimum effective stress (p') points of the undrained monotonic tests in table 7.1. The n^b and n^d parameters were then determined in figure 7.3 using surface evolution laws from table 3.1 and M^c from figure 7.2.

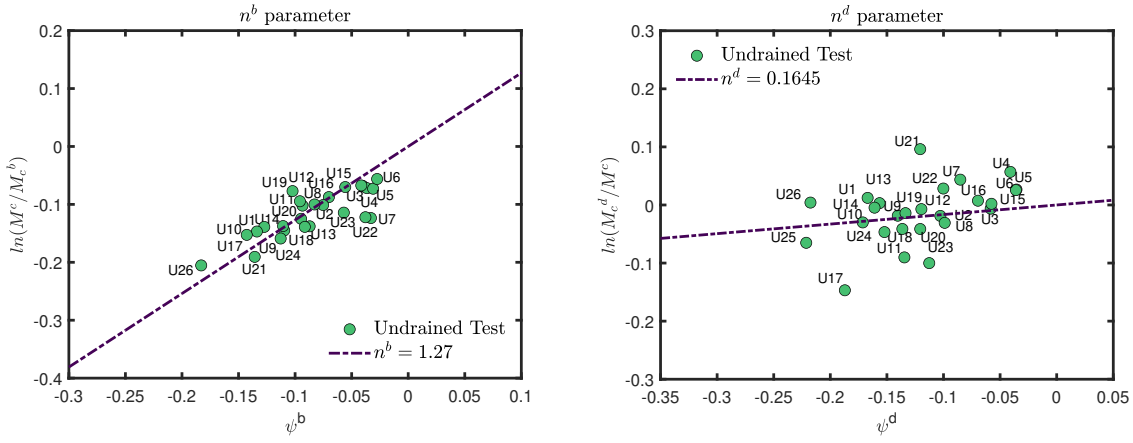

Figure 7.3: Calibration of bounding and dilatancy surface parameters n^b and n^d, respectively, for batch 1 of Hostun sand (refer to table 3.1)

Elastic moduli

The small strain elastic shear modulus G represented by equation 7.2 was detected using bender element tests on triaxial specimens of Hostun sand (batch 1) as described in section 5.4. The elastic bulk modulus K can then be obtained using Poisson's ratio, following the calibration process of equation 7.3 (Dafalias and Manzari, 2004). A Poisson's ratio, ν, value of 0.18 is adopted from Hoque and Tatsuoka (2000), following Azeiteiro et al. (2017). The bulk modulus expression can also be obtained from isotropic unloading tests (Taiebat and Dafalias, 2008). An expression for the elastic bulk modulus of batch 1 of Hostun sand is used in this study that was calibrated from isotropic unloading tests by Adamidis and Anastasopoulos (2022), see equation 7.4.

$$G = G_0\, p_{at} e^{-1.8} \left(\frac{p'}{p_{at}}\right)^{0.5} \quad where \quad G_0 = 530 \tag{7.2}$$

$$K = \frac{2(1+\nu)}{3(1-2\nu)} G \tag{7.3}$$

$$K = K_0\, p_{at} e^{-2} \left(\frac{p'}{p_{at}}\right)^{0.65} \quad where \quad K_0 = 180 \tag{7.4}$$

Fitting parameters

The dilatancy surface parameter, A_0 (refer to table 3.1) was estimated using stress-dilatancy curves obtained from drained monotonic tests of table 7.1 by plotting equation for dilatancy D (as in section 5.4.5). Figure 7.4 shows the estimate of D, expressed as the ratio of plastic strain increments per table 3.1, versus the difference in the dilatancy surface stress ratio M_c^d and current stress ratio η. Plastic strains were calculated by subtracting the elastic strains from the total strains using the definition of the elastic shear modulus (equation 7.2) and the two definitions of the elastic bulk moduli (equations 7.3 and 7.4). Both definitions result in a similar value of $A_0 = 1$.

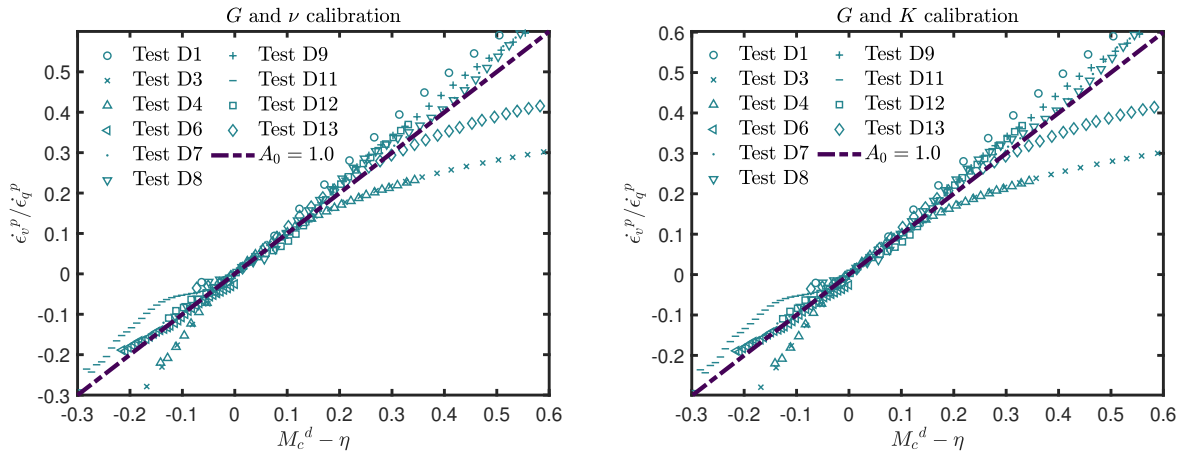

Figure 7.4: Estimation of dilatancy surface parameter A_0 using (a) $G-\nu$ calibration (equations 7.2 and 7.3) and (b) $G-K$ calibration (equations 7.2 and 7.4)

However, this value results in a highly contractive behaviour quickly leading to liquefaction in undrained cyclic tests. To capture the experimentally observed nature of the sand, a lower value of A_0 was estimated by fitting of the undrained monotonic stress paths in $q - p'$ (figure 7.5). This method is adopted from Taiebat et al. (2010) and results in a better approximation of the contraction rate per cycle and of the number of cycles to liquefaction. Parameters h_0 and c_h were estimated using trial-and-error, as shown in figure 7.5. Figure 7.6 presents an example of the exponential relation obtained for the hardening constants, using the combination of G and ν as elasticity parameters. The parameters capturing the effect of the fabric-dilatancy tensor z_{max} and c_z (refer to table 3.1) were determined from the unloading portion of undrained cyclic tests of Adamidis and Anastasopoulos (2022) when the stress ratio, η exceeds the dilatancy surface, $M^d_{c,e}$. The values chosen help eliminate stress locking across all the cyclic tests simulated.

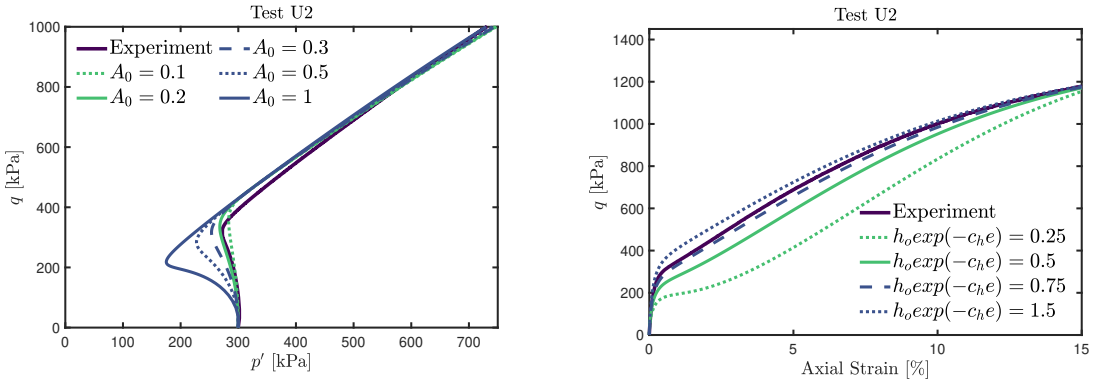

Figure 7.5: Calibration of dilatancy and hardening constants (refer to table 3.1)

Summary of model parameters

A summary of the final parameters for the DM04 model (Dafalias and Manzari, 2004) is listed in table 7.2 and selected/modified model equations are noted in table 7.3, which supersede the corresponding equations of chapter 3. The constants that depend on the choice of bulk modulus expression are noted separately for each option: $G - \nu$ calibration for the bulk modulus computed based on the elastic shear modulus and Poisson's ratio and $G - K$ calibration for the bulk modulus computed from isotropic unloading data.

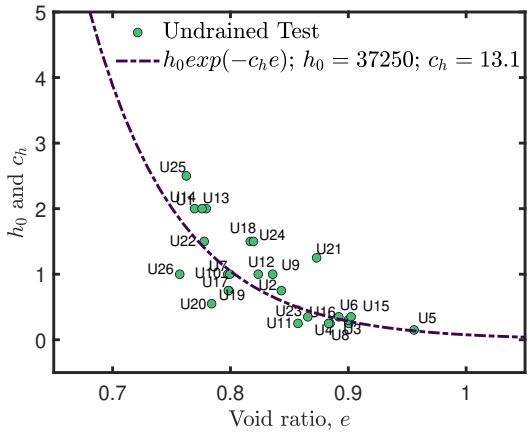

Figure 7.6: Exponential relation for hardening constants (refer to table 3.1)

Parameter	Value	Parameter	$G-\nu$ calibration	$G-K$ calibration
M^c	1.266	$G_0{}^{(2)}$	530	530
c	0.71	$\nu^{(3)}$	0.18	
$Q^{(1)}$	8.3	$K_0{}^{(4)}$		180
$R^{(1)}$	0.73	A_0	0.2	0.2
m	0.01	$h_0{}^{(5)}$	37250	19800
p_{at}	100	$c_h{}^{(5)}$	13.1	12.4
n^b	1.27	z_{max}	20	20
n^d	0.164	c_z	800	800

$^{(1)}$Implemented in CSL equation 7.1; $^{(2)}$Implemented in equation 7.2; $^{(3)}$Implemented in equation 7.3; $^{(4)}$Implemented in equation 7.4; $^{(5)}$Exponential function used, see section 7.2.1; refer to table 7.3 for model equations.

Table 7.2: Summary of DM04 model constants for batch 1 of Hostun sand

Equations	**Model Constants**	**Description**
Critical State Line:		
$e_{cs} = e_{max} - \frac{(e_{max}-e_{min})R}{Q-ln(p')}$	e_{max} , e_{min} , Q , R	Equation 7.1
Elasticity:		p_{at} : 100 kPa
$G = G_0\ p_{at} e^{-1.8}(\frac{p'}{p_{at}})^{0.5}$	G_0	Equation 7.2
$K = \frac{2(1+\nu)}{3(1-2\nu)}G$	ν	$G-\nu$ calibration, Equation 7.3
$K = K_0\ p_{at} e^{-2}(\frac{p'}{p_{at}})^{0.65}$	K_0	$G-K$ calibration, Equation 7.4
Hardening Rule:		
$b_0 = G_0 h_0 exp(-c_h e)(p'/p_{at})^{-1/2}$	h_0 , c_h	Exponential evolution of b_0

Table 7.3: Selected/modified equations for DM04 model to be used in conjunction with model parameters of table 7.2, refer to table 3.1 for the remaining equations

7.2.2 SANISAND-MSf model parameters

The SANISAND-MSf model by M. Yang et al. (2022) is described in detail in section 3.4 and the governing equations are listed in table 3.3. The DM04 model surface parameters and elastic moduli determined in section 7.2.1 and the critical state line of equation 7.1 are applicable to the SANISAND-MSf model. The dilatancy surface parameter, A_0 (or $A_0{}'$ per table 3.3) as determined in figure 7.4, can be used in this model as the model has new ingredients to mitigate the increased contractive behaviour observed in the DM04 model. The calibration of the remaining fitting parameters, memory surface parameters and semifluidised state parameters are discussed below.

Fitting parameters

With dilatancy constant $A_0 = 1$, the hardening constants h_0 (or $h_0{}'$ per table 3.3) and c_h were estimated in figure 7.7 from trial-and-error for both the elastic parameter combinations. The parameters capturing the effect of the fabric-dilatancy tensor z_{max} and c_z (refer to table 3.3) are the same as the DM04 model (section 7.2.1).

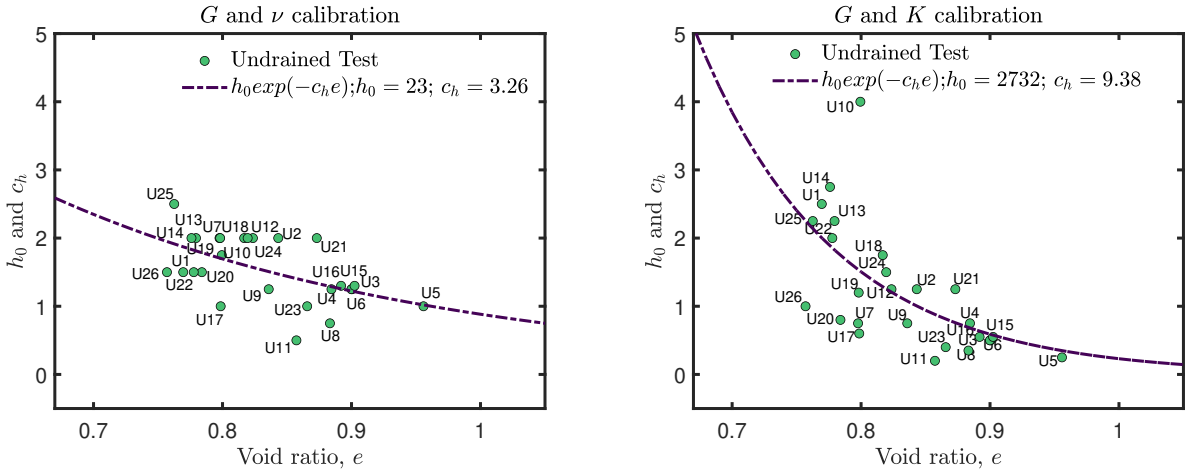

Figure 7.7: Estimation of hardening constants for (a) $G-\nu$ calibration (equations 7.2 and 7.3) and (b) $G-K$ calibration (equations 7.2 and 7.4)

Memory surface parameters

The two parameters required to define the memory surface are calibrated from the undrained liquefaction strength curves. Using the model parameters estimated in the prior sections, and starting values of μ_0 and u taken from M. Yang et al. (2022), the undrained cyclic tests from Adamidis and Anastasopoulos (2022) were simulated. Parameter n_g in table 3.3 was estimated from the stress-strain paths of the undrained cyclic tests of Adamidis and Anastasopoulos (2022) to capture the asymmetrical stress-strain accumulation. The liquefaction resistance curves were plotted next. Parameter μ_0 was adjusted to fit the number of cycles to liquefaction in the experiments for the higher CSR ($= q_{max}/2p_{in}{}'$) experiments and parameter u was adjusted to match the cycles to liquefaction for the lower CSR experiments and match the overall slope of the liquefaction resistance curves to the experimental curves. These parameters were determined for both the elastic bulk modulus calibration techniques.

Semifluidised state parameters

The threshold value of mean effective stress at which the semifluidised state is triggered was maintained at the default value of 10 kPa as it matched the stress cycles close to $p' = 0$ in the undrained cyclic tests of Adamidis and Anastasopoulos (2022), for both the calibration methods of elastic bulk modulus. Next, the deviatoric strain was plotted against the number of cycles. The value of x was determined through trial-and-error to match the maximum shear strain amplitudes. The value of c_l was then adjusted to capture the pace of shear strain accumulation.

Summary of model parameters

A summary of the final parameters for the SANISAND-MSf model (M. Yang et al., 2022) is listed in table 7.4. The constants that depend on the choice of bulk modulus expression are noted separately for each option. Equations updated from those listed in chapter 3 are given in table 7.5.

Parameter	Value	Parameter	$G-\nu$ calibration	$G-K$ calibration
M^c	1.266	$G_0{}^{(2)}$	530	530
c	0.71	$\nu^{(3)}$	0.18	
$Q^{(1)}$	8.3	$K_0{}^{(4)}$		180
$R^{(1)}$	0.73	A_0	1.0	1.0
m	0.01	$h_0{}^{(5)}$	23	2732
p_{at}	100	$c_h{}^{(5)}$	3.26	9.38
n^b	1.27	μ_0	10.3	0.835
n^d	0.164	u	0.9	2.85
z_{max}	20	c_l	50	35
c_z	800	x	10	2.2
n_g	0.95	p_{th}	10	10

$^{(1)}$Implemented in CSL equation 7.1; $^{(2)}$Implemented in equation 7.2; $^{(3)}$Implemented in equation 7.3; $^{(4)}$Implemented in equation 7.4; $^{(5)}$Exponential function used, see section 7.2.1; refer to table 7.5 for model equations.

Table 7.4: Summary of SANISAND-MSf model constants for batch 1 of Hostun sand

Equations	Model Constants	Description
Critical State Line:		
$e_{cs} = e_{max} - \frac{(e_{max}-e_{min})R}{Q-ln(p')}$	e_{max} , e_{min} , Q , R	Equation 7.1
Elasticity:		p_{at} : 100 kPa
$G = G_0\ p_{at} e^{-1.8}(\frac{p'}{p_{at}})^{0.5}$	G_0	Equation 7.2
$K = \frac{2(1+\nu)}{3(1-2\nu)}G$	ν	$G-\nu$ calibration, Equation 7.3
$K = K_0\ p_{at} e^{-2}(\frac{p'}{p_{at}})^{0.65}$	K_0	$G-K$ calibration, Equation 7.4
Hardening Rule:		
$b_0 = G_0 h_0 g^{-n_g} exp(-c_h e)(p'/p_{at})^{-1/2}$	h_0 , c_h, n_g	Exponential evolution of b_0

Table 7.5: Selected/modified equations for SANISAND-MSf model to be used in conjunction with model parameters of table 7.4, refer to table 3.3 for the remaining equations

7.2.3 PM4Sand3D model parameters

The PM4Sand3D model by Kippen et al. (2026) is described in detail in section 3.5 and the governing equations are listed in table 3.4. The PM4Sand3D model requires only three primary input parameters. The remaining secondary input parameters are derived from the primary input parameters through relations included in the model.

Primary input parameters

The primary input parameters include the apparent relative density D_r, the shear modulus coefficient G_0 and the contraction rate parameter h_{po}. The properties of batch 1 of Hostun sand used in the reference experiments were provided by Adamidis and Anastasopoulos (2022). Using the void ratio range, e_{max} and e_{min}, the relative density was determined for the experiments from void ratio data e per equation 7.5, also noted in table 3.4. For the undrained monotonic and cyclic tests, this value of density remained constant. However, for the non-standard drained tests simulated in later sections, this value varied with change in void ratio. Hence, the initial relative density D_{ro} was defined from the initial void ratio e_0 per equation 7.5, which was used to define secondary input parameters, as described later. Using the relative density values, the relative state parameter ξ_R was defined from equation 7.6, also noted in table 3.4 and similarly ξ_{Ro} was defined from D_{ro}.

$$D_r = \frac{e_{max} - e}{e_{max} - e_{min}} \tag{7.5}$$

$$\xi_R = D_{r,cs} - D_r \tag{7.6}$$

The shear and bulk modulus are defined per elasticity equations noted in table 3.4. The shear modulus coefficient G_0 is expressed as a function of the CPT or SPT penetration resistances which is indirectly a measure of the density. For the Hostun sand used, the small-strain shear modulus was obtained from bender elements as shown in equation 7.2, which includes a direct dependence on the void ratio. Using equation 7.2, the shear modulus expression for PM4Sand3D model is recast in equation 7.7 for Hostun sand to incorporate the density dependency in the G_0 parameter. Using the typical calibration of bulk modulus, K was defined in equation 7.3 using $\nu = 0.18$ per Hoque and Tatsuoka (2000), following Azeiteiro et al. (2017). For the direct calibration of K from isotropic unloading data, equation 7.4 was modified to equation 7.8 to include the stress ratio and fabric history terms, similarly to the shear modulus.

$$G = G_0 p_{at} \left(\frac{p'}{p_{at}} \right)^{0.5} C_{SR} \left(\frac{1 + \frac{z_{cum}}{z_{max}}}{1 + \frac{z_{cum}}{z_{max}} C_{GD}} \right) \quad where \quad G_0 = 530e^{-1.8} \tag{7.7}$$

$$K = K_0 p_{at} \left(\frac{p'}{p_{at}} \right)^{0.65} C_{SR} \left(\frac{1 + \frac{z_{cum}}{z_{max}}}{1 + \frac{z_{cum}}{z_{max}} C_{GD}} \right) \quad where \quad K_0 = 180e^{-2} \tag{7.8}$$

The contraction rate parameter h_{po} was determined from the target cyclic resistance ratio. Hence, this parameter was adjusted as the final step in undrained cyclic test simulations. For the monotonic tests, a starting value of $h_{po} = 0.2$ was taken from the example simulations in the PM4Sand3D manual (Kippen et al., 2026) and no further adjustment was needed. However, once the h_{po} values were calibrated based on the undrained liquefaction resistance curves, the monotonic simulations were repeated. The atmospheric pressure was taken as $p_{at} = 100$ kPa for the elastic moduli definitions of Hostun sand (equations 7.7 and 7.8) and also for the relative state parameter index given by equation 7.6.

Secondary input parameters

In this section, the secondary input parameters that were modified from their default values to simulate the tests on Hostun sand are discussed. The remaining parameters are summarised in the following section. The maximum and minimum void ratio values and the critical state line parameters Q and R were modified to follow the Hostun sand values given in equation 7.1, determined in section 7.2.1. The critical state friction angle (ϕ_{cs}') was modified from the default value of 33° to 31.5° to give a value of $M^c = 1.266$ ($M^c = \frac{6sin\phi_{cs}'}{3-sin\phi_{cs}'}$) as determined from figure 7.2.

Summary of model parameters

A summary of the final input parameters for the PM4Sand3D model (Kippen et al., 2026) is listed in table 7.6 and the selected/modified model equations are noted in table 7.7. The primary input parameters are listed in the first two rows, each row representing the type of calibration

method, (1) $G-\nu$ calibration and (2) $G-K$ calibration, respectively. The secondary input parameters listed thereafter are applicable to both the calibration methods. Equations updated from those listed in chapter 3 are given in table 7.7.

Parameter	Value	Parameter	Value	Parameter	Value
${G_0}^{(1)}$	$530e^{-1.8}$	${\nu}^{(1)}$	0.18	${h_{po}}^{(1)}$	0.038
${G_0}^{(2)}$	$530e^{-1.8}$	${K_0}^{(2)}$	$180e^{-2}$	${h_{po}}^{(2)}$	0.011
M^c	1.266	h_o	$max[0.3,(0.25+D_r)/2]$	c	0.9-0.15M^c
n^b	0.5	A_{do}	$3.125\frac{\left[\sin^{-1}\left(\frac{3M^{bo}}{6+M^{bo}}\right)-\sin^{-1}\left(\frac{3M^c}{6+M^c}\right)\right]}{(M^{bo}-M^{do})}$	M^{bo}	$M^c exp(-n^b\xi_{Ro})$
n^d	0.1	z_{max}	$min[0.7\cdot exp(-6.1\cdot\xi_{Ro}),20]$	M^{do}	$M^c exp(n^d\xi_{Ro})$
Q	8.3	n_g	$min[0.5(2.35-D_{ro}),1]$	C_{GD}	2
R	0.73	$C_{K\alpha f}$	$1+600\cdot(D_{ro}-0.37)^3\in[3.0;50.0]$	C_{rev}	1
e_{max}	1.049	C_ε	$max[50\cdot exp[-11.5(D_{ro}-0.35)],0.3]$	$C_{\gamma 1}$	$h_o/200$
e_{min}	0.671	c_z	$100+750(D_{ro}-0.35)\in[100;400]$	C_{Kp}	$\sqrt{2}$
m	0.01	C_{DR}	$min[5+25(D_{ro}-0.35),10]$	C_D	0.1
p_{at}	100	h_p	$h_{po}\cdot exp(0.9+6.1\langle 0.5-\xi_R\rangle^{2.1})$	p_{min}	$p'_{in}/200$
				p_{min2}	$p'_{in}/20$

$^{(1)}G-\nu$ calibration (equations 7.7 and 7.3); $^{(2)}G-K$ calibration (equations 7.7 and 7.8); refer to table 7.7 for model equations.

Table 7.6: Summary of PM4Sand3D model constants for batch 1 of Hostun sand

Equations	Model Constants	Description
Elasticity:		
$G=G_0p_{at}\left(\frac{p'}{p_{at}}\right)^{0.5}C_{SR}\left(\frac{1+\frac{z_{cum}}{z_{max}}}{1+\frac{z_{cum}}{z_{max}}C_{GD}}\right)$	G_0	Equation 7.7
$K=\frac{2(1+\nu)}{3(1-2\nu)}G$	ν	$G-\nu$ calibration, Equation 7.3
$K=K_0p_{at}\left(\frac{p'}{p_{at}}\right)^{0.65}C_{SR}\left(\frac{1+\frac{z_{cum}}{z_{max}}}{1+\frac{z_{cum}}{z_{max}}C_{GD}}\right)$	K_0	$G-K$ calibration, Equation 7.8

Table 7.7: Selected/modified equations for PM4Sand3D model to be used in conjunction with model parameters of table 7.6, refer to table 3.4 for the remaining equations

7.3 Model performance

The constitutive models were numerically implemented in MATLAB using the forward Euler method for integration of strain-controlled loading steps. In this integration scheme, the increment of strain can significantly impact the simulation results. For all models, a strain increment

of 1×10^{-6} or lower was used, which ensured convergence. The monotonic triaxial tests on batch 1 of Hostun sand from table 7.1 were simulated using each of the three constitutive models and the two calibration methods for the bulk modulus. Next, undrained cyclic triaxial tests on batch 1 of Hostun sand from Adamidis and Anastasopoulos (2022) were simulated followed by volumetric expansion cyclic triaxial tests. Each model's performance was evaluated through comparison with experimental results.

7.3.1 Undrained monotonic triaxial test simulations

Using the model parameters from tables 7.2, 7.4 and 7.6, the undrained monotonic tests listed in table 7.1 were simulated for the DM04, SANISAND-MSf and PM4Sand3D models, respectively. Figures 7.8 and 7.9 show the simulation results for undrained test $ICUMC/0.843/300$ (Test U2) for all three models corresponding to $G-\nu$ and $G-K$ calibrations, respectively.

For the typical $G-\nu$ calibration scheme, the DM04 model produced the best prediction out of all three models (see figure 7.8(a)), followed by the PM4Sand3D model (see figure 7.8(c)). Note that the only difference between the DM04 model parameters and the SANISAND-MSf model parameters was in the choice of the dilatancy constant A_0 and the corresponding hardening constants. With the exact same model parameters, both DM04 and SANISAND-MSf models are expected to produce the exact same monotonic behaviour. The DM04 model parameter A_0 had to be lowered from the actual value of 1.0 obtained from stress-dilatancy data of drained tests to match the rate of contraction observed in the cyclic tests. The actual value of $A_0 = 1.0$ was retained in the SANISAND-MSf model as the contraction rate could be controlled using the memory surface parameters. The over-estimation of the shear stiffness observed in figure 7.8(b), which was obtained with a shear modulus expression calibrated from small-strain bender element tests (G_{max}) and remaining parameters calibrated per Dafalias and Manzari (2004), have been reported previously by Andrianopoulos et al. (2010) and Papadimitriou et al. (2001, 2023). For monotonic tests, a value of $G_{max}/4$ to $G_{max}/2$ for the shear modulus, obtained from the initial stages of the stress-strain response of monotonic loading, is typically suggested to overcome

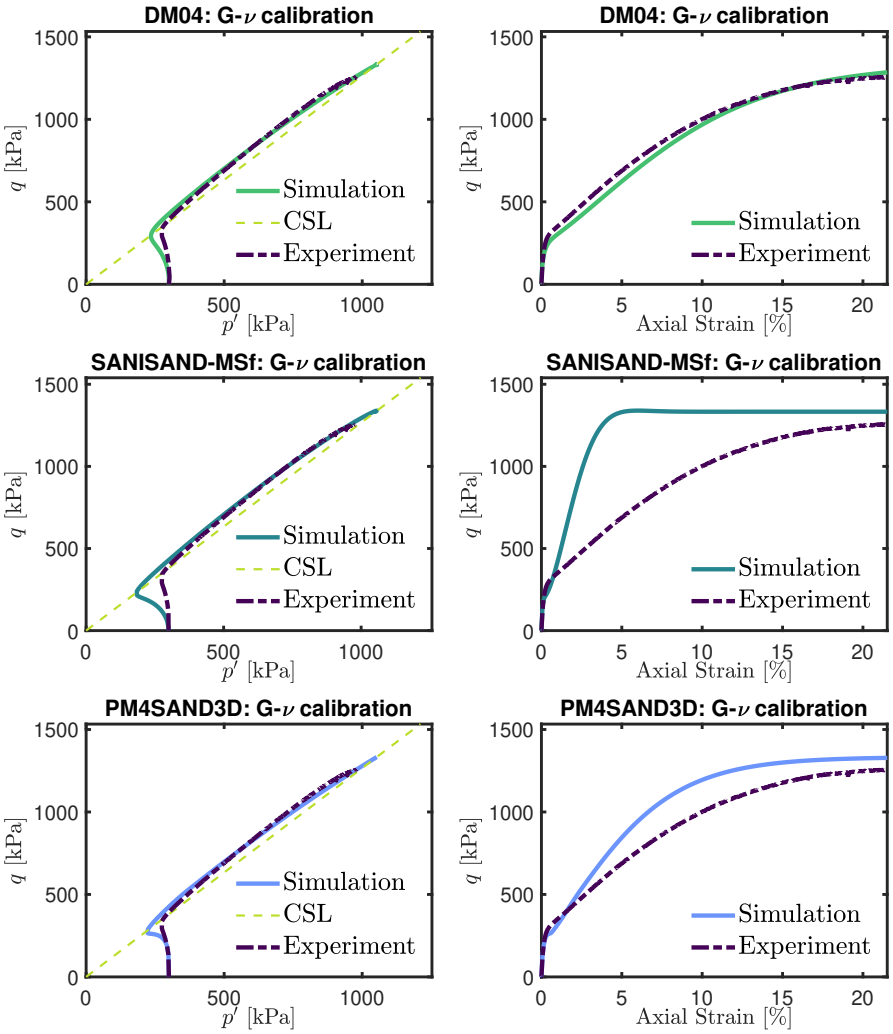

Figure 7.8: Simulations of undrained monotonic triaxial test ICUMC/0.843/300 (Test U2) on Hostun sand for $G-\nu$ calibration of (a) DM04 model, (b) SANISAND-MSf model and (c) PM4Sand3D model and comparison with experimental data from table 7.1

this issue and such an estimate yields reasonable response in large strain problems. Nevertheless, the goal of this study is to use these constitutive models for dynamic boundary value problems for which the small-strain stiffness G_{max} must be maintained to obtain reasonable soil dynamic response across small to large strain levels (Darvishi et al., 2022; Papadimitriou et al., 2023; Zeng et al., 2024).

With the $G-K$ calibration scheme, the SANISAND-MSf model produced the best estimate of monotonic behaviour (see figure 7.9(b)). Such a prediction could be obtained with the DM04 model if the dilatancy constant A_0 was chosen per the stress-dilatancy data as explained earlier.

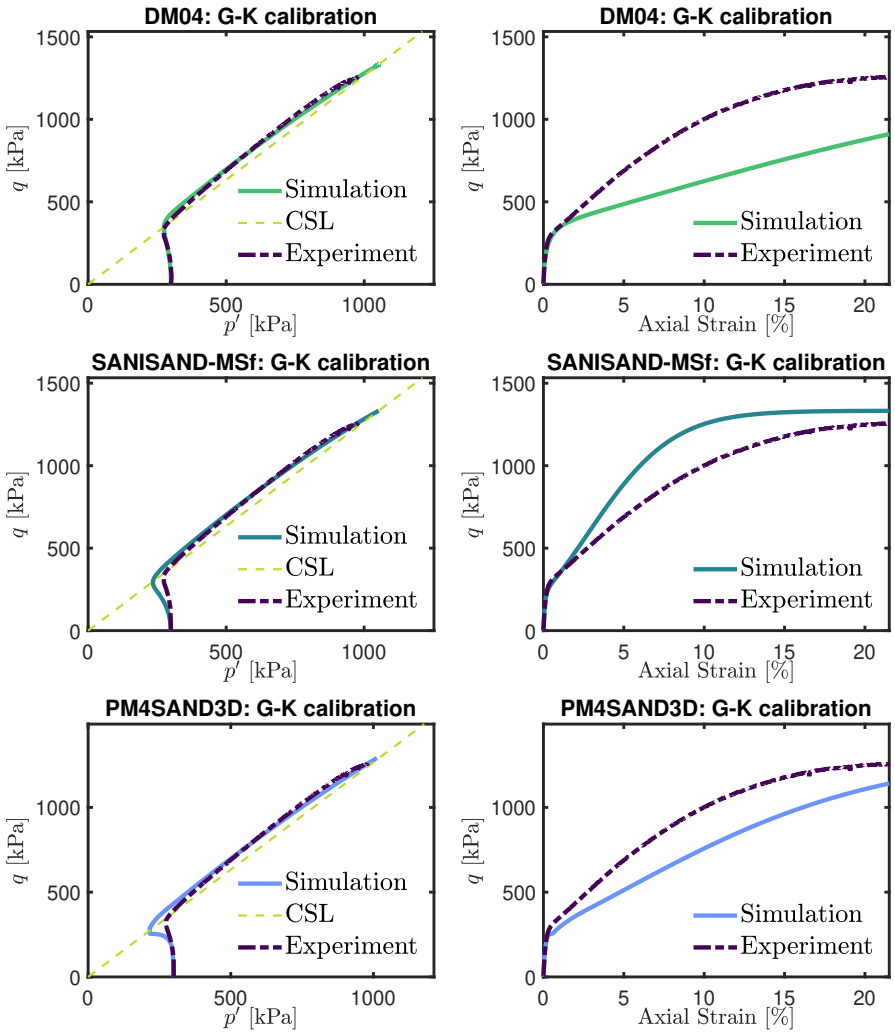

Figure 7.9: Simulations of undrained monotonic triaxial test ICUMC/0.843/300 (Test U2) on Hostun sand for $G-K$ calibration of (a) DM04 model, (b) SANISAND-MSf model and (c) PM4Sand3D model and comparison with experimental data from table 7.1

The calibration of stiffness from the isotropic unloading data gives a softer bulk modulus expression, equation 7.4 or 7.8, than the traditional use of G and ν to obtain K, equation 7.3. The use of a softer bulk modulus leads to a slower progression of the hardening modulus and the maximum strength is attained after accumulation of larger strains, as seen in figures 7.9(a) and 7.9(c). Figure 7.9(b) also exemplifies that monotonic behaviour may be better simulated with the small-strain bender element shear modulus G_{max} and bulk modulus K calibrated from isotropic unloading data, than with the combination of G_{max} and ν to get K from the typical calibration process in SANISAND-type models, thereby eliminating the need for arbitrary modifications to

G_{max} or the dilatancy constant A_0 in order to produce an adequate monotonic response.

The PM4Sand3D model has equations that are calibrated using the traditional $G-\nu$ calibration technique and therefore would require re-adjustments to the inbuilt expressions so as to improve the monotonic predictions using a softer bulk modulus from the $G-K$ calibration (figure 7.9(c)).

Note that the combination of G_{max} and K implies an effective Poisson's ratio (ν) that becomes negative over part of the investigated stress range. The negative ν arises because the two elastic moduli are calibrated independently, with G_{max} corresponding to small-strain and K to large-strain behaviour, before being combined within a hypoelastic framework. The examined models include a very small elastic zone in shearing, before plasticity takes hold, thus justifying the use of a small-strain shear modulus. On the contrary, elasticity persists at large strains under constant stress-ratio loading, necessitating the use of a large-strain bulk modulus. Overall, the used moduli should be interpreted as effective values tailored to the examined constitutive models, rather than as consistently defined stiffness moduli for an actual linear-elastic material. Hyperelastic formulations (Houlsby et al., 2019) that provide a thermodynamically consistent treatment of elasticity could be advantageous in that regard, though it is possible that more drastic changes of the constitutive framework are needed, engaging plasticity under constant stress-ratio loading. Investigation of such alternative formulations are outside the scope of the present study.

7.3.2 Undrained cyclic triaxial test simulations

The cyclic triaxial tests conducted on batch 1 of Hostun sand from Adamidis and Anastasopoulos (2022) were used for the simulations in this study. These tests pertain to an initial density of the samples in the range of medium to dense ($40\pm2\%$ to $66\pm3\%$). The two expressions for the bulk modulus were implemented in each of the three models and compared with experimental data. One experimental test simulation corresponding to $D_r = 55\pm2\%$ is presented using the DM04, the SANISAND-MSf and the PM4Sand3D models in figures 7.10, 7.11 and 7.12, respectively.

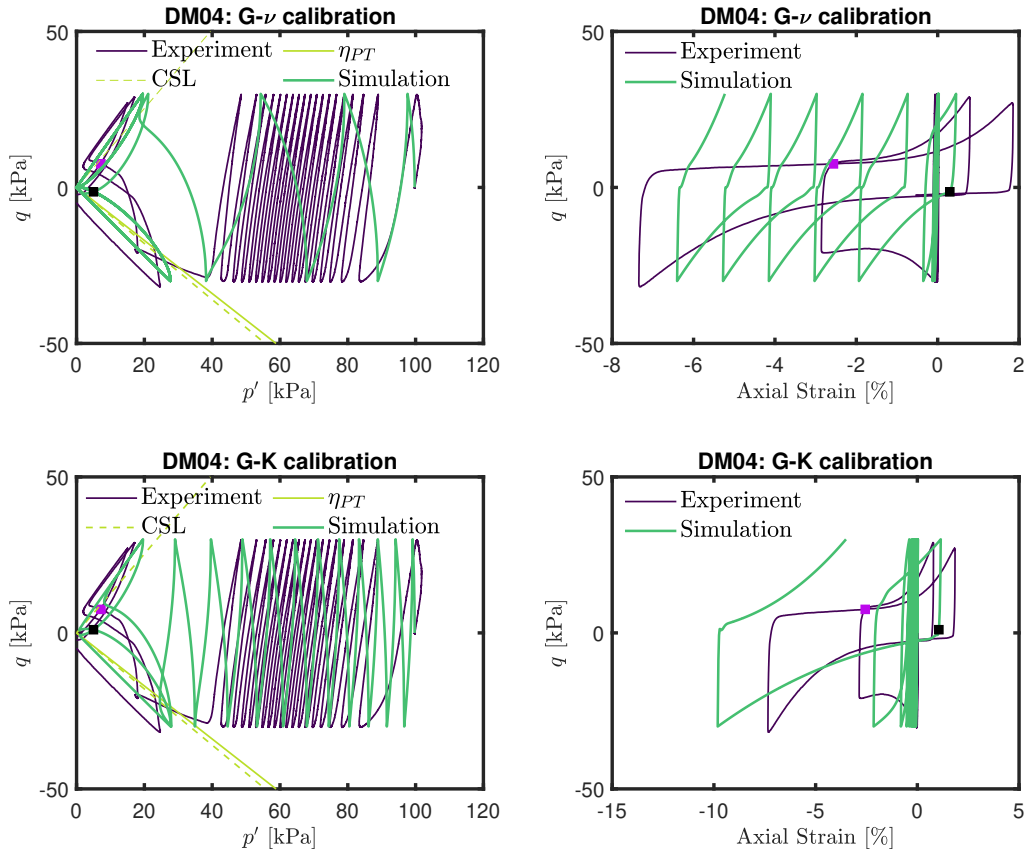

Figure 7.10: Simulation of undrained cyclic triaxial test ICT55/100/30/0 (Adamidis and Anastasopoulos, 2022) using (a) $G-\nu$ and (b) $G-K$ calibration of DM04 model; square markers indicate onset of liquefaction

The $q-p'$ plots in figures 7.10-7.12 show that simulations using the two calibration techniques for all three models captured the general undrained cyclic behaviour well. When crossing the instability line in monotonic extension, significant contraction is noted, increasing the excess pore pressures. After the phase transformation line (η_{PTS}) in extension is crossed, dilation leads to a decrease in excess pore pressures. Following which, significant excess pore pressures are generated upon loading reversal, that push the stress path towards vanishing p'. The formation of butterfly loops close to the origin is well captured. As expected, the softer bulk modulus case results in reduced contraction rates, increasing the number of cycles required to trigger liquefaction. The $q-\varepsilon_1$ plots in figures 7.10-7.12 show the accumulation of axial strains with each cycle. For the DM04 model (figure 7.10), the strain per cycle was much larger in extension

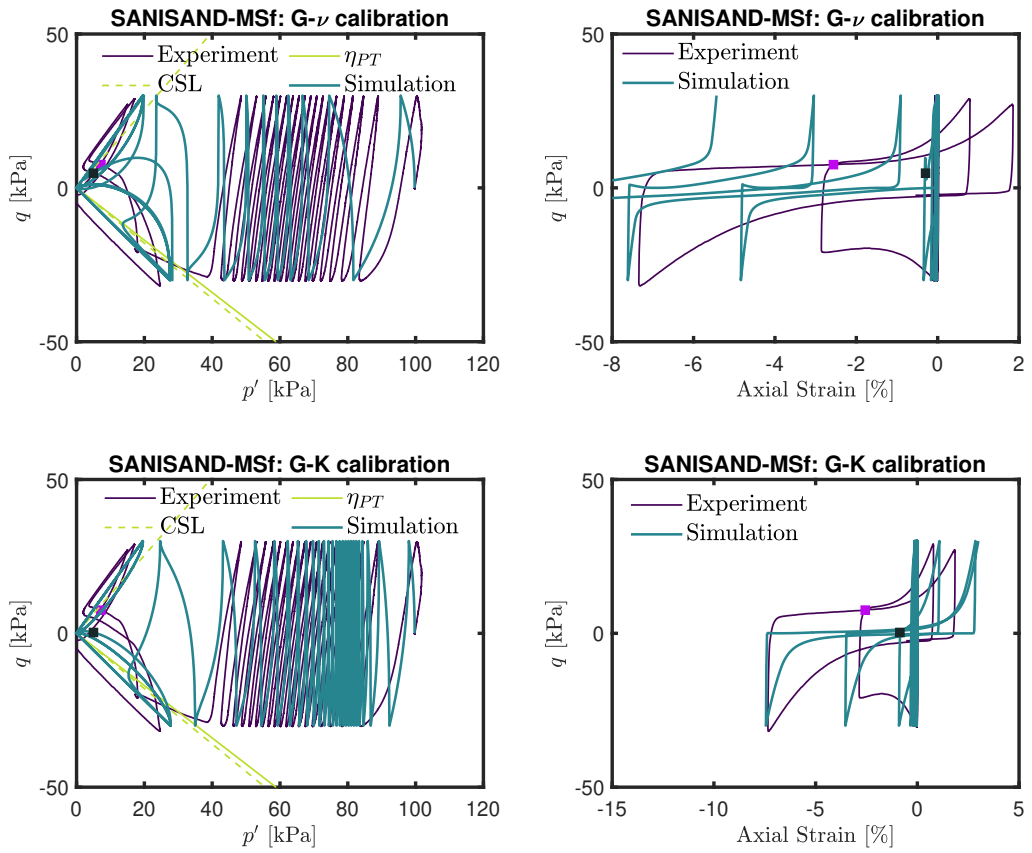

Figure 7.11: Simulation of undrained cyclic triaxial test ICT55/100/30/0 (Adamidis and Anastasopoulos, 2022) using (a) $G-\nu$ and (b) $G-K$ calibration of SANISAND-MSf model; square markers indicate onset of liquefaction

than in compression, leading to the accumulation of extension strains, that become smaller than the experimental values for the $G-\nu$ calibration and larger for the $G-K$ calibration. For the SANISAND-MSf model (figure 7.11), the $G-\nu$ calibration led to faster accumulation of axial strain with smaller strain amplitude cycles. With the $G-K$ calibration, the strain accumulation progresses slower with number of cycles but the cyclic strain amplitudes rapidly increase mimicking the experimental behaviour in a better way. The performance of PM4Sand3D model with both calibration techniques was very similar (see $q-p'$ plots in figure 7.12). The strain accumulation with number of cycles are larger than experimental values, with the $G-\nu$ calibration resulting in lower strain amplitude than the $G-K$ calibration. Overall, a realistic bulk modulus assumption slowed down the accumulation of excess pore pressure and axial strain with

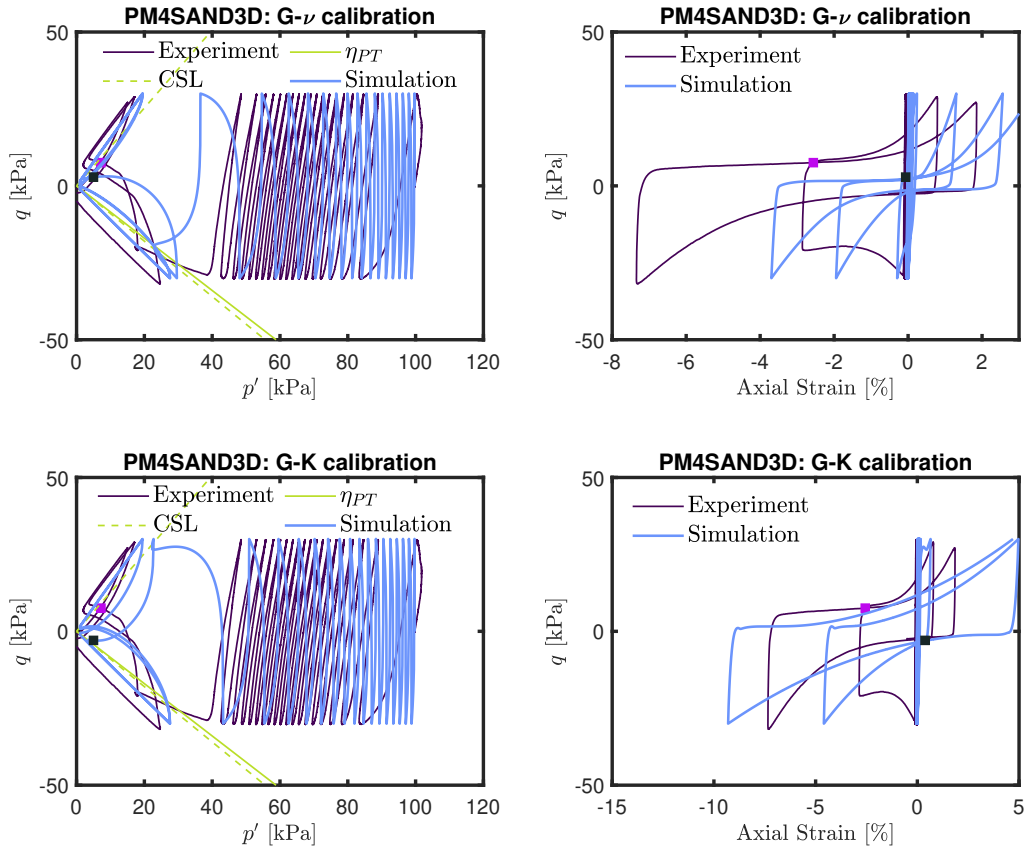

Figure 7.12: Simulation of undrained cyclic triaxial test ICT55/100/30/0 (Adamidis and Anastasopoulos, 2022) using (a) $G-\nu$ and (b) $G-K$ calibration of PM4Sand3D model; square markers indicate onset of liquefaction

subsequent loading cycles, as compared to typical $G-\nu$ calibration of bulk modulus.

Detailed progression of excess pore pressure (ΔU) with number of cycles normalized by the number cycles to liquefaction (N/N_{ult}) is shown in figures 7.13-7.15 for the undrained cyclic tests simulated before, using each of the three models. The SANISAND-MSf model was able to capture the trend of excess pore pressure accumulation better using both calibration methods (figure 7.14). The model features new constitutive ingredients and allows direct calibration of parameters from damage curves, which has led to a significant improvement in predictions from the base DM04 model (figure 7.13). Liquefaction was detected when the excess pore pressure ratio, $R_u = 95\%$, the number of cycles to which is denoted by N_{R_u} and indicated by solid square markers in figures 7.10-7.15. The number of cycles to double amplitude of axial

strain, $\varepsilon_{1,DA} = 5\%$ was also studied and the predictions were compared with experiments, shown in figures 7.13-7.15, denoted by N_{ε_1} and indicated by solid circles. As observed before, the softer bulk modulus delays the accumulation of axial strain but magnifies the strain amplitudes. The PM4Sand3D model was able to capture the formation of stress-strain loops better (figure 7.15) followed closely by the SANISAND-MSf model (figure 7.14), due to their improved simulative capacity as compared to the base DM04 model (figure 7.13).

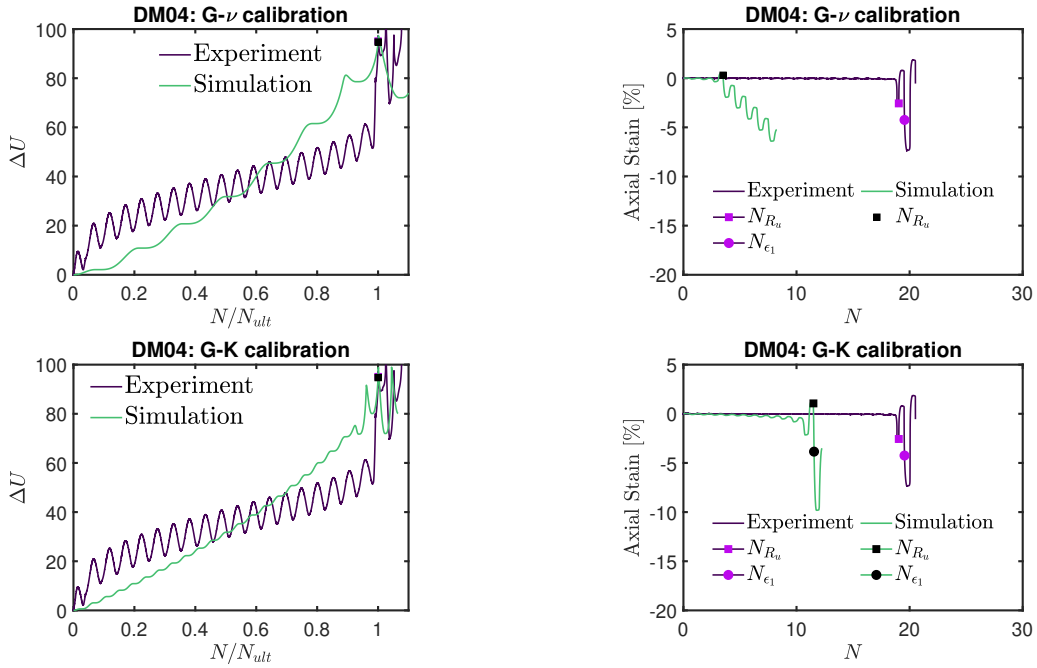

Figure 7.13: Progression of excess pore pressure and axial strain for undrained cyclic triaxial test ICT55/100/30/0 (Adamidis and Anastasopoulos, 2022) using (a) $G-\nu$ and (b) $G-K$ calibration of DM04 model

Test details with cycles to liquefaction (N_{R_u} and N_{ε_1}) for the undrained cyclic experiments and simulations using the two bulk modulus calibration parameters for the DM04 model, SANISAND-MSf model and PM4Sand3D model are listed in tables 7.8, 7.9 and 7.10, respectively. As seen from the N_{R_u} and N_{ε_1} values, the $G-\nu$ calibration produces steeper liquefaction strength curves than the $G-K$ calibration for the DM04 and SANISAND-MSf models. Additionally, for the DM04 model, the $G-\nu$ calibration predicts smaller strain amplitudes with growing cycles leading to double strain amplitudes never reaching 5% for all the experiments. On the contrary, the PM4Sand3D model can be calibrated to produce liquefaction strength curves having similar

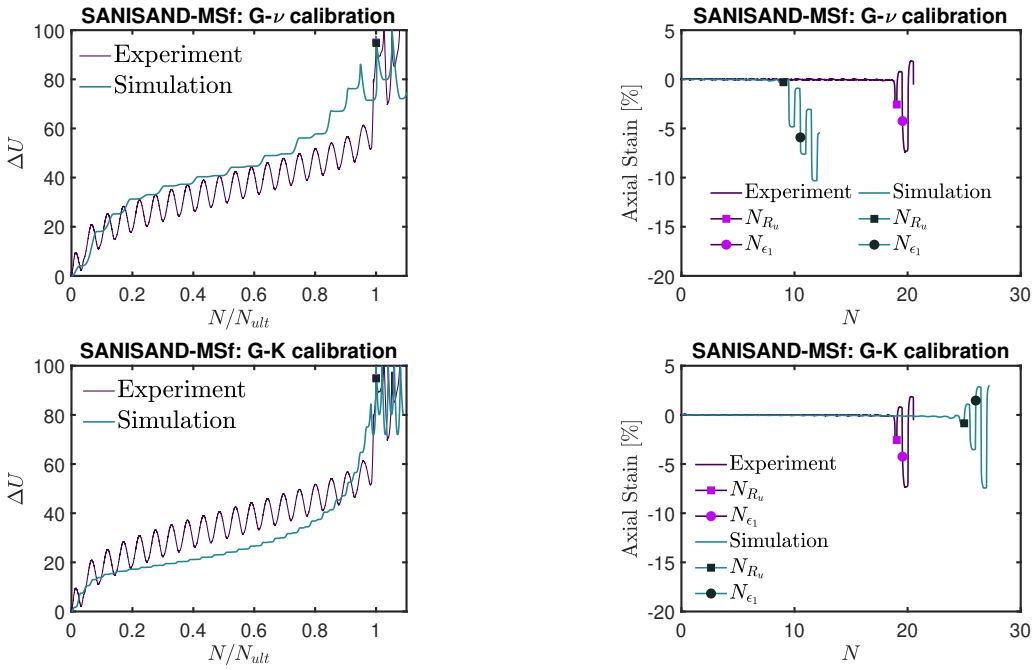

Figure 7.14: Progression of excess pore pressure and axial strain for undrained cyclic triaxial test ICT55/100/30/0 (Adamidis and Anastasopoulos, 2022) using (a) $G-\nu$ and (b) $G-K$ calibration of SANISAND-MSf model

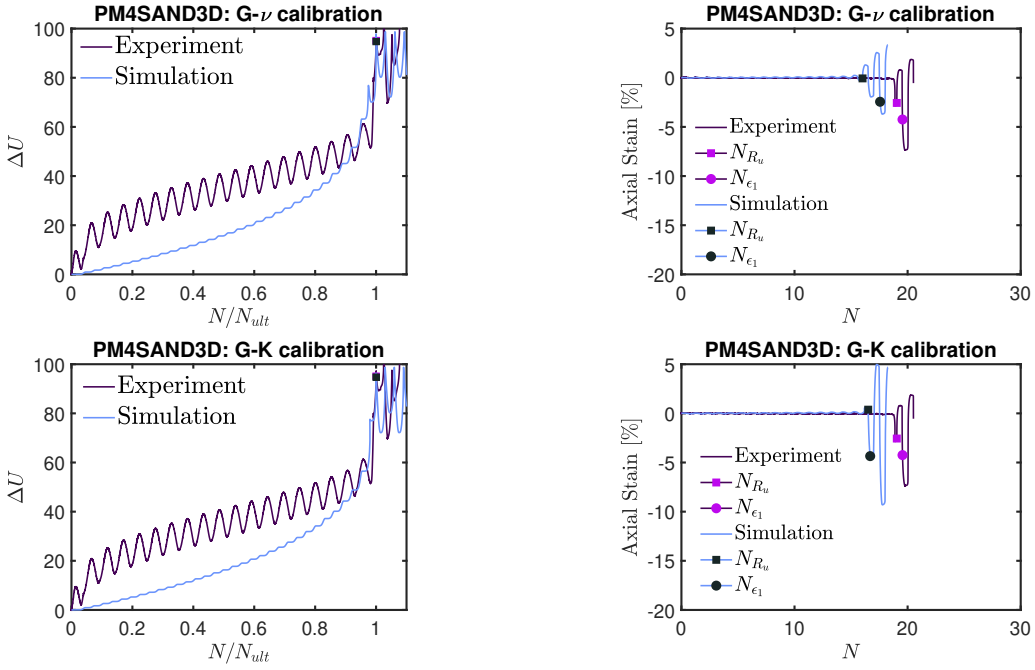

Figure 7.15: Progression of excess pore pressure and axial strain for undrained cyclic triaxial test ICT55/100/30/0 (Adamidis and Anastasopoulos, 2022) using (a) $G-\nu$ and (b) $G-K$ calibration of PM4Sand3D model

slopes for both the bulk modulus definitions. Progressive strain accumulation is also very similar as indicated by the N_{ε_1} values of table 7.10.

Test ID	CSR	$N_{R_u}{}^{(a)}$	$N_{R_u}{}^{(b)}$	$N_{R_u}{}^{(c)}$	$N_{\varepsilon_1}{}^{(a)}$	$N_{\varepsilon_1}{}^{(b)}$	$N_{\varepsilon_1}{}^{(c)}$
$ICT65/100/28/0$	0.14	144	8	25	-	-	26.7
$ICT65/100/30/0$	0.15	42.5	6	19	-	-	19.6
$ICT65/100/30/0$	0.15	77.1	6	19	-	-	19.6
$ICT65/100/36/0$	0.18	6	5	15.5	7.7	-	15.7
$ICT65/100/39/0$	0.20	3.5	4	11.5	4.6	-	11.6
$ICT65/100/40/0$	0.20	4	3.5	10.5	5.1	-	10.6
$ICT55/100/25/0$	0.12	70	6	19	71.2	-	19.6
$ICT55/100/30/0$	0.15	19	3.5	11.5	19.5	-	11.6
$ICT55/100/34/0$	0.17	4.5	3	9.5	4.6	-	9.6
$ICT40/100/19/0$	0.10	197	5	17	197.6	-	17.1
$ICT40/100/20/0$	0.10	98.1	4	14	99.5	-	14.1
$ICT40/100/23/0$	0.11	28.5	3	10	28.6	-	10.1
$ICT40/100/28/0$	0.14	8	2.5	8	8.1	-	8.1
$ICT40/100/30/0$	0.15	6	2	6.5	6.2	-	6.5
$ICT40/100/33/0$	0.16	2	1.5	5	2	-	5.1

$^{(a)}$Undrained cyclic triaxial tests from Adamidis and Anastasopoulos (2022);
$^{(b)}G-\nu$ calibration (equations 7.2 and 7.3); $^{(c)}G-K$ calibration (equations 7.2 and 7.4).

Table 7.8: Comparison of N_{R_u} and N_{ε_1} in undrained cyclic tests using $G-\nu$ and $G-K$ calibration of DM04 model

7.3.3 Volumetric expansion cyclic test simulations

The cyclic triaxial tests under water inflow conditions on batch 1 of Hostun sand published in Adamidis and Anastasopoulos (2022) were simulated. They pertain to the same density range of Hostun sand as the undrained tests presented above. In the simulations, the volumetric strain increment, $\dot{\varepsilon}_v$ was applied so as to impose a constant water inflow rate ε_v/cyc. These expansion rates were obtained from realistic values of inflow rates occurring at the interface of a liquefiable layer overlain by a low permeability layer (Adamidis and Anastasopoulos, 2022). One test simulation corresponding to $D_r = 55 \pm 2\%$ and $\varepsilon_v/cyc \simeq -0.04\%$ are presented for each of the three models; figure 7.16 using DM04 model, figure 7.17 using SANISAND-MSf model and figure 7.18 using PM4Sand3D model. Figures 7.19-7.21 show the accumulation of pore

Test ID	CSR	$N_{R_u}{}^{(a)}$	$N_{R_u}{}^{(b)}$	$N_{R_u}{}^{(c)}$	$N_{\varepsilon_1}{}^{(a)}$	$N_{\varepsilon_1}{}^{(b)}$	$N_{\varepsilon_1}{}^{(c)}$
$ICT65/100/28/0$	0.14	144	29	145.5	-	31.5	150.5
$ICT65/100/30/0$	0.15	42.5	13	51	-	14.7	54.5
$ICT65/100/30/0$	0.15	77.1	14	55.5	-	15.6	58.6
$ICT65/100/36/0$	0.18	6	5	15	7.7	-	20.6
$ICT65/100/39/0$	0.20	3.5	3.5	8	4.6	-	11.5
$ICT65/100/40/0$	0.20	4	2.5	6.5	5.1	-	8.7
$ICT55/100/25/0$	0.12	70	58.5	258.5	71.2	59.5	259.6
$ICT55/100/30/0$	0.15	19	9	25	19.5	10.5	26
$ICT55/100/34/0$	0.17	4.5	4	9.5	4.6	5.5	10.6
$ICT40/100/19/0$	0.10	197	696.5	3158	197.6	697	3158.5
$ICT40/100/20/0$	0.10	98.1	370.5	1424	99.5	371	1424.5
$ICT40/100/23/0$	0.11	28.5	75	187	28.6	75.5	187.5
$ICT40/100/28/0$	0.14	8	10.5	20	8.1	11.5	20.5
$ICT40/100/30/0$	0.15	6	5.5	9	6.2	6.5	9.5
$ICT40/100/33/0$	0.16	2	3	4.5	2	3.5	4.6

$^{(a)}$Undrained cyclic triaxial tests from Adamidis and Anastasopoulos (2022);
$^{(b)}G-\nu$ calibration (equations 7.2 and 7.3); $^{(c)}G-K$ calibration (equations 7.2 and 7.4).

Table 7.9: Comparison of N_{R_u} and N_{ε_1} in undrained cyclic tests using $G-\nu$ and $G-K$ calibration of SANISAND-MSf model

Test ID	CSR	$N_{R_u}{}^{(a)}$	$N_{R_u}{}^{(b)}$	$N_{R_u}{}^{(c)}$	$N_{\varepsilon_1}{}^{(a)}$	$N_{\varepsilon_1}{}^{(b)}$	$N_{\varepsilon_1}{}^{(c)}$
$ICT65/100/28/0$	0.14	144	142.5	148	-	145.6	148.6
$ICT65/100/30/0$	0.15	42.5	69	72	-	71.6	72.6
$ICT65/100/30/0$	0.15	77.1	69.5	72.5	-	71.7	72.6
$ICT65/100/36/0$	0.18	6	49.5	51.5	7.7	52.2	51.6
$ICT65/100/39/0$	0.20	3.5	23.5	24.5	4.6	25.6	24.6
$ICT65/100/40/0$	0.20	4	16.5	17	5.1	18.6	17.5
$ICT55/100/25/0$	0.12	70	54	57	71.2	56.1	57.1
$ICT55/100/30/0$	0.15	19	15.5	16.5	19.5	17.1	16.6
$ICT55/100/34/0$	0.17	4.5	11	11.5	4.6	12.6	11.6
$ICT40/100/19/0$	0.10	197	30	31.5	197.6	31.1	31.5
$ICT40/100/20/0$	0.10	98.1	20.5	22	99.5	21.2	22
$ICT40/100/23/0$	0.11	28.5	9.5	10	28.6	10.1	10.5
$ICT40/100/28/0$	0.14	8	6	6.5	8.1	7.1	6.5
$ICT40/100/30/0$	0.15	6	4	4	6.2	4.6	4.1
$ICT40/100/33/0$	0.16	2	2.5	2.5	2	3	2.5

$^{(a)}$Undrained cyclic triaxial tests from Adamidis and Anastasopoulos (2022);
$^{(b)}G-\nu$ calibration (equations 7.7 and 7.3); $^{(c)}G-K$ calibration (equations 7.7 and 7.8).

Table 7.10: Comparison of N_{R_u} and N_{ε_1} in undrained cyclic tests using $G-\nu$ and $G-K$ calibration of PM4Sand3D model

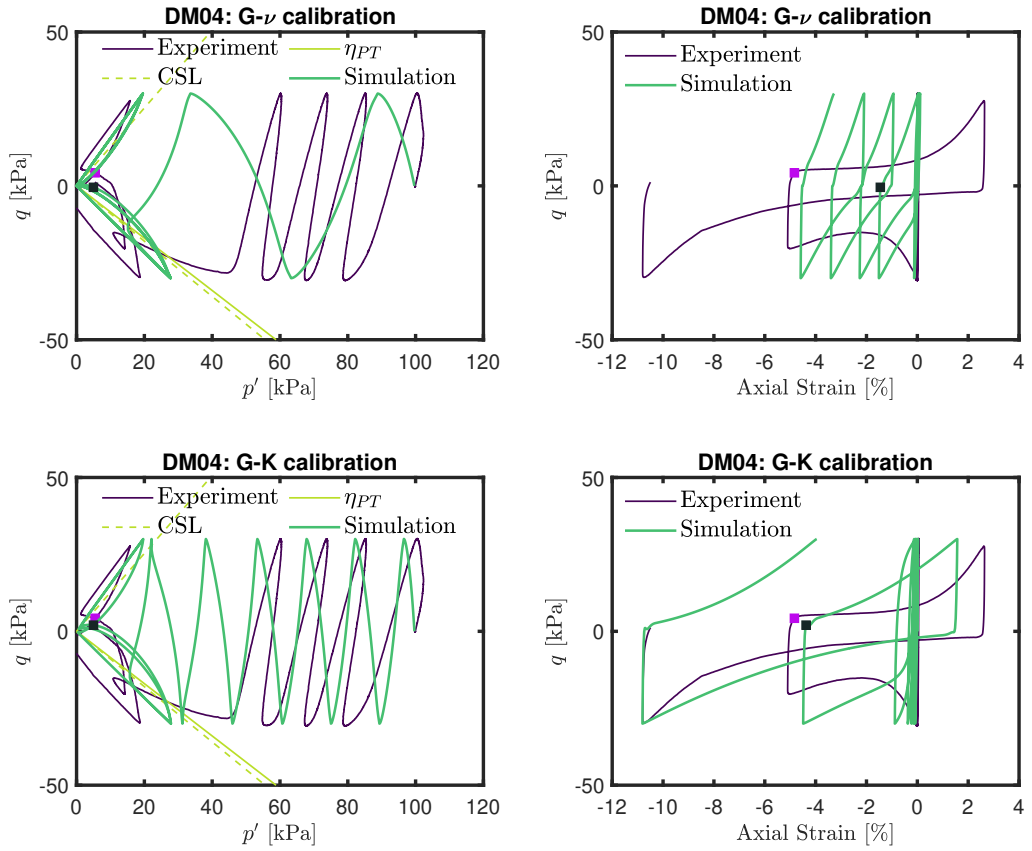

Figure 7.16: Simulation of non-standard drained cyclic triaxial test ICT55/100/30/5 (Adamidis and Anastasopoulos, 2022) using (a) $G-\nu$ and (b) $G-K$ calibration of DM04 model; square markers represent onset of liquefaction

pressure and axial strain with each cycle for the two calibration methods of bulk modulus, using the DM04 model, SANISAND-MSf model and PM4Sand3D model, respectively.

The non-standard drained cyclic stress-strain paths are qualitatively captured well by all three constitutive models for both calibration methods (see $q-p'$ plots in figures 7.16-7.18). The $G-\nu$ calibration results in quicker accumulation of excess pore pressure and strains, with smaller cyclic strain amplitudes than the $G-K$ calibration; a similar observation to the undrained test simulations. The simulation results indicate that even with small inflow rates ($\varepsilon_v/cyc \simeq -0.04\%$), the required number of cycles to liquefaction N_{R_u} is drastically lowered, which agrees with experimental observation. For instance, the experimental data presented in figures 7.11 and 7.17 correspond to the same cyclic stress ratio (CSR) of 0.15 and the same initial state.

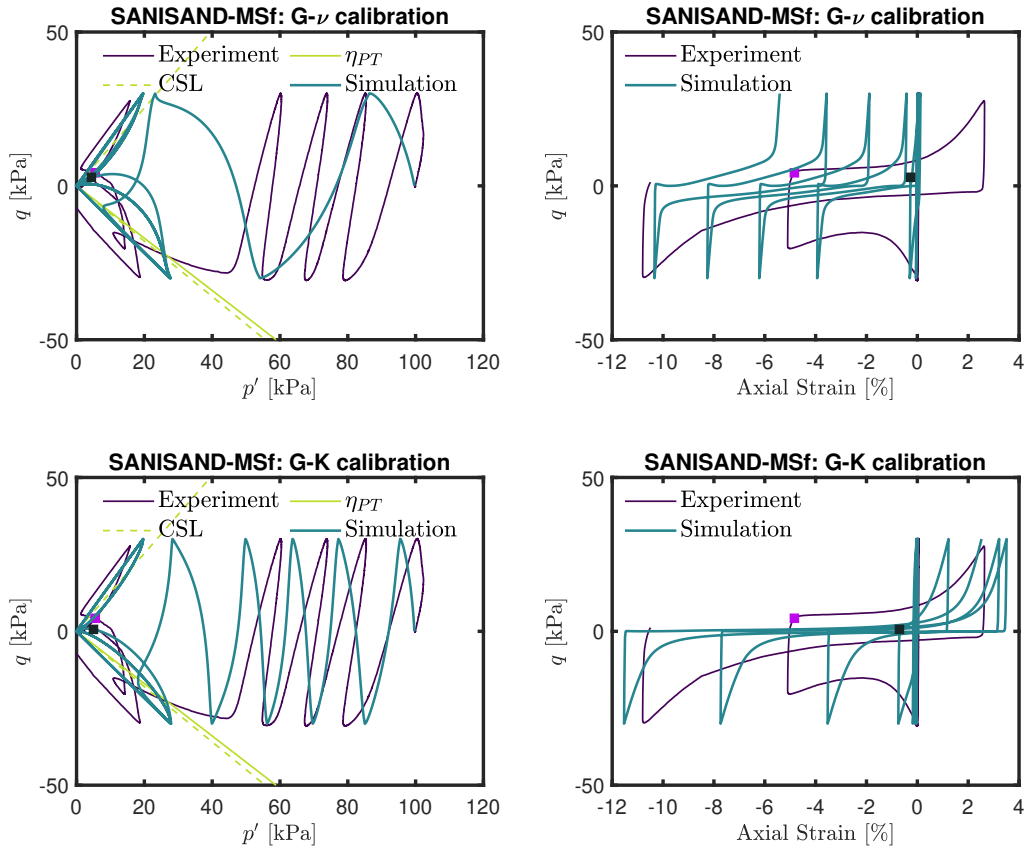

Figure 7.17: Simulation of non-standard drained cyclic triaxial test ICT55/100/30/5 (Adamidis and Anastasopoulos, 2022) using (a) $G-\nu$ and (b) $G-K$ calibration of SANISAND-MSf model; square markers represent onset of liquefaction

The cycles required to trigger liquefaction go down from 19 under undrained conditions to 4 under an inflow rate of -0.04%. With the $G-\nu$ calibration of SANISAND-MSf, the cycles to liquefaction reduce from 9 to 2, while for the $G-K$ calibration, the cycles reduce from 25 to 5. Similarly to the undrained case, crossing the η_{PTS} in extension leads to significant excess pore pressures upon loading reversal, with liquefaction triggering following.

As for the undrained case, the softer bulk modulus ($G-K$ calibration) captures the accumulation of excess pore pressure with normalised cycles (N/N_{ult}) better for all three models (figures 7.19-7.21). The accumulation of strain per cycle and cyclic strain amplitude is also better captured by the $G-K$ calibration than the $G-\nu$ calibration. Overall, the PM4Sand3D model predicted a closer trend of excess pore pressure and axial strain accumulation to the ex-

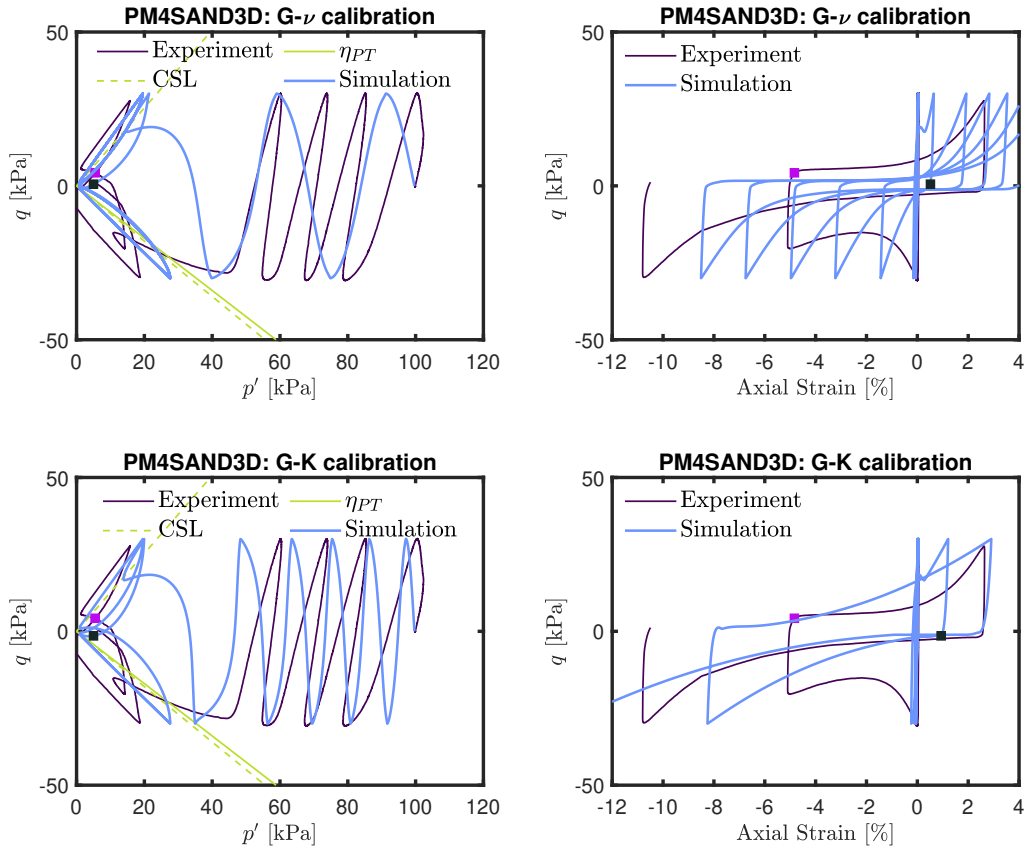

Figure 7.18: Simulation of non-standard drained cyclic triaxial test ICT55/100/30/5 (Adamidis and Anastasopoulos, 2022) using (a) $G-\nu$ and (b) $G-K$ calibration of PM4Sand3D model; square markers represent onset of liquefaction

perimentally observed (see figure 7.21).

Results including cycles to liquefaction (N_{R_u} and N_{ε_1}) for the non-standard drained cyclic experiments and simulations using the two bulk modulus calibration parameters for the DM04 model, SANISAND-MSf model and PM4Sand3D model are listed in tables 7.11, 7.12 and 7.13, respectively. As for the undrained case, the $G-\nu$ calibration predicted fewer cycles to trigger liquefaction than the $G-K$ calibration for the DM04 and SANISAND-MSf models. Although the N_{R_u} and N_{ε_1} predictions for the undrained cyclic tests were similar using both calibration methods for the PM4Sand3D model (refer to table 7.10), the $G-\nu$ calibration in the non-standard drained cyclic tests predicted fewer cycles to liquefaction than the $G-K$ calibration. For the N_{ε_1} values, the $G-\nu$ calibration predicted smaller cyclic axial strain amplitudes, that

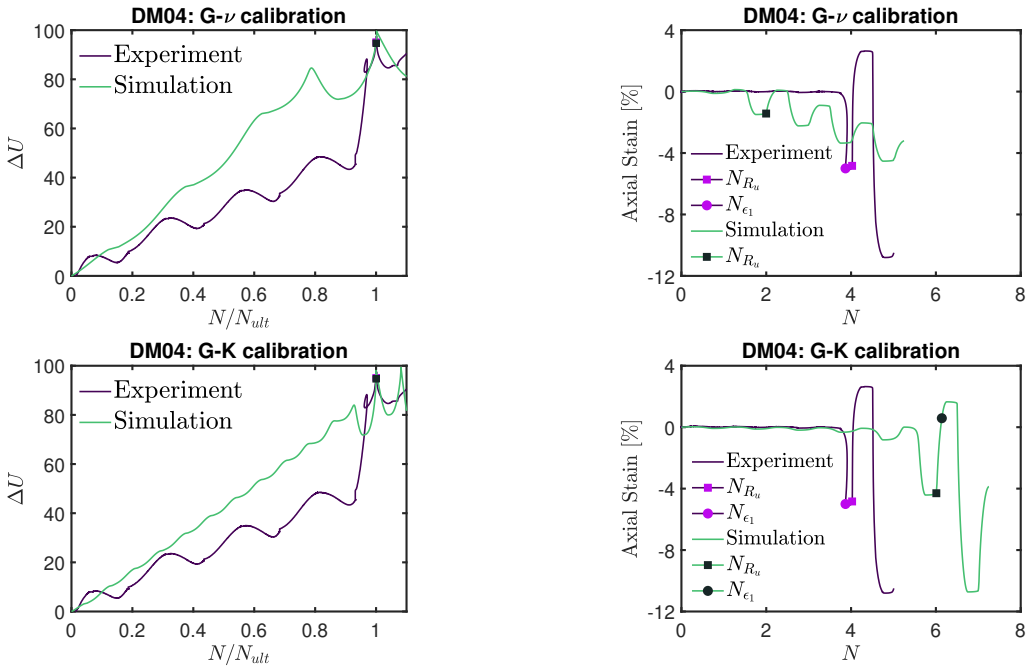

Figure 7.19: Progression of excess pore pressure and axial strain for non-standard drained cyclic triaxial test ICT55/100/30/5 (Adamidis and Anastasopoulos, 2022) using (a) $G-\nu$ and (b) $G-K$ calibration of DM04 model

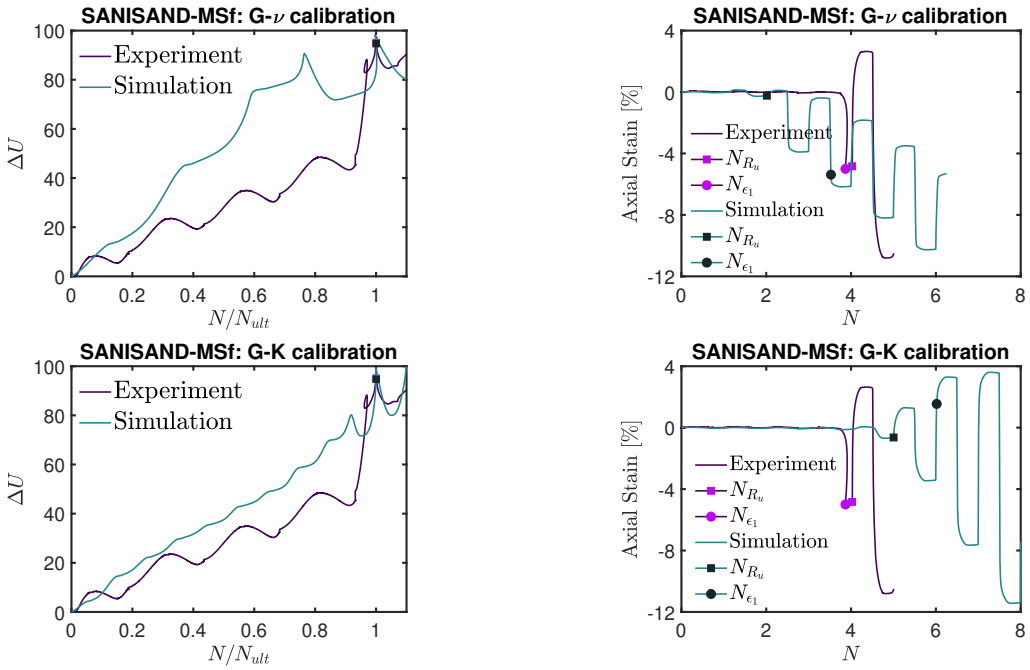

Figure 7.20: Progression of excess pore pressure and axial strain for non-standard drained cyclic triaxial test ICT55/100/30/5 (Adamidis and Anastasopoulos, 2022) using (a) $G-\nu$ and (b) $G-K$ calibration of SANISAND-MSf model

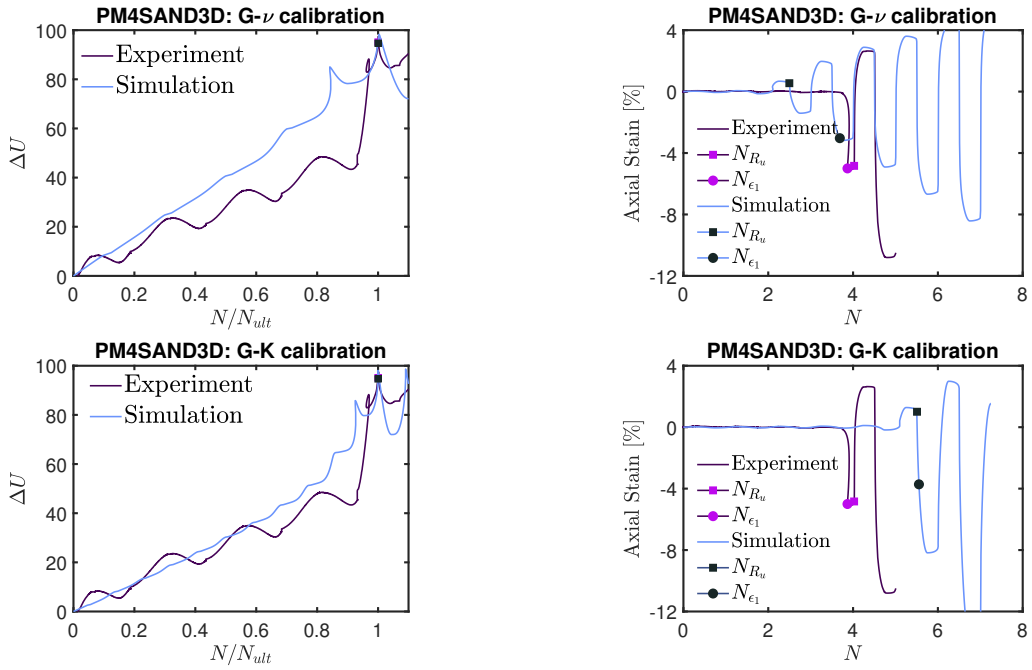

Figure 7.21: Progression of excess pore pressure and axial strain for non-standard drained cyclic triaxial test ICT55/100/30/5 (Adamidis and Anastasopoulos, 2022) using (a) $G-\nu$ and (b) $G-K$ calibration of PM4Sand3D model

never reached the double amplitude of 5% triggering criterion for all the experiments in the DM04 model. While, the SANISAND-MSf and the PM4Sand3D model predictions of the non-standard drained cyclic axial strain accumulation in the post-liquefaction stage using both calibration methods resulted in double amplitude cyclic axial strain of 5% as reflected in the N_{ε_1} values of tables 7.12 and 7.13.

7.4 Liquefaction resistance curves

Experimental and numerical liquefaction resistance curves for the baseline undrained case and water inflow cases using both definitions of bulk modulus in DM04, SANISAND-MSf and PM4Sand3D models are plotted in figures 7.22, 7.23 and 7.24 for three densities of Hostun sand, $66 \pm 3\%$, $55 \pm 2\%$ and $40 \pm 2\%$, respectively. The baseline undrained liquefaction resistance curves ($\varepsilon_v/cycle = 0\%$) are denoted by dashed lines with test data points in filled circles. Each undrained CSR-N set of data points was fitted with a power relationship ($CSR = a \cdot N^{-b}$) and the

Test ID	CSR	$\dot{\varepsilon}_v/\dot{\varepsilon}_{v,max}$	$\varepsilon_v/cyc(\%)$	${N_{R_u}}^{(a)}$	${N_{R_u}}^{(b)}$	${N_{R_u}}^{(c)}$	${N_{\varepsilon_1}}^{(a)}$	${N_{\varepsilon_1}}^{(b)}$	${N_{\varepsilon_1}}^{(c)}$
$ICT65/100/10/1$	0.05	1%	-0.01	67.1	10.5	40	-	-	-
$ICT65/100/13/1$	0.07	1%	-0.01	64.1	9.1	33.5	-	-	-
$ICT65/100/20/1$	0.10	1%	-0.01	40	6.5	22.5	-	-	-
$ICT65/100/28/1$	0.14	1%	-0.01	25.5	4	13.5	-	-	13.6
$ICT65/100/10/5$	0.05	5%	-0.04	15.2	4	14	-	-	-
$ICT65/100/20/5$	0.10	5%	-0.04	10.5	3	10	11.7	-	10.7
$ICT65/100/30/5$	0.15	5%	-0.03	4.5	3	8.5	5.6	-	8.6
$ICT65/100/15/15$	0.07	15%	-0.1	5	1.5	6	6.7	-	10.7
$ICT65/100/20/15$	0.1	15%	-0.1	5	1.5	5	-	-	6.7
$ICT65/100/25/15$	0.13	15%	-0.1	4	1.5	4.5	5.6	-	4.7
$ICT65/100/30/15$	0.15	15%	-0.08	3	1.5	5	3.7	-	5.6
$ICT55/100/15/5$	0.07	5%	-0.04	14.1	3	11	-	-	11.6
$ICT55/100/25/5$	0.13	5%	-0.04	7	2	7	7.5	-	7.5
$ICT55/100/30/5$	0.15	5%	-0.04	4	2	6	3.9	-	6.1
$ICT40/100/12/5$	0.06	5%	-0.05	11.8	2.5	9.5	-	-	9.5
$ICT40/100/20/5$	0.10	5%	-0.04	9.5	2	7	9.7	-	7.1
$ICT40/100/22/5$	0.11	5%	-0.05	6.9	2	6	6.9	-	5.7
$ICT40/100/25/5$	0.13	5%	-0.04	5	1.5	5.5	5.1	-	5.5

$^{(a)}$Non-standard drained cyclic triaxial tests from Adamidis and Anastasopoulos (2022);
$^{(b)}G-\nu$ calibration (equations 7.2 and 7.3); $^{(c)}G-K$ calibration (equations 7.2 and 7.4).

Table 7.11: Comparison of N_{R_u} and N_{ε_1} in non-standard drained cyclic tests using $G-\nu$ and $G-K$ calibration of DM04 model

value of the exponent $'b'$, which represents the slope of the curves in figures 7.22-7.24, is noted in the legend. The unfilled circles correspond to N_{ε_1} data points. In the legends, '*Exp*' stands for experiments and '*Sim*' stand for simulations. The non-standard drained cyclic tests are similarly shown with square markers for $\varepsilon_v/cycle = -0.01\%$, triangle markers for $\varepsilon_v/cycle = -0.04\%$, and diamond markers for $\varepsilon_v/cycle = -0.1\%$. The unfilled markers correspond to the N_{ε_1} data points, as for the undrained case. Across all three densities, the DM04 model produces much steeper baseline undrained liquefaction curves than the other two models using both the $G-\nu$ and $G-K$ calibration methods, matching numerical observations reported in literature (Möller et al., 2024). With a directly calibrated bulk modulus ($G-K$ calibration), the baseline liquefaction resistance curves of the DM04 model shift to the right with a slightly gentler slope for the upper and lower density ranges. The baseline curves are best matched by the SANISAND-MSf model for both calibration methods across the three densities. The change in bulk modulus

Test ID	CSR	$\dot{\varepsilon}_v/\dot{\varepsilon}_{v,max}$	$\varepsilon_v/cyc(\%)$	${N_{R_u}}^{(a)}$	${N_{R_u}}^{(b)}$	${N_{R_u}}^{(c)}$	${N_{\varepsilon_1}}^{(a)}$	${N_{\varepsilon_1}}^{(b)}$	${N_{\varepsilon_1}}^{(c)}$
$ICT65/100/10/1$	0.05	1%	-0.01	67.1	13.5	48.5	-	16.5	51.7
$ICT65/100/13/1$	0.07	1%	-0.01	64.1	12.1	42	-	14.5	46.6
$ICT65/100/20/1$	0.10	1%	-0.01	40	9	29.5	-	10.5	33.6
$ICT65/100/28/1$	0.14	1%	-0.01	25.5	5	16	-	6.5	18.6
$ICT65/100/10/5$	0.05	5%	-0.04	15.2	3.6	14.1	-	4.5	16.7
$ICT65/100/20/5$	0.10	5%	-0.04	10.5	2.5	9.5	11.7	4.5	12.5
$ICT65/100/30/5$	0.15	5%	-0.03	4.5	2	7	5.6	-	10.5
$ICT65/100/15/15$	0.07	15%	-0.1	5	1.4	5.5	6.7	-	8.5
$ICT65/100/20/15$	0.1	15%	-0.1	5	1.5	4.5	-	4.6	8.5
$ICT65/100/25/15$	0.13	15%	-0.1	4	1.5	4	5.6	-	6.6
$ICT65/100/30/15$	0.15	15%	-0.08	3	1.5	4	3.7	-	7.6
$ICT55/100/15/5$	0.07	5%	-0.04	14.1	3.5	12	-	4.5	13
$ICT55/100/25/5$	0.13	5%	-0.04	7	2	7	7.5	3.5	8
$ICT55/100/30/5$	0.15	5%	-0.04	4	2	5	3.9	3.5	6
$ICT40/100/12/5$	0.06	5%	-0.05	11.8	3.1	12	-	3.5	12.1
$ICT40/100/20/5$	0.10	5%	-0.04	9.5	2.5	9	9.7	3.1	9.5
$ICT40/100/22/5$	0.11	5%	-0.05	6.9	2	6.5	6.9	2.5	7
$ICT40/100/25/5$	0.13	5%	-0.04	5	2	6	5.1	2.5	6.5

$^{(a)}$Non-standard drained cyclic triaxial tests from Adamidis and Anastasopoulos (2022);
$^{(b)}G-\nu$ calibration (equations 7.2 and 7.3); $^{(c)}G-K$ calibration (equations 7.2 and 7.4).

Table 7.12: Comparison of N_{R_u} and N_{ε_1} in non-standard drained cyclic tests using $G-\nu$ and $G-K$ calibration of SANISAND-MSf model

calibration makes little difference to the PM4Sand3D baseline liquefaction resistance curves.

With increasing volumetric water inflow rates, the experimental liquefaction resistance curves shift to the left of the baseline undrained curve, indicating fewer cycles to trigger liquefaction than for the undrained case. The numerical liquefaction resistance curves for water inflow rates also follow the experimental trend of shift in position towards left of the undrained curve in all three models. However, the shift is more pronounced in the $G-\nu$ calibrated model simulations leading to overly conservative predictions of cycles to liquefaction. In figure 7.22, note that the distance between the experimental curves along the x-axis (N), which is logarithmic, decreases as the inflow strain rates increase. This is not very well captured by the DM04 model using either of the calibration techniques. However, the SANISAND-MSf and PM4Sand3D models are able to capture it adequately. SANISAND-MSf is able to closely match experimental results across all densities when using a $G-K$ calibration, with PM4Sand3D also showing good response

Test ID	CSR	$\dot{\varepsilon}_v/\dot{\varepsilon}_{v,max}$	$\varepsilon_v/cyc(\%)$	${N_{R_u}}^{(a)}$	${N_{R_u}}^{(b)}$	${N_{R_u}}^{(c)}$	${N_{\varepsilon_1}}^{(a)}$	${N_{\varepsilon_1}}^{(b)}$	${N_{\varepsilon_1}}^{(c)}$
$ICT65/100/10/1$	0.05	1%	-0.01	67.1	15.6	53.1	-	22.2	54.4
$ICT65/100/13/1$	0.07	1%	-0.01	64.1	14.1	47	-	19.7	48.6
$ICT65/100/20/1$	0.10	1%	-0.01	40	11.5	35.5	-	-	35.6
$ICT65/100/28/1$	0.14	1%	-0.01	25.5	8.5	21	-	10.7	21.6
$ICT65/100/10/5$	0.05	5%	-0.04	15.2	4.5	15.1	-	10.6	16.5
$ICT65/100/20/5$	0.10	5%	-0.04	10.5	3.5	10.5	11.7	6.7	11.2
$ICT65/100/30/5$	0.15	5%	-0.03	4.5	4	9.5	5.6	6.6	9.7
$ICT65/100/15/15$	0.07	15%	-0.1	5	2	6	6.7	6.6	6.7
$ICT65/100/20/15$	0.1	15%	-0.1	5	2	5	-	5.6	5.6
$ICT65/100/25/15$	0.13	15%	-0.1	4	1.5	4.5	5.6	4.6	4.6
$ICT65/100/30/15$	0.15	15%	-0.08	3	2	5	3.7	4.7	5.6
$ICT55/100/15/5$	0.07	5%	-0.04	14.1	4	12	-	6.6	12.2
$ICT55/100/25/5$	0.13	5%	-0.04	7	3	7	7.5	4.6	7.2
$ICT55/100/30/5$	0.15	5%	-0.04	4	2.5	5.5	3.9	3.7	5.6
$ICT40/100/12/5$	0.06	5%	-0.05	11.8	3	9.1	-	4.5	9.5
$ICT40/100/20/5$	0.10	5%	-0.04	9.5	3	6.5	9.7	4	6.5
$ICT40/100/22/5$	0.11	5%	-0.05	6.9	2	5	6.9	3.1	5.1
$ICT40/100/25/5$	0.13	5%	-0.04	5	2	4.5	5.1	3.1	4.5

$^{(a)}$Non-standard drained cyclic triaxial tests from Adamidis and Anastasopoulos (2022);
$^{(b)}G-\nu$ calibration (equations 7.7 and 7.3); $^{(c)}G-K$ calibration (equations 7.7 and 7.8).

Table 7.13: Comparison of N_{R_u} and N_{ε_1} in non-standard drained cyclic tests using $G-\nu$ and $G-K$ calibration of PM4Sand3D model

with the directly calibrated bulk modulus. Overall, a significant improvement to the predictions of cycles to liquefaction under volumetric expansion is observed with the $G-K$ calibration as compared with the conventional $G-\nu$ calibration.

To understand the dependence of non-standard drained cyclic behaviour on the bulk modulus, Adamidis and Anastasopoulos (2022) plotted the change in void ratio δe with mean effective stress p' for inflow cyclic tests with varying CSRs but under the same constant rate of water inflow. Their study showed that loss of effective stress upon cyclic shearing under water inflow is a cumulative effect of isotropic unloading through volume expansion and undrained shearing. In this study the results from the numerical simulations are added to the experimental $\delta e - p'$ plots, shown in solid lines. Figures 7.25-7.27 show the change in void ratio δe versus mean effective stress p' for cyclic tests under a constant volumetric expansion rate of $\varepsilon_v/cyc \simeq -0.04\%$. The isotropic unloading curves from equations 7.3 and 7.4 are also plotted. The experimental

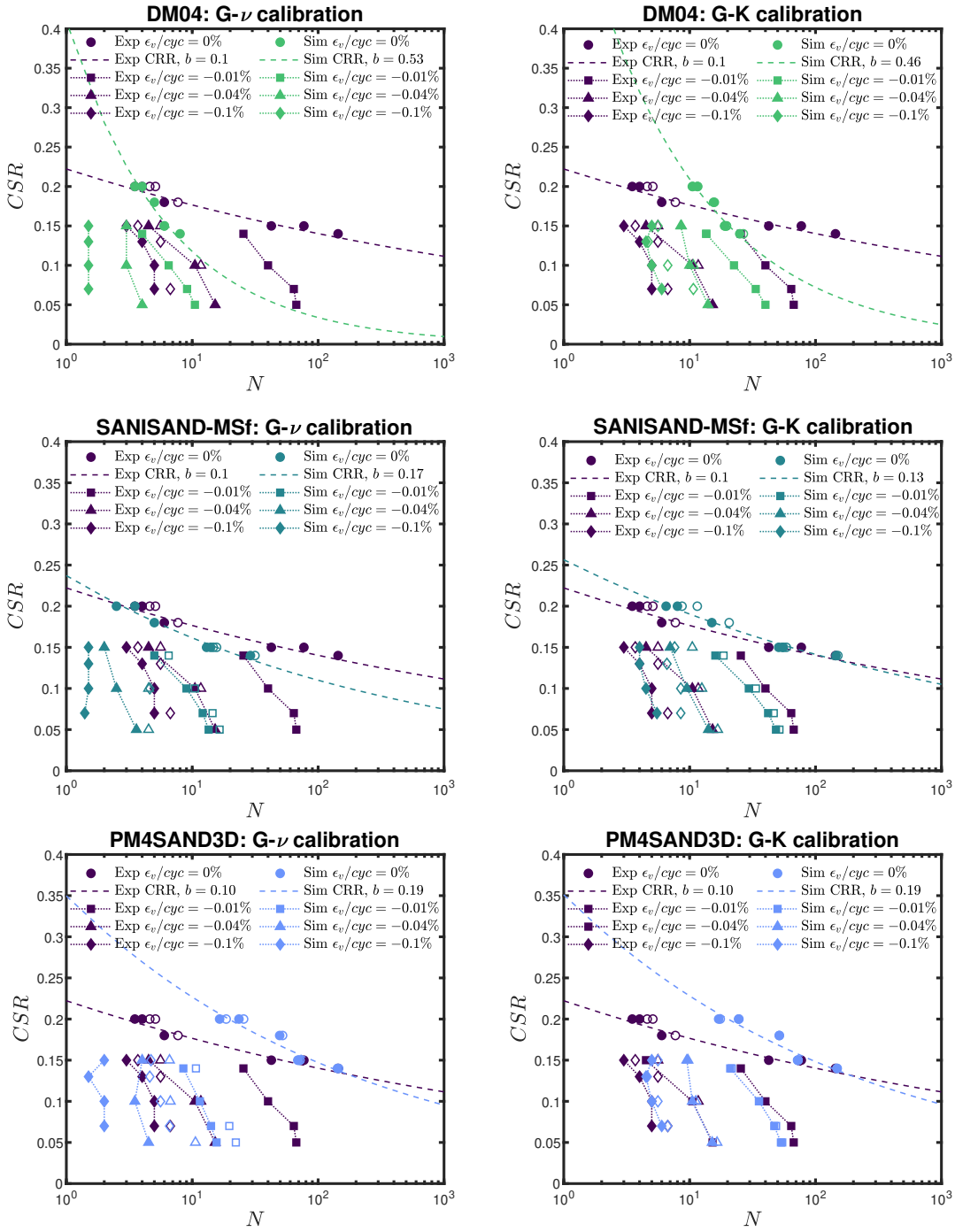

Figure 7.22: Cyclic resistance under undrained and inflow conditions of medium dense Hostun sand ($D_r = 66 \pm 3\%$) using $G-\nu$ and $G-K$ calibration of (a) DM04, (b) SANISAND-MSf and (c) PM4Sand3D models

paths, shown in dotted lines, indicate that the tests under low CSRs follow the unloading curve until considerable reduction in p'. This implies that at low CSRs, the isotropic unloading related

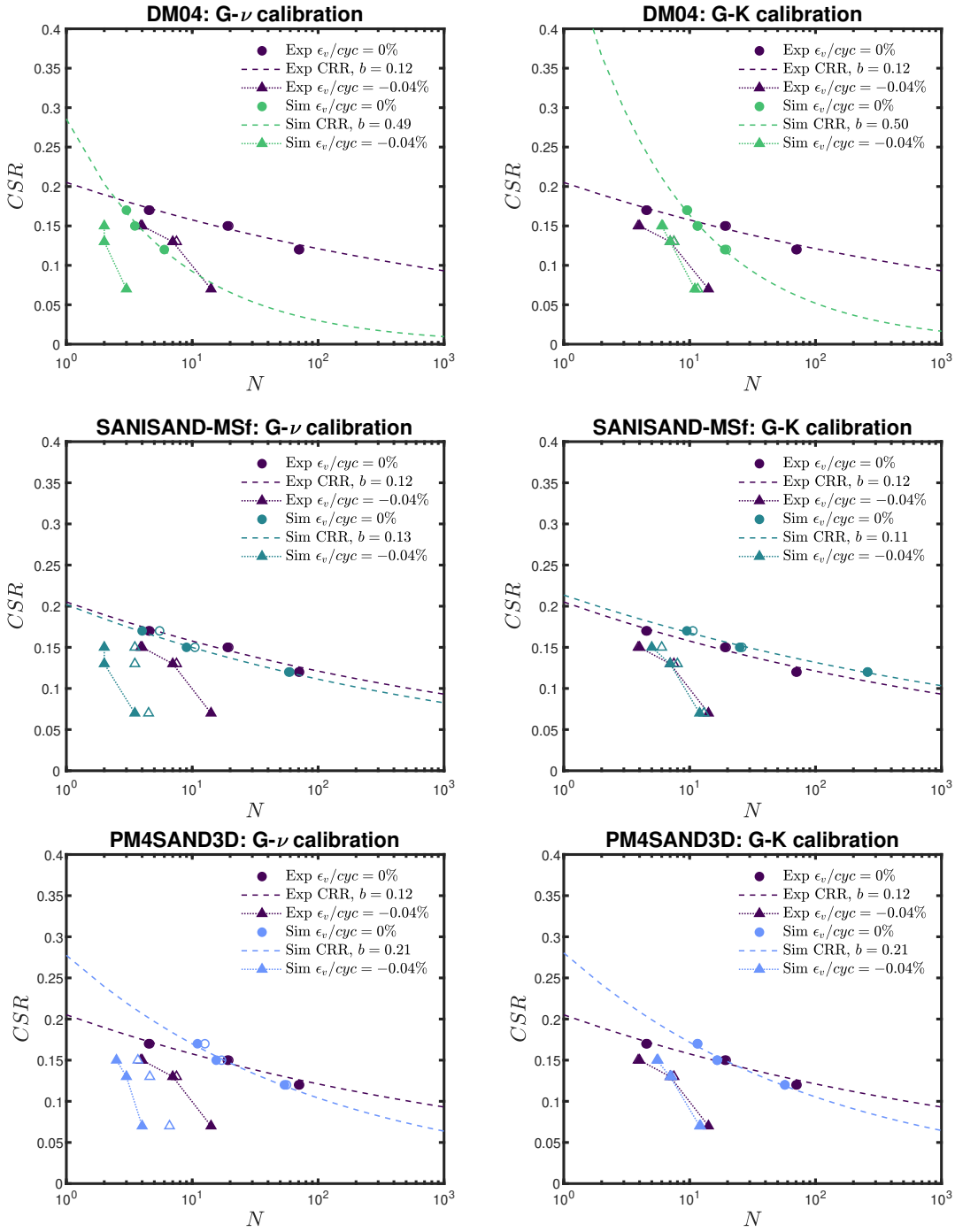

Figure 7.23: Cyclic resistance under undrained and inflow conditions of medium dense Hostun sand ($D_r = 55 \pm 2\%$) using $G-\nu$ and $G-K$ calibration of (a) DM04, (b) SANISAND-MSf and (c) PM4Sand3D models

reduction in p' is predominant. For high CSRs, the reduction in p' is much higher than that from only isotropic unloading, indicating that cyclic shearing has a greater contribution.

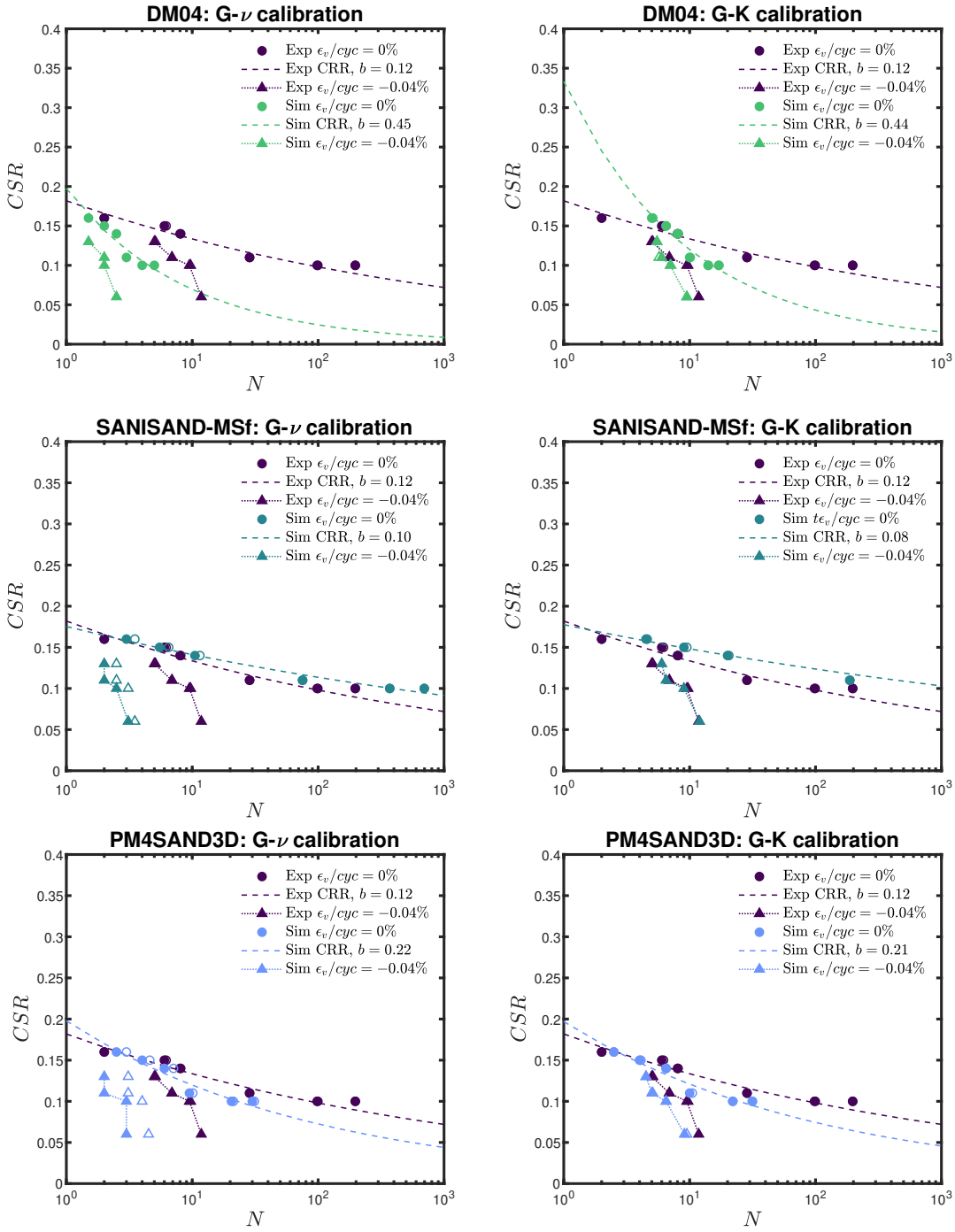

Figure 7.24: Cyclic resistance under undrained and inflow conditions of medium dense Hostun sand ($D_r = 40 \pm 2\%$) using $G - \nu$ and $G - K$ calibration of (a) DM04, (b) SANISAND-MSf and (c) PM4Sand3D models

With the typical calibration of K, using G and ν (see figures 7.25(a), 7.26(a) and 7.27(a)), the isotropic unloading curve used in the simulation (denoted by a solid line) is much flatter than the

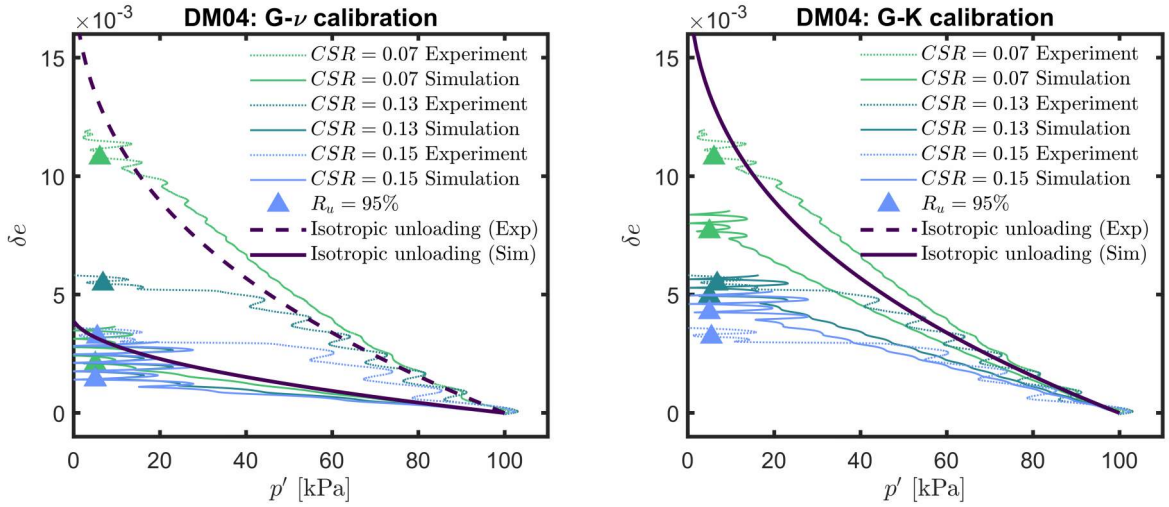

Figure 7.25: δe vs. p' for cyclic tests on medium dense Hostun sand ($D_r = 55 \pm 2\%$) under $\varepsilon_v/cyc \simeq -0.04\%$ simulated in DM04 model using (a) $G-\nu$ calibration and (b) $G-K$ calibration

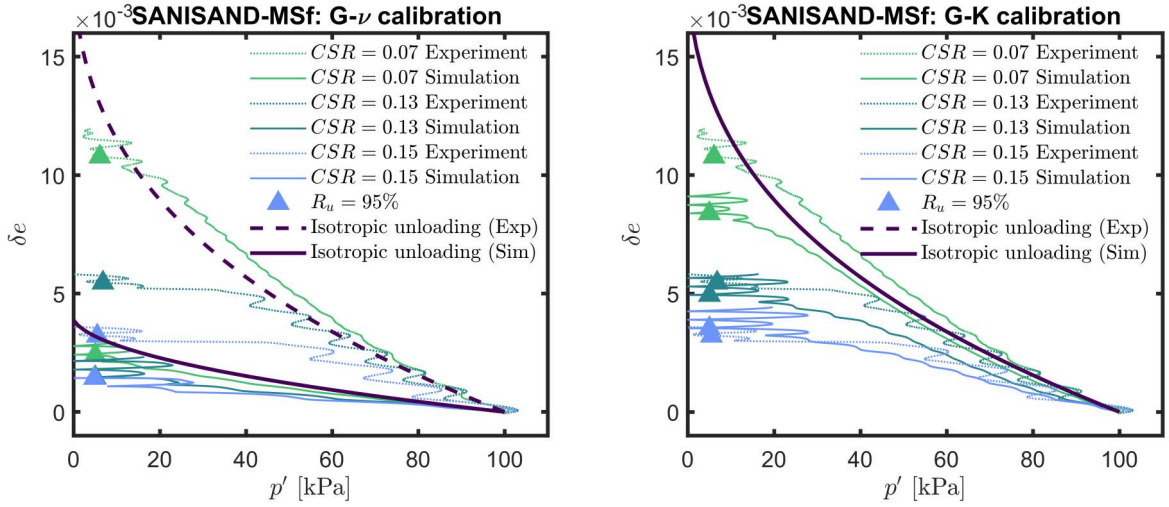

Figure 7.26: δe vs. p' for cyclic tests on medium dense Hostun sand ($D_r = 55 \pm 2\%$) under $\varepsilon_v/cyc = -0.04\%$ simulated in SANISAND-MSf model using (a) $G-\nu$ calibration and (b) $G-K$ calibration

experimental unloading curve (denoted by dashed line). The simulated paths under all ranges of CSR lie below the unloading curve defined in the constitutive model, with reducing slopes as CSR increases. The undrained shearing line would be a flat line from p' of 100 to 0 at $\delta e = 0$. Though the models qualitatively capture the inclination towards the isotropic unloading curve with reducing CSRs, quantitatively the predictions are inadequate. The stiff bulk modulus in the $G-\nu$ calibration predicts significantly fewer cycles to liquefaction than in the experiments.

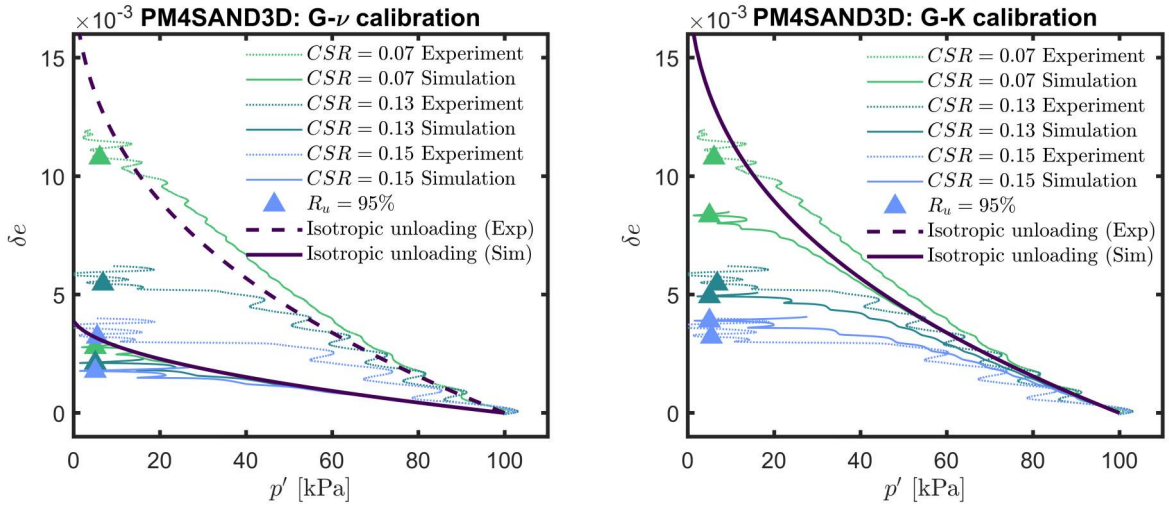

Figure 7.27: δe vs. p' for cyclic tests on medium dense Hostun sand ($D_r = 55 \pm 2\%$) under $\varepsilon_v/cyc \simeq -0.04\%$ simulated in PM4Sand3D model using (a) $G-\nu$ calibration and (b) $G-K$ calibration

By directly calibrating K based on its experimental isotropic unloading data, the simulations capture the experimental data in a satisfactory way (see figures 7.25(b), 7.26(b) and 7.27(b)). The predictions are very close to the experiments for the SANISAND-MSf and the PM4Sand3D models. At high CSR values, the experimental reduction in p' can deviate from that simulated, especially for the DM04 model. This echoes the observation that at high CSRs it is mostly the cyclic shearing that results in p' reduction for the element. The difference between the experimental and numerical results matches the differences observed for a given CSR and density in the undrained liquefaction resistance curves of the previous section.

7.5 Impact of updated SANISAND state parameter on liquefaction resistance

In this section, the impact of a modified state parameter definition, determined using the concept of the Locus of Constant State parameter Instability (LCSI) for coupled-strain monotonic tests (developed in chapter 5), on undrained and non-standard drained cyclic test simulations is studied. The SANISAND-MSf model (M. Yang et al., 2022) is chosen for the simulations with

the modified state parameter definition as it produced good predictions of liquefaction resistance across all three densities. The model parameters affected by the state parameter are re-calibrated for both bulk modulus definitions and the resulting simulations are compared. Finally, liquefaction resistance curves are generated and compared with the curves of section 7.4.

7.5.1 State parameter definition

The dataset of coupled strain monotonic compression tests conducted on batch 1 of Hostun HN31 sand by OA at ETH Zurich were used for the determination of the updated state parameter definition as listed in table 7.14, presented with permission. Note that the dataset does not include sufficient data points to satisfactorily determine the shape of the LCSI curves for more than one strain coupling ratio. But due to the sand batch variability observed for Hostun sand as mentioned in chapter 4, the updated state parameter definition was based on coupled strain tests conducted on batch 1 of Hostun sand only. Using the CSL function in equation 7.1 and figure 7.1, the state parameter by Been and Jefferies (1985), was found to appropriately describe the shape of the LCSI curves, i.e. $\psi_F = e - e_{cs}$. The CSL, LCSIs and the corresponding state parameter form ψ_F (refer section 5.5.3) values are shown in figure 7.28. The updated state parameter definition is a function of the state parameter form given by $\psi_D = sign(\psi_F)|\psi_F|^w$ (refer section 5.5.3). From the LCSI curve equation for exponential bounding surface evolution presented in section 5.3.3, equation 5.8, dilatancy constant $A_0 = 1.0$ determined in section 7.2.1 and $\alpha^c = M^c - m = 1.256$ determined in section 7.2.1, the updated state parameter function exponent 'w' was determined through an iterative process following figure 5.23, with k^b and k^d replaced by n^b and n^d, respectively. The best-fit was found at $w = 0.7$ (refer figure 7.29) and the updated state parameter definition is defined in equation 7.9.

$$\psi_D = sign\,(e - e_{cs})\,|e - e_{cs}|^{0.7} \tag{7.9}$$

Test ID[a]	e_{in}[b]	p'_{in}[b]	e_{INST}[c]	p'_{INST}[c]
ICPDMC/0.830/300/-5	0.830	300	0.849	708.7
ICPDMC/0.845/300/-5	0.845	300	0.862	730.3
ICPDMC/0.915/300/-5	0.915	300	0.937	234.5
ICPDMC/0.841/300/-15	0.841	300	0.871	344.8
ICPDMC/0.781/300/-15	0.781	300	0.814	814.2
ICPDMC/0.879/50/-15	0.879	50	0.922	186.3
ICPDMC/0.891/30/-15	0.891	30	0.928	117.7
ICPDMC/0.890/80/-15	0.890	80	0.925	73.8
ICPDMC/0.812/300/-15	0.812	300	0.847	671.8
ICPDMC/0.779/300/-30	0.779	300	0.826	409.8
ICPDMC/0.862/30/-30	0.862	30	0.906	60.6
ICPDMC/0.838/300/-30	0.838	300	0.864	172.8

[a](1) type of consolidation: IC for isotropic consolidation; (2) type of drainage: PD for coupled strain conditions; (3)type of loading: MC for monotonic compression; (4) void ratio after consolidation; (5) mean effective stress after consolidation; and (6) coupled strain ratio during the shearing stage, $\zeta = \dot{\varepsilon}_v/\dot{\varepsilon}_1$, in percentage. [b]Post consolidation values; [c]INST: Instability Point.

Table 7.14: Results of coupled strain monotonic triaxial tests performed on batch 1 of Hostun sand by OA under different values of inflow rate $\zeta(=\dot{\varepsilon}_v/\dot{\varepsilon}_1)$, produced with permission

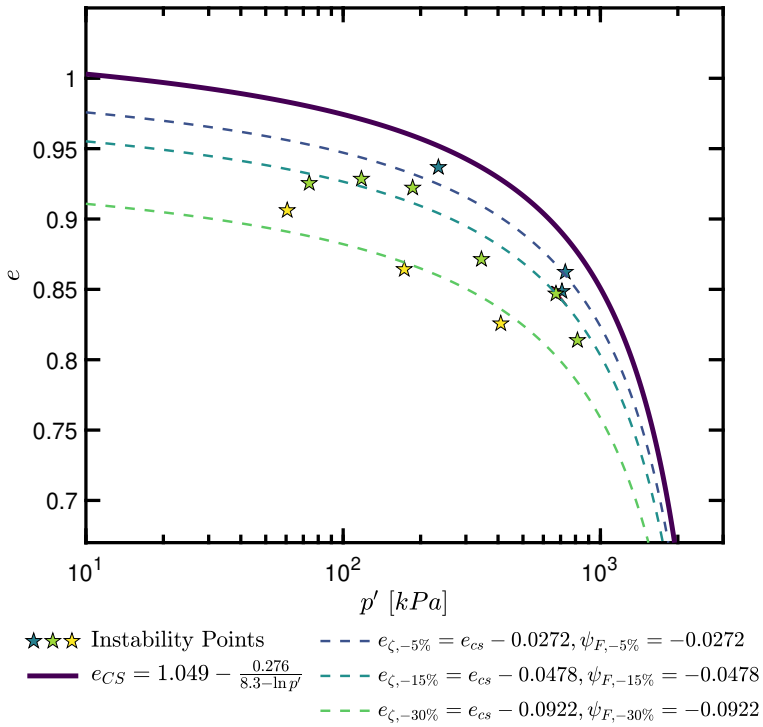

Figure 7.28: LCSI and corresponding state parameter forms for batch 1 of Hostun sand

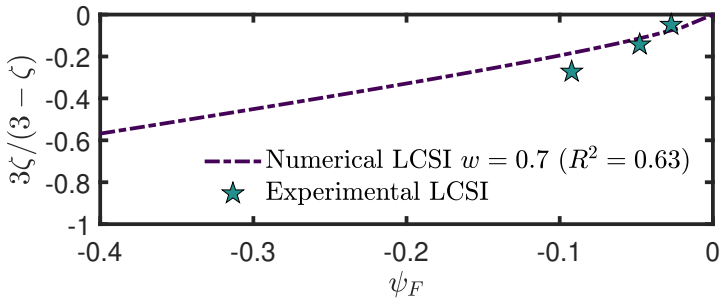

Figure 7.29: Determination of parameter w using exponential bounding evolution of LCSI

7.5.2 Calibration of model parameters

The model parameters dependent on the state parameter were re-calibrated for both bulk modulus definitions. The bounding surface parameter and the dilatancy surface parameter were obtained from the undrained monotonic tests, as described in section 7.2.1, and are shown in figure 7.30. The dilatancy constant A_0 was shown to remain unchanged with the modified state parameter function in section 5.6.1. Figure 7.31 shows the stress-dilatancy curves for drained tests with updated state parameter definition and confirms that the value remains unchanged. Parameters h_0 and c_h were obtained from trial-and-error and are shown in figure 7.32. The fabric-dilatancy parameters, the memory surface parameters and the semifluidised state parameters remain unchanged from the state parameter update. A summary of the model parameters using both bulk modulus definitions and the updated state parameter ψ_D (equation 7.9) is shown in table 7.15 and the selected/modified SANISAND-MSf model equations are listed in table 7.16.

7.5.3 Simulation results with updated SANISAND state parameter

The simulation of undrained cyclic test $ICT/55/100/30/0$ using the SANISAND-MSf model with model parameters calibrated for ψ_D in table 7.15 is presented in figures 7.33 and 7.34. The predictions using model parameters for state parameter $\psi = e - e_{cs}$ of table 7.4 are also included for comparison. As can be seen from the figures, the predictions with the two state parameter definitions are not drastically different. Using the updated state parameter ψ_D, the rate of con-

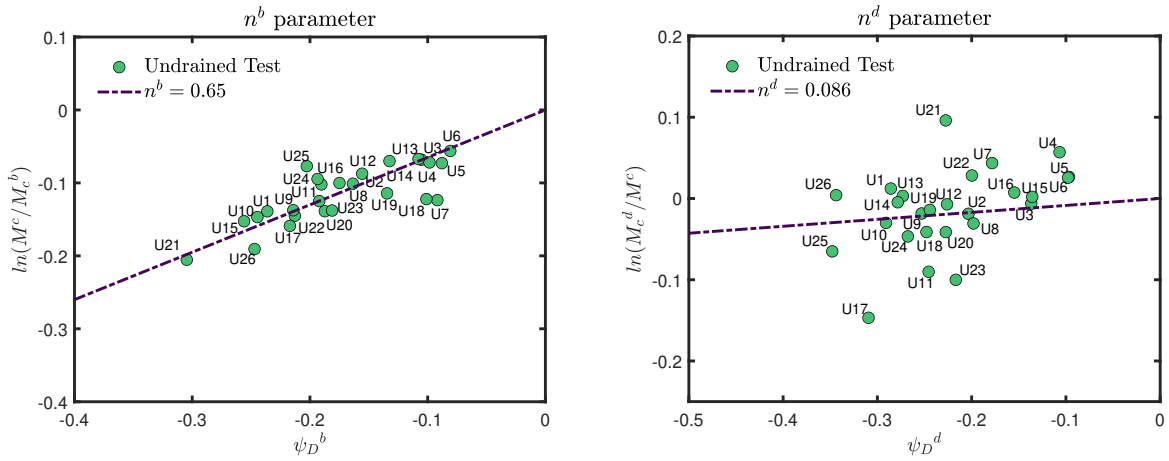

Figure 7.30: Calibration of bounding surface parameter n^b and dilatancy surface parameter n^d using updated state parameter function ψ_D (equation 7.9) for batch 1 of Hostun sand

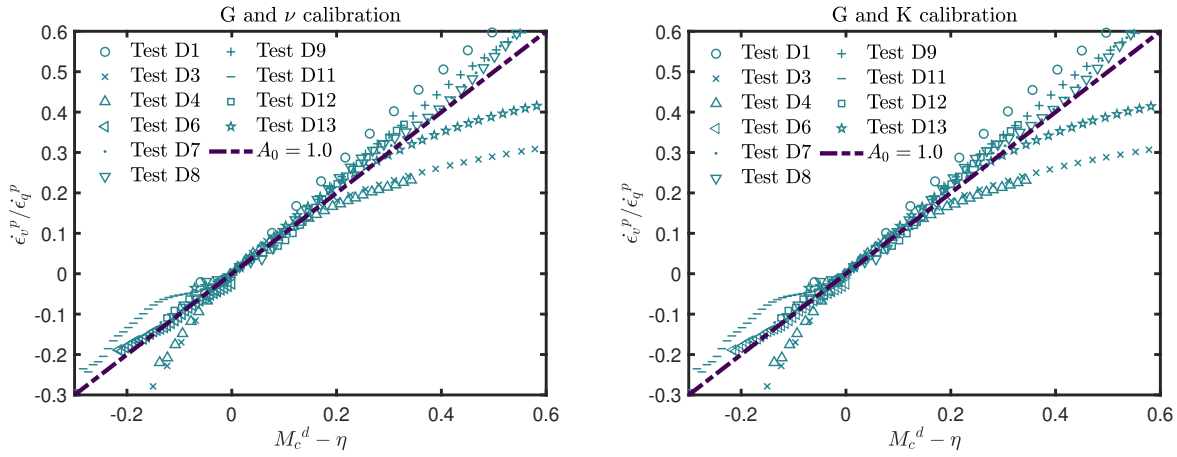

Figure 7.31: Estimation of dilatancy surface parameter A_0 using ψ_D (equation 7.9) and (a) $G-\nu$ calibration (equations 7.2 and 7.3) and (b) $G-K$ calibration (equations 7.2 and 7.4) for batch 1 of Hostun sand

traction is slower for the $G-\nu$ calibration and the same for the $G-K$ calibration for this test, as compared to the results using the original state parameter ψ. Also, the cyclic strain amplitude is larger in magnitude than with the original state parameter ψ, for both bulk modulus calibration methods. The differences observed in the predictions with the two bulk modulus calibration methods using the original state parameter ψ are maintained for the updated state parameter ψ_D. The new state parameter function alters the rate of contraction and strain accumulation so

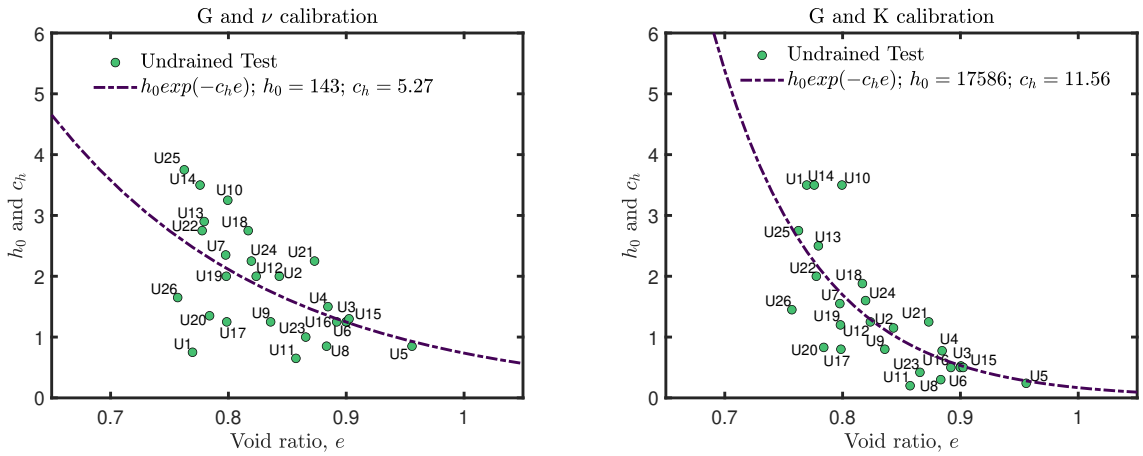

Figure 7.32: Estimation of hardening constants h_0 and c_h using ψ_D (equation 7.9) and (a) $G-\nu$ calibration (equations 7.2 and 7.3) and (b) $G-K$ calibration (equations 7.2 and 7.4) for batch 1 of Hostun sand

Parameter	**Value**	**Parameter**	$G-\nu$ **calibration**	$G-K$ **calibration**
M^c	1.266	$G_0{}^{(2)}$	530	530
c	0.71	$\nu^{(3)}$	0.18	
$Q^{(1)}$	8.3	$K_0{}^{(4)}$		180
$R^{(1)}$	0.73	A_0	1.0	1.0
m	0.01	$h_0{}^{(5)}$	143	17586
p_{at}	100	$c_h{}^{(5)}$	5.27	11.56
n^b	0.65	μ_0	10.3	0.835
n^d	0.086	u	0.9	2.85
z_{max}	20	c_l	50	35
c_z	800	x	10	2.2
n_g	0.95	p_{th}	10	10

$^{(1)}$Implemented in CSL equation 7.1; $^{(2)}$Implemented in equation 7.2; $^{(3)}$Implemented in equation 7.3; $^{(4)}$Implemented in equation 7.4; $^{(5)}$Exponential function used, see section 7.5.2; refer to table 7.16 for model equations.

Table 7.15: Summary of SANISAND-MSf model constants using ψ_D (equation 7.9) for batch 1 of Hostun sand

slightly that the overall impact on liquefaction resistance curves can be neglected.

The inflow cyclic test $ICT/55/100/30/5$ is presented in figures 7.35 and 7.36 using SANISAND-MSf model with model parameters calibrated for ψ and ψ_D. As for the undrained case, the non-standard drained cyclic simulations with ψ_D closely resemble the predictions for $\psi = e - e_{cs}$ as the state parameter. In this particular test, the rate of contraction was exactly similar for the

Equations	Model Constants	Description
Critical State Line:		
$e_{cs} = e_{max} - \frac{(e_{max}-e_{min})R}{Q-ln(p')}$	e_{max} , e_{min} , Q , R	Equation 7.1
Elasticity:		p_{at} : 100 kPa
$G = G_0\ p_{at} e^{-1.8}(\frac{p'}{p_{at}})^{0.5}$	G_0	Equation 7.2
$K = \frac{2(1+\nu)}{3(1-2\nu)}G$	ν	$G-\nu$ calibration, Equation 7.3
$K = K_0\ p_{at} e^{-2}(\frac{p'}{p_{at}})^{0.65}$	K_0	$G-K$ calibration, Equation 7.4
Hardening Rule:		
$b_0 = G_0 h_0 g^{-n_g} exp(-c_h e)(p'/p_{at})^{-1/2}$	h_0 , c_h, n_g	Exponential evolution of b_0
Surface Evolution Laws:		$M^{b,d}_{c/e}$: Surfaces in Compression/Extension
$M^b_c = M^c exp(-n^b \psi_D)$		M^c : Critical Surface Stress Ratio
$M^b_e = cM^c exp(-n^b \psi_D)$	M^c, n^b , n^d , c	cM^c : Critical Surface in Extension
$M^d_c = M^c exp(n^d \psi_D)$		ψ_D: State Parameter
$M^d_e = cM^c exp(n^d \psi_D)$		$(= sign\,(e-e_{cs})\,\lvert e-e_{cs}\rvert^{0.7})$

Table 7.16: Selected/modified equations for SANISAND-MSf model to be used in conjunction with model parameters of table 7.15, refer to table 3.3 for the remaining equations

two state parameters and the cyclic strain amplitude was only slightly increased compared to the Been and Jefferies (1985) state parameter. Again, general trends observed for the two bulk modulus calibrations are replicated in the simulations with the modified state parameter as well. The overall liquefaction resistance prediction remains unchanged.

The cycles to liquefaction using the excess pore pressure and the double strain amplitude criteria for the undrained and non-standard drained cyclic tests of Adamidis and Anastasopoulos (2022), using the updated state parameter ψ_D (equation 7.9), are listed in tables 7.17 and 7.18, respectively. The cycles to liquefaction are comparable with the values in tables 7.9 and 7.12. The liquefaction resistance curves are plotted in figure 7.37 and compared with figures 7.22-7.24. Upon comparison of the liquefaction resistance curves, it is found that only for the dense Hostun sand ($D_r = 66 \pm 3\%$), the slope of the liquefaction resistance curve reduces (from $b = 0.17$ to $b = 0.15$) for the $G-\nu$ calibration. For all other cases, the liquefaction resistance curve has the exact same slope as with the original state parameter $\psi = e - e_{cs}$ simulations. The absence of any significant variation in results of cyclic tests using the updated state parameter ψ_D as opposed to the significant variation observed in monotonic coupled strain tests (refer chapter

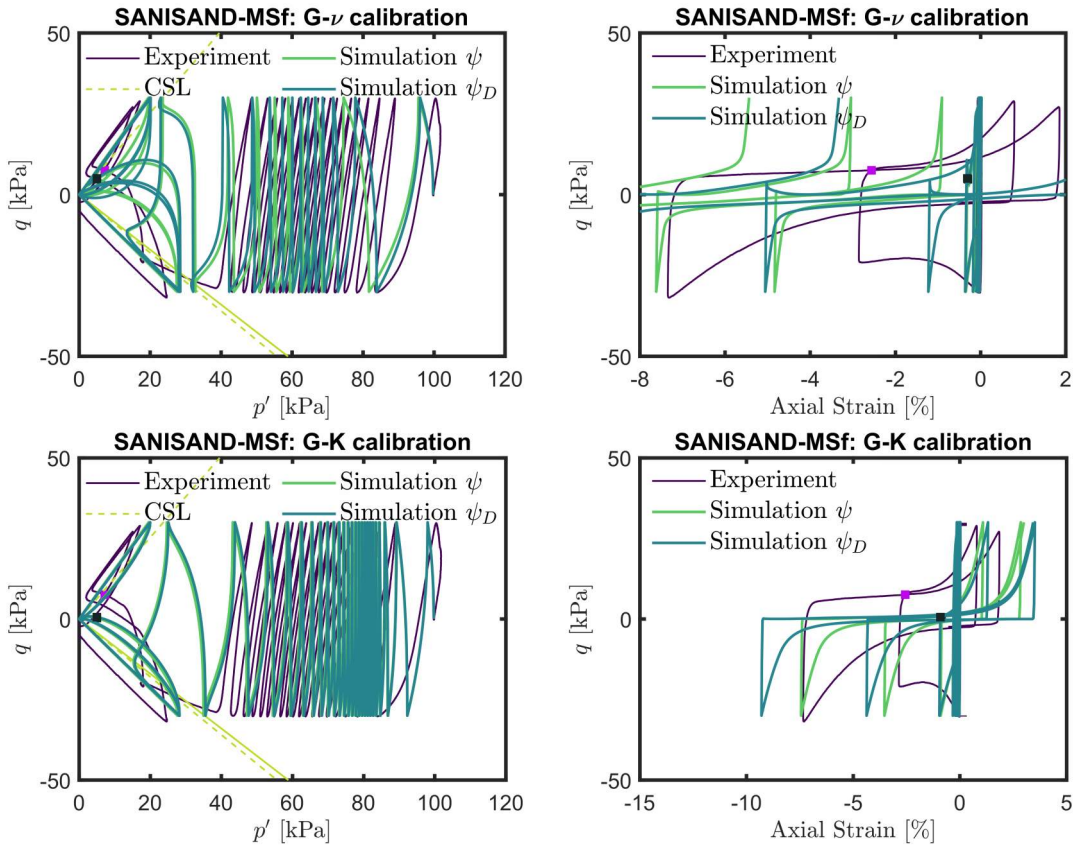

Figure 7.33: Simulation of undrained cyclic triaxial test ICT55/100/30/0 (Adamidis and Anastasopoulos, 2022) using ψ ($= e - e_{cs}$) and ψ_D (equation 7.9) for (a) $G-\nu$ and (b) $G-K$ calibration of SANISAND-MSf model

5) can be attributed to the fact that the cyclic tests were initiated from isotropic consolidation stress of 100 kPa and subjected only to small void ratio changes before liquefaction. In $e-p'$ space, the cyclic tests progress towards lower p' under undrained and water inflow conditions. The critical state line at pressures ≤ 100 kPa has a very gentle slope and the change in void ratio from $p' = 100$ kPa to $p' = 0$ is small due to the high bulk modulus in unloading. These conditions result in very slight changes for the state parameter value, irrespective of its definition. For the water inflow cases, the positive but limited magnitude changes in void ratio ($\delta e < 0.015$ for the tests presented) resulted in even smaller changes in the state parameter values as compared to the undrained cases. On the contrary, for the undrained and coupled strain monotonic tests, even though the change in void ratio is small, the stress path progresses towards higher p' due to dilation and the change in e_{cs} values are significant, leading to quantifiable changes in predic-

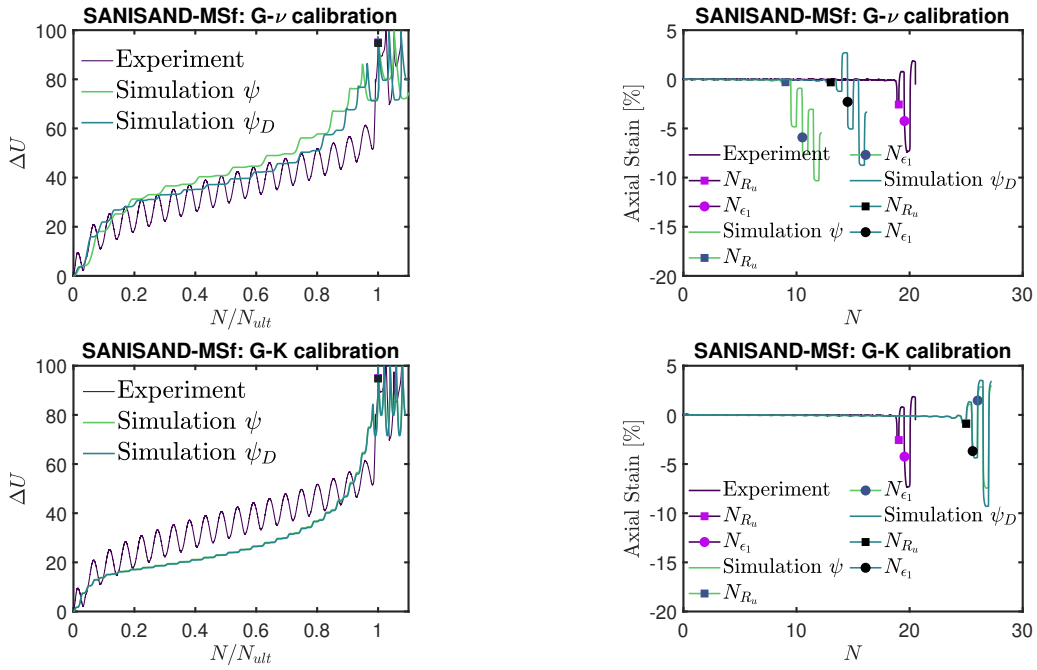

Figure 7.34: Progression of excess pore pressure and axial strain for undrained cyclic triaxial test ICT55/100/30/0 (Adamidis and Anastasopoulos, 2022) using ψ ($=e-e_{cs}$) and ψ_D (equation 7.9) for (a) $G-\nu$ and (b) $G-K$ calibration of SANISAND-MSf model

tions based on the choice of the state parameter definition. As such, it can be concluded that for stress-controlled cyclic loading of isotropically consolidated specimens, the state parameter definition need not be updated in order to achieve better predictions of non-standard drained cyclic behaviour using double surface plasticity models. Instead, this update could become important for cases where static shear can lead to dilation and thus high levels of p', as for instance due to a flow liquefaction failure of a slope.

7.6 Conclusions

In this study, popular double surface plasticity models used for liquefaction-related problems, namely DM04, SANISAND-MSf and PM4Sand3D, were evaluated on their ability to capture non-standard drained cyclic behaviour at an element level under volumetric expansion conditions, that can manifest at the interface of a liquefiable layer and an overlying low permeability layer. The models were calibrated using undrained monotonic and cyclic tests on Hostun sand.

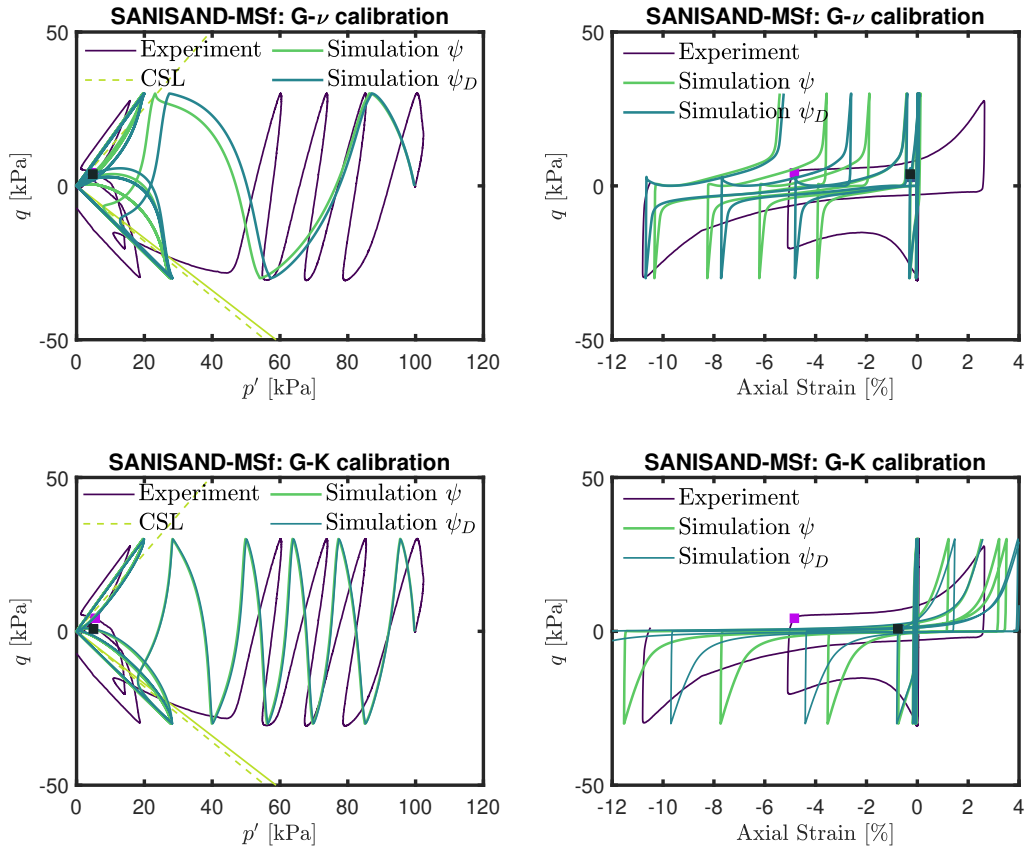

Figure 7.35: Simulation of non-standard drained cyclic triaxial test ICT55/100/30/5 (Adamidis and Anastasopoulos, 2022) using ψ ($= e - e_{cs}$) and ψ_D (equation 7.9) for (a) $G-\nu$ and (b) $G-K$ calibration of SANISAND-MSf model

Two calibration approaches for the bulk modulus K were used: (a) $G-\nu$ calibration - typical calibration of K from G and ν and (b) $G-K$ calibration - direct calibration of K from isotropic unloading tests. The direct calibration of K results in a softer bulk modulus than the typical calibration.

In monotonic tests, a shear modulus G obtained from bender element tests and a K obtained from isotropic unloading data were shown to improve predictions as compared to the typical $G-\nu$ calibration of K for the SANISAND-MSf model and similarly for the DM04 model with the same model parameters. This updated calibration eliminates the need to reduce the small-strain shear modulus G in order to obtain better monotonic simulation results for SANISAND family of models. On the contrary, the PM4Sand3D model performed better with the typical

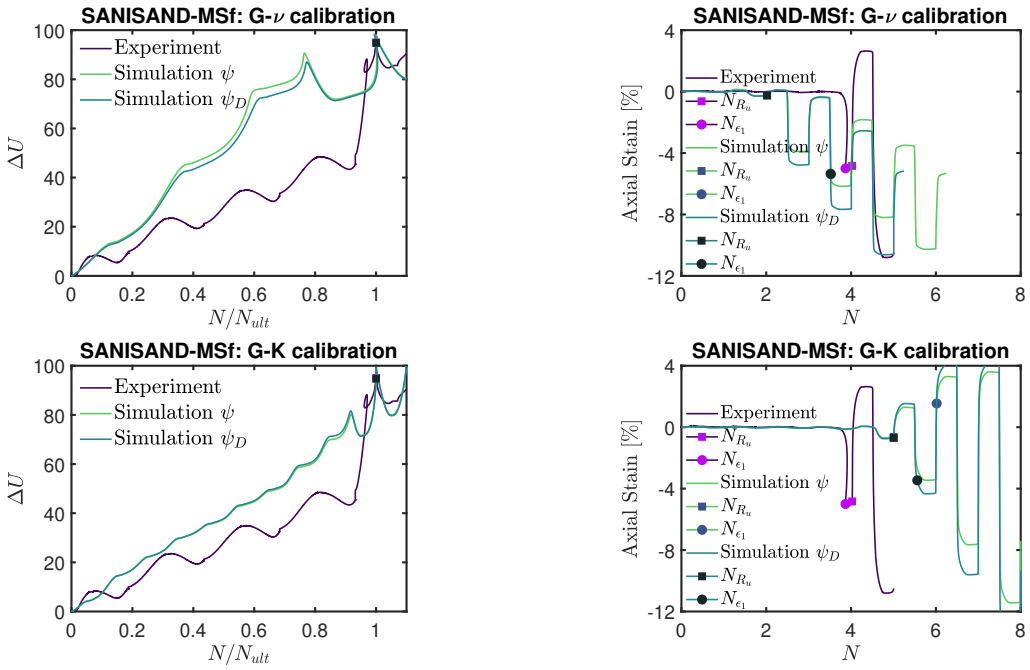

Figure 7.36: Progression of excess pore pressure and axial strain for non-standard drained cyclic triaxial test ICT55/100/30/5 (Adamidis and Anastasopoulos, 2022) using ψ ($= e - e_{cs}$) and ψ_D (equation 7.9) for (a) $G-\nu$ and (b) $G-K$ calibration of SANISAND-MSf model

Test ID	CSR	$N_{R_u}{}^{(a)}$	$N_{R_u}{}^{(b)}$	$N_{R_u}{}^{(c)}$	$N_{\varepsilon_1}{}^{(a)}$	$N_{\varepsilon_1}{}^{(b)}$	$N_{\varepsilon_1}{}^{(c)}$
$ICT65/100/28/0$	0.14	144	50	165	-	52.5	169.6
$ICT65/100/30/0$	0.15	42.5	21.5	58	-	23.5	60.6
$ICT65/100/30/0$	0.15	77.1	23.5	62.5	-	25.5	65.5
$ICT65/100/36/0$	0.18	6	8	17.5	7.7	9.7	21.6
$ICT65/100/39/0$	0.20	3.5	4.5	9	4.6	6.5	11.6
$ICT65/100/40/0$	0.20	4	3.5	7	5.1	5.5	9.5
$ICT55/100/25/0$	0.12	70	85	267	71.2	86.5	268.2
$ICT55/100/30/0$	0.15	19	13	25	19.5	14.5	25.6
$ICT55/100/34/0$	0.17	4.5	5.5	10	4.6	6.5	10.6
$ICT40/100/19/0$	0.10	197	777.5	2739.5	197.6	778.5	2739.5
$ICT40/100/20/0$	0.10	98.1	406.5	1188.5	99.5	407	1189
$ICT40/100/23/0$	0.11	28.5	80.5	145	28.6	81	145.5
$ICT40/100/28/0$	0.14	8	12.5	16.5	8.1	13.5	17
$ICT40/100/30/0$	0.15	6	6.5	7	6.2	6.5	7.5
$ICT40/100/33/0$	0.16	2	3.5	4	2	3.5	4.1

$^{(a)}$Undrained cyclic triaxial tests from Adamidis and Anastasopoulos (2022);
$^{(b)}G-\nu$ calibration (equations 7.2 and 7.3); $^{(c)}G-K$ calibration (equations 7.2 and 7.4).

Table 7.17: Comparison of N_{R_u} and N_{ε_1} in undrained cyclic tests with ψ_D (equation 7.9) and using $G-\nu$ and $G-K$ calibration of SANISAND-MSf model

Test ID	CSR	$\dot{\varepsilon}_v/\dot{\varepsilon}_{v,max}$	$\varepsilon_v/cyc(\%)$	${N_{R_u}}^{(a)}$	${N_{R_u}}^{(b)}$	${N_{R_u}}^{(c)}$	${N_{\varepsilon_1}}^{(a)}$	${N_{\varepsilon_1}}^{(b)}$	${N_{\varepsilon_1}}^{(c)}$
$ICT65/100/10/1$	0.05	1%	-0.01	67.1	13.5	49	-	-	51.6
$ICT65/100/13/1$	0.07	1%	-0.01	64.1	12.5	42	-	-	45.6
$ICT65/100/20/1$	0.10	1%	-0.01	40	10	29.5	-	12.5	33.5
$ICT65/100/28/1$	0.14	1%	-0.01	25.5	6	17	-	7.5	18.7
$ICT65/100/10/5$	0.05	5%	-0.04	15.2	4.0	14	-	4.6	16.5
$ICT65/100/20/5$	0.10	5%	-0.04	10.5	3	10	11.7	4.5	11.7
$ICT65/100/30/5$	0.15	5%	-0.03	4.5	2.5	7.5	5.6	4.5	9.6
$ICT65/100/15/15$	0.07	15%	-0.1	5	1.5	5.1	6.7	2.5	7.6
$ICT65/100/20/15$	0.1	15%	-0.1	5	1.5	4.5	-	2.5	7.6
$ICT65/100/25/15$	0.13	15%	-0.1	4	1.5	4	5.6	3.5	6.5
$ICT65/100/30/15$	0.15	15%	-0.08	3	1.5	4	3.7	3.5	7.5
$ICT55/100/15/5$	0.07	5%	-0.04	14.1	3.5	12	-	4.5	13
$ICT55/100/25/5$	0.13	5%	-0.04	7	2.5	7	7.5	3.5	7.6
$ICT55/100/30/5$	0.15	5%	-0.04	4	2	5	3.9	3.5	5.6
$ICT40/100/12/5$	0.06	5%	-0.05	11.8	3.1	11.1	-	3.5	11.5
$ICT40/100/20/5$	0.10	5%	-0.04	9.5	3	9	9.7	3.5	9.2
$ICT40/100/22/5$	0.11	5%	-0.05	6.9	2	6.5	6.9	2.5	6.5
$ICT40/100/25/5$	0.13	5%	-0.04	5	2	5.5	5.1	2.5	6

$^{(a)}$Non-standard drained cyclic triaxial tests from Adamidis and Anastasopoulos (2022);
$^{(b)}G-\nu$ calibration (equations 7.2 and 7.3); $^{(c)}G-K$ calibration (equations 7.2 and 7.4).

Table 7.18: Comparison of N_{R_u} and N_{ε_1} in non-standard drained cyclic tests with ψ_D (equation 7.9) and using $G-\nu$ and $G-K$ calibration of SANISAND-MSf model

calibration as its underlying equations are calibrated implicitly using K derived from G and ν.

The undrained cyclic behaviour was simulated next using both calibration methods for the bulk modulus. The general cyclic behaviour was captured well for both calibration methods by all three models, although the direct calibration of K resulted in a reduced contraction rate, increasing the number of cycles to liquefaction, which was a desirable outcome. Additionally, the strain accumulation progressed slower per cycle for DM04 and SANISAND MSf, with rapid increase in amplitude on approach to liquefaction, thus resulting in better predictions of observed behaviour than the $G-\nu$ calibration. The PM4Sand3D model however, produced very similar behaviour under the two bulk modulus calibration methods, suggesting that the dependence of the governing equations on the choice of bulk modulus is limited. The SANISAND-MSf model undrained liquefaction resistance curves using both calibration methods closely matched the experimental baseline undrained curves across all densities. It should be noted that the latter

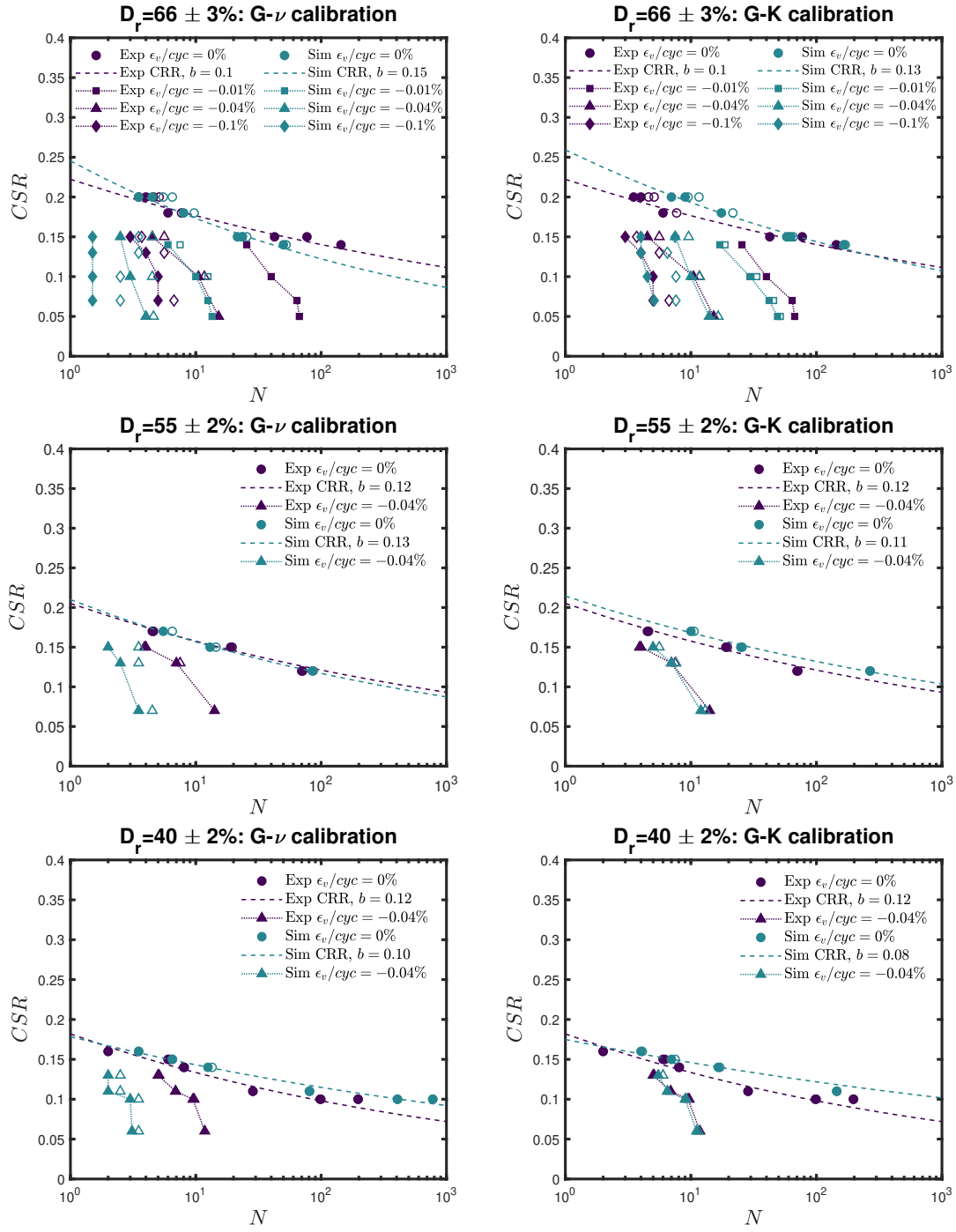

Figure 7.37: Cyclic resistance under undrained and inflow conditions of batch 1 of Hostun sand with ψ_D (equation 7.9) and using $G-\nu$ and $G-K$ calibration of SANISAND-MSf model

two models have input parameters that can be directly calibrated from the actual liquefaction resistance curves, allowing a closer prediction of the observed behaviour.

Finally, the volumetric expansion tests were simulated by imposing constant water inflow

rates. Using both calibration techniques for the bulk modulus, the cycles to trigger liquefaction drastically lowered from the undrained case even with a small water inflow rate, similarly to the experimental observations, indicating quicker loss of strength and manifestation of liquefaction than for the undrained case. The inflow liquefaction resistance curves were again found to be steeper with the typical calibration of K using G and ν and the shift to the left of the baseline curves was more pronounced than that observed in experiments, leading to overly conservative predictions. In contrast, the direct calibration of K resulted in significantly better predictions of the water inflow liquefaction resistance curves across all three models.

To quantify the implications of bulk modulus calibration, the change in void ratio δe with mean effective stress p' for low to high CSR cyclic tests under the same water inflow rate were plotted for the experiments and the simulations using both bulk modulus calibrations. The directly calibrated K was found to capture the cumulative effect of isotropic unloading and undrained shearing, under water inflow conditions, significantly better than the $G-\nu$ calibration. Overall, the SANIDAND-MSf and the PM4Sand3D models were found to adequately capture all aspects of the cyclic behaviour under water inflow conditions. In particular, the SANISAND MSf model was able to closely predict the experimentally observed liquefaction resistance values across all densities and inflow rates when using the direct calibration of K.

The updated state parameter definition, proposed in chapter 5 to improve predictions of coupled strain monotonic behaviour in SANISAND models, was implemented in the SANISAND-MSf model to understand its impact on undrained and inflow cyclic performance using both bulk modulus calibration methods. The cyclic performance was found to be minimally impacted by the updated state parameter definition which was attributed to the minimal changes in the state parameter value in $e-p'$ space experienced by the soil samples upon cyclic shearing. However, under monotonic shearing the state parameter definition plays a significant role in model performance as the change in p' experienced by the soil specimens is large enough to induce drastic changes in the values of e_{cs} and consequently the values of the state parameter. Therefore, it can be concluded that a bulk modulus calibrated directly from isotropic unloading experimental

data is essential for realistic modelling of cyclic behaviour under drainage conditions that deviate from the undrained assumption whereas, the updated state parameter definition has minimal impact on the cyclic behaviour.

Chapter 8

Numerical analysis of liquefaction triggering in layered deposits

8.1 Introduction

The effects of drainage have so far been studied at the element level, using constant strain coupling ratios under monotonic loading and constant volumetric strain rates under cyclic loading, thus providing a fundamental understanding of how they impact liquefaction triggering. Nevertheless, the volumetric strain evolution within a soil deposit is a complex process involving soil properties, such as permeability and stiffness, and system properties, such as the arrangement of different permeability layers (Cubrinovski et al., 2019; Ntritsos and Cubrinovski, 2022; Sinha et al., 2024; Tsaparli et al., 2020).

This chapter examines the consequences of drainage-induced void redistribution at a system level, considering several idealised stratified deposits. Comparisons are drawn between numerical simulations performed with a 'traditional' shear modulus - Poisson's ratio ($G-\nu$) elasticity calibration, versus the direct shear and bulk modulus ($G-K$) calibration process, which in the previous chapter was shown to significantly improve predictions of cyclic liquefaction triggering at the element level.

Numerical simulations at the system level were run using the open-source finite-element code OpenSees (McKenna, 2011), with a fully coupled u-p formulation (Zienkiewicz and Shiomi, 1984) element. As demonstrated in chapter 7, the updated state parameter definition had minimal influence on the cyclic liquefaction resistance curves. Therefore, its impact on liquefaction triggering is not evaluated in this chapter, which focuses on level deposits. The updated state parameter is expected to become important for slopes, where a flow failure could be triggered; however, such an investigation is beyond the scope of this work. The SANISAND-MSf constitutive model (M. Yang et al., 2022) as described in section 3.4 was selected to model liquefiable sand layers, as it was found to adequately capture cyclic behaviour under undrained and inflow conditions across all densities in chapter 7. Moreover, the model has already been implemented in OpenSees by Zeng et al., 2024.

The chapter proceeds in three stages. First, it was verified that the OpenSees implementation yields consistent results with the MATLAB implementation used so far in the thesis, through comparisons of element-level monotonic and cyclic undrained behaviour of Hostun sand, for both a $G-\nu$ and a $G-K$ calibration, with parameters listed in table 7.4. Next, a validation exercise was conducted, versus centrifuge test results on a free-field liquefiable layer of Hostun sand from Adamidis and Madabhushi (2018). The impact of the two calibration options was examined as part of this exercise. Finally, liquefaction triggering in layered deposits was investigated numerically through a series of parametric simulations. The layer arrangement was altered to target cases of false predictions by the simplified liquefaction susceptibility evaluation procedure (Seed and Idriss, 1971). The parametric investigation results were used to quantify the range of reliability for simplified methodology predictions that are driven by the undrained assumption. Conclusions were drawn regarding co-seismic drainage and layer interaction effects for liquefaction triggering, as well as on the implications of the bulk modulus calibration in numerical simulations of such problems.

8.2 Verification of element-level behaviour in OpenSees

OpenSees (McKenna, 2011) is an open source finite-element software developed for earthquake engineering simulations of structural and geotechnical engineering systems. The framework is written in C++ but can also interact with Python. The main difference between OpenSees and other seismic analysis software is the flexibility offered to users in accessing and modifying the material, element and analysis source codes, so that modifications to material definitions can be easily implemented and the framework rebuilt using Visual Studio. Both because this research involves the modification of the bulk modulus definition and due to the seismic problems studied, OpenSees was deemed an appropriate platform. In this section, an overview of the model setup for the element-level simulations is demonstrated and comparisons of OpenSees simulation results with the MATLAB code used thus far are presented.

8.2.1 Model setup

The element-level study, replicating triaxial tests presented in chapter 7, was performed in OpenSees using a 3D single brick (1.0 m $\times$ 1.0 m $\times$ 1.0 m) SSPbrickUP element (McGann et al., 2015). This element is an eight-noded hexahedron with stabilised single-point integration (SSP), developed for use in dynamic analysis of saturated porous media incorporating a mixed displacement-pressure (u-p) formulation (Zienkiewicz and Shiomi, 1984). The single integration point avoids hour-glass locking modes and is computationally more efficient. The stabilisation constant was set to 1.5×10^{-9}. The element has four nodal degrees-of-freedom; three for translation and one for pore pressure. During the consolidation stage, the translation degrees-of-freedom at each node were released as shown in figure 8.1(a). A quarter value of the confinement pressure was applied as nodal loads along the free degrees-of-freedom, summing to the full confinement pressure along the three directions. The confinement pressure was applied as a linear timeseries under 'Plain' load pattern that incrementally increased from zero to the desired pressure during consolidation. The pore pressure degrees-of-freedom were fixed at this

stage, which eliminated any pore-pressure buildup, thereby imposing a fully drained condition.

Prior to the shearing stage, the void ratio was updated to the post-consolidation value obtained in the corresponding experiment using the setParameter command in OpenSees. The pore pressure fixity was removed at all nodes, represented by red circles in figure 8.1(b). This allowed pore pressures to accumulate with time depending on the permeability of the material during shearing. To approximate an undrained condition, the permeability was set to a very low value of $1x10^{-10}$ m/s. Note that the pore pressure values at nodes are recorded during analysis as velocity vectors in OpenSees and therefore all analysis stages were defined as 'transient'. The monotonic triaxial test simulations were sheared by applying a linear timeseries of vertical displacement at nodes 5, 6, 7 and 8 (as shown in figure 8.1(b)) with the maximum displacement corresponding to the target axial strain of 30%. The cyclic triaxial experiments were conducted as stress-controlled and hence a sinusoidal load timeseries was applied at nodes 5, 6, 7 and 8 in the vertical direction (as shown in figure 8.1(b)) with a nodal load amplitude equaling a quarter of the deviatoric stress.

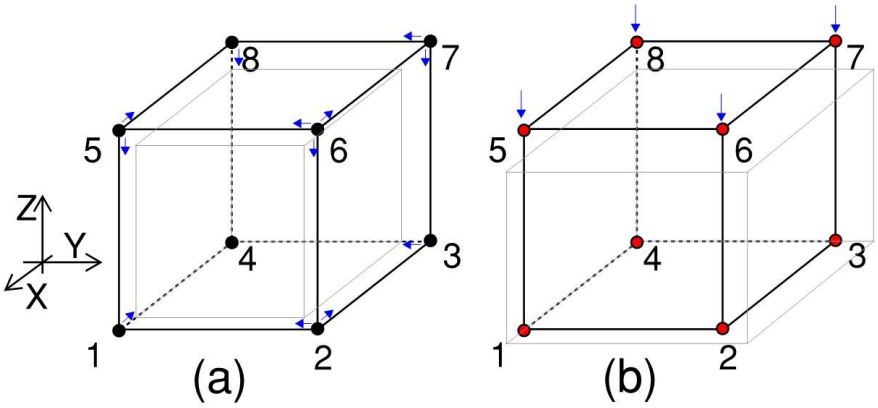

Figure 8.1: SSPbrickUP element configuration for undrained triaxial test during (a) consolidation stage and (b) shearing stage

8.2.2 Analysis parameters

The boundary constraints were applied using the penalty method with a penalty number of 10^{18}. The solution algorithm employed was the Krylov-Newton method with Full General system to

solve the equations. The integration in time was computed using the constant average acceleration Newmark method ($\gamma = 0.5$ and $\beta = 0.25$). Convergence at the end of each iteration was checked using the norm of the displacement increment with a tolerance of 10^{-3} and a maximum number of 100 iterations. The SANISAND family of material models lack small-strain damping (Chen, 2020). Therefore, frequency dependent Rayleigh damping coefficients corresponding to 2% damping ratio at frequencies 0.0025 Hz and 10 Hz were applied to the analysis.

8.2.3 Material model

The SANISAND-MSf constitutive model, implemented in OpenSees by Zeng et al., 2024 was used. The model is implemented using modified-Euler and forward-Euler explicit integration schemes with automatic sub-stepping and error control. The modified-Euler integration scheme was used in all the OpenSees simulations conducted in this study. A cut-off treatment at low mean effective stresses (Ghofrani, 2018) has been introduced in the model's implementation in OpenSees (Zeng et al., 2024), which was not included in the MATLAB implementation used in chapter 7, which exclusively followed the proposed SANISAND-MSf formulation (M. Yang et al., 2022). The p_{cut} was set at $= 0.5$ kPa for all simulations in this study. This cut-off is expected to create a discrepancy between the OpenSees and MATLAB simulation results in the semifluidised region, for very low effective stresses. However, it is not expected to be consequential for liquefaction triggering, which is the main objective of this research.

The source code of the SANISAND-MSf implementation in OpenSees had to be modified to cater to the Hostun sand calibrated parameters from table 7.4, summarised in table 7.5. The critical state line was changed from a power law to Bolton's form as per equation 7.1. The elastic moduli were updated to equation 7.2 for the shear modulus and equation 7.3 for the bulk modulus in the $G-\nu$ (typical) calibration, or equation 7.4 in the $G-K$ (direct) calibration. Finally, the hardening parameter b_0 was updated to an exponential form, as listed in table 7.5. These changes were incorporated in Visual Studio and the OpenSees application was rebuilt.

8.2.4 Simulation results

This section presents comparisons of monotonic and cyclic undrained triaxial test simulations in OpenSees, as outlined above, and MATLAB, as presented in chapter 7. Additionally, comparisons of resulting cyclic resistance curves are given.

Undrained monotonic behaviour

Monotonic tests listed in table 7.1 were simulated in OpenSees using the SANISAND-MSf parameters from table 7.4. As an example, figure 8.2 shows the simulation results for Test ICUMC/0.843/300 (U2) for the $G-\nu$ calibration and the $G-K$ calibration. As seen from the figure, the monotonic responses from the two implementations are effectively coincident over the investigated strain range.

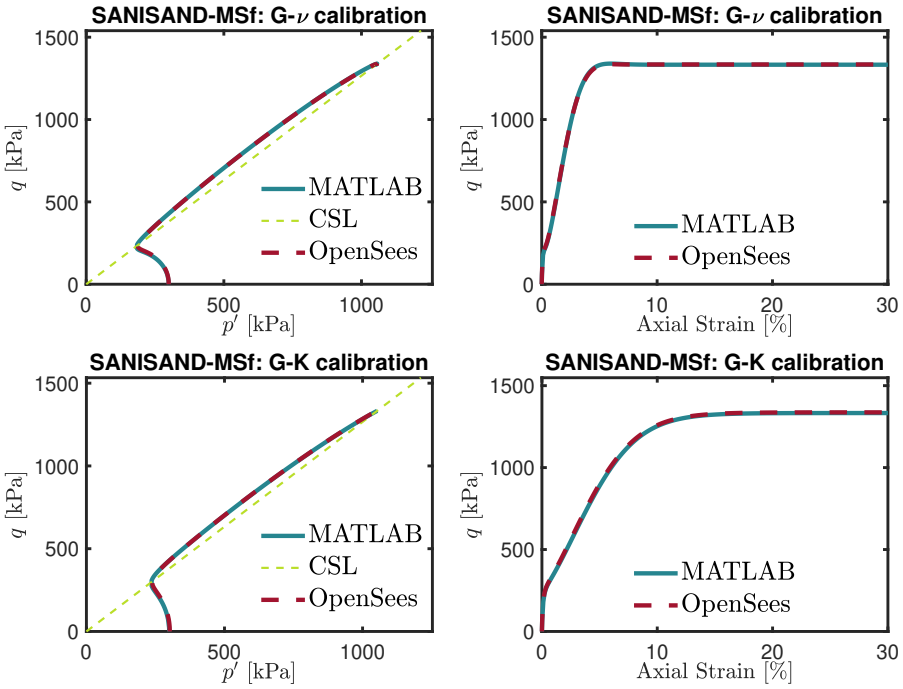

Figure 8.2: Comparison of undrained monotonic triaxial test simulations of ICUMC/0.843/300 (Test U2) on Hostun sand for (a) $G-\nu$ calibration (top) and (b) $G-K$ calibration (bottom) of SANISAND-MSf model

Undrained cyclic behaviour

The undrained cyclic triaxial tests on Hostun sand from Adamidis and Anastasopoulos (2022) were simulated next in OpenSees for the two bulk modulus calibration methods. The results were compared with MATLAB simulations using two strain increment values, 1×10^{-6} and 1×10^{-8}. The comparison for Test ICT65/100/28/0 is presented in figures 8.3 and 8.5, for the $G-\nu$ and the $G-K$ calibration, respectively. Additional plots showing the accumulation of excess pore pressure and axial strains are presented in figures 8.4 and 8.6, for the $G-\nu$ and the $G-K$ calibration, respectively. For both calibration schemes, the OpenSees simulations matched better with the MATLAB simulations using a strain increment of 1×10^{-8}, with respect to both excess pore water pressure and axial strain accumulation. Overall, the results produced by both the MATLAB and the OpenSees implementations are very similar up to the onset of liquefaction.

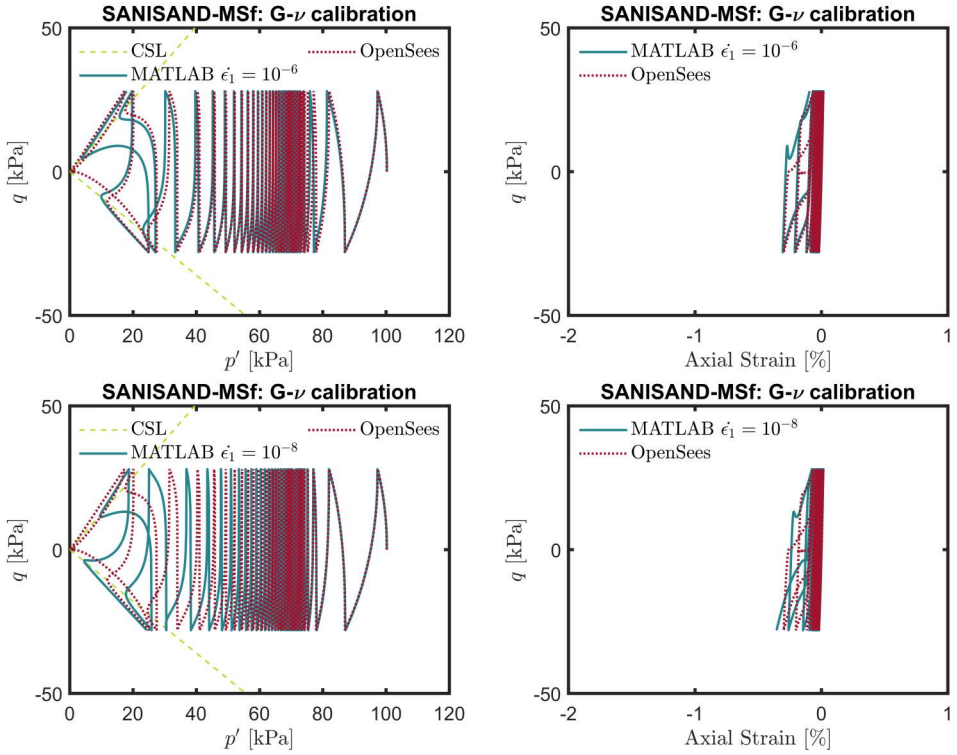

Figure 8.3: Comparison of undrained cyclic triaxial test simulations of ICT65/100/28/0 on Hostun sand with (a) strain increment of 1×10^{-6} (top) and (b) strain increment of 1×10^{-8} (bottom) for $G-\nu$ calibration of SANISAND-MSf model

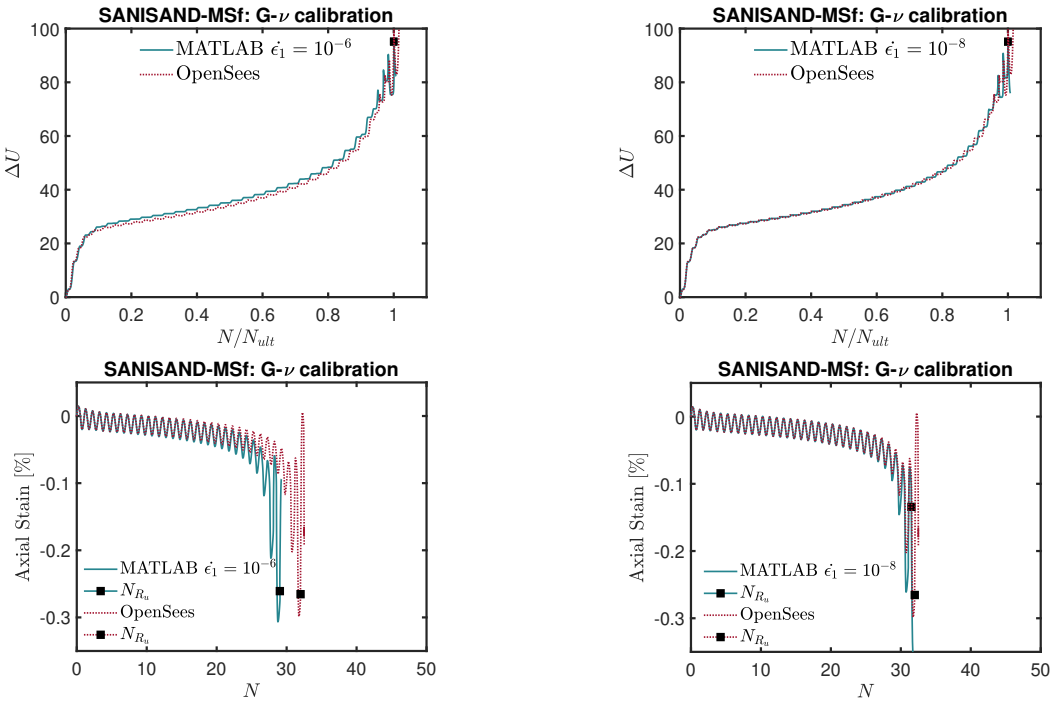

Figure 8.4: Comparison of pore pressure and axial strain accumulation for undrained cyclic triaxial test ICT65/100/28/0 on Hostun sand with (a) strain increment of 1×10^{-6} (left) and (b) strain increment of 1×10^{-8} (right) for $G - \nu$ calibration of SANISAND-MSf model

It should be noted that the sensitivity of the MATLAB implementation to the strain increment value is expected for the explicit integration scheme used. Differences in the cyclic simulation results between OpenSees and MATLAB can be attributed to the different integration schemes: forward Euler for MATLAB and modified Euler for OpenSees. In the MATLAB implementation, the cyclic load was applied through strain increments with stress reversals initiated upon reaching the prescribed maximum magnitude of deviatoric stress within a tolerance. The tolerance to attain the maximum amplitude of deviator stress in OpenSees was stricter than in MATLAB. Also, as mentioned before, the cut-off treatment at low p' of OpenSees was not included in the MATLAB implementation. Nonetheless, the cycles to liquefaction triggering based on excess pore pressure ratio was not significantly impacted by the aforementioned differences and therefore the comparison between the two implementations was deemed to be satisfactory.

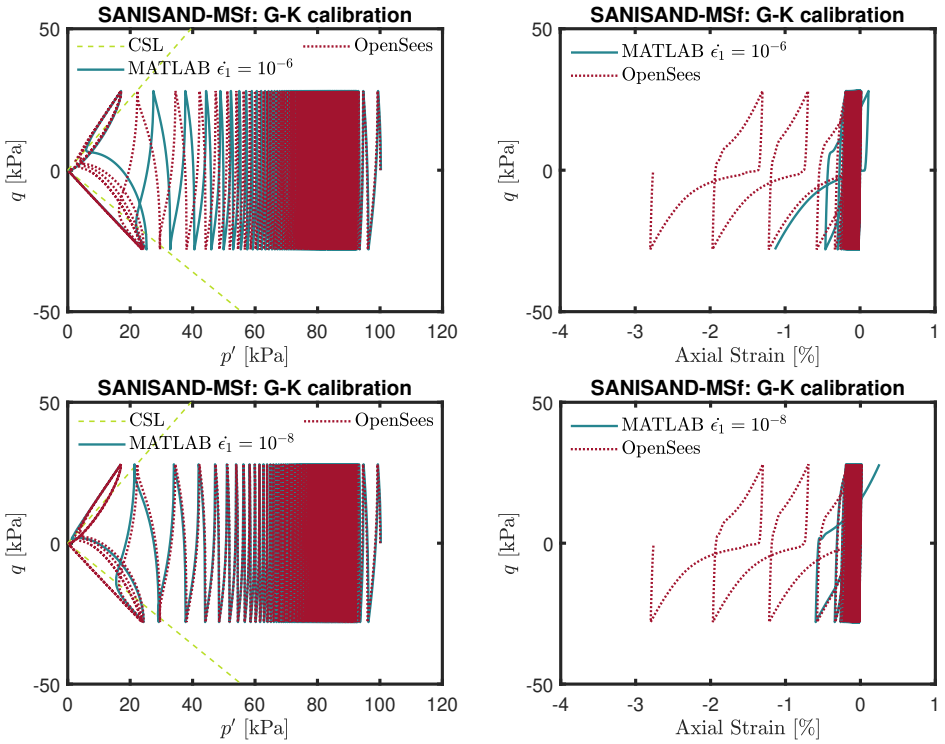

Figure 8.5: Comparison of undrained cyclic triaxial test simulations of ICT65/100/28/0 on Hostun sand with (a) strain increment of 1×10^{-6} (top) and (b) strain increment of 1×10^{-8} (bottom) for $G-K$ calibration of SANISAND-MSf model

Cyclic resistance curves

The cyclic resistance curves presented in chapter 7 based on the excess pore pressure ratio reaching $R_u = 95\%$ were generated in OpenSees for all three available densities and compared with the corresponding MATLAB implementation results. Figure 8.7 shows the cyclic resistance curves for density $D_r = 66 \pm 3\%$ as an example, using both bulk modulus calibrations considered.

As noted in the previous section, the cycles to trigger liquefaction in OpenSees matches very well with the corresponding MATLAB results using a strain increment of 1×10^{-8} for both bulk modulus calibration methods. The good match in both monotonic and cyclic behaviour verifies that the results of this chapter, generated using the OpenSees implementation, are consistent with the results of the previous chapters, generated using the MATLAB implementation.

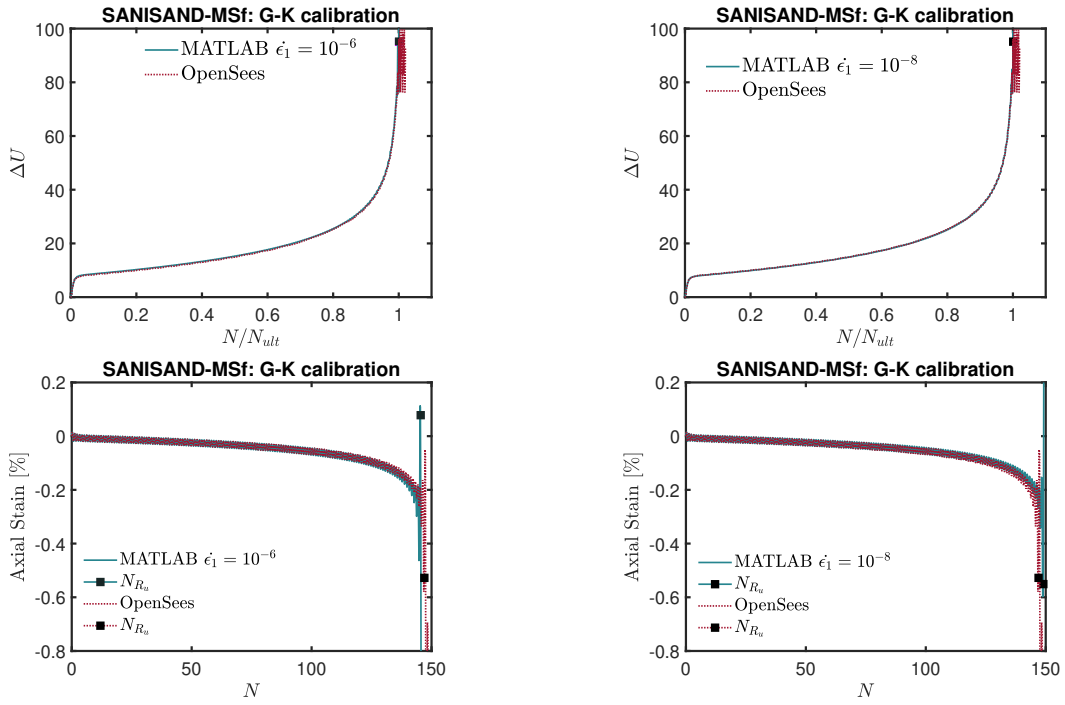

Figure 8.6: Comparison of pore pressure and axial strain accumulation for undrained cyclic triaxial test ICT65/100/28/0 on Hostun sand with (a) strain increment of 1×10^{-6} (left) and (b) strain increment of 1×10^{-8} (right) for $G-K$ calibration of SANISAND-MSf model

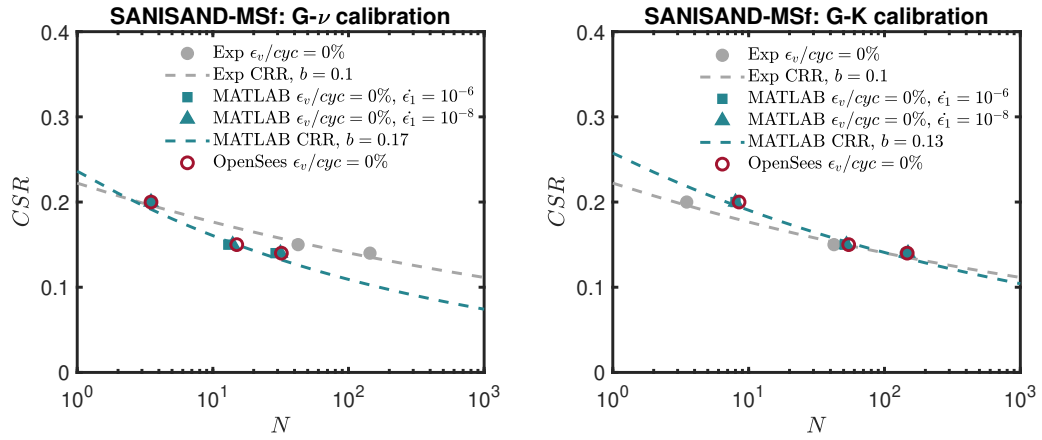

Figure 8.7: Comparison of cyclic resistance curves for Hostun sand for $D_r = 66 \pm 3\%$ using $G-\nu$ and $G-K$ calibration methods in OpenSees and MATLAB implementation

8.3 Validation versus centrifuge testing data

In this section, the simulations produced in OpenSees using the model implementation discussed above are validated for a uniform density, free-field deposit versus centrifuge test results. In par-

ticular, centrifuge experiment OA3 is studied, as detailed in Adamidis and Madabhushi (2018). A schematic of the model cross-section is given in figure 8.8. The dimensions are noted in model scale and the centrifugal acceleration was $50g$. Accelerometers are denoted by '*A*', pore pressure transducers are denoted by '*P*' and displacement transducers by '*L*'. The left side of the model represents a free-field soil column. On the right side of the model, a flexible but impermeable chamber was introduced to study the effects of drainage. In this section, the soil column representing a free-field condition is examined. The effects of the two alternative bulk modulus calibration schemes are also investigated.

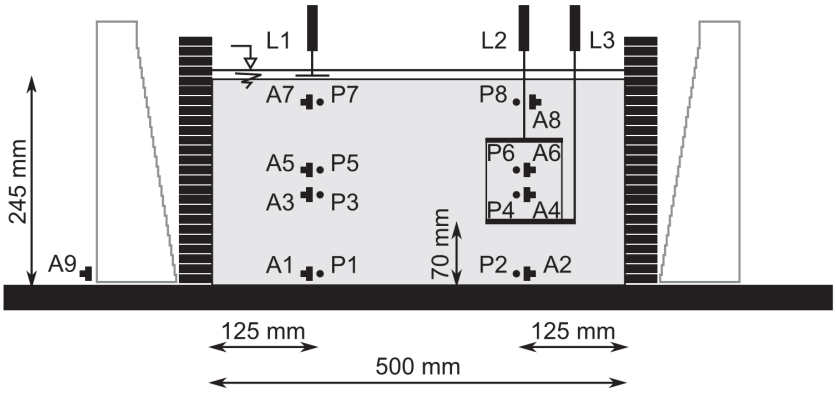

Figure 8.8: Schematic of model cross-section in centrifuge experiment OA3, reproduced from Adamidis and Madabhushi (2018)

8.3.1 Model setup

A 1D soil column was created in OpenSees, matching the prototype scale ($= 50\times$ model scale) geometry of the instrumented column in the centrifuge experiment. Nodes at the same vertical elevation were tied using the equalDOF command, to have the same displacements and thus represent a shear beam model. Element type SSPQuadUP (McGann et al., 2012) was used, with a stabilisation constant of 1×10^{-9}. The water table was set at the top of the column by fixing the pore pressure degrees-of-freedom at the top two nodes, to reproduce the fully saturated sand deposit of the centrifuge test. The base nodes were fixed against translation in vertical direction and the input motion was applied in the horizontal direction. The mesh size

was determined based on the small-strain shear wave velocity (V_s), calculated from the small-strain shear modulus (G_{max}) and the saturated density (ρ), as per equation 8.1. The small-strain shear modulus was determined from equation 7.2 with mean effective stress (p') calculated from the vertical effective stress (σ'_v) and the coefficient of earth pressure at rest (K_o), assuming plane-strain conditions (equation 8.2). Following Ramirez et al., 2018, the minimum wavelength was calculated from V_s and a conservatively assumed maximum input motion frequency (f_{max}) of 10 Hz. As an alternative, one could assume a lower maximum frequency and an appropriately reduced shear modulus corresponding to a liquefied deposit. For instance, the same wavelength calculated here could have been produced by a combination of $f_{max} = 1$ Hz and G_{max} reduced by 100. Equation 8.3 calculates the height corresponding to the first mode shape, which is reduced by a factor C to produce the maximum mesh height. The shear wave velocity profile, mesh height calculation and the corresponding soil column mesh profile in OpenSees are shown in figure 8.9. Elements of 0.25 m height were chosen, which correspond to > 8 elements per quarter wavelength, for all but the very top of the layer.

$$V_s = \sqrt{\frac{G_{max}}{\rho}} \tag{8.1}$$

$$p' = \sigma'_v \frac{(1+2K_o)}{3}; \quad K_o = \frac{\nu}{1-\nu} \tag{8.2}$$

$$h_{max} = \frac{V_s}{4Cf_{max}}; \quad f_{max} = 10\,Hz; \quad C = reduction\ factor \tag{8.3}$$

8.3.2 Analysis parameters

Constraints were applied using the penalty method with a penalty number of 10^{12}. The solution algorithm used was the Krylov-Newton method with ProfileSPD system to solve the equations. The integrator was defined as the constant average acceleration Newmark method ($\gamma = 0.5$ and $\beta = 0.25$). The norm of the displacement increment with a tolerance of 10^{-3} was used to check convergence at the end of each iteration with a maximum number of 50 iterations. Initially,

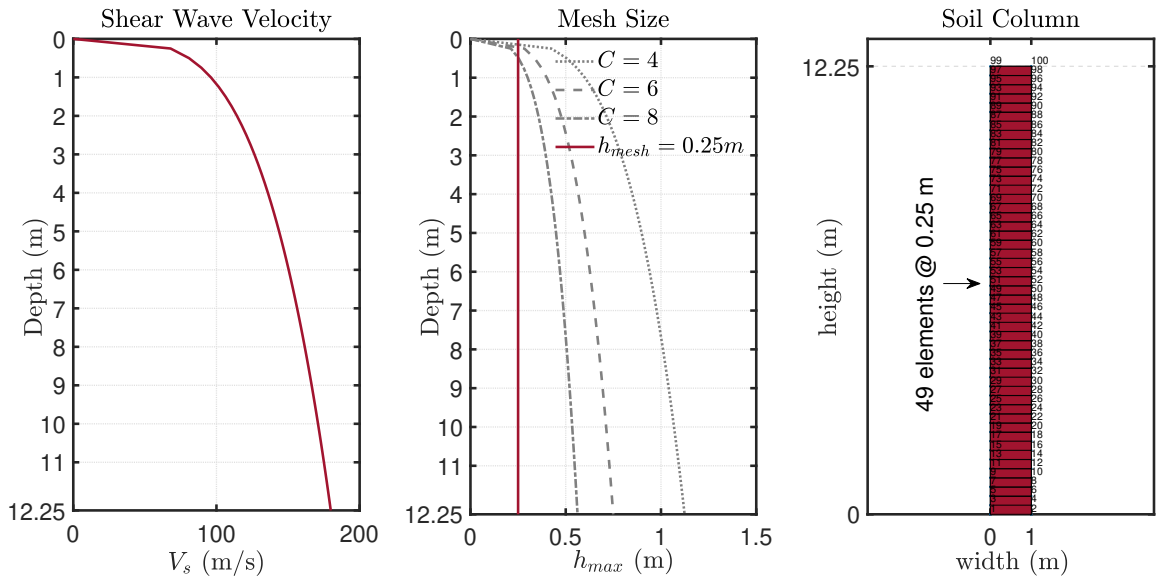

Figure 8.9: Shear wave velocity profile (left); mesh height calculation along soil depth (centre) and schematic of soil column in OpenSees (right)

modal analysis of the soil deposit using a linear elastic column underlain by rigid bedrock was conducted. The uniform shear stiffness was computed from the initial soil state ($G = 41.6$ MPa). Frequency-dependent Rayleigh damping was applied with 2% damping ratio (Chen et al., 2021) corresponding to the modal analysis results for first and third modal frequencies of the soil column, $f_1 = 3$ Hz and $f_3 = 15$ Hz, respectively (Kwok et al., 2007). An initial, gravity analysis was conducted using a permeability of 1.0 m/s and large time steps to attain convergence with pure elastic behaviour. Elastoplastic behaviour was then initiated using the updateMaterialStage command and the gravity analysis was run for some further steps, using smaller time increments. During the gravity analysis, an earth pressure coefficient corresponding to Poisson's ratio $\nu = 0.3$ was applied to generate appropriate horizontal soil stresses. Post gravity analysis, the soil permeability was updated to 1×10^{-3} m/s at the prototype scale, following Adamidis and Madabhushi (2018). Appropriate changes to the Poisson's ratio (for $G - \nu$ calibration) and the bulk modulus definition (for $G - K$ calibration) were applied. For the dynamic analysis, a sensitivity study was conducted to determine the maximum time step based on the maximum shear wave velocity and the minimum vertical element size in the model (LeVeque,

2007; Tasiopoulou et al., 2015). A time step of $\Delta t = 1\text{x}10^{-3}$ s was adopted to achieve a balance between result accuracy and computational efficiency. The input base acceleration for the first earthquake OA3-EQ1 was reproduced from Adamidis and Madabhushi (2018). It was a pseudo-harmonic motion with a frequency around 1 Hz in prototype scale, as shown in figure 8.10.

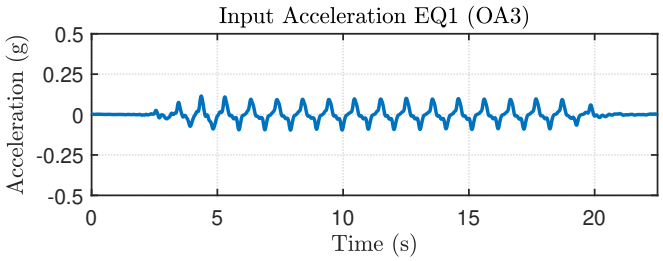

Figure 8.10: Input acceleration time history for centrifuge test OA3-EQ1 (Adamidis and Madabhushi, 2018)

8.3.3 Soil properties and material model

Hostun sand was used in the centrifuge experiments where the sand layers were prepared using air pluviation (Adamidis and Madabhushi, 2018). The voids ratio obtained in the centrifuge tests was $e = 0.825$ (Adamidis and Madabhushi, 2016), which gives a relative density of 55.9%, based on a maximum void ratio of $e_{max} = 1.049$ and a minimum void ratio of $e_{min} = 0.648$, as reported by Kassas et al. (2021). The saturated density of the sand was calculated based on the voids ratio and the specific gravity of solids, $G_s = 2.65$ from Adamidis and Madabhushi (2018). The critical state line given by equation 7.1 was used. The material model in OpenSees was defined as the SANISAND-MSf model (M. Yang et al., 2022) with slight modifications to the memory surface parameters and fabric-dilatancy constants, calibrated and reported in chapter 7. The modifications were made so as to generate undrained cyclic resistance curve as close as possible for the two bulk modulus expressions to the experimental cyclic resistance curve corresponding to $D_r = 55 \pm 2\%$. The memory surface parameters and fabric dilatancy constants for the two bulk modulus calibration are listed in table 8.1. The remaining parameters can be

obtained from table 7.4.

Parameter	$G-\nu$ calibration	$G-K$ calibration
μ_0	10.3	0.6
u	0.9	3.0
c_z	800	8000

Note: Refer table 7.4 for remaining parameters.

Table 8.1: Memory surface parameters for SANISAND-MSf model for Hostun sand

8.3.4 Simulation results

The gravity analysis results are presented first followed by the dynamic analysis results.

Gravity analysis results

The imposed initial state of vertical, horizontal and shear stresses, and pore pressures at the prototype scale is presented in figures 8.11. Note that compressive stresses and strains are denoted by a negative sign in OpenSees. The distribution of stresses and pore pressures represents the gravity loading appropriately.

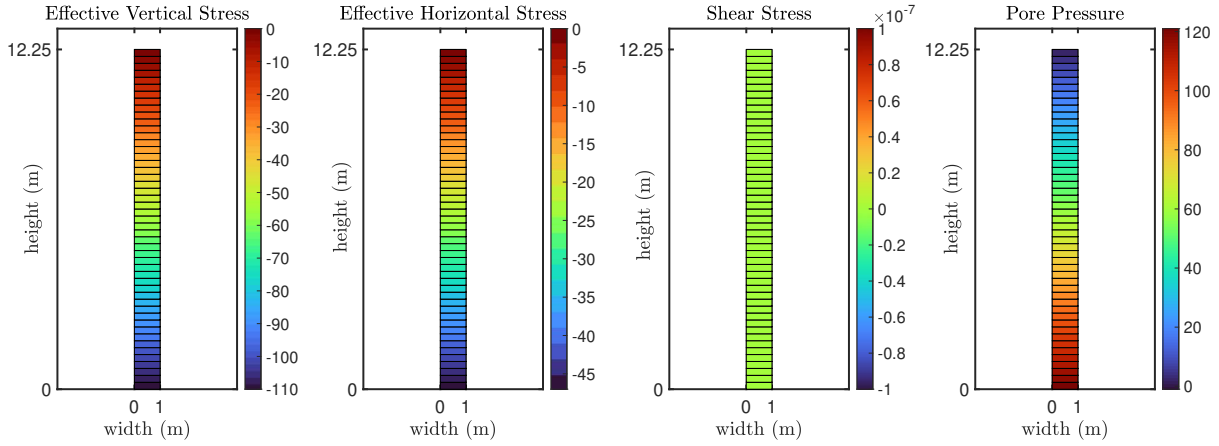

Figure 8.11: Variation of vertical stress, horizontal stress, shear stress and pore pressure along the height of the soil column under gravity loading

Dynamic analysis results

The input acceleration time history shown in figure 8.10 was applied as a UniformExcitation load pattern in OpenSees at the base nodes of the soil column in the horizontal direction. The applied motion was not sufficiently strong to cause full liquefaction of the deposit, offering a more meaningful validation case. The analysis was run longer than the duration of the earthquake, to allow for some post-shaking excess pore pressure dissipation. The responses at the prototype scale were compared at the locations of accelerometers (figure 8.12) and pore pressure transducers (PPTs) (figure 8.13), for both bulk modulus calibration methods. Additionally, the simulated settlement at the top of the soil column was compared to the centrifuge LVDT (L1) recordings, in figure 8.14.

The acceleration time histories at A1, shown in figure 8.12, match perfectly with the centrifuge data for both calibration methods as there is minimal amplification/de-amplification of the response closer to the input. At the higher accelerometer locations, the $G-K$ calibration shows a significant improvement in simulation results. The $G-\nu$ calibration shows a stiffer response across the entire height of the soil column and fails to capture the observed de-amplification of accelerations at the top half of the soil column. On the contrary, the $G-K$ calibration captures softening, especially as observed at A7. The pore pressure time histories in figure 8.13 show more pore pressure accumulation with the $G-K$ calibration, along the entire height of the soil column, which better matches the centrifuge test results. In the centrifuge test, pore pressure accumulation after the first few cycles was faster than in the numerical simulations, indicating faster redistribution of pore pressures in the numerical simulations, though the $G-K$ calibration presents a marked improvement to the $G-\nu$ alternative. A more collapsible fabric in the centrifuge would lead to lower constrained stiffness and slower pore pressure dissipation, consistent with the recordings of figure 8.13. Note that the calibrated parameters used in the simulations were based on element tests that were prepared using wet pluviation, whereas the soil in the centrifuge test was prepared using air pluviation. At the end of shaking, the numerically modelled rapid pore pressure dissipation, as compared to the centrifuge data, is

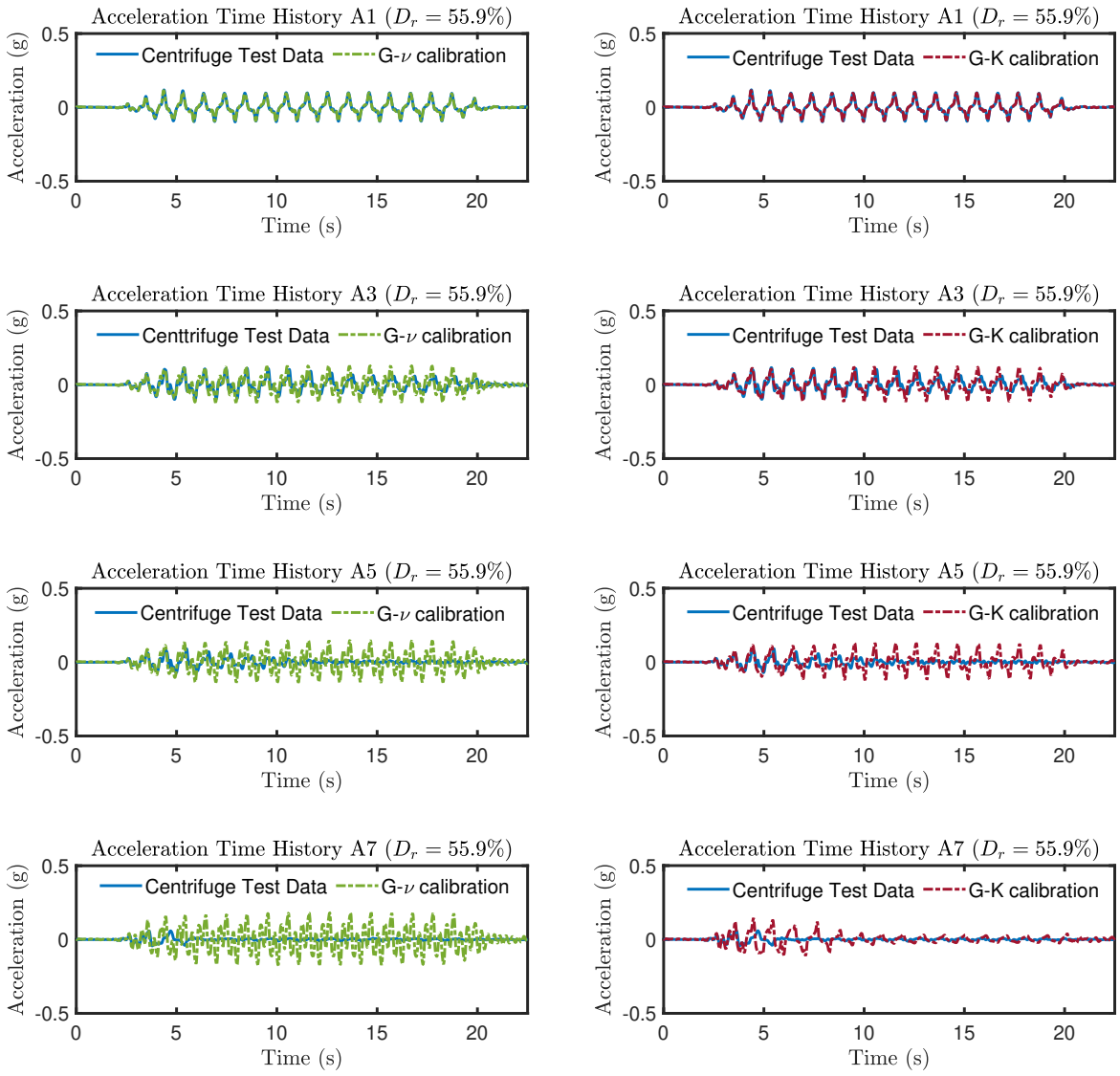

Figure 8.12: Comparison of simulated acceleration time histories in OpenSees with centrifuge test data

another indication of reduced constrained stiffness in the centrifuge soil. Though this trend has in the past been attributed to non numerically captured mechanisms such as sedimentation, it is worth pointing out that the modelled dissipation is too rapid even at locations such as P1 or P3, which did not fully liquefy and where sedimentation would not have taken place.

Excess pore pressure accumulation and liquefaction triggering is compared in time during shaking along the height of the soil column for the two bulk modulus calibration methods in figure 8.15. In the centrifuge experiment, the locations of pore pressure transducers P5 and

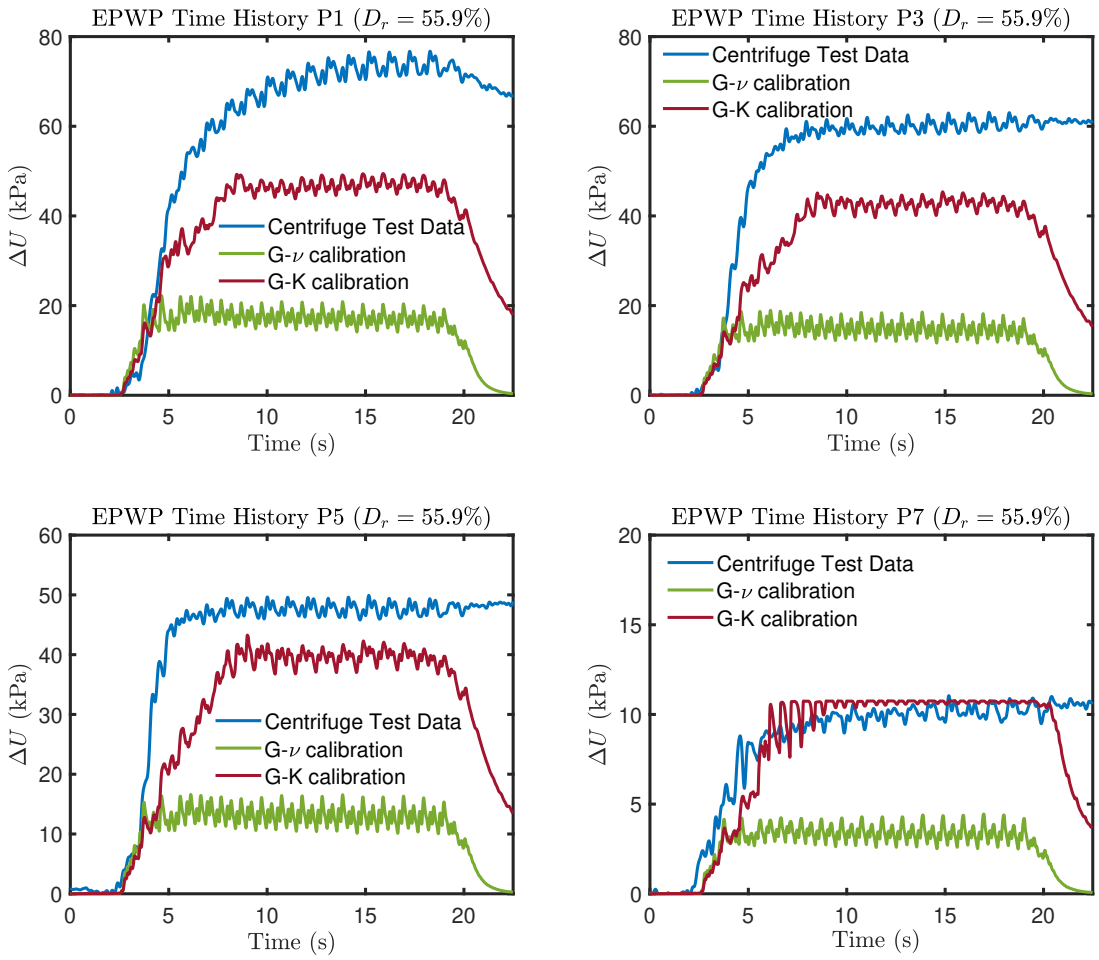

Figure 8.13: Comparison of simulated excess pore water pressure (EPWP) time histories in OpenSees with centrifuge test data

P7 liquefied within 6 seconds of shaking, as seen in figure 8.15. Location P3 developed high excess pore pressure and was reported to have also liquefied. The recorded acceleration time history at A3 shows deamplification after 10 seconds of shaking, indicating that this location liquefied later than the locations of P5 and P7, which were closer to the surface (refer figure 8.12). At P5 and P7, the temporal and spatial distribution of excess pore pressures are matched closely by the $G-K$ calibration, including liquefaction triggering. At P1 and P3, excess pore pressures predicted with the $G-K$ calibration rise, but fall short of the values recorded in the centrifuge, due to the more rapid redistribution discussed above. The $G-\nu$ calibration predicts no liquefaction triggering along the entire depth of the soil column, which is a 'false-negative'

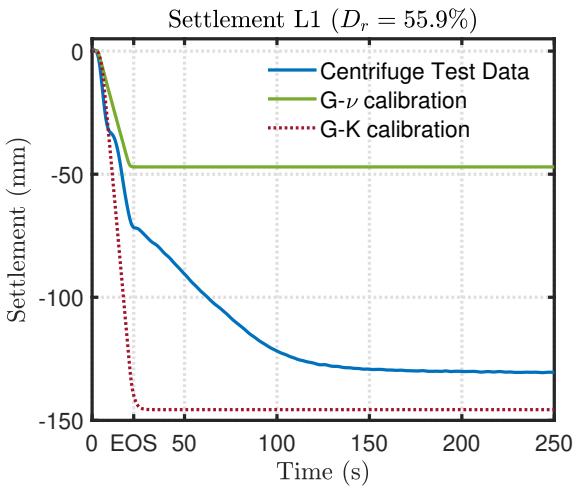

Figure 8.14: Comparison of simulated displacement time histories in OpenSees with centrifuge test data at L1, EOS: end of shaking

prediction.

Lastly, the settlement at the top of the soil column is compared with centrifuge test data in figure 8.14. As expected, the $G-K$ calibration, which leads to a lower value for the bulk modulus, predicts higher settlement than the $G-\nu$ calibration. The $G-\nu$ calibration under-predicted the final settlement, which has been typically observed in numerical simulations conducted using the traditional $G-\nu$ calibration, even for lower values of Poisson's ratio and elastic shear modulus (Ramirez et al., 2018). The permeability coefficient is often increased as a function of excess pore pressure ratio to improve predictions of settlement (e.g., Shahir et al., 2012; Tsaparli et al., 2016). Ma et al. (2025) recently showed from dynamic centrifuge tests that soil hydraulic conductivity significantly varies throughout the loading process; continually increasing from early shaking stages through liquefaction, reducing subsequently to varying degrees in the later stages of the co-seismic phase and eventually reducing to values below initial upon ensuing solidification in the post-shaking phase. Haigh et al. (2012) showed through fluidisation tests that for Hostun sand permeability increases when mean effective stress falls below 1 kPa, with notable increase observed below 0.1 kPa, up to a maximum of 20%, which if implemented would not substantially impact the numerical simulation results presented here. Additionally, an increase in permeability would make pore pressure redistribution even faster, leading to a

worse co-seismic comparison of pore pressure with the centrifuge. The $G-K$ calibration, on the contrary, gives a slightly conservative estimate for settlement, which nevertheless at 145 mm is very close to the 130 mm corresponding to the experiment. Consistently with the simulated pore pressure dissipation time-histories, almost all of the predicted settlement occurred during shaking whereas in the actual test, the reconsolidation process was much slower. The varying porosity of the soil mass, the varying tortuosity of flow paths and the evolution of fabric during shaking and post liquefaction may all play a role in altering the soil's permeability and compressibility, impacting the rate of dissipation of excess pore pressures. This is an area of known weakness for bounding surface models, which requires further study to refine their performance (Ma et al., 2025; Tsaparli et al., 2016).

Overall, the $G-K$ calibration parameters show a significant improvement in predicting the centrifuge test results, regarding settlement (figure 8.14), accelerations (figure 8.12) and pore pressures (figure 8.13).

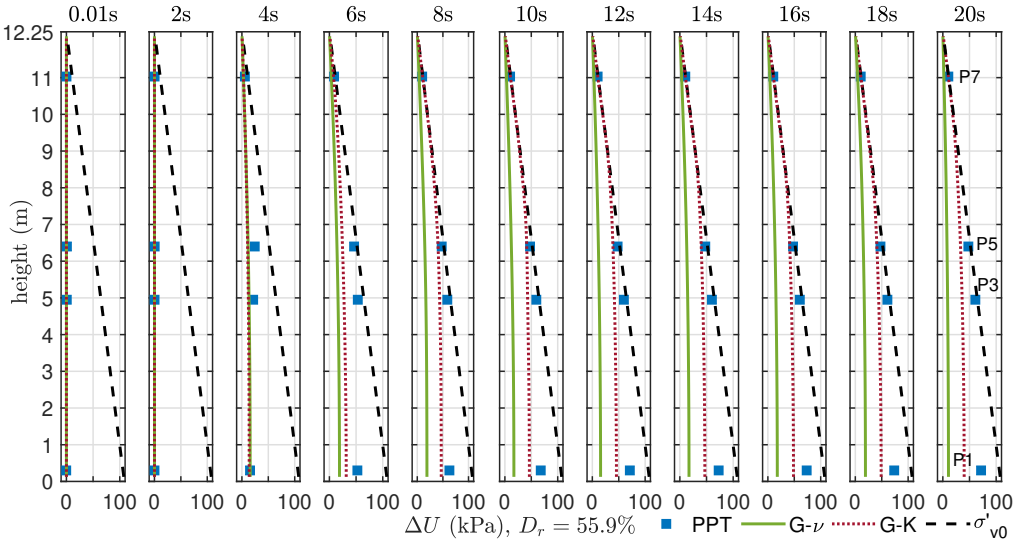

Figure 8.15: Comparison of simulated excess pore pressure time histories in OpenSees with centrifuge test data along the height of the soil column

8.3.5 Mechanisms of excess pore pressure accumulation and liquefaction triggering

The soil column presented in the previous section and examined in the centrifuge was shown to only liquefy up to a certain depth. The two calibration schemes for the bulk modulus, despite maintaining similar undrained cyclic resistance curves, as shown in figure 8.16, resulted in completely different outcomes for the soil column. The $G-K$ calibration matched the experimental results adequately, while the $G-\nu$ calibration gave a 'false-negative' prediction. In this section, the mechanisms that lead to excess pore pressure accumulation and liquefaction triggering are examined in more detail.

Simplified procedure

First, a liquefaction susceptibility assessment of the examined soil column was performed, using the simplified procedure of Seed and Idriss (1971). The peak ground acceleration (PGA) was obtained using a 1D wave propagation analysis in OpenSees performed in accordance with the OpenSees Documentation (McKenna, 2011), assuming a uniform elastoplastic soil deposit on rigid bedrock with shear modulus reduction curves for Hostun sand from Kassas et al. (2021). In addition to the inherent hysteretic damping of the elastoplastic soil, a 2% Rayleigh damping was defined to induce damping at low strains. A PGA of 0.16g was obtained from the site response analysis and compared with the PGA obtained by adjusting the input acceleration (figure 8.10) using the stress reduction factor r_d (Idriss and Boulanger, 2008) at the depth of the input motion ($r_d = 0.86$, $PGA = 0.14$g). Simplified assessment results corresponding to the maximum PGA thus obtained, at the locations of the pore pressure transducers are presented in table 8.2 and the factor of safety against liquefaction along the soil column depth is shown in figure 8.17. The CRR value was obtained from the experimental cyclic resistance curve of figure 8.16, for the number of cycles of sinusoidal shaking of the input acceleration. A factor of safety value ≤ 1 was obtained along the depth of soil column suggesting liquefaction triggering of the entire deposit. In effect, the simplified procedure correctly predicts liquefaction triggering at locations

P3, P5 and P7 while yielding a 'false-positive' prediction at P1, at the base of the deposit. The simplified method is unable to account for any water flow effects during the earthquake and is thus unable to capture the excess pore pressure redistribution that could be the reason for the base of the layer not reaching liquefaction in reality.

Location	σ_{v0} (kPa)	σ'_{v0} (kPa)	r_d	a_{max} (g)	τ_{cyc} (kPa)	CSR	N	CRR_{tx}	CRR_{ss}	FS_L
P7	22.0	10.0	1.0	0.16	2.3	0.23	18	0.15	0.11	0.47
P5	105.4	48.0	0.95	0.152	10.4	0.22	18	0.15	0.11	0.49
P3	131.6	59.9	0.93	0.149	12.8	0.21	18	0.15	0.11	0.50
P1	215.4	98.1	0.87	0.139	19.4	0.20	18	0.15	0.11	0.54

Table 8.2: Calculation of factor of safety against liquefaction using simplified procedure (Seed and Idriss, 1971) and baseline undrained curves for $D_r = 55.9\%$ from figure 8.16

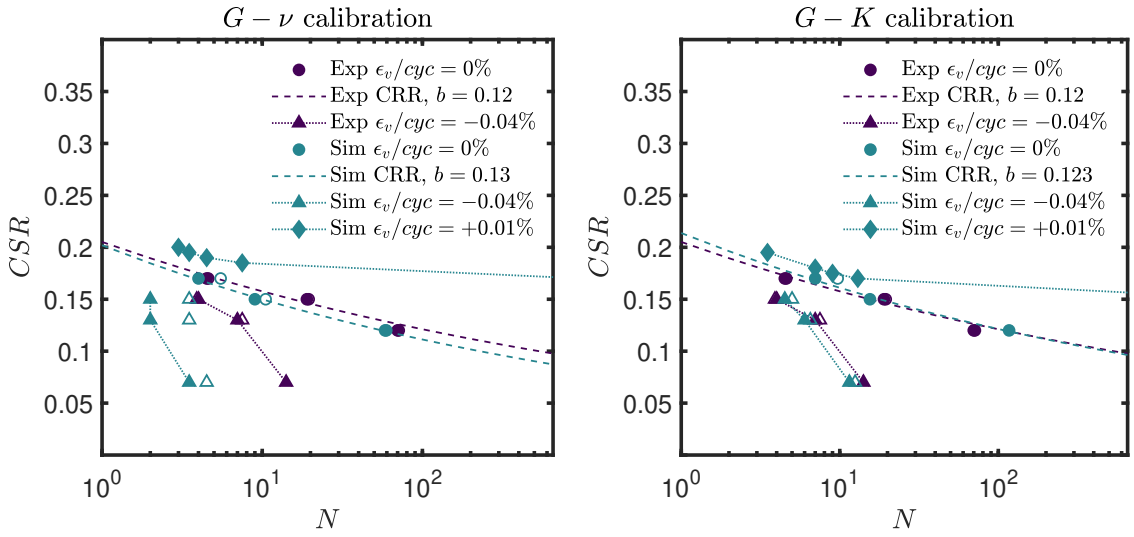

Figure 8.16: Cyclic resistance curves in triaxial space for Hostun sand ($D_r = 55 \pm 2\%$) with model parameters from table 7.4 and table 8.1

Numerical simulations

The OpenSees numerical simulations presented above were able to capture drainage effects, as manifested due to co-seismic water flow. Co-seismic drainage produced volumetric strains, presented in figure 8.18 as isochrones, along the height of the soil column. The $G-\nu$ calibration resulted in small, positive volumetric strains (volume contraction) along the entire height of the soil column, while the $G-K$ calibration led to greater volumetric contraction all along the layer,

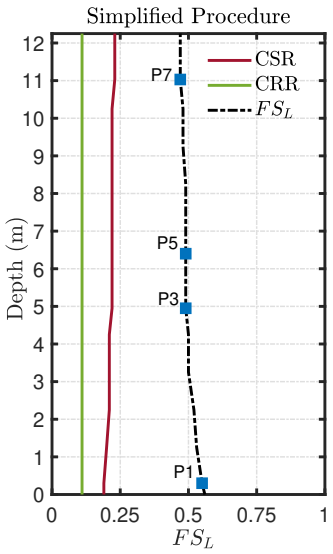

Figure 8.17: Factor of safety against liquefaction

apart from the top 1.0 m, where expansion was calculated. To aid the discussion of these results, the stress-strain paths of soil elements at P1, P5, P7, and of the top element, are plotted in figure 8.19. Note that the 'butterfly loops' at P7 and at the top of the column do not reach the origin due to the low mean effective stress cut-off implemented in OpenSees for SANISAND-MSf. The vertical stress-void ratio paths ($e - \sigma'_v$), are also shown in figure 8.20.

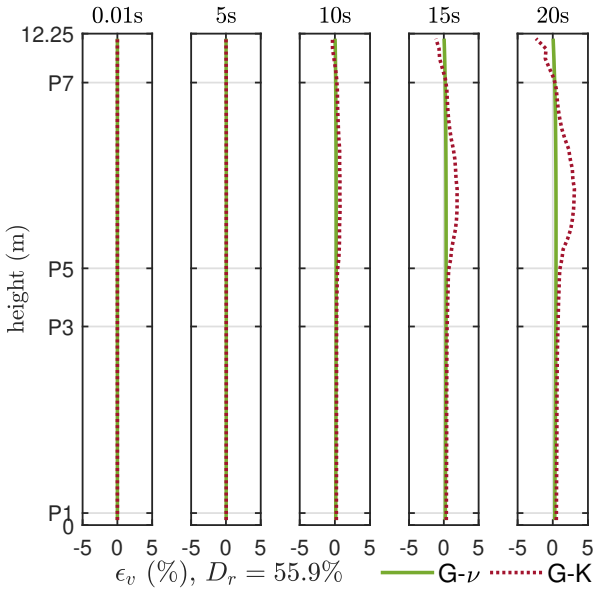

Figure 8.18: Comparison of volumetric strain isochrones in OpenSees along the height of the soil column

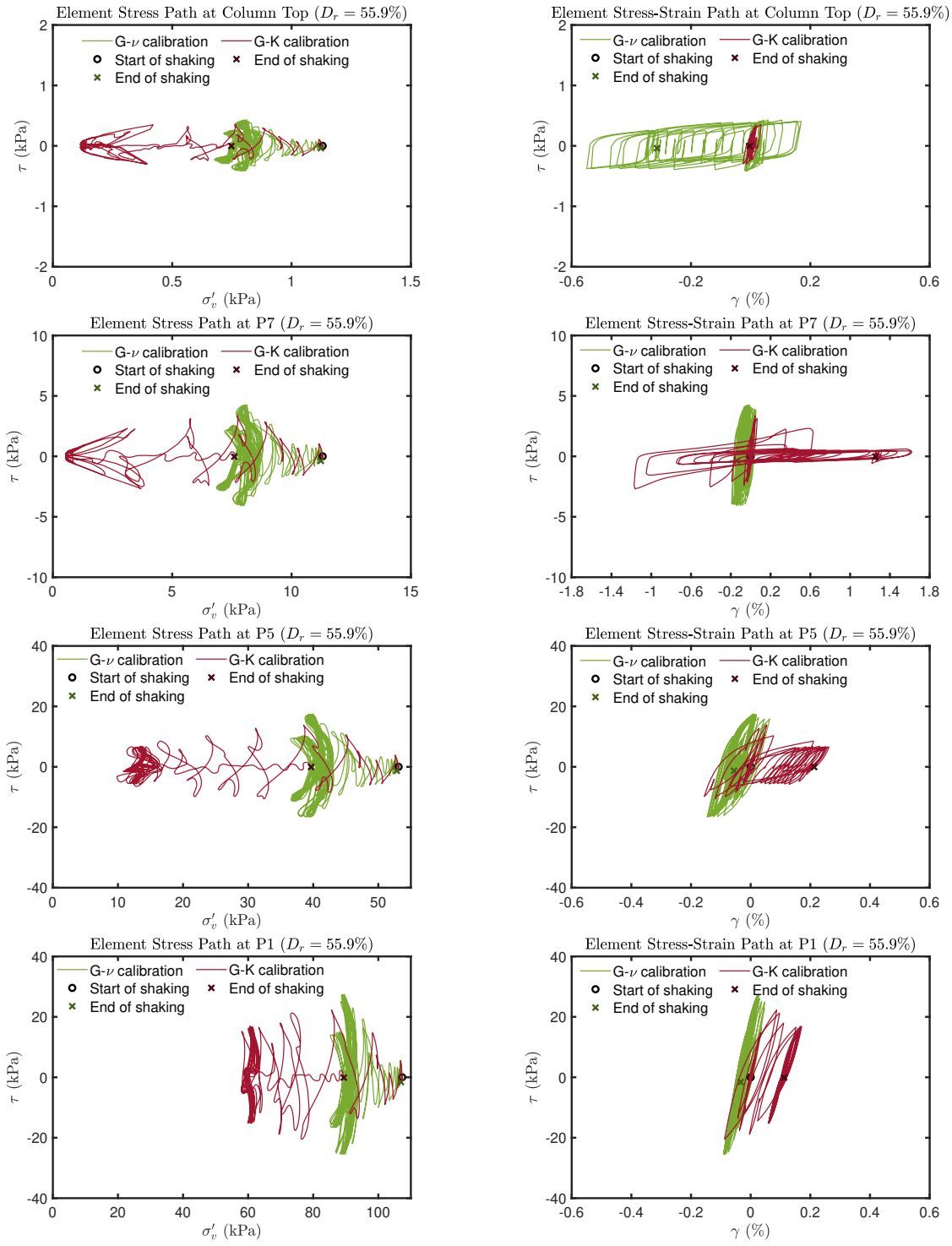

Figure 8.19: Comparison of stress paths in OpenSees using the two bulk modulus calibration methods at P1, P5, P7 and soil column top

The differences for the two bulk modulus calibration methods can be explained by qualitatively thinking of a superposition of excess pore water pressure accumulation due to undrained

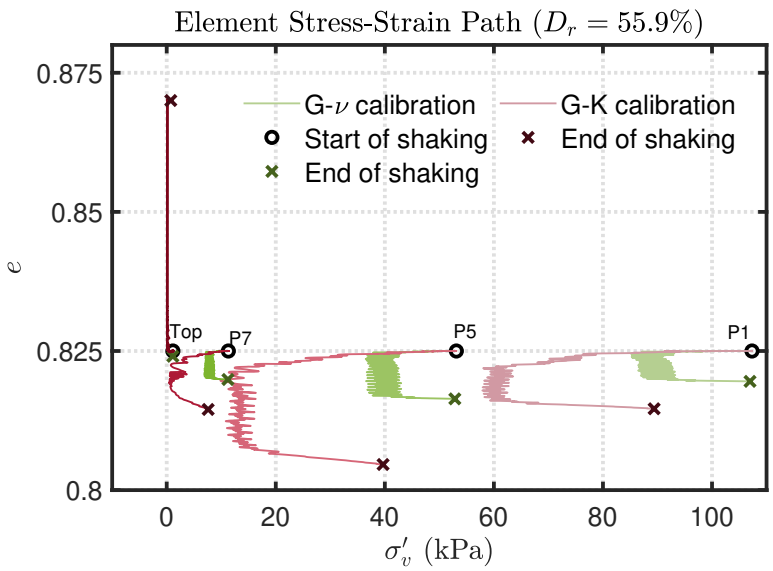

Figure 8.20: Comparison of stress-strain paths in OpenSees using the two bulk modulus calibration methods in $e - \sigma'_v$ space

cyclic shearing and excess pore water pressure dissipation due to Terzaghi's consolidation equation ($\frac{\partial \bar{u}}{\partial t} = c_v \frac{\partial^2 \bar{u}}{\partial z^2}$) which simultaneously applies. The undrained shearing behaviour for both bulk modulus calibrations is expected to be fairly similar, as indicated by the cyclic resistance curves of figure 8.16. However, the $G-\nu$ calibration gives a stiffer bulk modulus than the $G-K$ calibration, resulting in a higher coefficient of consolidation c_v ($= k/(m_v \gamma_w)$; stiffness $\propto 1/m_v$) and thus faster dissipation.

At the start of shaking, similar accelerations at the base of the column and equal rise of excess pore pressures were produced for both bulk modulus calibrations due to cyclic shearing. Simultaneously, excess pore pressures began to dissipate following the consolidation equation. The higher c_v of the $G-\nu$ calibration led to faster dissipation, which prevented further increases in pore pressure due to cyclic shearing. While shaking continued, the dissipation produced for the $G-\nu$ calibration was sufficiently fast to counteract any additional accumulation of excess water pressures from cyclic shearing, throughout the layer. As a result, a quasi 'steady-state' excess pore water pressure distribution with depth was maintained during shaking, as seen in the time-histories of figure 8.13 and the isochrones of figure 8.15. Despite being quasi 'steady-state', this distribution did not correspond to a constant value of excess pore water pressure with

depth, producing rather a quasi 'steady-state' $\frac{\partial^2 \bar{u}}{\partial z^2}$ term at each depth, as required for a practically constant dissipation rate. Constant dissipation necessitated an equally constant volumetric contraction rate at each depth. Given the high bulk modulus of the $G-\nu$ calibration, only small changes in volume were required to counteract the tendency to reduce mean effective stress due to cyclic shearing, as reported in figures 8.18 and 8.20. In turn, a practically constant co-seismic accumulation of surface settlement was produced (figure 8.14), with a low final value compared to the centrifuge experiment. The fast dissipation caused by the $G-\nu$ calibration and the resulting limited decrease in effective stress allowed much of the initial shear stiffness to be maintained throughout the deposit, leading to predictions of increased acceleration from wave propagation towards the top of the layer, as opposed to the centrifuge testing results, where the top of the layer liquefied.

The predicted layer response under the $G-K$ calibration much better matched the experimentally observed behaviour. The $G-K$ calibration produced lower bulk modulus and thus lower c_v values, leading to slower dissipation of excess pore pressures. As a result, higher excess pore water pressures were allowed to accumulate, caused by cyclic shearing. A quasi 'steady-state' was eventually reached during seismic shaking, though later in the earthquake as compared to the $G-\nu$ calibration, and at higher levels of excess pore water pressure (figure 8.13). During this quasi 'steady-state', the top part of the layer was fully liquefied, matching more closely the response recorded in the centrifuge, as seen in the isochrones of figure 8.15. From these isochrones, one can infer that at the transition zone from fully liquefied to non-liquefied material, the term $\frac{\partial^2 \bar{u}}{\partial z^2}$ was maximised. This fact, in combination with the overall higher compressibility (lower bulk modulus) produced from the $G-K$ calibration led to the volumetric strain isochrones of figure 8.18. Within the non-liquefied zone at the bottom part of the layer, positive (volumetric contraction) strains were produced due to water outflow, in a similar mechanism to the one described for the $G-\nu$ calibration, where the entire layer remained non-liquefied. The magnitude of volumetric strains was higher than for the $G-\nu$ calibration as the layer was overall softer for the $G-K$ calibration, both due to the definition of the bulk modulus

and the reduced values of effective stress achieved. Once liquefaction was reached at the top of the layer, large values of contractive volumetric strains started accumulating at the transition zone from non-liquefied to liquefied material, where $-\frac{\partial^2 \bar{u}}{\partial z^2}$ was maximum. The higher volumetric strains led to larger settlement prediction, as shown in figure 8.14. This result indicates an uneven density profile at the end of the earthquake, with most densification happening at this transition zone.

At the top of the layer a perhaps unexpected zone of volumetric expansion was calculated. This zone was the result of significant upwards flow coming from the transition zone that could not be expelled as fast from the top elements. Despite the top part of the layer being nominally liquefied, it is worth pointing out that (i) full liquefaction was actually a transient condition as cyclic loading temporarily increased effective stress due to dilation and (ii) the low effective stress cut-off in the OpenSees formulation limited the lowest value of p' to 0.5 kPa. The simulation appropriately de-amplified accelerations towards the top of the layer (see A7 in figure 8.12). However, sufficient shear stress reached the location of P7 to cause transient dilation spikes and result in temporarily elevated effective stress and thus coefficient of consolidation, as seen in figures 8.19 and 8.20. In fact, at the location of P7 some densification still took place (figure 8.20). In contrast, at the top of the layer, the amplitude of shear stress soon reduced to practically zero (figure 8.19), maintaining effective stresses practically at the cut-off value (figure 8.20). As a result, the very top of the layer after the first few seconds of shaking did not experience any cyclic shearing and related tendency for accumulation of excess pore water pressure, as opposed to the soil just below, but still within the nominally 'liquefied' zone. The outcome was a local change in sign in $\frac{\partial^2 \bar{u}}{\partial z^2}$, leading to volumetric expansion, the magnitude of which was exacerbated by the very low values of the bulk modulus corresponding to the near zero levels of effective stress in this zone.

Recalling from chapter 7, pore water inflow in a soil element shifts the CRR curve to lower cycles of liquefaction than the undrained curve, with the stiffer bulk modulus of the $G-\nu$ calibration leading to fewer cycles to liquefaction than the $G-K$ calibration. Even a small

amount of inflow was shown to lead to more rapid liquefaction triggering than under undrained conditions. For water outflow conditions, as plotted in figure 8.16, CRR curves shift to the right compared to the undrained curve, with the $G-\nu$ calibration causing a more dramatic shift than the $G-K$ calibration. This implies that for the same level of shaking, under an outflow condition, the $G-\nu$ calibration requires more cycles to liquefy, resulting in slower generation of excess pore pressures than the $G-K$ calibration. Depending on the rate of outflow, liquefaction could be completely mitigated for CSRs that could trigger liquefaction under undrained loading (Grey and Adamidis, 2024). The $G-\nu$ calibration requires smaller volumetric contraction rates to combat the unloading effect from undrained cyclic shearing than the $G-K$ calibration, as inferred from figure 8.16. This is consistent with the soil column results of figure 8.20, where the $G-\nu$ calibration is shown to require less densification along the depth of the soil column than the $G-K$ calibration, to fully mitigate liquefaction. In contrast, liquefaction was manifested with the $G-K$ calibration at location P7, even though larger densification took place. At P1, close to the base of the layer, water outflow prevented liquefaction triggering in both cases. Despite more densification for the $G-K$ calibration, the larger bulk modulus of the $G-\nu$ calibration was more effective in limiting the maximum excess pore water pressure.

8.3.6 Comparison with traditional calibration of elastic moduli

The dynamic analysis simulation results of section 8.3.4 highlight the impact of the choice of elastic moduli in boundary value problems. Traditionally, the elastic shear modulus is calibrated from element tests and the bulk modulus is then derived using Poisson's ratio. The coefficient (G_0) in SANISAND family of models is often measured at strain levels of the order of 10^{-4} from deviatoric stress-strain plots of drained monotonic tests. The shear modulus coefficient obtained from bender element tests (G_{max}) is calculated at smaller strain levels, $\sim 1\times10^{-6}$ and has been reported to be $2-4$ times the value of G_0 as derived from monotonic tests (Chaloulos and Papadimitriou, 2025; Darvishi et al., 2022; Papadimitriou et al., 2023). The elastic bulk modulus is then obtained from Poisson's ratio (typical calibration).

Boundary value problem simulations using the shear modulus coefficient calibrated at the two strain levels have been compared in numerous numerical studies (Chaloulos and Papadimitriou, 2025; McAllister et al., 2015; Papadimitriou et al., 2023). These studies show that the low shear modulus coefficient from monotonic tests overestimates the elastic soil deposit period in dynamic analyses (McAllister et al., 2015), with potential effects on excess pore pressure accumulation and the onset of liquefaction (Papadimitriou et al., 2023). However, it offers better results in static boundary value problems (Chaloulos and Papadimitriou, 2025). Free-field ground surface displacements have also been reported to be lower using the shear modulus calibrated from bender element tests (Chaloulos and Papadimitriou, 2025). Note that the bulk modulus from bender elements G_{max} and ν is roughly three times of that calculated from monotonic test G_0 and ν. Therefore, the settlements predicted in liquefaction analyses by a monotonic G_0 calibration are closer to the actual displacements than with a bender element G_{max} calibration.

A small Poisson's ratio value of 0.05 is often assumed in the SANISAND family of models for dynamic analyses, with limited physical justification. In this study, for Hostun sand, when used, the Poisson's ratio was taken as 0.18 from Hoque and Tatsuoka (2000), following Azeiteiro et al. (2017). In turn, G_{max} was determined from bender element tests to appropriately capture the dynamic response in the layer. For a range from low to high mean effective stresses ($0-10000$ kPa), the bulk modulus K determined directly from isotropic unloading-reloading tests was $0.1-0.6$ times the bulk modulus from a G_{max} and $\nu = 0.18$ calibration and would have been $0.2-0.9$ times that determined from a G_{max} and $\nu = 0.05$ calibration. If instead the shear modulus was calibrated from monotonic tests and a $\nu = 0.05$ was still used, then the resulting bulk modulus would more closely match the one directly determined here. While such a calibration might offer good settlement predictions, it would be at the expense of acceleration and excess pore pressure time histories, as indicated by Papadimitriou et al., 2023. By using a combination of bender element G_{max} and an isotropic unloading-reloading K, we were able to correctly capture the fundamental soil period and adequately reproduce the recorded acceleration, pore pressure, and settlement time histories. Thus, the proposed calibration scheme

appears to combine the benefits of a bender element $G_{max} - \nu$ calibration at small-strains and a monotonic loading $G_0 - \nu$ at large strains.

Overall, this validation exercise highlighted the importance of the bulk modulus calibration in simulating boundary value problems in a fully coupled analysis of a homogeneous soil deposit. It is worth pointing out that the shear modulus from bender elements corresponds to small-strain behaviour, whereas the bulk modulus from isotropic unloading-reloading tests corresponds to larger strains. As a result, this pair of elastic moduli are not necessarily physically consistent and their corresponding Poisson's ratio might not be meaningful. However, as shown in this validation study, they can be appropriate as parameters that can be directly derived from experiments to calibrate SANISAND models. In shearing, SANISAND models include a very narrow elastic wedge in stress space, in which the calibrated shear modulus applies before plasticity is engaged and reduces secant stiffness, at small levels of shear strain. As a result, the bender element value of shear strain is appropriate. In constant stress-ratio unloading-reloading however, the stress path stays within the typically open-ended elastic wedge, maintaining the calibrated bulk modulus at larger strains, which is an indication why the proposed calibration of the bulk modulus is appropriate. While this study focuses on liquefaction triggering, further work is needed on how SANISAND models capture post-shaking reconsolidation, which appears too rapid. In more detail, work should examine how the calibrated elasticity moduli evolve once liquefaction is triggered, for instance identifying if the pre-liquefaction elastic bulk modulus is still appropriate once liquefaction has been triggered.

8.4 Effects of layering

The validation exercise of section 8.3 examined a case of a uniform liquefiable deposit with unrestricted drainage, where the simplified procedure correctly predicted the manifestation of liquefaction, although the prediction was not accurate for the bottom part of the soil column where co-seismic drainage inhibited the triggering of liquefaction. A numerical simulation us-

ing SANISAND-MSf with direct calibration of the bulk modulus ($G-K$ calibration) was shown to adequately capture the co-seismic response throughout the examined layer, while a traditional elasticity calibration using the shear modulus and Poisson's ratio ($G-\nu$ calibration) compared poorly to experimental results. In the sequel, a parametric numerical study is undertaken of selected idealised stratified deposits. The aim of this section is threefold. Firstly, to investigate the triggering of liquefaction in deposits where permeability changes between layers can locally exacerbate the effects of drainage. Secondly, to showcase the shortcomings of a traditional $G-\nu$ calibration in cases with significant drainage effects, as opposed to a $G-K$ calibration, which following the preceding validation section is expected to yield results that better correspond to reality. Finally, to highlight the shortcomings of currently used simplified liquefaction susceptibility assessments (Seed and Idriss, 1971) in layered deposits, by targeting profile and excitation combinations for which unaccounted drainage effects can result in false predictions (Cubrinovski et al., 2019).

8.4.1 Parametric cases

In this section, idealised cases of layering are presented, aiming to capture scenarios of false predictions in the critical layer using the simplified procedure (Seed and Idriss, 1971). The amplitude of shearing, as represented in simplified assessments through the cyclic stress ratio (CSR), plays a crucial role in predictions of undrained liquefaction triggering. At low amplitudes of shearing, pore pressure accumulation is slow and pore pressure redistribution can have a severe influence on triggering. In such cases, the simplified procedures may not predict liquefaction triggering in the critical layer due to a disregard for layer interactions. Under higher amplitudes of shaking, cyclic shearing plays the dominant role in liquefaction triggering with smaller contribution from pore fluid flow (Adamidis and Madabhushi, 2018; Adamidis and Anastasopoulos, 2022). In such cases, the simplified procedure will almost always predict the onset of liquefaction in a critical layer. The layered profiles of Cases 2 and 3 (refer figure 8.21) in the following sections, where a low permeability layer overlies a liquefiable layer, were developed to repre-

sent cases that might not liquefy under low amplitude shaking and undrained conditions, but for which co-seismic net water inflow could lead to liquefaction triggering. For these cases, the simplified procedure could lead to 'false-negative' predictions (Cubrinovski et al., 2019). The amplitude of shaking required to trigger 'false-negative' predictions by the simplified procedure in such layered conditions depends on the relative density of the critical layer, illustrated by Case 4 (refer figure 8.23), which focuses on a dense sand layer that does not reach liquefaction under higher amplitudes of shaking based on the simplified liquefaction assessment, but liquefies due to layering effects.

On the contrary, shaking amplitudes that trigger liquefaction under undrained conditions may not be sufficient for triggering at locations of net pore water outflow, due to the specific arrangement of soil layers. Such cases could lead to 'false-positive' simplified predictions (Cubrinovski et al., 2019). A 'false-positive' was identified at location P1 of the centrifuge experiment results described in section 8.3. The CSR value at P1 was calculated as 0.20 (table 8.2), yet liquefaction was not triggered. The large pore volume outflow resulted in the mitigation of liquefaction at the deeper layer, a behaviour adequately captured by the $G-K$ calibration of the SANISAND-MSf model. However, the centrifuge soil column analysis was for a uniform deposit. Layered Case 5 (refer figure 8.37) was developed to represent a 'false-positive' scenario where a low permeability layer is sandwiched between liquefiable layers. Table 8.3 summarises the parametric cases studied in the following sections. In all cases, the differences in numerical results obtained with a $G-\nu$ and a $G-K$ calibration are examined.

'False-negative' prediction	'False-positive' prediction
Cases 2, 3 and 4	Case 5

Table 8.3: Parametric studies of hypothetical scenarios of false predictions by the simplified liquefaction susceptibility assessment procedure (Seed and Idriss, 1971)

8.4.2 'False-negative' case: Model setup

1D soil columns representing saturated soil deposits on bedrock were created in OpenSees for three cases of layering to demonstrate 'false-negative' simplified predictions, as shown in figure 8.21. Case 1 models a uniform 6 m liquefiable soil deposit, that was analysed assuming two values of permeability - (a) $k = 1 \times 10^{-10}$ m/s, to approximate undrained conditions and (b) drainage as dictated based on a realistic permeability value. Soil properties for the liquefiable deposit were specified for Hostun sand with relative density $D_r = 40\%$, which gives a void ratio of $e = 0.8978$ with e_{max} and e_{min} per equation 7.1. A soil permeability constant of 9.2×10^{-4} m/s per Adamidis and Anastasopoulos (2022) was specified. The material model in OpenSees was defined as the SANISAND-MSf model (M. Yang et al., 2022) with model parameters calibrated and reported in table 7.4. Case 2 models the uniform soil deposit on bedrock from Case 1, overlain by a lower permeability layer of sandy silt of 2 m. The silt layer was modelled with a permeability of $k = 1 \times 10^{-5}$ m/s for Case 2a and a permeability of $k = 1 \times 10^{-7}$ m/s for Case 2b. The sandy silt layer was defined by the ManzariDafalias model (Dafalias and Manzari, 2004) with properties of dense Monterey sand ($D_r = 95\%$ and $e = 0.551$) from Ramirez et al. (2018), which made it a very difficult layer to liquefy under undrained conditions. Note that for this investigation, the sandy silt layer's permeability was of more consequence than its stress-strain behaviour. Finally, Case 3 models the soil profile of Case 2 with the addition of a dense sand layer of 4 m between the looser, liquefiable layer and the bedrock. The denser sand layer was defined as Hostun sand with relative density $D_r = 80\%$ ($e = 0.7466$). The same permeability was assigned to this layer as to the critical liquefiable layer of $D_r = 40\%$.

The input acceleration time history for Cases 1, 2 and 3 was a sinusoidal wave with 50 cycles at a frequency of 1 Hz, as shown in figure 8.22. A very low amplitude was used (0.02g), to ensure liquefaction was not manifested under undrained conditions. The combination of low amplitude and long duration of the applied motion represents a case where drainage effects are exacerbated. The maximum amplitude and duration of shaking where drainage effects are consequential for prediction of liquefaction depend on the density of the critical layer. To showcase the importance

of density, the soil columns in figure 8.23 were modelled. Case 4a demonstrates the approximate undrained behaviour of a 6 m deep denser sand deposit with a relative density $D_r = 80\%$ ($e = 0.7466$) and a low permeability constant of 1×10^{-10} m/s. Case 4b models the 6 m deep denser sand deposit of Case 4a with the realistic permeability value of 9.2×10^{-4} m/s, overlain by a 2 m deep low permeability sandy silt layer with permeability constant of 1×10^{-7} m/s. The denser sand layer and the sandy silt layer were modelled in OpenSees as in Cases 2 and 3. The input acceleration for the Case 4 models was a sinusoidal wave of 6 cycles at 1 Hz, with an increased amplitude of 0.06g, as shown in figure 8.24. The permeability constant of the sandy silt layer was parametrically investigated in Cases 2 and 3 to quantify its effect on liquefaction manifestation, with Cases 2a and 3a corresponding to a higher permeability ($k = 1 \times 10^{-5}$ m/s) than Cases 2b and 3b ($k = 1 \times 10^{-7}$ m/s). The element definitions and nodal boundary conditions were defined as in section 8.3.1. The mesh size was determined based on the shear wave velocity V_s and maximum frequency content (f_{max}) of the input motion, as described in 8.3.1. The soil column mesh profile in OpenSees is shown in figures 8.21 and 8.23. The analysis parameters were defined as per section 8.3.2. Time step for dynamic analysis was set to $\Delta t = 1 \times 10^{-3}$ s.

8.4.3 'False-negative' case: Simulation results

In this section, the simulation results for Cases 1 to 4 are presented. The gravity and dynamic analyses were conducted as in section 8.3.2. The acceleration time histories at the base, mid-depth and top of the loose liquefiable deposit for Cases 1 to 3 are shown in figures 8.25, 8.26 and 8.27, respectively, for both bulk modulus calibration methods. The pore pressure time histories at the base, mid-depth and top of the liquefiable deposit are shown in figures 8.28, 8.29 and 8.30, respectively, for both bulk modulus calibration methods. Figure 8.31 shows isochrones of excess pore pressures across the height of the soil columns in the liquefiable sand layer for Cases 1a, 2a and 2b and figure 8.32 shows the same isochrones for Cases 3a and 3b. For Case 1b, the pore pressure build-up was minimal along the height of the liquefiable layer in the entire duration of shaking as behaviour was practically drained and therefore, is not shown here. Figure 8.33

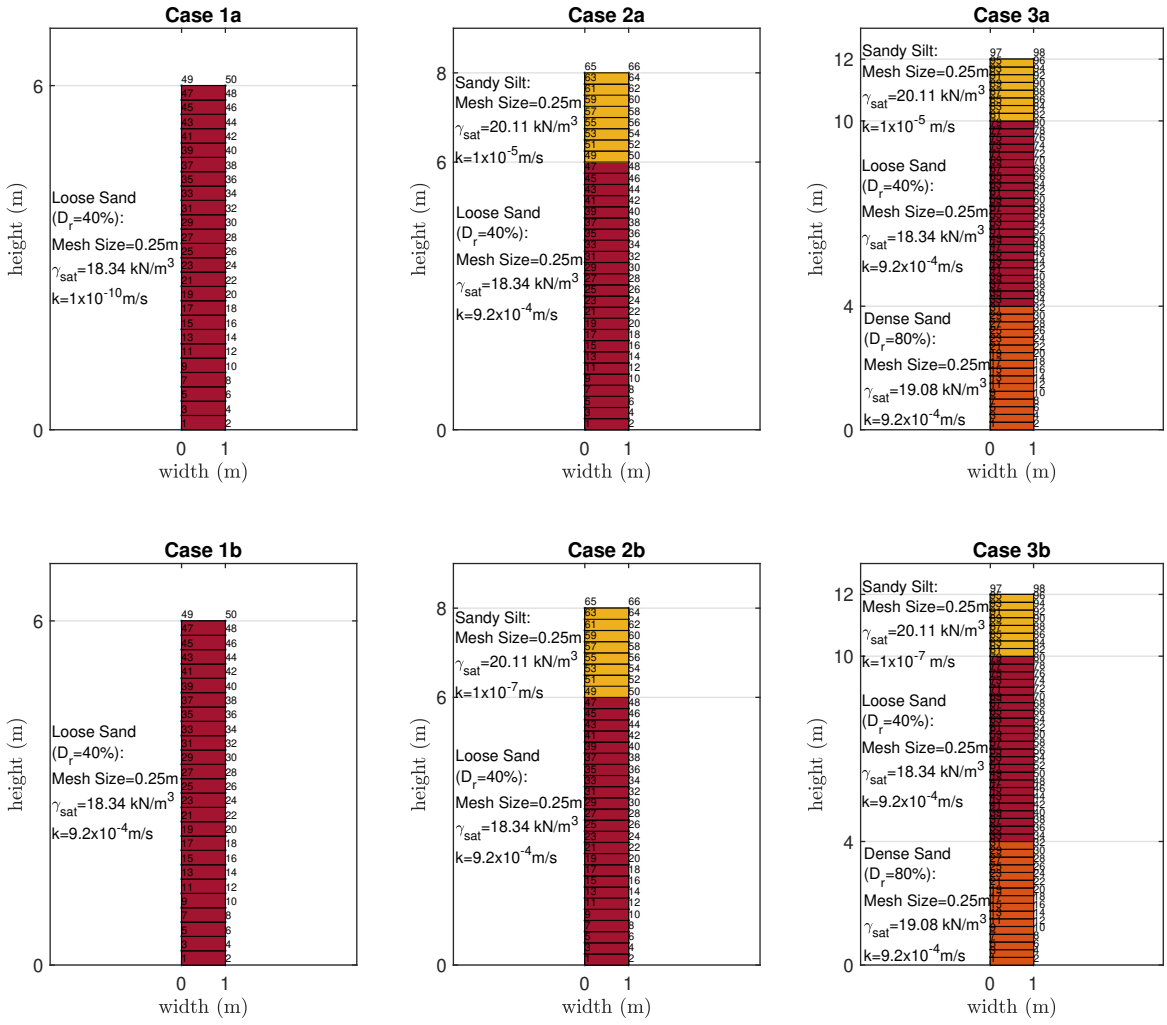

Figure 8.21: Schematic representation of layered soil column mesh profiles for Cases 1, 2 and 3

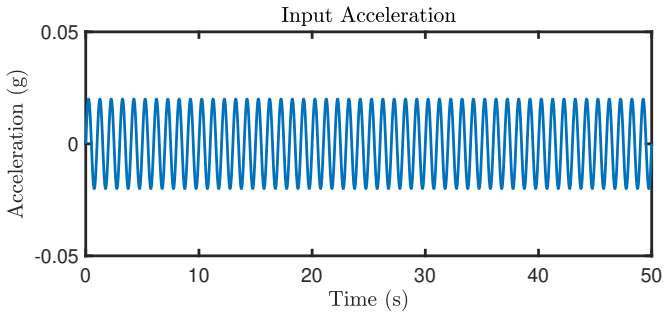

Figure 8.22: Input acceleration time history for Cases 1, 2 and 3

shows the temporal variation of volumetric strains across the height of the soil columns in the liquefiable sand layer for Cases 1b, 2a and 2b and figure 8.34 shows the volumetric strains for

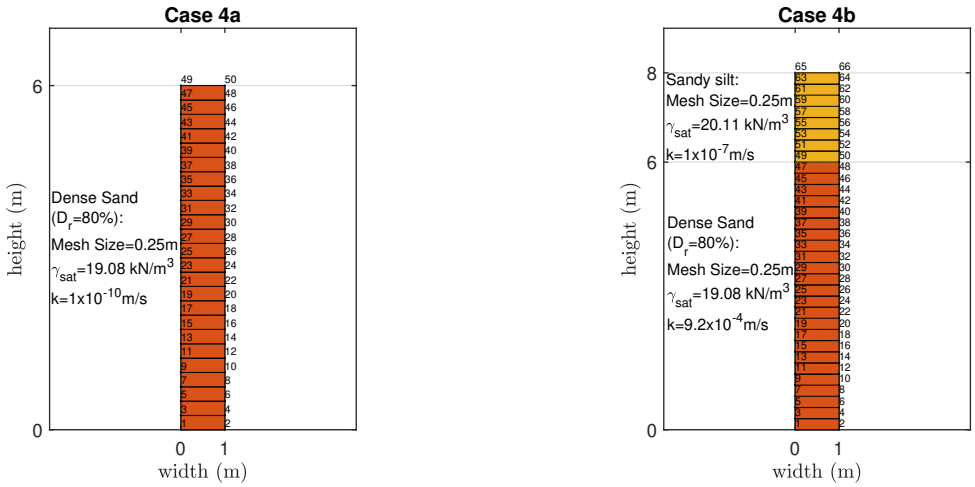

Figure 8.23: Schematic representation of layered soil column mesh profiles for Case 4

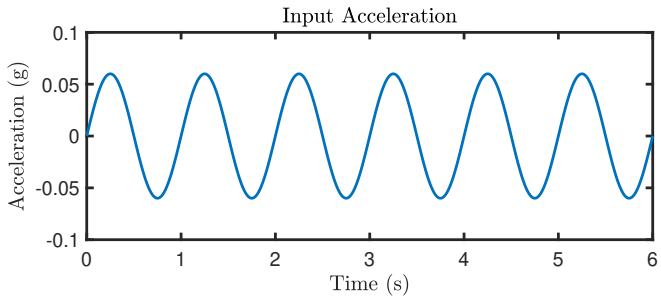

Figure 8.24: Input acceleration time history for Case 4

Cases 3a and 3b. Case 1a, being practically undrained, led to negligible volumetric strains and is thus not shown.

For the low amplitude excitation imposed, neither the undrained (Case 1a) nor the drained (Case 1b) acceleration responses of the uniform deposit showed signs of liquefaction triggering along the height of the soil column, irrespective of the calibration method. The pore pressure time histories for the undrained case (Case 1a) in figure 8.31, show similar accumulation of excess pore pressures with no traces of liquefaction for either calibration method. This is consistent with the fact that the model parameters were calibrated using the same baseline (undrained) cyclic resistance curve and with the simplified procedure calculations giving a factor of safety against liquefaction, $FS_L > 1$. Table 8.4 shows the simplified procedure calculation, computed similar to the centrifuge soil column in section 8.3.5, at the critical layer for Case 3 as it re-

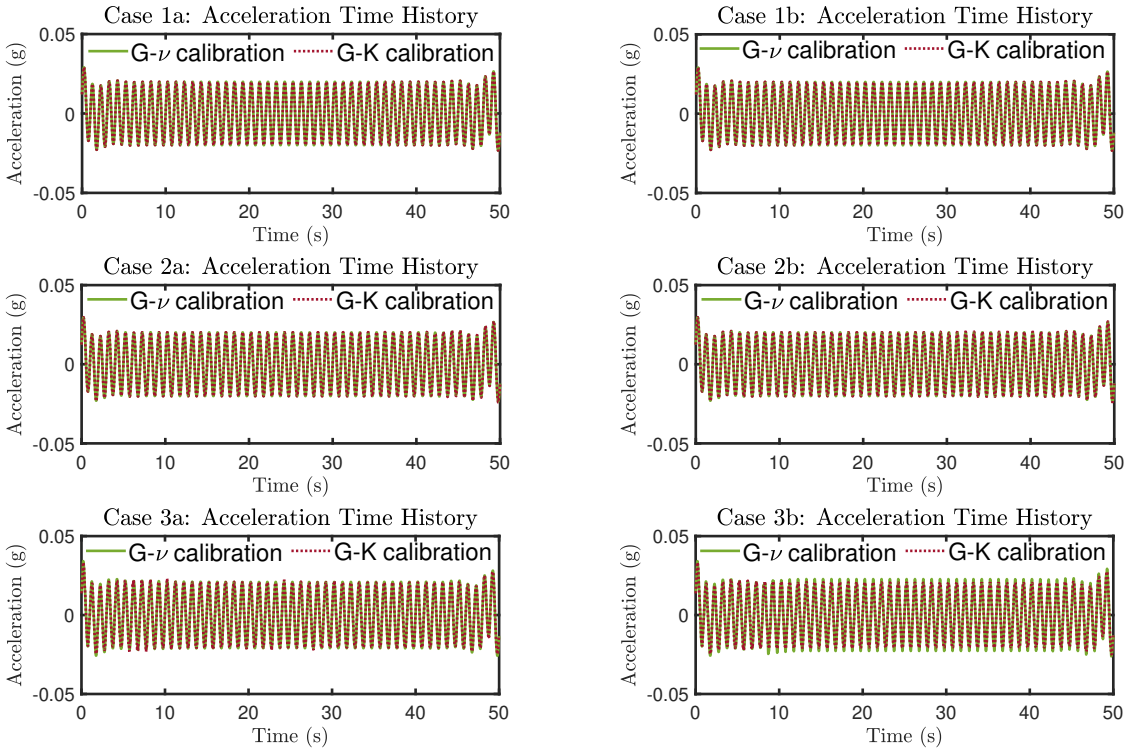

Figure 8.25: Acceleration time history at the base of the liquefiable layer

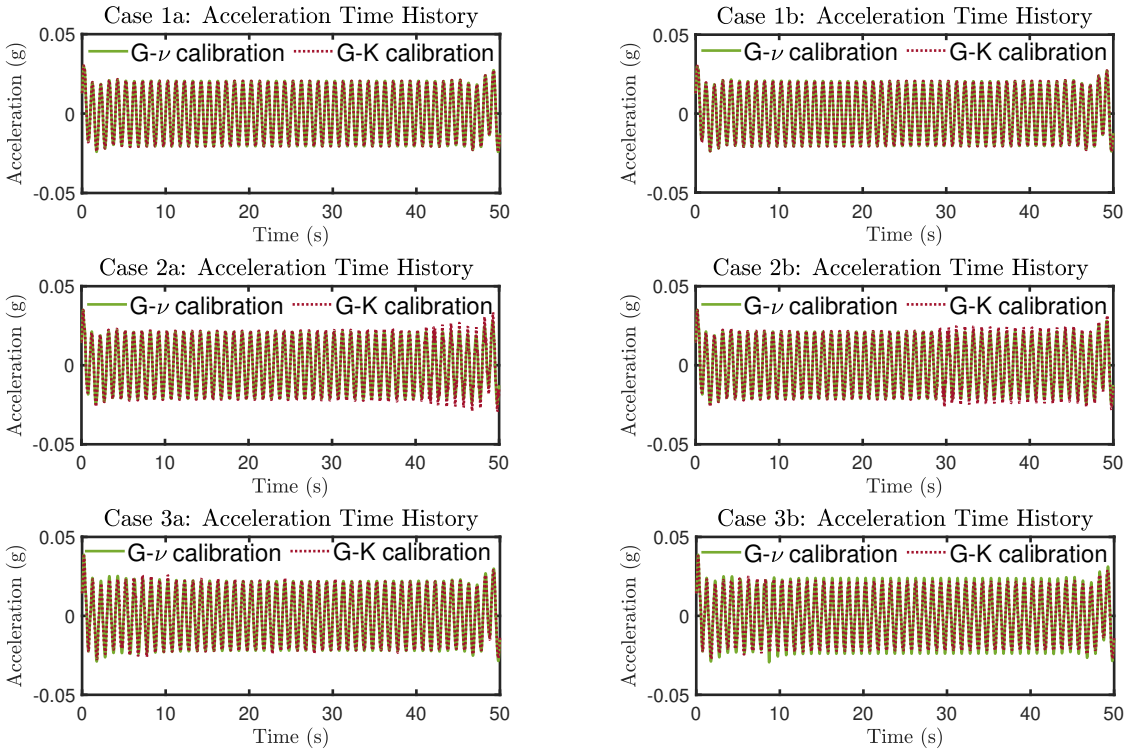

Figure 8.26: Acceleration time history at the mid-depth of the liquefiable layer

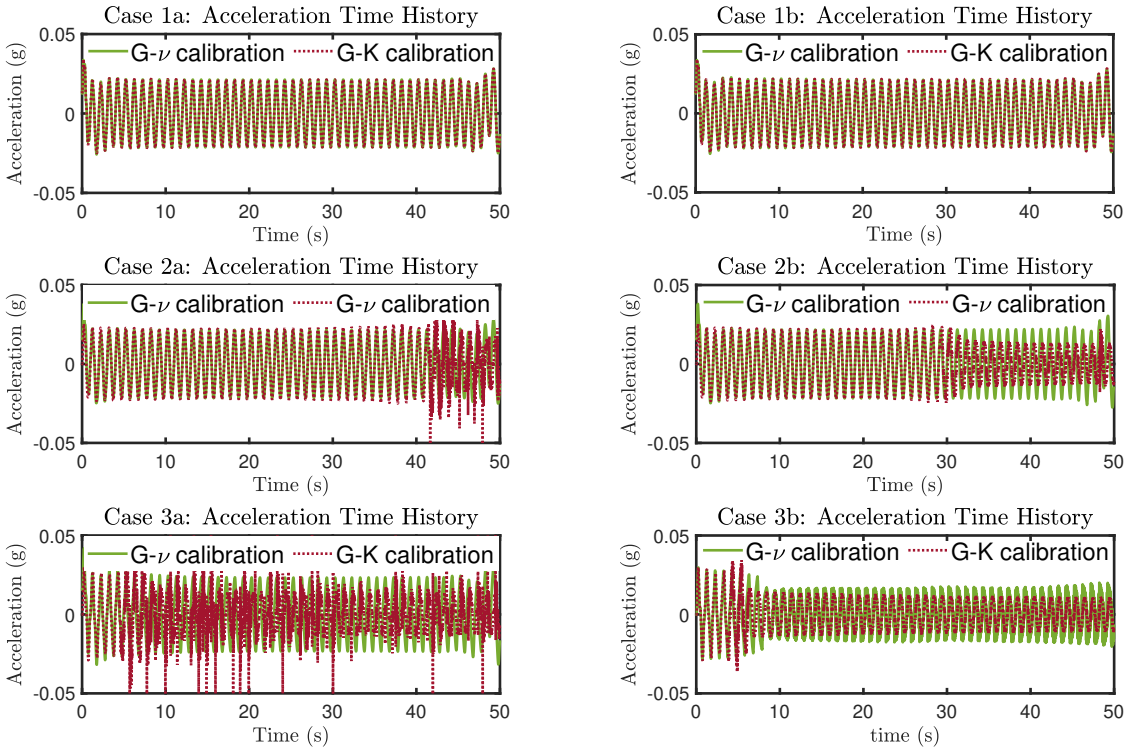

Figure 8.27: Acceleration time history at the top of the liquefiable layer

sulted in the highest PGA ($= 0.025g$) and the lowest factor of safety against liquefaction among Cases 1, 2 and 3, albeit all cases resulted in $FS_L > 1$. For the practically drained case (Case 1b), pore pressure build-up was minimal for both calibration methods, as volume changes were mostly unrestricted due to the combination of high permeability and low amplitude shaking. Positive volumetric strains were generated due to pore water outflow along the entire height of the soil column, refer figure 8.33. Due to the softer bulk modulus of the $G-K$ calibration, the volumetric strains were larger and the corresponding surface settlement was bigger.

Depth (m)	σ_{v0} (kPa)	σ'_{v0} (kPa)	r_d	a_{max} (g)	τ_{cyc} (kPa)	CSR	N	CSR_{tx}	CSR_{ss}	FS_L
Top	49.4	24.9	0.99	0.0247	1.22	0.05	50	0.11	0.08	1.57
Mid	113.6	54.7	0.95	0.0237	2.70	0.05	50	0.11	0.08	1.56
Bottom	150.3	71.8	0.92	0.0231	3.47	0.05	50	0.11	0.08	1.59

Table 8.4: Simplified procedure calculation (Seed and Idriss, 1971) for Case 3 and input acceleration of figure 8.22

For Case 2 and for the $G-K$ calibration, at the top of the critical layer the acceleration response (figure 8.27) underwent deamplification due to the presence of a low permeability

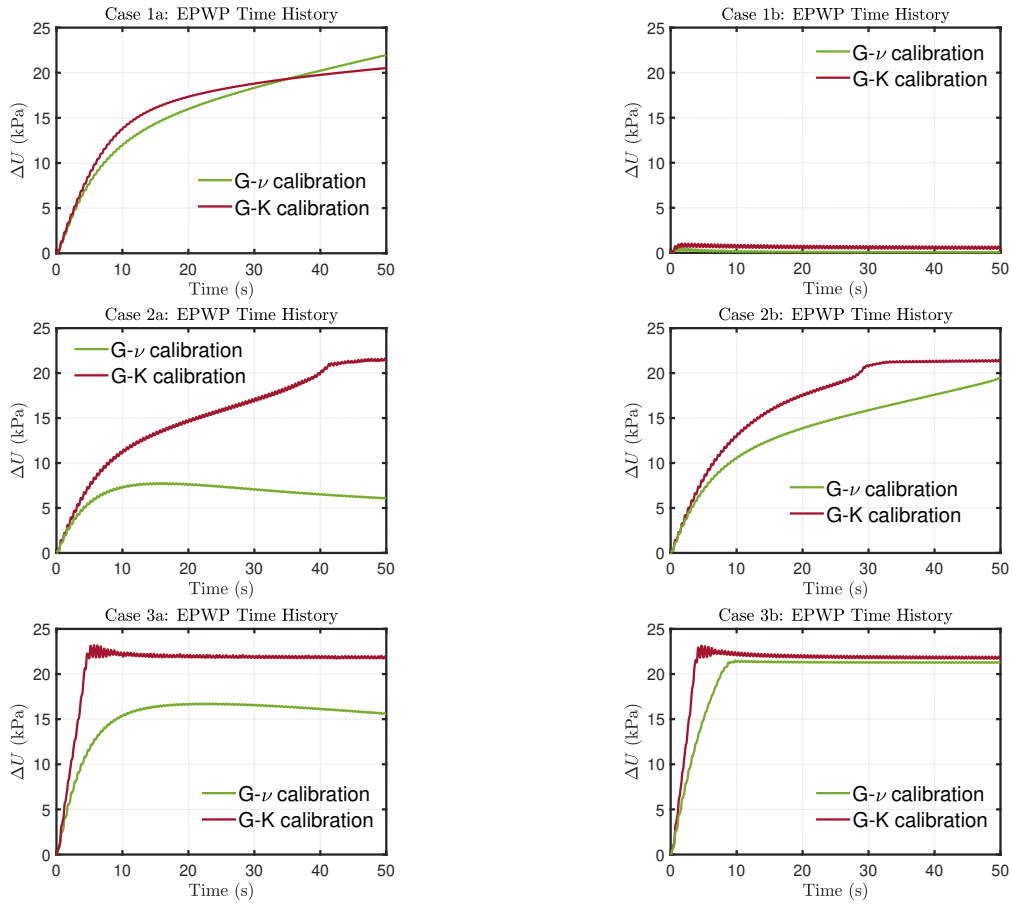

Figure 8.28: Excess pore pressure time history at the base of the liquefiable layer

layer overlying the liquefiable sand layer. The deamplification of accelerations simulated by the $G-K$ calibration implied the onset of liquefaction which was triggered faster for Case 2b (refer figure 8.31). The $G-\nu$ calibration, on the other hand, did not reach liquefaction triggering for Cases 2a and 2b as seen from the pore pressure time histories in figures 8.28-8.30, consistent with the acceleration time histories of figures 8.25-8.27. The difference in the simulation results of $G-\nu$ and $G-K$ calibration options stem from the difference in bulk modulus that ultimately impacts the rate of generation and dissipation of excess pore pressures ($\frac{\partial \bar{u}}{\partial t} = c_v \frac{\partial^2 \bar{u}}{\partial z^2}$, where $c_v \propto K$). The stiffer bulk modulus of the $G-\nu$ calibration resulted in a higher coefficient of consolidation c_v that dissipated the accumulated excess pore pressures at a faster rate than the $G-K$ calibration along the height of the soil column as seen in Case 2a (figure 8.31). The volumetric strains generated were also lower in magnitude for the $G-\nu$ calibration

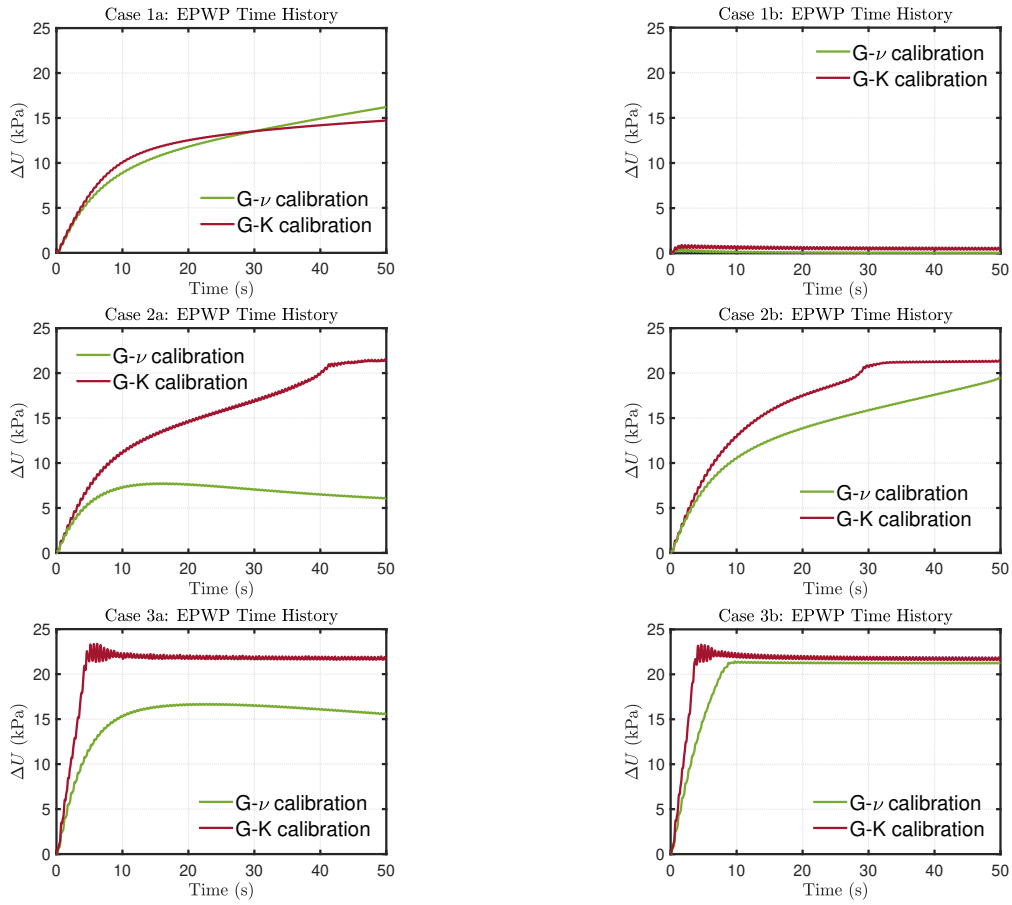

Figure 8.29: Excess pore pressure time history at the mid-depth of the liquefiable layer

than the $G-K$ calibration due to the stiffer bulk modulus, and remained contractive (positive) along the height of the soil column in Case 2a (figure 8.33), similar to the drained case (Case 1b). The small volume of water expelled from the bottom sand layer could be dissipated to the ground surface through the low permeability layer. Although very limited volumetric expansion was noted at the upper layers in Case 2b upon the introduction of the even lower permeability cap, liquefaction was not triggered for Case 2b by the $G-\nu$ calibration. The excess pore pressure trend indeed showed an upward rise at the end of shaking, indicating that liquefaction could be triggered given few additional cycles of shaking. In the $G-K$ calibration results for Case 2a, the pore pressure build-up was more rapid than the undrained case (figures 8.28-8.30), with the onset of liquefaction detected after $t = 40$ s at the top layer (figure 8.31). The triggering of liquefaction is followed by dilation spikes in the acceleration response, evident in Case 2a

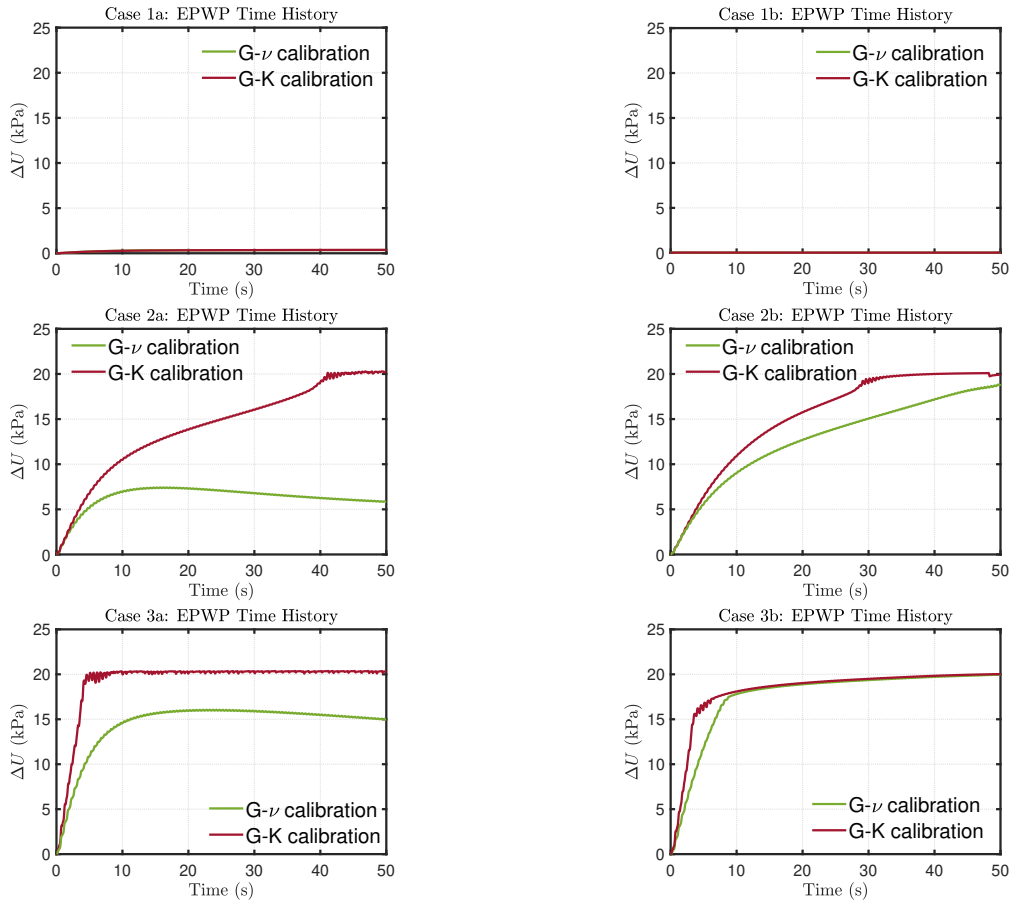

Figure 8.30: Excess pore pressure time history at the top of the liquefiable layer

(figure 8.27). Faster still, liquefaction was triggered at $t = 30$ s with the $G-K$ calibration for Case 2b, where the hydraulic conductivity of the crust layer was further reduced. However, because of the increased volumetric expansion rate, the dilation spikes were far less evident in Case 2b. The $G-K$ calibration, produced larger negative volumetric strains at the top half of the liquefiable layer, indicating net water inflow, while larger compressive strains accumulated at the bottom half, indicating net water outflow (figure 8.33) in both Cases 2a and 2b. For the slower dissipation rate by the $G-K$ calibration and the larger pore volume flow due to the softer bulk modulus, expansive volumetric strains were accumulated below the interface of the sandy silt layer. The inflow condition at the interface led to the reduction of the cyclic resistance, as was shown in chapter 7, and liquefaction was manifested. For Case 2b, the simulation results of pore pressure time histories by both calibration methods, as seen in figure 8.31, were very

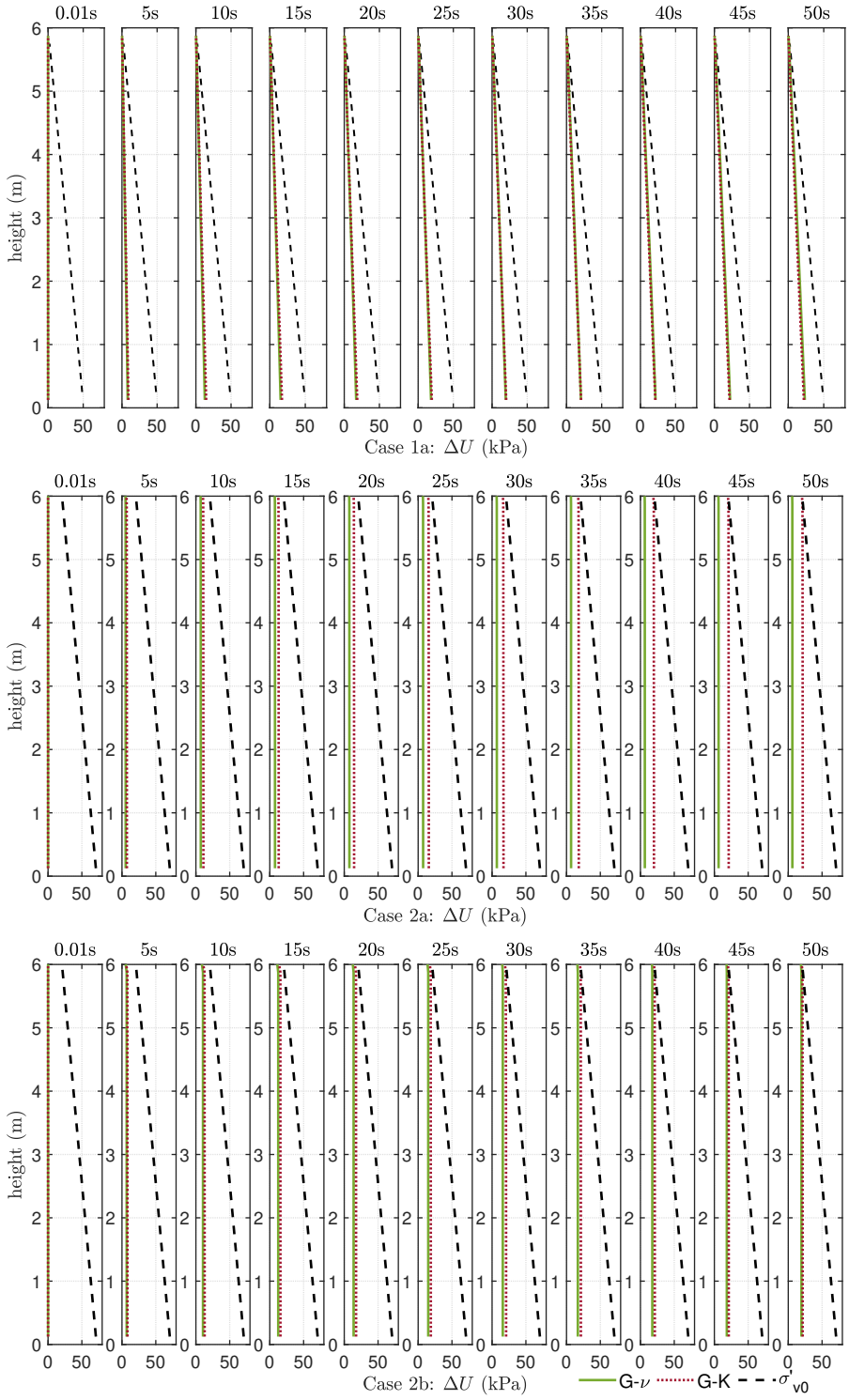

Figure 8.31: Comparison of simulated excess pore pressure time histories in OpenSees along the height of the soil column

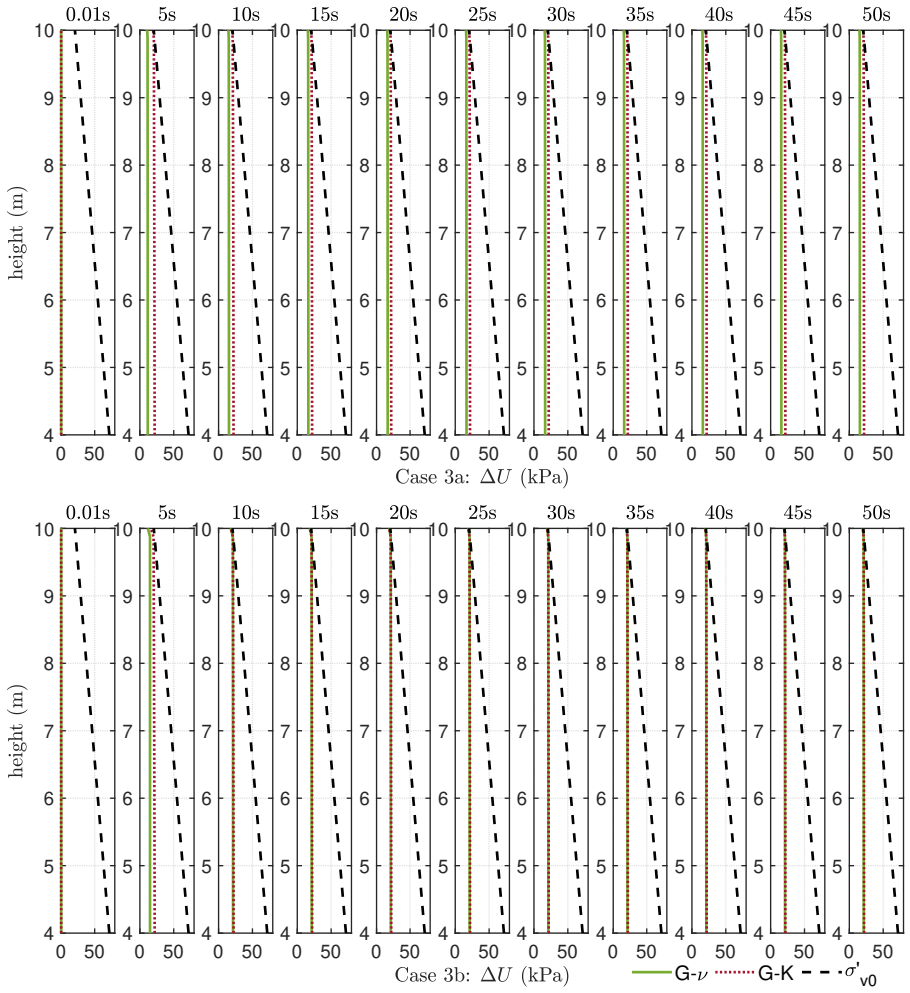

Figure 8.32: Comparison of simulated excess pore pressure time histories in OpenSees along the height of the soil column

similar; the similarity in responses emanating from the further reduction of permeability of the overlying sandy silt layer as compared to the critical sand layer, by an order of magnitude of 4 in the 'b' case as opposed to an order of magnitude of 2 in the 'a' case.

The sandy silt layer was liquefied in the numerical simulations in Case 2a by the $G-K$ calibration due to the dense sand material model used to capture the stress-strain behaviour of the silt layer in OpenSees and the sustained cycles of acceleration, that allowed the accumulation of excess pore water pressure from cyclic shearing. Additionally, larger pore volume inflow from the sand layer below further intensified the accumulation of excess pore pressures. The liquefaction front thus progressed downwards within the sandy silt in Case 2a, and reached a

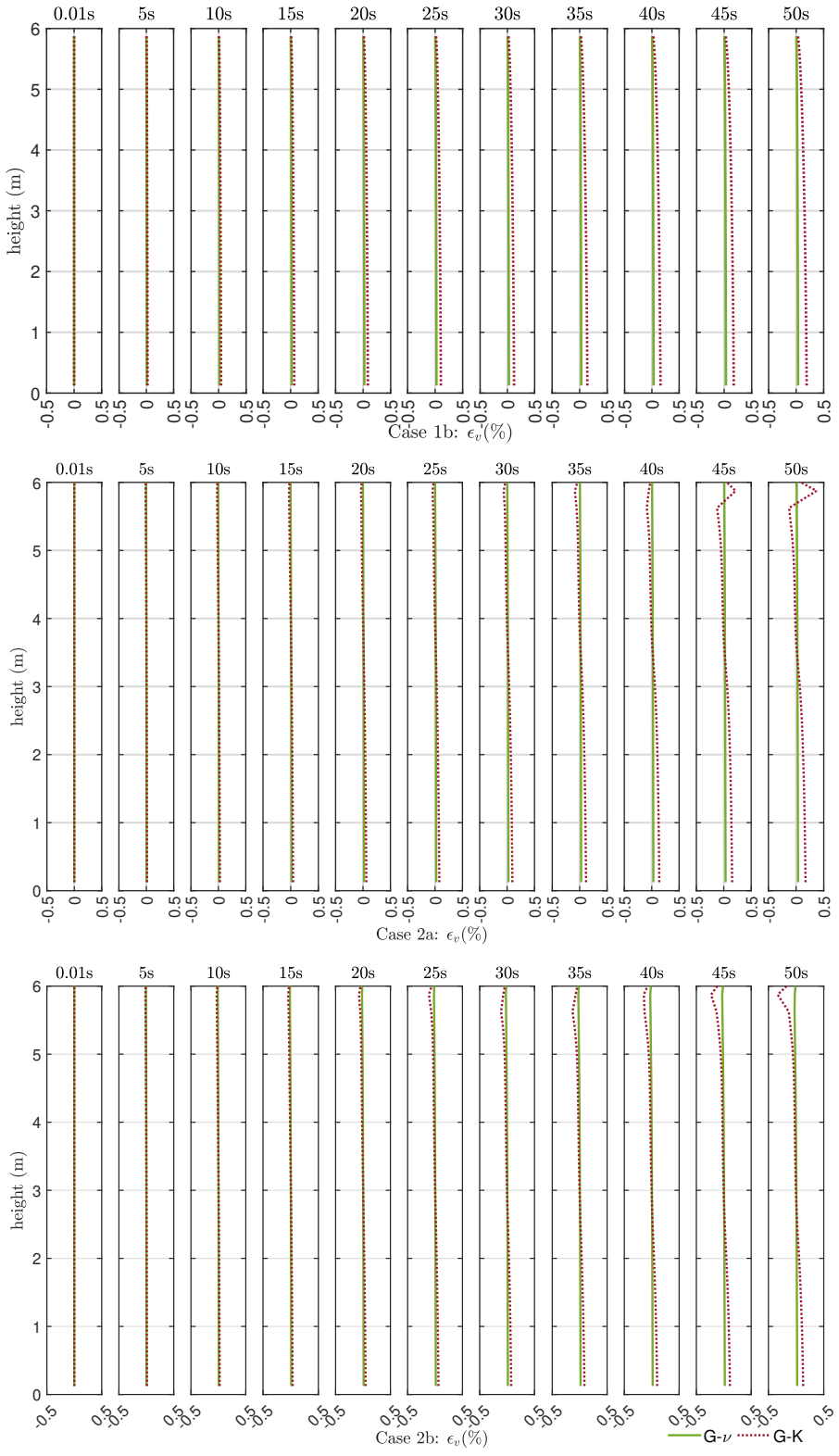

Figure 8.33: Comparison of simulated volumetric strain isochrones in OpenSees along the height of the soil column

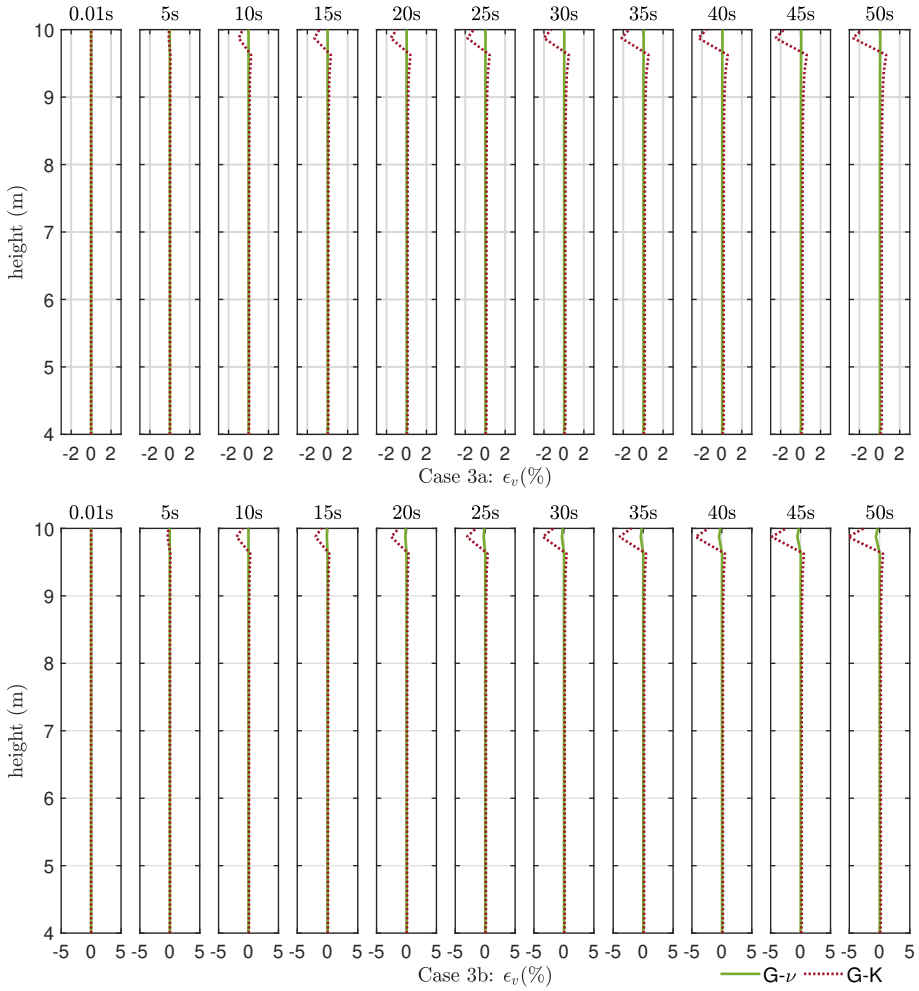

Figure 8.34: Comparison of simulated volumetric strain isochrones in OpenSees along the height of the soil column

depth just below the interface with the loose sand layer, leading to volumetric contraction at the finite-element below the interface after $t = 45$ s (refer figure 8.31), due to the large positive value of $-\frac{\partial^2 \bar{u}}{\partial z^2}$ at the location of the front. However, in Case 2b for the $G-K$ calibration, the early deamplification of accelerations compared to Case 2a due to the early onset of liquefaction below the interface limited the cyclic shearing within the sandy silt layer and the resulting excess pore pressure accumulation, which was not sufficient to trigger liquefaction. The finite-element below the sandy silt layer underwent larger volume expansion from water inflow earlier on, due to the presence of a very low permeability overlying layer which restricted flow, and remained dilated throughout shaking. The dilation zone penetrated deeper into the critical layer.

For Case 3a, where a denser sand layer was added at the base of the deposit in Case 2a, the $G-\nu$ calibration gave no traces of liquefaction triggering, similar to Case 2a (figure 8.27). In Case 3a and for the $G-K$ calibration, liquefaction occurred in less than $t = 10$ s at the top of the looser sand layer (figure 8.32) as opposed to the onset of liquefaction at $t = 40$ s in Case 2a (figure 8.27). The presence of a denser layer at the base of the deposit in Case 3 created additional upwards flow that further added to the excess pore pressure accumulation for both calibration methods (figures 8.28-8.30), and resulted in even faster liquefaction triggering by the $G-K$ calibration. As in previous cases, the $G-\nu$ calibration was able to redistribute and dissipate the accumulated pore pressures fast enough to avoid liquefaction triggering. As the permeability constant of the sandy silt layer was further reduced (Case 3b), the difference in simulation results became negligible as the excess pore pressures were unable to dissipate and pore volume flow was mostly restricted at the interface leading to significant dilation of the top element of the critical layer (figures 8.32 and 8.34). Liquefaction was predicted by both calibration methods in Case 3b, although, the $G-K$ calibration showed faster onset of liquefaction due to the softer bulk modulus, as discussed previously for Case 2. Dilation spikes in the acceleration response were prominent in Case 3a than in Case 3b, similar to Cases 2. For Case 3a with the $G-K$ calibration, the entire depth of the liquefiable soil layer underwent contraction apart from the element just below the sandy silt layer, which underwent considerable dilation, similar to Case 2a. The denser layer at the bottom, despite not liquefying, produced additional upwards water flow, which kept more of the critical layer under increased pore pressures, forcing the positive values of the second order derivative of excess pore pressure or dilation ($d\varepsilon_v(t) = -\frac{k}{\gamma_w}\frac{\partial^2 \bar{u}}{\partial z^2}dt$) closer to the reduced flow boundary condition at the layer interface. For Case 3b, the volumetric expansion below the silt layer was even more pronounced which further reduced cyclic resistance (refer figure 7.24). The $G-\nu$ calibration, with its resulting higher bulk modulus, led to the gradual accumulation of limited volumetric expansion at the interface of the sandy silt and the critical layer for Case 3b and to a lesser extent for Case 2b.

The simplified liquefaction assessment prediction for the denser critical layer in the layered

deposit of Case 4 (figure 8.23), shown in table 8.5, predicts a factor of safety against liquefaction $FS_L > 1$ under the higher amplitude shaking of figure 8.24 ($PGA = 0.074g$), which is thrice the amplitude of shaking for Cases 1, 2 and 3. The undrained cyclic resistance curve for $D_r =$ 80% Hostun sand was determined from the CRR curve equation for Hostun sand in Adamidis and Anastasopoulos (2022). The isochrones of excess pore pressure and volumetric strains for Case 4 are shown in figures 8.35 and 8.36, respectively. For the undrained case (Case 4a), the excess pore pressure plots do not show the onset of liquefaction, in conformance with the simplified procedure calculations. Note that the excess pore pressures rose faster for the $G-\nu$ calibration method due to the simulated undrained cyclic resistance curves being positioned slightly to the right of those for the $G-K$ calibration, as seen in figure 7.22, requiring few more cycles to liquefaction for the $G-K$ calibration under the same amplitude of shaking. When the low permeability silt layer was added (Case 4b) and the soil's permeability was set to its realistic value, dissipation through upwards pore volume outflow, faster for the $G-\nu$ calibration due to its higher c_v, was restricted at the interface with the low permeability layer. Volume of pore fluid accumulated below the sandy silt layer, leading to an inflow condition at the finite-element below the interface and a small volumetric contraction or outflow condition for the rest of the layer. Liquefaction was triggered below the interface for both calibration methods, rendering a 'false-negative' prediction by the simplified procedure. The excess pore pressures again rose faster under an inflow condition for the $G-\nu$ calibration as expected based on the liquefaction resistance curves presented for an inflow condition in chapter 7. Therefore, the onset of liquefaction at the top of the sand layer occurred faster for the $G-\nu$ calibration than for the $G-K$ calibration. Note that the expansive volumetric strains for the $G-K$ calibration were initially accumulated slower than the $G-\nu$ calibration, but eventually the volumetric strains attained a larger magnitude due to the softer bulk modulus than the $G-\nu$ calibration (figure 8.36). The sandy silt layer was also not liquefied in the numerical simulations in Case 4 as seen in figure 8.35 due to the low number of shaking cycles, even though the amplitude of shaking was tripled.

Depth (m)	σ_v (kPa)	σ'_v (kPa)	r_d	a_{max} (g)	τ_{cyc} (kPa)	CSR	N	CSR_{tx}	CSR_{ss}	FS_L
Top	49.8	25.2	0.99	0.0730	3.63	0.14	6	0.21	0.15	1.05
Mid	116.5	57.7	0.95	0.0702	8.18	0.14	6	0.21	0.15	1.06
Bottom	154.7	76.2	0.92	0.0683	10.57	0.14	6	0.21	0.15	1.09

Table 8.5: Simplified procedure calculation (Seed and Idriss, 1971) for Case 4 and input acceleration of figure 8.24

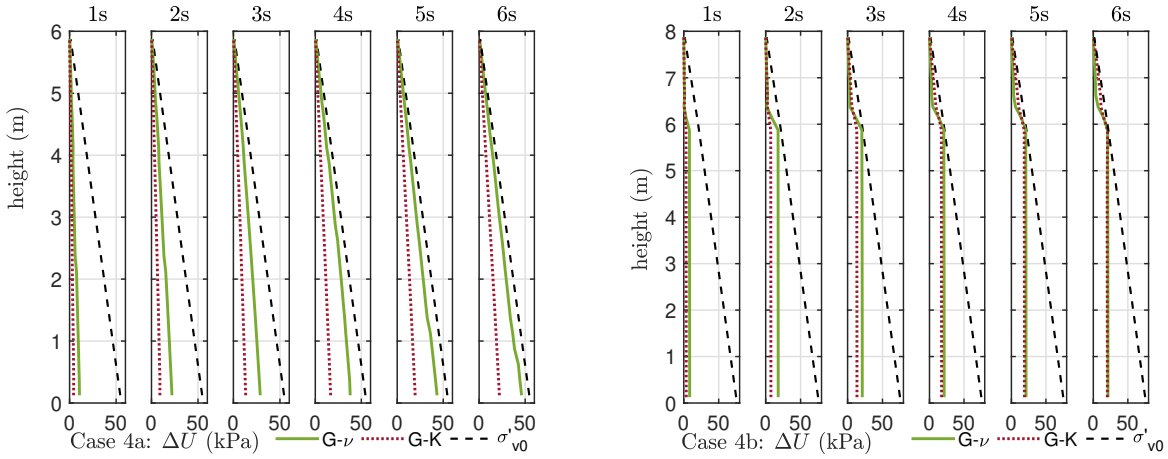

Figure 8.35: Comparison of simulated excess pore pressure time histories in OpenSees along the height of the soil column

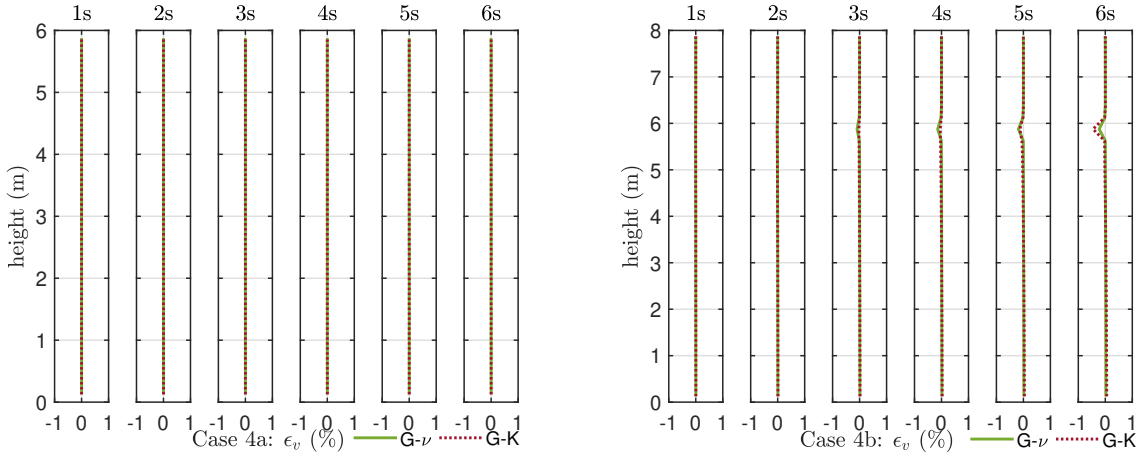

Figure 8.36: Comparison of simulated volumetric strain isochrones in OpenSees along the height of the soil column

The effects of layering captured by the $G-K$ calibration method are expected to be closer to reality, as this calibration was validated for a uniform deposit in section 8.3. The $G-K$ calibration predicted the onset of liquefaction at the interface of the liquefiable and the over-

lying lower permeability layer in all layered cases examined thus far. Although the undrained condition (Cases 1a and 4a) and the simplified prediction (tables 8.4 and 8.5) did not predict the triggering of liquefaction for the given input load, the presence of a low permeability layer led to the onset of liquefaction (Cases 2a, 2b and 4b). With the addition of dense sand below the liquefiable loose sand, liquefaction triggering was more pronounced for the same level of shaking (Cases 3a and 3b). Larger volumetric strains were accumulated at the interface of the sandy silt layer and the liquefiable sand layer where liquefaction was manifested by the $G-K$ calibration (figures 8.33 and 8.34). Such mechanisms of liquefaction triggering were observed in the Christchurch earthquakes, where excess pore pressures in underlying non-liquefied layers aggravated the liquefaction of the critical layer through seepage (Cubrinovski et al., 2019; Ntritsos and Cubrinovski, 2022). The excess pore pressures developed below the interface equaled in magnitude to the initial vertical effective stress at the interface (Cases 2, 3 and 4), representing a hydrostatic distribution below the liquefied interface as this now becomes the relevant drainage boundary condition. Equalisation of excess pore pressures below the interface is consistent with hydraulic conditions that may promote localised water accumulation or water-film formation in a real deposit. Although such a discontinuity cannot be explicitly represented by a continuum model (Kokusho et al., 2025), it has been reported previously in experimental testing (Adamidis and Madabhushi, 2018; Kokusho, 2003; Sinha et al., 2022) and could lead to large displacements of the top layer if at a slope (Kokusho and Fujita, 2001).

The typical $G-\nu$ calibration of bulk modulus predicted onset of liquefaction only in the 'b' cases where drainage was severely restricted at the interface. The similar results for both calibration methods noted in the 'b' cases suggests that the relative permeability ratio of the adjacent layers is crucial in determining when the bulk modulus expression is critical in capturing the triggering response. As seen from the validation exercise in section 8.3, when pore fluid flow was unrestricted, the choice of bulk modulus directly impacted the predicted onset of liquefaction. When pore fluid flow was partially restricted by a lower permeability overlying layer (in Cases 2a and 3a, with permeability constant 2 orders of magnitude lower than the critical layer),

the bulk modulus definition still played a role in capturing liquefaction triggering. However, when the permeabilities of the critical and the overlying layer differed very significantly (by 4 orders of magnitude in Cases 2b, 3b and 4b), the restriction to pore fluid flow was such that excess pore pressure built-up quickly and pushed the stress paths towards the onset of liquefaction irrespective of calibration method. Hence, it can be concluded that the direct bulk modulus calibration from isotropic unloading/reloading data is crucially important when layered deposits of relatively similar permeability constants are assessed (permeability ratio of critical layer to adjacent layer $\sim 1-1000$).

8.4.4 'False-positive' case: Model setup

This section presents a layered deposit that targeted potential 'false-positive' simplified predictions, as shown in figure 8.37. Case 5 models a saturated soil deposit of 12 m deep, where a 2 m thick low permeability sandy silt layer was sandwiched between loose liquefiable sand layers of 6 m at the top and 4 m at the bottom, above the bedrock (figure 8.37). The material properties of the loose sand layer were specified for $D_r = 40\%$ ($e = 0.8978$) Hostun sand and a soil permeability constant of 9.2×10^{-4} m/s as in Cases 2 and 3. The SANISAND-MSf model (M. Yang et al., 2022) was used to define the soil material, with calibration parameters reported in table 7.4. Note that in this case too, the permeability rather than the stress-strain behaviour of the sandy silt layer was consequential for this study. To ensure that the presence of the sandy silt layer between the loose sand layers does not shift the amplitude or frequency content of the input motion which could be of significance for the liquefaction study of the top liquefiable sand layer, the shear modulus coefficient G_0 of the DafaliasManzari material used to model the silt layer in OpenSees was increased by over 3 times (model parameters obtained from Ramirez et al. (2018) for $D_r = 95\%$ of Monterey sand) to match the small-strain shear modulus of a realistic sandy silt layer at a vertical effective stress calculated at 7 m depth of the deposit. Similar acceleration time histories obtained at the top and bottom of the sandy silt layer ascertained minimal influence of the low permeability layer on the response of the critical layer above. Case

5 was excited with a sinusoidal wave of 5 cycles at a frequency of 1 Hz and with an amplitude of 0.10g (figure 8.38), five times that used for Cases 1 to 3. This acceleration time history was intended to trigger liquefaction in the loose, critical sand layer under undrained conditions (Case 1a in figure 8.21) and generate high excess pore pressures in a drained case with soil's actual permeability (Case 1b in figure 8.21). Similar to the 'false-negative' cases, two variants were examined, with Case 5a defined with a higher permeability constant ($k = 1 \times 10^{-5}$ m/s) for the sandy silt layer than Case 5b ($k = 1 \times 10^{-7}$ m/s). For the element definitions, nodal boundary conditions and mesh size determination, refer to section 8.3.1. The soil column mesh profile in OpenSees is shown in figure 8.37. The analysis parameters were defined as in section 8.4.2.

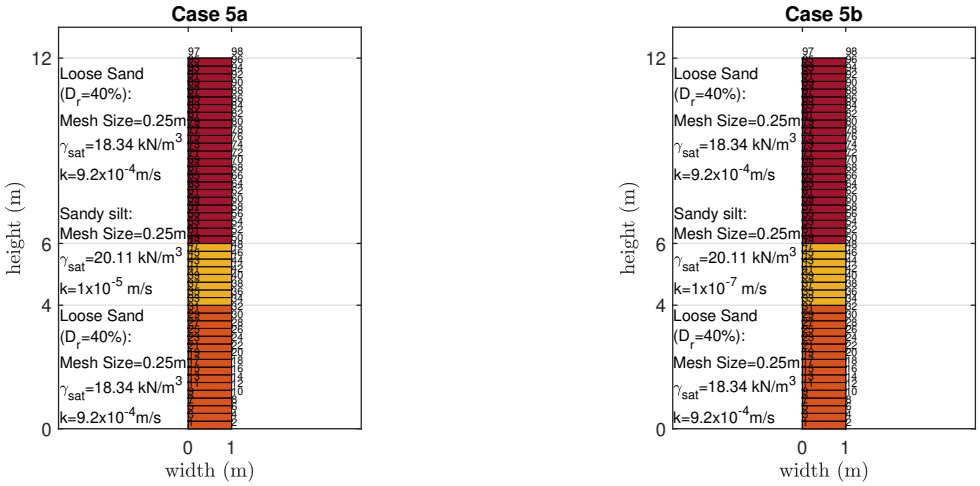

Figure 8.37: Schematic representation of layered soil column mesh profiles for Case 5

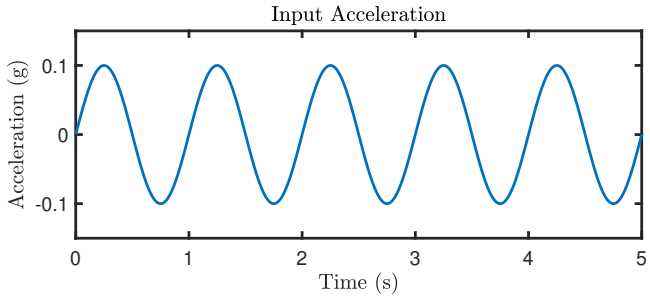

Figure 8.38: Input acceleration time history for Cases 1 and 5

8.4.5 'False-positive' case: Simulation results

In this section, the simulation results for Cases 5a and 5b are presented. Cases 1a and 1b were also analysed under the input acceleration time history of figure 8.38 and act as benchmarks. The acceleration time histories at the bottom, mid-depth and top of the critical layer are shown in figures 8.39, 8.40 and 8.41, respectively, for both bulk modulus calibration methods. The isochrones of pore pressures along the depth of the soil column are given in figure 8.42. The volumetric strain isochrones along the depth of soil column is shown for all cases in figure 8.43. The simplified liquefaction assessment calculations for a peak ground acceleration of $0.139g$, computed as in section 8.3.5 using the input acceleration of figure 8.38, at the top critical layer in Case 5 resulted in a factor of safety against liquefaction $FS_L \leq 1$, indicating the onset of liquefaction. Table 8.6 shows the simplified procedure calculations. From the acceleration time history plots of the critical layer, deamplification of accelerations was seen at the top and the mid-depth of the soil layer in the approximate undrained case (Case 1a), indicating liquefaction triggering by both bulk modulus calibration methods, in accordance with the simplified procedure. The fully drained case (Case 1b) resulted in limited positive volumetric strains along the height of the soil column with minimal rise in excess pore pressures and no manifestation of liquefaction, for the $G-\nu$ calibration. However, for the $G-K$ calibration in Case 1b, the high shaking amplitude resulted in considerable rise of excess pore pressures that dissipated at a slower rate due to the lower value of c_v ($\frac{\partial \bar{u}}{\partial t} = c_v \frac{\partial^2 \bar{u}}{\partial z^2}$) owing to a softer bulk modulus. The larger pore fluid outflow from the bottom of the layer led to volumetric expansion at the top 1 m of the soil deposit (refer figure 8.43). Subsequent softening, as noted in the acceleration time history at the top of the critical layer pushed the soil closer to liquefaction (refer figure 8.42).

For Cases 5a and 5b, both calibration methods did not predict liquefaction triggering at the top liquefiable sand layer (top 6 m of the soil column), as seen in figure 8.42, contradicting simplified predictions. The same input acceleration almost liquefied the uniform sand deposit at the top of the layer in the fully drained Case 1b using the $G-K$ calibration, however in

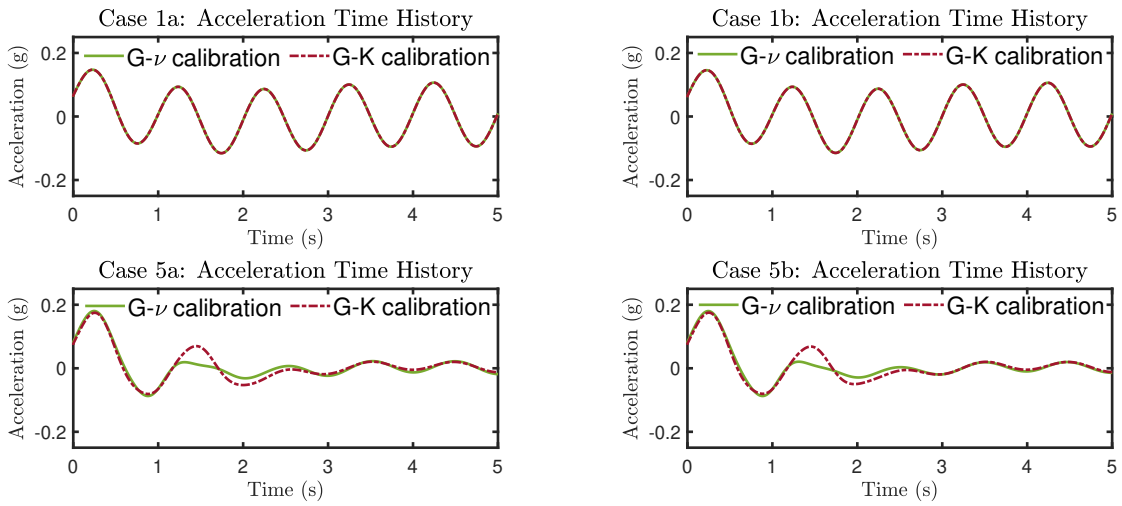

Figure 8.39: Acceleration time history at the base of the top liquefiable layer

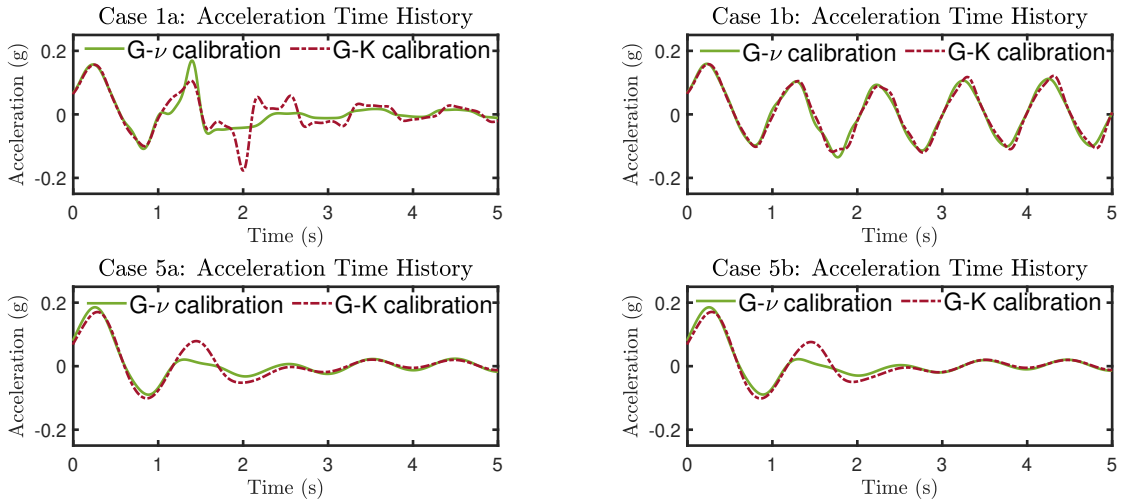

Figure 8.40: Acceleration time history at the mid-depth of the top liquefiable layer

Depth (m)	σ_{v0} (kPa)	σ'_{v0} (kPa)	r_d	a_{max} (g)	τ_{cyc} (kPa)	CSR	N	CSR_{tx}	CSR_{ss}	FS_L
Top	9.2	4.3	1.00	0.1387	1.27	0.30	5	0.15	0.10	0.35
Mid	73.4	34.1	0.97	0.1347	9.89	0.29	5	0.15	0.10	0.36
Bottom	110	51.2	0.95	0.1316	14.48	0.28	5	0.15	0.10	0.37

Table 8.6: Simplified procedure calculation (Seed and Idriss, 1971) for Case 5 and input acceleration of figure 8.38

both Cases 5a and 5b, the excess pore pressure rise was lower than that observed in the drained condition using both calibration methods. The acceleration plots at the top and bottom of the top critical layer, figures 8.39 and 8.41, respectively are identical and indicate minimal straining of the top sand layer. Also, the acceleration plots at the base show significant deamplification

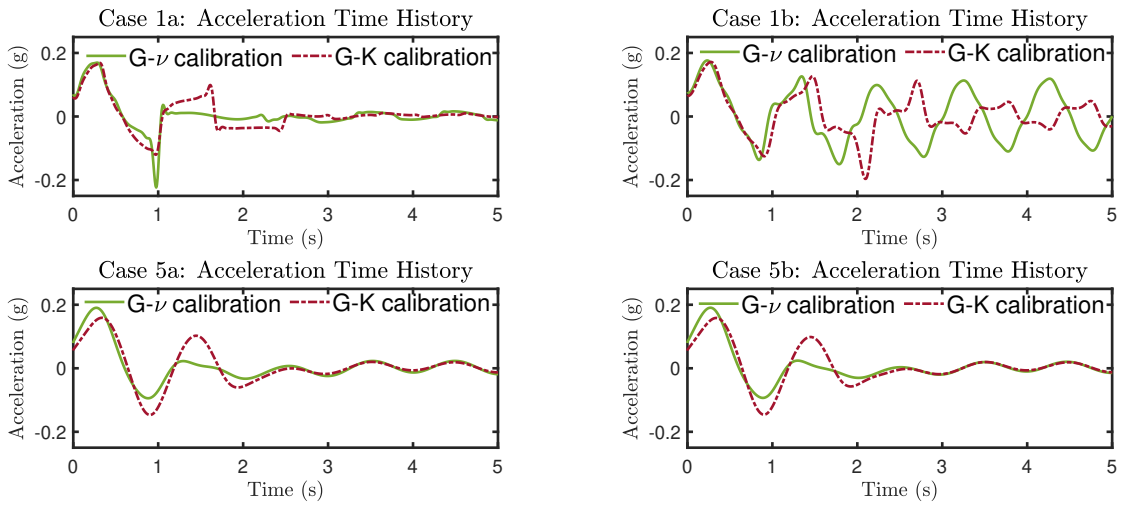

Figure 8.41: Acceleration time history at the top of the top liquefiable layer

of the input motion of figure 8.38 after the first loading cycle. Due to reduced accelerations, the top critical layer developed minimal excess pore pressures in both Cases 5a and 5b, that were dissipated simultaneously owing to unrestricted flow towards the surface, which averted the triggering of liquefaction. For the lower bulk modulus in the $G-K$ calibration, the accumulated volumetric contraction in the top sand layer was larger than the $G-\nu$ calibration resulting in larger settlements at the top surface.

In the deeper sand layer of Cases 5a and 5b, rapid generation of excess pore pressures from high amplitude cyclic shearing led to upwards pore volume flow that was obstructed at the interface between the bottom sand layer and the sandy silt layer. The drainage restriction resulted in volume expansion at the interface reducing cyclic resistance and triggering liquefaction within the first two cycles. Under the same inflow condition, the $G-\nu$ calibration results in more severe degradation of cyclic resistance than the $G-K$ calibration (refer to trends for degradation of cyclic resistance under an inflow condition in figure 7.24). However, in this case, the $G-K$ calibration resulted in larger volumetric strains due to a softer bulk modulus, generating a greater magnitude of inflow than the $G-\nu$ calibration, such that the rise in excess pore pressures were identical. The formation of the softened dilation zone (or a potential water-film in reality) at the interface acted as isolation for the upper layers, minimising the amplitude of the accelerations

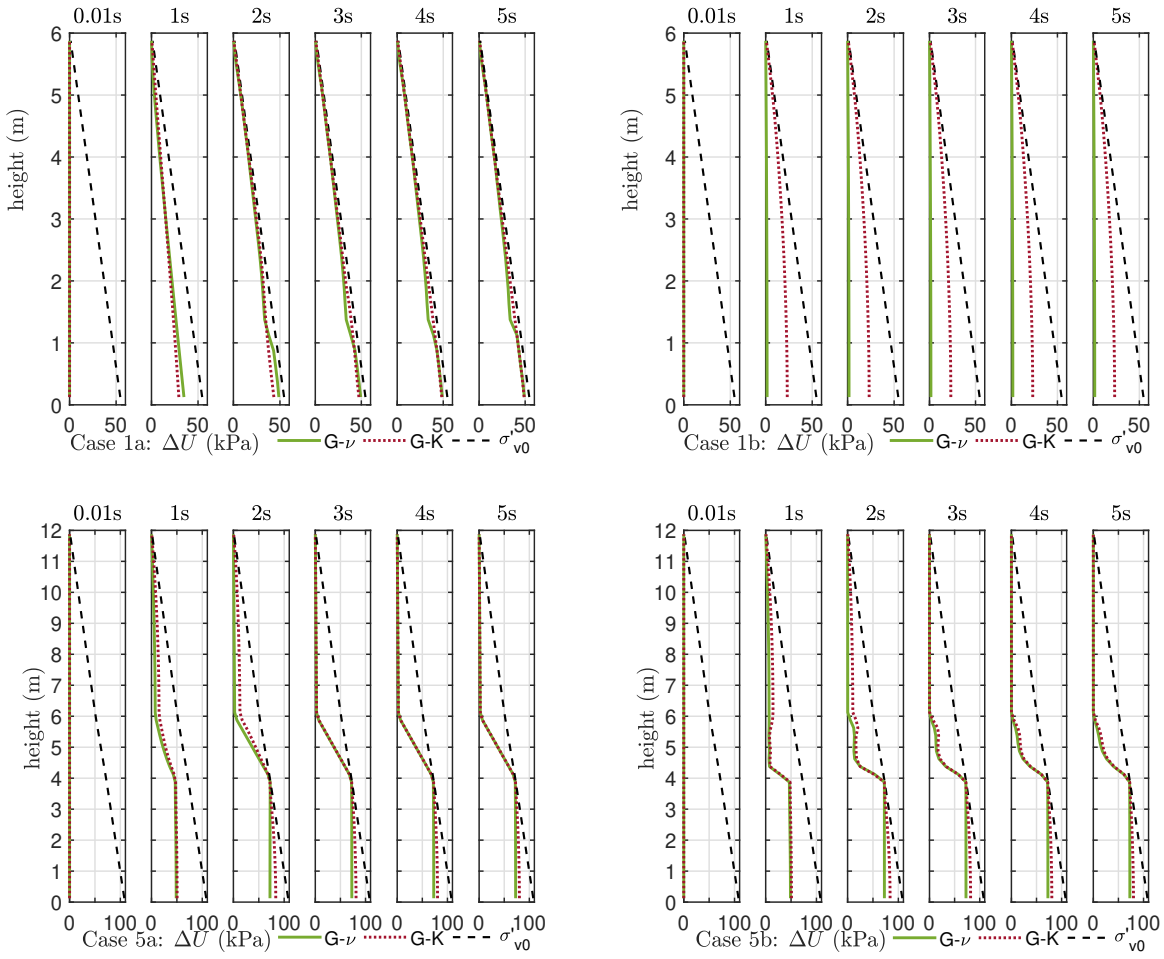

Figure 8.42: Comparison of simulated excess pore pressure time histories in OpenSees along the height of the soil column

propagating above. The difference in permeability of the sandy silt layer in Cases 5a and 5b did not alter results for liquefaction triggering in the two calibration methods, unlike in the 'false-negative' cases, due to the higher amplitude of shaking. In Case 5b, the second-order derivative $\frac{\partial^2 \bar{u}}{\partial z^2}$, which is related to the volumetric strain rate ($d\varepsilon_v(t) = -\frac{k}{\gamma_w}\frac{\partial^2 \bar{u}}{\partial z^2}dt$), was larger at the bottom interface of the silt layer than in Case 5a (figure 8.42), indicating greater magnitude of expansive strains at the interface in Case 5b, for both calibration methods, as seen in figure 8.43.

Contrary to the simplified assessment of liquefaction triggering for the layered deposit (table 8.6) and the positive prediction by the undrained case (Case 1a), this analysis indicated mitigation of liquefaction due to the presence of a lower permeability layer sandwiched between the

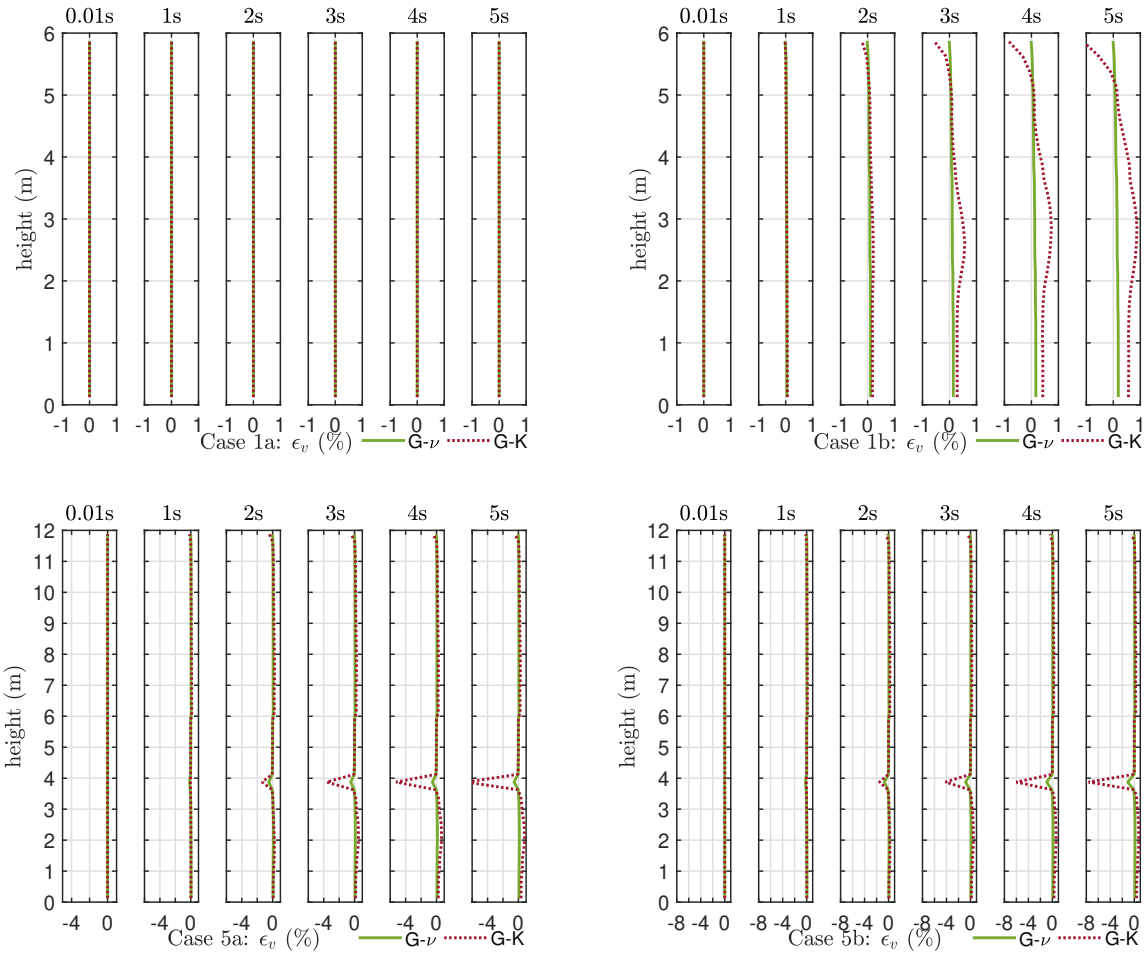

Figure 8.43: Comparison of simulated volumetric strain isochrones in OpenSees along the height of the soil column

liquefiable sand layers. Softening due to rise of excess pore pressures at the interface between the sandy silt layer and the bottom sand layer de-amplified the acceleration reaching the layers above, resulting in mitigation of liquefaction in the more vulnerable, top sand layer. Such alleviation of liquefaction in a critical layer due to softening of deeper layers has been reported for non-liquefied sites in the Christchurch earthquake sequence (Cubrinovski et al., 2019). The differences between the two calibration methods are noted in Cases 1b, 5a and 5b where the $G-K$ calibration indicated greater rise of excess pore pressures due to the slower dissipation rate and formation of a more severe dilation zone at the interface, owing to the softer bulk modulus.

8.5 Conclusions

The implications of the elasticity calibration for reproducing element-level cyclic behaviour under non-standard drained conditions were demonstrated in chapter 7. In this chapter, the importance of the calibration scheme in capturing liquefaction triggering at the system level was assessed. One-dimensional boundary value problems were simulated using fully coupled effective stress analyses in the finite-element software OpenSees (McKenna, 2011). Two calibration strategies were compared: the conventional $G-\nu$ strategy, in which the bulk modulus is derived from the shear modulus and Poisson's ratio, and the proposed $G-K$ strategy, in which the shear and bulk moduli are independently calibrated. The analyses examined liquefaction triggering in a uniform Hostun sand deposit and in a series of idealised layered profiles. Particular attention was given to the effects of co-seismic pore-fluid redistribution and layer interaction, which are not represented explicitly in simplified liquefaction assessment procedures.

The SANISAND-MSf implementation in OpenSees was modified to incorporate the Hostun-specific critical-state line, as well as elasticity and hardening expressions calibrated in chapter 7. The modified implementation was first verified against the MATLAB implementation using undrained monotonic and cyclic element simulations, for which the two implementations produced closely matching responses up to liquefaction triggering. The modelling framework was then evaluated against centrifuge test results for a uniform free-field Hostun sand deposit. Although the $G-\nu$ and $G-K$ schemes were calibrated to capture the same undrained cyclic resistance curves, the deposit-level simulations produced substantially different responses. The $G-K$ calibration reproduced the acceleration de-amplification, the excess pore pressure accumulation and the settlement observed in the centrifuge experiment much more closely than the conventional $G-\nu$ scheme. The $G-\nu$ calibration predicted rapid pore-pressure redistribution, which led to a stiffer deposit response and no liquefaction triggering at locations where liquefaction was experimentally observed.

Idealised layered deposits were subsequently analysed, targeting potential 'false-negative' and 'false-positive' predictions by the simplified procedure. For the 'false-negative' cases, a

low permeability layer over the critical layer was considered. The simplified assessment and the corresponding undrained analyses did not predict liquefaction within the critical layer for the selected amplitude of shaking. However, when drainage was allowed, upward pore-fluid flow restricted by the low permeability layer led to net inflow beneath the layer interface. The resulting volumetric expansion reduced the local cyclic resistance and promoted liquefaction triggering. The effect became more pronounced when a denser sand layer was introduced beneath the critical layer, because the lower layer provided an additional source of upward pore-fluid flow. The $G-K$ calibration predicted stronger interface effects and earlier liquefaction triggering than the $G-\nu$ calibration, which required several orders of magnitude more severe hydraulic restriction before similar triggering could occur. As a result, a 'false-negative' prediction by an undrained or simplified framework risks being confirmed by a numerical simulation incorporating drainage, if a conventional $G-\nu$ calibration that overestimates the rate of pore pressure dissipation is used.

For the 'false-positive' case, a profile where a low permeability layer is sandwiched between two layers of loose sand was considered, subjected to a higher amplitude input motion. Both the simplified prediction for the layered deposit and the undrained analysis for the isolated upper loose sand layer predicted liquefaction triggering. However, when drainage was allowed, liquefaction triggering was not reached at the top critical layer by either calibration scheme. Instead, rapid excess pore-pressure accumulation and consequent softening developed at the bottom interface of the low permeability layer. This resulted in deamplification of accelerations transmitted to the critical upper layer, where liquefaction was averted.

Under low amplitudes of shaking, the calibration of bulk modulus in numerical simulations was shown to be critical for capturing liquefaction triggering at the interface of adjacent layers, particularly when their permeabilities differ by less than three orders of magnitude. Under high amplitudes of shaking, false predictions by the simplified procedure were shown to be contradicted by both calibration methods, indicating that the bulk modulus plays a stronger role in liquefaction susceptibility assessment when the rate of accumulation of excess pore pressure is

not much greater than the rate of dissipation through pore fluid flow. Overall, incorporation of the proposed calibration of elastic moduli can significantly improve the reliability of conventional numerical simulations of liquefaction.

Chapter 9

Conclusions

9.1 Research conclusions

This thesis assessed the ability of state-of-the-art bounding surface plasticity models stemming from the Dafalias and Manzari (2004) framework to capture the effects of non-standard drainage on flow liquefaction and cyclic mobility at the element level, and on liquefaction triggering at the deposit-system level, with improvements proposed where necessary. Current simplified liquefaction assessment procedures generally assume that pore-fluid flow during earthquake shaking is negligible and assess individual soil layers in isolation. Nevertheless, experimental, theoretical, and field evidence indicate that co-seismic pore-pressure redistribution can significantly affect liquefaction triggering in stratified deposits. Reliable assessment of drainage effects requires constitutive models that can reproduce soil behaviour under non-standard drainage conditions, used within fully coupled analyses that can represent interaction between adjacent layers. Two lines of research were pursued here, relating to the triggering of flow liquefaction and cyclic mobility. The methodology for the flow liquefaction investigation involved an experimental and a numerical campaign at element level under non-standard drained monotonic shearing, while the cyclic mobility investigation included numerical analyses at the element and the system level under non-standard drained cyclic shearing, informed by experimental data from literature. Salient

conclusions from this study are listed below.

9.1.1 Performance evaluation and model improvements under coupled strain monotonic shearing

The SANISAND 2008 model was selected as a representative member of the SANISAND family for the evaluation of monotonic performance under non-standard drained conditions. Its comparatively compact formulation was deemed preferable for monotonic loading, as it does not include additional memory variables introduced in more recent versions to better capture cyclic loading. The model follows similar constitutive relations to other models of the SANISAND family for confining stresses away from the region of grain crushing. Therefore, conclusions drawn from the evaluation are transferable to other SANISAND models when replicating monotonic behaviour.

Non-standard drained conditions were imposed in triaxial compression by maintaining a ratio of volumetric to axial strain rate. Undrained, fully drained and coupled strain triaxial compression tests were conducted on a single batch of Hostun HN31 sand. The constitutive model was calibrated using conventional undrained and fully drained tests, after which the coupled-strain tests were used to assess predictive performance.

SUMMARY OF FINDINGS

Performance evaluation

- The reference power-law CSL and elasticity expressions adopted in SANISAND 2008 did not provide an adequate fit to the Hostun sand dataset over the investigated stress and void ratio ranges.

- The calibration of bounding parameters h_0 and c_h using a conventional, linear function with respect to void ratio e resulted in a negative value for the hardening parameter b_0 at

the upper range of void ratio for the Hostun sand used, violating the required positivity of the hardening modulus.

- The conventional model calibration using undrained and fully drained tests captured the coupled strain behaviour only qualitatively. The baseline model did not consistently reproduce the experimentally identified, post-phase transformation and post-peak stress-ratio points of instability in such coupled strain paths.

- The state parameter at specific instability points of coupled-strain paths (LCSI points) was analytically shown to be related to the prescribed strain coupling ratio, in simulated coupled shear-volumetric strain paths. For the Hostun sand tested, the conventional state parameter by Been and Jefferies, 1985 ($\psi = e - e_{cs}$) that is used in SANISAND models could not consistently satisfy this relationship across the experimentally identified LCSI curves.

Model improvements

- The modified equations proposed based on the experiments on Hostun sand are presented in table 9.1. The table includes expressions for the CSL, the shear, and the bulk modulus. To ensure positivity of the hardening modulus, an exponential void ratio dependence is adopted. As these expressions are sand specific, they should not be interpreted as universal replacements for the reference SANISAND functions.

Reference Equations	Modified Equations (Hostun Sand)
Critical State Line: $e_{cs} = e_0 - \lambda(p'/p_{at})^{\xi}$ Model Constants: e_0 , λ , ξ	$e_{cs} = e_{max} - \frac{(e_{max}-e_{min})R}{Q-ln(p')}$ e_{max} , e_{min} , Q , R
Elasticity: $G = G_0 p_{at} \frac{(2.97-e)^2}{1+e}(p'/p_{at})^{1/2}$ $K = K_0 p_{at} \frac{(1+e)}{e}(p'/p_{at})^{2/3}$ Model Constants: G_0, K_0	$G = G_0\ p_{at} e^{-1.8}(\frac{p'}{p_{at}})^{0.5}$ $K = K_0\ p_{at} e^{-2}(\frac{p'}{p_{at}})^{0.65}$ G_0, K_0
Hardening Rule: $b_0 = G_0 h_0 (1 - c_h e)(p'/p_{at})^{-1/2}$ Model Constants: h_0 , c_h	$b_0 = G_0 h_0 exp(-c_h e)(p'/p_{at})^{-1/2}$ h_0 , c_h

Table 9.1: Reference SANISAND 2008 expressions and Hostun-specific expressions adopted in the monotonic model assessment

- The state dependence of the SANISAND surface evolution laws was separated into two components: the state parameter form, ψ_F, which captures the shape of the experimental LCSI curves and also the distance to the CSL in $e - p'$ space; and the state parameter definition ψ_D, which through a sand-specific, relative state mapping rule transforms ψ_F into a state variable appropriate for the bounding and dilatancy surface evolution laws. The revised surface evolution laws incorporating the state parameter definition ψ_D are presented in table 9.2. The experimental LCSI curves were first determined using post-phase transformation and post-peak stress-ratio instability points. The state parameter form ψ_F was then selected, so that the shape of the LCSI curves is captured. Finally, the state parameter definition ψ_D was calibrated through an iterative process, to verify that it could appropriately map the relative state at each strain coupling ratio examined.

IMPLICATIONS

- The CSL and elasticity functions should be selected and calibrated using material-specific data rather than adopted from the reference constitutive formulation.
- The LCSI framework provides a direct means of testing whether the relative state mapping adopted in a SANISAND formulation is consistent with experimentally observed

Reference Equations	**Modified Equations (Hostun Sand)**
Surface Evolution Laws:	
Linear evolution: $\alpha^b_{c,e} = s(\alpha^c_{c,e} - k^b\psi)$ $\alpha^d_{c,e} = s(\alpha^c_{c,e} + k^d\psi)$	 $\alpha^b_{c,e} = s(\alpha^c_{c,e} - k^b\psi_D)$ $\alpha^d_{c,e} = s(\alpha^c_{c,e} + k^d\psi_D)$
Model Constants: α^c , c , k^b, k^d	α^c , c , k^b, k^d
Exponential evolution: $\alpha^b_{c,e} = s\alpha^c_{c,e}exp(-n^b\psi)$ $\alpha^d_{c,e} = s\alpha^c_{c,e}exp(n^d\psi)$	 $\alpha^b_{c,e} = s\alpha^c_{c,e}exp(-n^b\psi_D)$ $\alpha^d_{c,e} = s\alpha^c_{c,e}exp(n^d\psi_D)$
Model Constants: α^c , c , n^b, n^d	α^c , c , n^b, n^d
SANISAND State Parameter: $\psi = e - e_{cs}$	 $\psi_D = sign(\psi_F)\lvert\psi_F\rvert^w$

Table 9.2: Reference and revised SANISAND surface evolution laws and associated state parameter definitions

instability loci under coupled shear-volumetric strain paths.

- Separating the state parameter form ψ_F and the state parameter definition ψ_D, facilitates the calibration process while conveniently preserving the established SANISAND surface evolution laws. However, ψ_D represents a material-specific relative state mapping rule, as demonstrated by the different expressions obtained for Hostun and Congleton sand.

- The LCSI framework also provides a way to indirectly identify the CSL, where conventional tests cannot provide reliable critical state points. The proposed method requires experimental LCSI curves for three strain coupling ratios, which are used to identify a suitable state parameter form, ψ_F. The parameters of a selected CSL function, can then be determined by imposing $\psi_F = 0$. This method was benchmarked using Hostun sand, for which the inferred CSL agreed closely with the independently determined CSL over the investigated stress range. It was also used to identify the CSL of Congleton sand, which was not possible to obtain directly due to experimental constraints regarding attainable strain, load capacity, and water cavitation.

- The coupled-strain datasets used for CSL identification can also be used to calibrate additional SANISAND parameters.

- For the experimental data examined, the revised state mapping proposed allowed a better replication of non-standard drained paths, improving the simulation of the maximum deviatoric stress, the development of the stress path and the axial strain at the identified instability points.

LIMITATIONS

- The monotonic assessment for state mapping was based on two sands, Hostun and Congleton, and a limited number of coupled strain paths.

- The calibrated state parameter definition differed between Hostun and Congleton sands, indicating that state mapping is material-specific and should not be transferred between sands without additional calibration or validation.

- Within this study, series of coupled strain tests that can be used to produce LCSI curves were identified as appropriate to inform the state mapping calibration process. Such tests require devices where user-defined water inflow or outflow rates can be imposed. Also, at least three LCSI curves are needed for calibration, with a minimum of four tests required per curve. Therefore, a large dataset of coupled strain tests are required to apply the proposed state mapping calibration, in addition to conventional undrained and fully drained tests.

- In the datasets examined, three strain coupling ratios provided the minimum information required to fit the assumed state-mapping and CSL functions. Additional coupling ratios would improve confidence in the uniqueness and precise position of the LCSI and CSL curves.

- The Hostun CSL determination exercise was benchmarked against an independently de-

termined CSL, whereas the Congleton CSL remains an indirect estimate because independent critical-state points could not be obtained.

- The revised state definition improved the simulation of the expansive coupled shear-volumetric strain paths examined, but it has not been demonstrated to improve all non-standard drained paths. In field deposits, void redistribution due to water flow is expected to evolve nonlinearly, and an individual soil element may experience both expansive and contractive paths.

- Finally, the LCSI relationship was derived within the SANISAND surface-evolution framework and should be interpreted as a SANISAND-consistent constitutive diagnostic tool.

9.1.2 Performance evaluation and model improvements under water inflow cyclic shearing

Three popular double surface plasticity models used for liquefaction-related problems, namely DM04, SANISAND-MSf and PM4Sand3D, were evaluated on their ability to capture element-level cyclic behaviour under volumetric expansion. DM04 provides the baseline formulation, SANISAND-MSf incorporates memory and semifluidised-state mechanisms developed to improve the undrained cyclic response, and PM4Sand3D represents an engineering-oriented evolution, incorporating several empirical calibration relationships.

The models were calibrated using undrained and fully drained monotonic compression tests as well as undrained cyclic tests on a specific batch of Hostun HN31 sand, reported in literature. Cyclic tests under constant volumetric expansion, conducted on the same batch of Hostun sand at three relative densities, were then used as the principal assessment dataset under non-standard drainage conditions. Two calibration strategies were compared. In the conventional $G-\nu$ scheme, the bulk modulus was derived from the shear modulus and an assumed Poisson's ratio. In the proposed $G-K$ scheme, the shear and bulk moduli were calibrated independently using bender-element and isotropic unloading data, respectively. Parameters controlling cyclic

contraction, hardening, and fabric evolution were recalibrated separately for the two strategies. Therefore, the comparison does not represent an isolated sensitivity analysis in which only K was changed.

A system-level validation exercise for the proposed $G-K$ calibration scheme was conducted in the finite-element analysis software OpenSees by modelling a soil column representing a uniform free-field deposit from a published centrifuge test on Hostun sand (Adamidis and Madabhushi, 2018). OpenSees was selected to conduct the system-level analysis as it allows flexibility in incorporating changes to the model formulation. The two calibration methods were implemented in Opensees, using the modified equations of SANISAND-MSf. The updated state parameter definition obtained in chapter 5 was not included as it was shown in chapter 7 to produce only minor changes in modelling cyclic mobility in level deposits. Finally, idealised layered deposits were simulated, to investigate potential 'false-negative' and 'false-positive' outcomes from simplified liquefaction assessments.

SUMMARY OF FINDINGS

Performance evaluation

- Similarly to the monotonic evaluation using Hostun sand, sand-specific CSL, elasticity and hardening expressions were required for the cyclic loading dataset. In particular, the experimentally obtained critical state line could not be described by the default SANISAND power law, the reference expression for the elastic shear modulus could not capture the bender element results for this batch of Hostun sand, and the calibration of bounding parameters h_0 and c_h using a linear function with respect to void ratio resulted in a negative value for the hardening parameter b_0 at the upper range of void ratio.

- The calibration of the dilatancy parameter A_0 from drained monotonic tests resulted in a more contractive response than desired for the undrained cyclic tests by the DM04 model, producing steep liquefaction resistance curves. The same issue was not encoun-

tered with the SANISAND-MSf and PM4Sand3D models, which contain additional constitutive mechanisms to prevent it.

- The monotonic tests were replicated using the conventional $G-\nu$ calibration - shear moduli deduced from bender element tests, G_{max}, and bulk moduli deduced from Poisson's ratio, ν, while the dilatancy parameter A_0 was modified to reduce the contraction rate only for the DM04 model. The experimentally observed undrained monotonic behaviour was captured well by DM04 and PM4Sand3D, while due to its higher value of A_0, SANISAND-MSf exaggerated the prediction of plastic contractive strain prior to phase transformation, leading to excessive reduction in mean effective stress. Note that with the same calibration set, DM04 and SANISAND-MSf would replicate the same monotonic response.

- All three models reproduced the principal qualitative features of the undrained cyclic response using the conventional $G-\nu$ calibration scheme. SANISAND-MSf provided the most consistent match to the experimental liquefaction resistance curves for Hostun sand, across three examined densities, whereas DM04 retained excessively steep slopes for the liquefaction resistance curves.

- All three models, calibrated with the conventional $G-\nu$ scheme, qualitatively reproduced the experimentlly observed reduction in liquefaction resistance caused by constant volumetric expansion during cyclic loading. However, the predictions of cycles to liquefaction were overly conservative across all densities by all three models. The change in void ratio with reducing p' indicated a stiffer volumetric response than observed in the experiments.

- At the system level, SANISAND-MSf was used to simulate a uniform liquefiable deposit in a centrifuge test, acting as a validation study. The conventional $G-\nu$ calibration was not able to adequately capture the observed response, producing too rapid pore water pressure redistribution, reduced excess pore pressure accumulation, and limited contractive strains across the liquefied soil deposit, thus underestimating surface settlement.

- In the idealised layered profiles examined, co-seismic pore fluid redistribution either promoted or inhibited liquefaction triggering depending on the stratigraphy. Net inflow beneath a lower permeability interface can reduce local cyclic resistance and promote triggering, whereas severe softening in a deeper layer can limit the acceleration transmitted to an overlying critical layer and inhibit triggering there. The conventional $G-\nu$ calibration was only sensitive to the effects of layer interaction when significant changes in permeability were implemented between layers.

Model improvements

- The modified, Hostun-specific equations proposed for model improvement based on the cyclic experiments on Hostun sand are presented in table 9.3. It should be noted that these equations correspond to the $G-K$ calibration scheme, which uses the small strain shear modulus G_{max} from bender elements and the bulk modulus from isotropic unloading data.

- In DM04, the dilatancy parameter A_0 obtained from drained monotonic tests was reduced based on undrained monotonic stress paths in $q-p'$ space. The updated calibration resulted in a reduced contraction rate per cycle, as appropriate for undrained cyclic tests. A similar adjustment in A_0 was not needed for the other models.

- The $G-K$ calibration resulted in significant improvement of monotonic undrained predictions for the SANISAND-MSf model, as compared to the conventional $G-\nu$ scheme. Notably, the model was able to adequately capture monotonic response while using G_{max} and without reduction to A_0. Often in SANISAND calibrations, the shear modulus used for monotonic loading is reduced to approximately a third of G_{max}. However, G_{max} must be retained in dynamic simulations where wave propagation is important. The $G-K$ calibration allowed SANISAND-MSf to reliably capture both monotonic and cyclic undrained behaviour.

- The $G-K$ calibration scheme improved the prediction of the number of undrained cycles to liquefaction with the DM04 model, as well as the accumulation of excess pore pressure

Reference Equations	**Modified Equations (Hostun Sand)**
Critical State Line:	
For DM04 and SANISAND-MSf	
$e_{cs} = e_0 - \lambda (p'/p_{at})^{\xi}$	$e_{cs} = e_{max} - \frac{(e_{max}-e_{min})R}{Q-ln(p')}$
Model Constants: e_0 , λ , ξ	e_{max} , e_{min} , Q , R
Elasticity:	
For DM04 and SANISAND-MSf	
$G = G_0 p_{at} \frac{(2.97-e)^2}{1+e} (p'/p_{at})^{1/2}$	$G = G_0 \; p_{at} e^{-1.8} (\frac{p'}{p_{at}})^{0.5}$
$K = \frac{2(1+\nu)}{3(1-2\nu)} G$	$K = K_0 \; p_{at} e^{-2} (\frac{p'}{p_{at}})^{0.65}$
Model Constants: G_0, ν	G_0, K_0
For PM4Sand3D	
$G = G_0 p_{at} \left(\frac{p'}{p_{at}}\right)^{1/2} C_{SR} \left(\frac{1+\frac{z_{cum}}{z_{max}}}{1+\frac{z_{cum}}{z_{max}} C_{GD}}\right)$	$G = G_0 e^{-1.8} p_{at} \left(\frac{p'}{p_{at}}\right)^{1/2} C_{SR} \left(\frac{1+\frac{z_{cum}}{z_{max}}}{1+\frac{z_{cum}}{z_{max}} C_{GD}}\right)$
$K = \frac{2(1+\nu)}{3(1-2\nu)} G$	$K = K_0 e^{-2} p_{at} \left(\frac{p'}{p_{at}}\right)^{0.65} C_{SR} \left(\frac{1+\frac{z_{cum}}{z_{max}}}{1+\frac{z_{cum}}{z_{max}} C_{GD}}\right)$
Model Constants: G_0, ν	G_0, K_0
Hardening Rule:	
DM04	
$b_0 = G_0 h_0 (1 - c_h e)(p'/p_{at})^{-1/2}$	$b_0 = G_0 h_0 exp(-c_h e)(p'/p_{at})^{-1/2}$
Model Constants: h_0 , c_h	h_0 , c_h
SANISAND-MSf	
$b_0 = G_0 h_0 g^{-n_g} (1 - c_h e)(p'/p_{at})^{-1/2}$	$b_0 = G_0 h_0 g^{-n_g} exp(-c_h e)(p'/p_{at})^{-1/2}$
Model Constants: h_0 , c_h , n_g	h_0 , c_h , n_g

Table 9.3: Reference constitutive expressions and Hostun-specific expressions adopted in the cyclic model assessment

and strain per cycle with both DM04 and SANISAND-MSf. PM4Sand3D showed comparatively limited sensitivity to the calibration strategy under cyclic undrained loading.

- The $G-K$ calibration significantly improved the prediction of liquefaction resistance curves under water inflow conditions for all three models. It produced a much closer representation of the experimentally observed evolution of void ratio and mean effective stress compared to the conventional calibration. Among the model and calibration combinations examined, SANISAND-MSf with the $G-K$ calibration provided the most consistent representation of the experimental liquefaction resistance curves for Hostun sand,

across the investigated densities and inflow rates.

- At system level, the $G-K$ calibration led to substantially improved replication of the centrifuge testing validation case, reproducing the acceleration deamplification, the excess pore pressure accumulation, and the surface settlement much more closely than the conventional $G-\nu$ scheme. This demonstrated that capturing the undrained cyclic resistance curves alone does not ensure reliable performance in a fully coupled boundary-value analysis.

- In the idealised layered analyses, net pore fluid inflow beneath a lower permeability layer promoted liquefaction triggering, with the effect intensified by the addition of a dense sand layer under the critical. The predicted mechanism was consistent with pore pressure redistribution mechanisms reported in field and experimental studies. The $G-K$ calibration led to more significant layer interaction than the conventional $G-\nu$ calibration, predicting liquefaction triggering at the layer interface for smaller differences in layer permeability.

IMPLICATIONS

- Cyclic resistance under water inflow conditions depends on both the constitutive representation of cyclic shearing and the volumetric stiffness governing isotropic unloading. Calibration against undrained cyclic resistance alone is therefore insufficient where co-seismic pore fluid redistribution is expected. Instead, direct calibration of the bulk modulus using isotropic unloading data is necessary.

- The updated state parameter definition in SANISAND models did not create a significant impact in the simulated cyclic response under undrained and water inflow conditions, as the relative state did not substantially change during these tests. The updated state mapping is expected to be more relevant for paths involving larger changes in state, for instance under high initial confinement, or under static shear promoting a flow liquefaction failure.

- The layered deposit analyses demonstrated that co-seismic pore fluid redistribution can either promote or inhibit liquefaction relative to simplified undrained assessments. Therefore, simplified procedures that assess layers in isolation cannot capture liquefaction triggering within layered deposits adequately.

- The proposed $G-K$ calibration scheme combined the benefits of a small strain ($\sim 1\times 10^{-6}$) shear modulus conventional calibration ($G_{max}-\nu$), typically used for dynamic behaviour, and of a larger strain ($\sim 1\times 10^{-4}$) shear modulus conventional calibration ($G_0-\nu$), typically used for monotonic behaviour. Indeed, it was able to capture both monotonic and cyclic behaviour at the element level, and also the fundamental soil period, acceleration response, and surface settlement at the system level.

- For the soil profiles examined, the bulk modulus calibration was most significant at low shaking amplitudes, when pore fluid flow-related dissipation of excess pore pressure is comparable to its accumulation from cyclic shearing and therefore the calibration becomes critical in promoting or mitigating liquefaction triggering.

- When a low permeability layer overlying a liquefiable layer was examined, the choice of bulk modulus calibration was found to only play a significant role in capturing the onset of liquefaction when the difference in permeability between the two layers was below a threshold. For the idealised layers examined, the threshold was 10^3. For higher permeability contrasts, both calibration schemes predicted the onset of liquefaction.

LIMITATIONS

- Cyclic mobility was found to be better predicted with an updated bulk modulus definition obtained from isotropic unloading data. However, the cyclic assessment was based on one batch of Hostun sand subjected to water inflow loading paths. Experimental assessment under cyclic water outflow conditions, initial static shear, irregular loading and multidirectional stress paths was not performed and therefore the transferability of the calibrated

parameters under these conditions remains to be established.

- The independently calibrated elastic moduli, i.e. the shear modulus from bender element tests and the bulk modulus from isotropic unloading-reloading tests, are not physically compatible as they correspond to different strain magnitude regimes. As a result, Poisson's ratio calculated from the elastic moduli pair selected lacks physical meaning and can actually yield negative values for a range of stresses. Nevertheless, the selected moduli remain appropriate for the selected constitutive models, which use a very narrow elastic region in shear loading, quickly engaging plasticity and reducing the secant shear modulus value, while maintaining elastic response at large strains under constant stress-ratio loading.

- The system level validation was limited to one centrifuge experiment on a uniform, level Hostun sand deposit. No validation was performed for established case histories where 'false-negative' or 'false-positive' predictions of liquefaction triggering were produced by simplified procedures. Such analyses would require sufficient site-investigation data for the calibration of the advanced constitutive models used in this thesis.

- The layered analyses were idealised and one dimensional, and the lower permeability material was represented using a simplified constitutive surrogate. The potential 'false-positive' and 'false-negative' cases should therefore be interpreted as mechanistic demonstrations rather than as design guidelines.

- The variation of permeability and soil compressibility because of agitation during seismic shaking was not included in this thesis, although variations because of effective stress changes were considered. There is significant uncertainty regarding agitation effects, though they could be important for co-seismic water flow.

- Finally, the process of reconsolidation post shaking and the impact of the proposed updates in modelling the reconsolidation phase were not evaluated in this study, which primarily focused on liquefaction triggering.

9.2 Future research

Non-standard drainage was imposed in simplified ways in this thesis: constant ratios of expansive volumetric strain rate to axial strain rate for monotonic tests and constant expansive volumetric strain per cycle for cyclic tests. In reality, at the interface of different layers, the net water inflow/outflow evolves with time, as excess pore pressures, hydraulic gradients, stiffness, and hydraulic conductivity change. To estimate realistic, variable volumetric strain rates, a combined experimental-numerical approach could be pursued. In order to produce realistic time histories of volumetric expansion, numerical modelling of layered deposits with varying depths of liquefiable layer, hydraulic conductivity and varying duration, frequency and magnitude of seismic excitation should be pursued. The produced depths of water inflow and outflow zones could be studied and characteristic volumetric strain time histories could be derived to inform an element testing campaign that captures cyclic resistance as a function of relative permeability and depth of neighbouring layers. In an iterative approach, element testing under time-varying volumetric strain rates could further improve constitutive model simulations.

Future research should aim to produce simplified ways of estimating liquefaction triggering in layered deposits. Malvick et al. (2008) proposed the thickness of the dilation zone at imminent instability or shear localization from the inherent dilation capacity of the liquefiable layer in an infinite slope overlain by a low-permeability layer. The zone was determined to be unstable once the peak angle of dilatancy was attained, beyond which the layer acted as a shear failure plane. More recently, Sinha et al. (2024) developed an analytical criterion for estimating the layer thickness over which pore pressure redistribution may prevent liquefaction in soil classified as susceptible by conventional simplified procedures. The method was shown to better predict excess pore pressures in soil layers than existing simplified procedures and was reasonably validated using two centrifuge tests. However, the method assumed constant values of soil compressibility and disregarded input motion characteristics such as the duration of shaking. Future liquefaction triggering methods should account for layer geometry, permeability contrast, evolving compressibility and hydraulic conductivity as well as ground-motion duration

characteristics to inform the relative timescales of pore pressure accumulation and limitation. A reliable, simplified, analytical method that accomplishes all the above is difficult to produce. One avenue is the use of reliable numerical simulations, such as those developed in this thesis, for extensive parametric studies performed using high performance computing, to inform machine learning tools that could finally produce quick but reliable predictions for triggering.

Further research is also required on the evolution of hydraulic conductivity and bulk stiffness during and after liquefaction. Shahir et al. (2012) proposed a different relationship between the permeability coefficient and the excess pore pressure ratio during pore pressure generation, liquefaction and pore pressure dissipation. Ma et al. (2025) estimated that hydraulic conductivity significantly increases upon the commencement of shaking through to liquefaction, only to reduce later in the co-seismic phase and eventually reach values below the initial. Adamidis and Madabhushi (2016) postulated that at very low effective stresses, one-dimensional stiffness might not follow a power law with respect to effective stress, which would suffice to accurately predict post-liquefaction reconsolidation without increasing permeability beyond what was experimentally observed at the element level by Haigh et al. (2012). Further studies on the evolution of these parameters is needed to improve the reliability of numerical simulations capturing co-seismic water flow.

While this study focuses on liquefaction triggering, further work is needed on how SANISAND models capture post-shaking reconsolidation, which appears too rapid. In more detail, work should examine how the calibrated elasticity moduli evolve once liquefaction is triggered, for instance identifying if the pre-liquefaction elastic bulk modulus is still appropriate once liquefaction has been triggered. Another aspect that could be looked at is the elasticity formulation implemented in these models. Lan et al. (2023) show that the use of hypoelastic relationships, built into the models used in this thesis, may result in the spurious accumulation of elastic deformation energy under high-cyclic loads which leads to an unconservative response. The hyperelasticity law proposed by Houlsby et al. (2019) was implemented in the SANISAND-MS model (Liu et al., 2019) by Lan et al. (2023) and was shown to capture the stress-induced anisotropy in

the initial unloading stage more accurately. A hyperelastic formulation could be implemented and evaluated for cyclic performance under co-seismic drainage effects.

References

Abeling, S., Horspool, N., Johnston, D., Dizhur, D., Wilson, N., Clement, C., & Ingham, J. (2020). Patterns of earthquake-related mortality at a whole-country level: New zealand, 1840–2017. *Earthquake spectra*, *36*(1), 138–163. https://doi.org/10.1177/8755293019878190

Adamidis, O., & Madabhushi, G. S. P. (2016). Post-liquefaction reconsolidation of sand. *Proceedings of the Royal Society A: Mathematical, Physical and Engineering Sciences*, *472*(2186), 20150745. https://doi.org/10.1098/rspa.2015.0745

Adamidis, O., & Madabhushi, S. P. G. (2018). Experimental investigation of drainage during earthquake-induced liquefaction. *Géotechnique*, *68*(8), 655–665. https://doi.org/10.1680/jgeot.16.P.090

Adamidis, O., & Anastasopoulos, I. (2022). Cyclic liquefaction resistance of sand under a constant inflow rate. *Géotechnique*, 1–40. https://doi.org/10.1680/jgeot.21.00082

Andrade, J. E. (2009). A predictive framework for liquefaction instability. *Géotechnique*, *59*(8), 673–682. https://doi.org/10.1680/geot.7.00087

Andrade, J. E., Ramos, A. M., & Lizcano, A. (2013). Criterion for flow liquefaction instability. *Acta Geotechnica*, *8*(5), 525–535. https://doi.org/10.1007/s11440-013-0223-x

Andrianopoulos, K. I., Papadimitriou, A. G., & Bouckovalas, G. D. (2010). Bounding surface plasticity model for the seismic liquefaction analysis of geostructures. *Soil Dynamics and Earthquake Engineering*, *30*(10), 895–911. https://doi.org/10.1016/j.soildyn.2010.04.001

Azeiteiro, R. J., Coelho, P. A., Taborda, D. M., & Grazina, J. C. (2017). Critical state-based interpretation of the monotonic behaviour of hostun sand. https://doi.org/10.1061/(ASCE)GT.1943-5606.0001659

Bandini, V., & Coop, M. R. (2011). The influence of particle breakage on the location of the critical state line of sands. *Soils and Foundations*, *51*(4), 591–600. https://doi.org/10.3208/sandf.51.591

Bardet, J. (1986). Bounding surface plasticity model for sands. *Journal of Engineering Mechanics*, *112*(11), 1198–1217. https://doi.org/10.1061/(ASCE)0733-9399(1986)112:11(1198)

Barrero, A. R., Taiebat, M., & Dafalias, Y. F. (2020). Modeling cyclic shearing of sands in the semifluidized state. *International Journal for Numerical and Analytical Methods in Geomechanics*, *44*(3), 371–388. https://doi.org/10.1002/nag.3007

Been, K., Jefferies, M. G., & Hachey, J. (1991). The critical state of sands. *Géotechnique*, *41*(3), 365–381. https://doi.org/10.1680/geot.1991.41.3.365

Been, K., & Jefferies, M. G. (1985). A state parameter for sands. *Géotechnique*, *35*(2), 99–112. https://doi.org/10.1680/geot.1985.35.2.99

Ben-Zeev, S., Goren, L., Toussaint, R., & Aharonov, E. (2023). Drainage explains soil liquefaction beyond the earthquake near-field. *Nature Communications*, *14*(1), 5791. https://doi.org/10.1038/s41467-023-41405-4

Berrill, J. B., & Davis, R. O. (1985). Energy dissipation and seismic liquefaction of sands: Revised model. *Soils and Foundations*, *25*(2), 106–118. https://doi.org/10.3208/sandf1972.25.2_106

Bhattacharya, S., Hyodo, M., Goda, K., Tazoh, T., & Taylor, C. A. (2011). Liquefaction of soil in the tokyo bay area from the 2011 tohoku (japan) earthquake. *Soil Dynamics and Earthquake Engineering*, *31*(11), 1618–1628. https://doi.org/10.1016/j.soildyn.2011.06.006

Bolton, M. D. (1986). The strength and dilatancy of sands. *Géotechnique*, *36*(1), 65–78. https://doi.org/10.1680/geot.1986.36.1.65

Boulanger, R. W., & Idriss, I. M. (2006). Liquefaction susceptibility criteria for silts and clays. *Journal of Geotechnical and Geoenvironmental Engineering*, *132*(11), 1413–1426. https://doi.org/10.1061/(ASCE)1090-0241(2006)132:11(1413)

Boulanger, R. W., & Idriss, I. M. (2014). Cpt and spt based liquefaction triggering procedures. *Report No. UCD/CGM.-14*, *1*.

Boulanger, R. W., & Idriss, I. M. (2016). Cpt-based liquefaction triggering procedure. *Journal of Geotechnical and Geoenvironmental Engineering*, *142*(2), 04015065. https://doi.org/10.1061/(ASCE)GT.1943-5606.0001388

Boulanger, R. W., & Ziotopoulou, K. (2015). Pm4sand (version 3): A sand plasticity model for earthquake engineering applications. *Center for Geotechnical Modeling Report No. UCD/CGM-15/01, Department of Civil and Environmental Engineering, University of California, Davis, Calif*.

Boulanger, R. W., & Ziotopoulou, K. (2022). Pm4sand (version 3.2): A sand plasticity model for earthquake engineering applications. *Center for Geotechnical Modeling Report No. UCD/CGM-22/02, Department of Civil and Environmental Engineering, University of California, Davis, Calif*.

Bray, J. D., Sancio, R. B., Durgunoglu, T., Onalp, A., Youd, T. L., Stewart, J. P., Seed, R. B., Cetin, O. K., Bol, E., Baturay, M. B., et al. (2004). Subsurface characterization at ground failure sites in adapazari, turkey. *Journal of Geotechnical and Geoenvironmental Engineering*, *130*(7), 673–685. https://doi.org/10.1061/(ASCE)1090-0241(2004)130:7(673)

Bullock, Z., Dashti, S., Liel, A., & Porter, K. (2022). Physics-informed probabilistic models for peak pore pressure and shear strain in layered, liquefiable deposits. *Géotechnique*, 1–14. https://doi.org/10.1680/jgeot.21.00110

Castro, G. (1969). Liquefaction of sands. *Ph.D. Thesis, Harvard Soil Mech.*

Chaloulos, Y. K., & Papadimitriou, A. G. (2025). Calibration of elastic moduli in models for granular soils used in seismic analyses of geostructures. *International Journal of Geomechanics*, *25*(4), 04025045. https://doi.org/10.1061/IJGNAI.GMENG-10550

Chen, L. (2020). *Implementation, verification, validation, and application of two constitutive models for earthquake engineering applications*. University of Washington.

Chen, L., Ghofrani, A., & Arduino, P. (2021). Remarks on numerical simulation of the leap-asia-2019 centrifuge tests. *Soil Dynamics and Earthquake Engineering*, *142*, 106541. https://doi.org/10.1016/j.soildyn.2020.106541

Chu, J., & Leong, W. K. (2001). Pre-failure strain softening and pre-failure instability of sand: A comparative study. *Géotechnique*, *51*(4), 311–321. https://doi.org/10.1680/geot.2001.51.4.311

Chu, J., Wanatowski, D., Loke, W. L., & Leong, W. K. (2015). Pre-failure instability of sand under dilatancy rate controlled conditions. *Soils and Foundations*, *55*(2), 414–424. https://doi.org/10.1016/j.sandf.2015.02.015

Corti, R., Diambra, A., Wood, D. M., Escribano, D. E., & Nash, D. F. (2016). Memory surface hardening model for granular soils under repeated loading conditions. *Journal of Engineering Mechanics*, *142*(12), 04016102. https://doi.org/10.1061/(ASCE)EM.1943-7889.0001174

Crowley, K., & Elliott, J. R. (2012). Earthquake disasters and resilience in the global north: Lessons from new zealand and japan. *The Geographical Journal*, *178*(3), 208–215. https://doi.org/10.1111/j.1475-4959.2011.00453.x

Cubrinovski, M. (2013). Liquefaction-induced damage in the 2010-2011 christchurch (new zealand) earthquakes. *Proceedings of International Conference on Case Histories in Geotechnical Engineering, Chicago, IL, USA*. https://scholarsmine.mst.edu/icchge/7icchge/session12/1

Cubrinovski, M., & Ntritsos, N. (2024). Incorporating dynamic interactions and system effects in simplified liquefaction assessment. *Japanese Geotechnical Society Special Publication*, *10*(4), 54–63. https://doi.org/10.3208/jgssp.v10.KL-1-01

Cubrinovski, M., Rhodes, A., Ntritsos, N., & Van Ballegooy, S. (2019). System response of liquefiable deposits. *Soil Dynamics and Earthquake Engineering*, *124*, 212–229. https://doi.org/10.1016/j.soildyn.2018.05.013

Dafalias, Y. F. (1986). Bounding surface plasticity. i: Mathematical foundation and hypoplasticity. *Journal of Engineering Mechanics*, *112*(9), 966–987. https://doi.org/10.1061/(ASCE)0733-9399(1986)112:9(966)

Dafalias, Y. F., & Manzari, M. T. (2004). Simple plasticity sand model accounting for fabric change effects. *Journal of Engineering Mechanics*, *130*(6), 622–634. https://doi.org/10.1061/(ASCE)0733-9399(2004)130:6(622)

Dafalias, Y. F., Papadimitriou, A. G., & Li, X. S. (2004). Sand plasticity model accounting for inherent fabric anisotropy. *Journal of Engineering Mechanics*, *130*(11), 1319–1333. https://doi.org/10.1061/(ASCE)0733-9399(2004)130:11(1319)

Dafalias, Y. F., & Popov, E. P. (1975). A model of nonlinearly hardening materials for complex loading. *Acta Mechanica*, *21*(3), 173–192. https://doi.org/10.1007/BF01181053

Dafalias, Y. F., & Taiebat, M. (2016). Sanisand-z: Zero elastic range sand plasticity model. *Géotechnique*, *66*(12), 999–1013. https://doi.org/10.1680/jgeot.15.P.271

Darvishi, R., Jafarian, Y., Lashgari, A., & Askari, F. (2022). On evaluation of shear modulus parameter (g0) in sanisand constitutive model. *Soil Dynamics and Earthquake Engineering*, *163*, 107525. https://doi.org/10.1016/j.soildyn.2022.107525

Dilip, A., & Adamidis, O. (2024a). State parameter for partially drained paths using a sanisand model. *Computers and Geotechnics*, *170*, 106295. https://doi.org/10.1016/j.compgeo.2024.106295

Dilip, A., & Adamidis, O. (2024b). Two-surface plasticity prediction of the cyclic resistance of a medium dense sand under water inflow condition. *Japanese Geotechnical Society Special Publication*, *10*(19), 674–679. https://doi.org/10.3208/jgssp.v10.OS-8-04

Dilip, A., Wang, Y., & Adamidis, O. (2026). Identification of the critical state line of sands using coupled shear-volumetric strain paths. *Acta Geotechnica*, 1–25. https://doi.org/10.1007/s11440-025-02892-5

DIN-18126. (1996). *Bestimmung der dichte nichtbindiger böden bei lockerster und dichtester lagerung*. (DIN Standard No. DIN 18126:1996-11). Deutsches Institut für Normung. Berlin, Germany.

Dobry, R., Ladd, R., Yokel, F., Chung, R., & Powell, D. (1982). Prediction of pore water pressure buildup and liquefaction of sands during earthquakes by the cyclic strain method. *NBS Building Science Series*, *138*.

Eckstein, A. (2026). *Liquefaction susceptibility of levees considering partial drainage – an element level investigation* [Doctoral dissertation, University of Oxford].

Elgamal, A. W., & Yang, Z. (2000). Numerical modeling of liquefaction-induced lateral spreading. *Proceedings of the Twelfth World Conference on Earthquake Engineering*.

Galli, P. (2000). New empirical relationships between magnitude and distance for liquefaction. *Tectonophysics*, *324*(3), 169–187. https://doi.org/10.1016/S0040-1951(00)00118-9

Garcia, F. E., Andò, E., Viggiani, G., & Sitar, N. (2024). Influence of depositional fabric on mechanical properties of naturally deposited sands. *Géotechnique*, *74*(3), 250–264. https://doi.org/10.1680/jgeot.21.00230

Ghofrani, A. (2018). *Development of numerical tools for the evaluation of pile response to laterally spreading soil* [Doctoral dissertation, University of Washington].

Goren, L., Aharonov, E., Sparks, D., & Toussaint, R. (2010). Pore pressure evolution in deforming granular material: A general formulation and the infinitely stiff approximation. *Journal of Geophysical Research: Solid Earth*, *115*(B9). https://doi.org/10.1029/2009JB007191

Green, R. A., Mitchell, J. K., & Polito, C. P. (2000). An energy-based excess pore pressure generation model for cohesionless soils. *Proceedings of the John Booker Memorial Symposium, Sidney Australia, AA Balkema Publishers, Rotterdam, Netherlands*, *3*.

Grey, L. J.-R., & Adamidis, O. (2024). Liquefaction resistance of medium-dense hostun sand under volumetric contraction. *Japanese Geotechnical Society Special Publication*, *10*(23), 866–871. https://doi.org/10.3208/jgssp.v10.OS-12-05

Haigh, S. K., Eadington, J., & Madabhushi, S. P. G. (2012). Permeability and stiffness of sands at very low effective stresses. *Géotechnique*, *62*(1), 69–75. https://doi.org/10.1680/geot.10.P.035

Hardin, B. O. (1978). The nature of stress-strain behavior for soils. *From Volume I of Earthquake Engineering and Soil Dynamics–Proceedings of the ASCE Geotechnical Engineering Division Specialty Conference, June 19-21, 1978, Pasadena, California. Sponsored by Geotechnical Engineering Division of ASCE in cooperation with:* (Proceeding).

Hashash, Y. M. A., Musgrove, M. I., & Harmon, J. A. (2018). Nonlinear and equivalent linear seismic site response of one-dimensional soil columns. *User Manual v7. 0, Deepsoil Software*, *12*(10).

Hill, R. (1958). A general theory of uniqueness and stability in elastic-plastic solids. *Journal of the Mechanics and Physics of Solids*, *6*(3), 236–249. https://doi.org/10.1016/0022-5096(58)90029-2

Hoque, E., & Tatsuoka, F. (2000). Kinematic elasticity of a granular material. *ISRM International Symposium*, ISRM–IS.

Houlsby, G., Amorosi, A., & Rollo, F. (2019). Non-linear anisotropic hyperelasticity for granular materials. *Computers and Geotechnics*, *115*, 103167.

Hwang, J. H., Yang, C. W., & Chen, C. H. (2003). Investigations on soil liquefaction durlng the chi-chi earthquake. *Soils and Foundations*, *43*(6), 107–123. https://doi.org/10.3208/sandf.43.6_107

Idriss, I. M., & Boulanger, R. W. (2008). *Soil liquefaction during earthquakes*. Earthquake Engineering Research Institute.

Idriss, I. M., & Boulanger, R. W. (2010). Spt-based liquefaction triggering procedures. *Rep. UCD/CGM-10*, *2*, 4–13.

Imposimato, S., & Nova, R. (1998). An investigation on the uniqueness of the incremental response of elastoplastic models for virgin sand. *Mechanics of Cohesive-frictional Materials: An International Journal on Experiments, Modelling and Computation of Materials and Structures*, *3*(1), 65–87. https://doi.org/10.1002/(SICI)1099-1484(199801)3:1%3C65::AID-CFM42%3E3.0.CO;2-9

Ishihara, K. (1993). Liquefaction and flow failure during earthquakes. *Géotechnique*, *43*(3), 351–451. https://doi.org/10.1680/geot.1993.43.3.351

Ishihara, K., Araki, K., & Toshiyuki, K. (2014). Liquefaction in tokyo bay and kanto regions in the 2011 great east japan earthquake. In *Earthquake geotechnical engineering design* (pp. 93–140). Springer. https://doi.org/10.1007/978-3-319-03182-8_4

Ishihara, K., Tatsuoka, F., & Yasuda, S. (1975). Undrained deformation and liquefaction of sand under cyclic stresses. *Soils and Foundations*, *15*(1), 29–44. https://doi.org/10.3208/sandf1972.15.29

Itasca. (2011). Flac-fast lagrangian analysis of continua, version 7.0. *Itasca Consulting Group Inc*.

Jefferies, M. G. (1993). Nor-sand: A simle critical state model for sand. *Géotechnique*, *43*(1), 91–103. https://doi.org/10.1680/geot.1993.43.1.91

Jrad, M., Sukumaran, B., & Daouadji, A. (2012). Experimental analyses of the behaviour of saturated granular materials during axisymmetric proportional strain paths. *European Journal of Environmental and Civil Engineering*, *16*(1), 111–120. https://doi.org/10.1080/19648189.2012.666900

Kamai, R., & Boulanger, R. W. (2012). Single-element simulations of partial-drainage effects under monotonic and cyclic loading. *Soil Dynamics and Earthquake Engineering*, *35*, 29–40. https://doi.org/10.1016/j.soildyn.2011.10.002

Kamai, R. (2011). *Liquefaction-induced shear strain localization processes in layered soil profiles*. University of California, Davis.

Kassas, K., Adamidis, O., Gerolymos, N., & Anastasopoulos, I. (2021). Numerical modelling of a structure with shallow strip foundation during earthquake-induced liquefaction. *Géotechnique*, *71*(12), 1099–1113. https://doi.org/10.1680/jgeot.19.P.277

Kikumoto, M., Wood, D. M., & Russell, A. (2010). Particle crushing and deformation behaviour. *Soils and Foundations*, *50*(4), 547–563. https://doi.org/10.3208/sandf.50.547

Kippen, M. P., Boulanger, R. W., & Ziotopoulou, K. (2026). Pm4sand3d (version 1): A sand plasticity model for earthquake engineering applications. *Center for Geotechnical Modeling Report No. UCD/CGM-26/01, Department of Civil and Environmental Engineering, University of California, Davis, Calif.*

Kokusho, T., Sawada, T., Hazarika, H., & Isobe, Y. (2025). Long-distance flow mechanism of gentle slopes under seepage due to liquefaction-induced water film during 2018 sulawesi earthquake, indonesia. *Soils and Foundations*, *65*(3), 101611. https://doi.org/10.1016/j.sandf.2025.101611

Kokusho, T. (2003). Current state of research on flow failure considering void redistribution in liquefied deposits. *Soil Dynamics and Earthquake Engineering*, *23*(7), 585–603. https://doi.org/10.1016/S0267-7261(03)00067-8

Kokusho, T. (2013). Liquefaction potential evaluations: Energy-based method versus stress-based method. *Canadian Geotechnical Journal*, *50*(10), 1088–1099. https://doi.org/10.1139/cgj-2012-0456

Kokusho, T. (1999). Water film in liquefied sand and its effect on lateral spread. *Journal of Geotechnical and Geoenvironmental Engineering*, *125*(10), 817–826. https://doi.org/10.1061/(ASCE)1090-0241(1999)125:10(817)

Kokusho, T., & Fujita, K. (2001). Water films involved in post-liquefaction flow failure in niigata city during the 1964 niigata earthquake. https://scholarsmine.mst.edu/icrageesd/04icrageesd/session05/25

Konrad, J. M. (1993). Undrained response of loosely compacted sands during monotonic and cyclic compression tests. *Géotechnique*, *43*(1), 69–89. https://doi.org/10.1680/geot.1993.43.1.69

Kramer, S. L. (1996). Geotechnical earthquake engineering. *Prentice-Hall Civil Engineering and Engineering Mechanics Series*.

Kramer, S. L., & Seed, H. B. (1988). Initiation of soil liquefaction under static loading conditions. *Journal of Geotechnical Engineering*, *114*(4), 412–430. https://doi.org/10.1061/(ASCE)0733-9410(1988)114:4(412)

Krinitzsky, E. L. (2005). Earthquakes and soil liquefaction in flood stories of the ancient near east. *Engineering Geology*, *76*(3-4), 295–311. https://doi.org/10.1016/j.enggeo.2004.07.027

Kwok, A. O., Stewart, J. P., Hashash, Y. M., Matasovic, N., Pyke, R., Wang, Z., & Yang, Z. (2007). Use of exact solutions of wave propagation problems to guide implementation of nonlinear seismic ground response analysis procedures. *Journal of Geotechnical and Geoenvironmental Engineering*, *133*(11), 1385–1398. https://doi.org/10.1061/(ASCE)1090-0241(2007)133:11(1385)

Lade, P. V. (2016). *Triaxial testing of soils*. John Wiley & Sons.

Lakeland, D. L., Rechenmacher, A., & Ghanem, R. (2014). Towards a complete model of soil liquefaction: The importance of fluid flow and grain motion. *Proceedings of the Royal Society A: Mathematical, Physical and Engineering Sciences*, *470*(2165), 20130453. https://doi.org/10.1098/rspa.2013.0453

Lan, H., Liu, H., & Zhao, H. (2023). Impact of hyper-elasticity on cyclic sand modelling: A numerical study based on sanisand-ms. *Computers and Geotechnics*, *159*, 105428.

Lancelot, L., Shahrour, I., & Al Mahmoud, M. (2004). Instability and static liquefaction on proportional strain paths for sand at low stresses. *Journal of Engineering Mechanics*, *130*(11), 1365–1372. https://doi.org/10.1061/(ASCE)0733-9399(2004)130:11(1365)

Lashkari, A., Falsafizadeh, S. R., & Rahman, M. M. (2021). Influence of linear coupling between volumetric and shear strains on instability and post-peak softening of sand in direct simple shear tests. *Acta Geotechnica*, *16*(11), 3467–3488. https://doi.org/10.1007/s11440-021-01288-5

Lashkari, A., & Yaghtin, M. S. (2018). Sand flow liquefaction instability under shear–volume coupled strain paths. *Géotechnique*, *68*(11), 1002–1024. https://doi.org/10.1680/jgeot.17.P.164

Lashkari, A. (2009). On the modeling of the state dependency of granular soils. *Computers and Geotechnics*, *36*(7), 1237–1245. https://doi.org/10.1016/j.compgeo.2009.06.003

LeVeque, R. J. (2007). *Finite difference methods for ordinary and partial differential equations: Steady-state and time-dependent problems*. SIAM.

Li, X. S., & Dafalias, Y. F. (2000). Dilatancy for cohesionless soils. *Géotechnique*, *50*(4), 449–460. https://doi.org/10.1680/geot.2000.50.4.449

Li, X. S., Dafalias, Y. F., & Wang, Z. L. (1999). State-dependant dilatancy in critical-state constitutive modelling of sand. *Canadian Geotechnical Journal*, *36*(4), 599–611. https://doi.org/10.1139/t99-029

Li, X. S., & Wang, Y. (1998). Linear representation of steady-state line for sand. *Journal of Geotechnical and Geoenvironmental Engineering*, *124*(12), 1215–1217. https://doi.org/10.1061/(ASCE)1090-0241(1998)124:12(1215)

Li, X. S., & Dafalias, Y. F. (2002). Constitutive modeling of inherently anisotropic sand behavior. *Journal of Geotechnical and Geoenvironmental Engineering*, *128*(10), 868–880. https://doi.org/10.1061/(ASCE)1090-0241(2002)128:10(868)

Li, X. S., & Dafalias, Y. F. (2012). Anisotropic critical state theory: Role of fabric. *Journal of Engineering Mechanics*, *138*(3), 263–275. https://doi.org/10.1061/(ASCE)EM.1943-7889.0000324

Liu, H. Y., Abell, J. A., Diambra, A., & Pisanò, F. (2019). Modelling the cyclic ratcheting of sands through memory-enhanced bounding surface plasticity. *Géotechnique*, *69*(9), 783–800. https://doi.org/10.1680/jgeot.17.P.307

Liu, H. Y., Kementzetzidis, E., Abell, J. A., & Pisanò, F. (2022). From cyclic sand ratcheting to tilt accumulation of offshore monopiles: 3d fe modelling using sanisand-ms. *Géotechnique*, *72*(9), 753–768. https://doi.org/10.1680/jgeot.20.P.029

Ma, S., Kontoe, S., & Taborda, D. M. (2025). Quantifying the variation of hydraulic conductivity during seismic liquefaction. *Soil Dynamics and Earthquake Engineering*, *197*, 109518. https://doi.org/10.1016/j.soildyn.2025.109518

Malvick, E. J., Kutter, B. L., & Boulanger, R. W. (2008). Postshaking shear strain localization in a centrifuge model of a saturated sand slope. *Journal of Geotechnical and Geoenvironmental Engineering*, *134*(2), 164–174. https://doi.org/10.1061/(ASCE)1090-0241(2008)134:2(164)

Malvick, E. J., Kutter, B. L., Boulanger, R. W., & Kulasingam, R. (2006). Shear localization due to liquefaction-induced void redistribution in a layered infinite slope. *Journal of Geotechnical and Geoenvironmental Engineering*, *132*(10), 1293–1303. https://doi.org/10.1061/(ASCE)1090-0241(2006)132:10(1293)

Manzari, M. T., & Dafalias, Y. F. (1997). A critical state two-surface plasticity model for sands. *Géotechnique*, *47*(2), 255–272. https://doi.org/10.1680/geot.1997.47.2.255

McAllister, G., Taiebat, M., Ghofrani, A., Chen, L., & Arduino, P. (2015). Nonlinear site response analyses and high frequency dilation pulses. *Proceedings of the 68th Canadian Geotechnical Conference, Quebec, QC, Canada*.

McDowell, G. R., & Bolton, M. D. (1998). On the micromechanics of crushable aggregates. *Géotechnique*, *48*(5), 667–679. https://doi.org/10.1680/geot.1998.48.5.667

McGann, C. R., Arduino, P., & Mackenzie-Helnwein, P. (2012). Stabilized single-point 4-node quadrilateral element for dynamic analysis of fluid saturated porous media. *Acta Geotechnica*, *7*(4), 297–311. https://doi.org/10.1007/s11440-012-0168-5

McGann, C. R., Arduino, P., & Mackenzie-Helnwein, P. (2015). A stabilized single-point finite element formulation for three-dimensional dynamic analysis of saturated soils. *Computers and Geotechnics*, *66*, 126–141. https://doi.org/10.1016/j.compgeo.2015.01.002

McKenna, F. (2011). Opensees: A framework for earthquake engineering simulation. *Computing in Science & Engineering*, *13*(4), 58–66. https://doi.org/10.1109/MCSE.2011.66

Moller, J. K., Kontoe, S., Taborda, D., & Tantivangphaisal, P. (2024). Assessment of a constitutive model for simulating the post-liquefaction response of sand. *Japanese Geotechnical Society Special Publication*, *10*(35), 1347–1352.

Möller, J., Taborda, D., Kontoe, S., & Potts, D. (2024). A shear history model for capturing the liquefaction resistance of sands at various cyclic stress ratios. *Computers and Geotechnics*, *166*, 105940. https://doi.org/10.1016/j.compgeo.2023.105940

Mrŏz, Z., Norris, V. A., & Zienkiewicz, O. C. (1978). An anisotropic hardening model for soils and its application to cyclic loading. *International Journal for Numerical and Analytical Methods in Geomechanics*, *2*(3), 203–221. https://doi.org/10.1002/nag.1610020303

Nicot, F., Daouadji, A., Hadda, N., Jrad, M., & Darve, F. (2013). Granular media failure along triaxial proportional strain paths. *European Journal of Environmental and Civil Engineering*, *17*(9), 777–790. https://doi.org/10.1080/19648189.2013.819301

NRC. (1985). *Liquefaction of soils during earthquakes*. The National Academies Press. https://doi.org/10.17226/19275

Ntritsos, N., & Cubrinovski, M. (2022). Liquefaction assessment of level-ground sites: Key lessons from the canterbury earthquakes. *Proc., 3rd Int. Conf. on Natural Hazards Infrastructure*.

Ntritsos, N., & Cubrinovski, M. (2024). Effects of partial saturation on the liquefaction response of two christchurch deposits. *Japanese Geotechnical Society Special Publication*, *10*(23), 854–859. https://doi.org/10.3208/jgssp.v10.OS-12-03

Obermeier, S. F. (1996). Use of liquefaction-induced features for paleoseismic analysis—an overview of how seismic liquefaction features can be distinguished from other features and how their regional distribution and properties of source sediment can be used to infer the location and strength of holocene paleo-earthquakes. *Engineering Geology*, *44*(1-4), 1–76. https://doi.org/10.1016/S0013-7952(96)00040-3

Obermeier, S. F. (1997). *Overview of liquefaction evidence for strong earthquakes of holocene and latest pleistocene ages in southern indiana and illinois* (tech. rep.). US Geological Survey,

Papadimitriou, A. G., Bouckovalas, G. D., & Dafalias, Y. F. (2001). Plasticity model for sand under small and large cyclic strains. *Journal of Geotechnical and Geoenvironmental Engineering*, *127*(11), 973–983. https://doi.org/10.1061/(ASCE)1090-0241(2001)127:11(973)

Papadimitriou, A. G., Limnaiou, T. G., & Chaloulos, Y. K. (2023). Benefits and pitfalls of advanced numerical modelling in earthquake geotechnical engineering. *10th European Conference on Numerical Methods in Geotechnical Engineering, London, UK, Paper*, (440). https://doi.org/10.53243/NUMGE2023-440

Parra, E. (1996). Numerical modeling of liquefaction and lateral ground deformation including cyclic mobility and dilation response in soil systems. *Rensselaer Polytechnic Institute, Troy, NY, USA*.

Petalas, A. L., Dafalias, Y. F., & Papadimitriou, A. G. (2019). Sanisand-fn: An evolving fabric-based sand model accounting for stress principal axes rotation. *International Journal for Numerical and Analytical Methods in Geomechanics*, *43*(1), 97–123. https://doi.org/10.1002/nag.2855

Petalas, A. L., Dafalias, Y. F., & Papadimitriou, A. G. (2020). Sanisand-f: Sand constitutive model with evolving fabric anisotropy. *International Journal of Solids and Structures*, *188*, 12–31. https://doi.org/10.1016/j.ijsolstr.2019.09.005

Poulos, S. J. (1981). The steady state of deformation. *Journal of the Geotechnical Engineering Division*, *107*(5), 553–562. https://doi.org/10.1061/AJGEB6.0001129

Prévost, J. H. (1982). Two-surface versus multi-surface plasticity theories: A critical assessment. *International Journal for Numerical and Analytical Methods in Geomechanics*, *6*(3), 323–338. https://doi.org/10.1002/nag.1610060305

Prévost, J. H. (1985). A simple plasticity theory for frictional cohesionless soils. *International Journal of Soil Dynamics and Earthquake Engineering*, *4*(1), 9–17. https://doi.org/10.1016/0261-7277(85)90030-0

Prévost, J. H. (1978). Plasticity theory for soil stress-strain behavior. *Journal of the Engineering Mechanics Division*, *104*(5), 1177–1194. https://doi.org/10.1061/JMCEA3.0002411

Ramirez, J., Barrero, A. R., Chen, L., Dashti, S., Ghofrani, A., Taiebat, M., & Arduino, P. (2018). Site response in a layered liquefiable deposit: Evaluation of different numerical tools and methodologies with centrifuge experimental results. *Journal of Geotechnical and Geoenvironmental Engineering*, *144*(10), 04018073. https://doi.org/10.1061/(ASCE)GT.1943-5606.0001947

Roscoe, K. H. (1963). A fundamental principle of similarity in model tests for earth pressure problems. *Proc. 2nd Asian Regional Conf. on SMFE*, *1*, 134–140.

Roscoe, K. H., & Burland, J. B. (1968). On the generalized stress-strain behaviour of wet clay.

Roscoe, K. H., Schofield, A. N., & Wroth, C. P. (1958). On the yielding of soils. *Géotechnique*, *8*(1), 22–53. https://doi.org/10.1680/geot.1958.8.1.22

Schofield, A. N., & Wroth, P. (1968). *Critical state soil mechanics* (Vol. 310). McGraw-hill London.

Seed, H. B. (1983). Earthquake resistant design of earth dams. *Proceedings of the Symposium on Seismic Design of Embankments and Caverns, ACSE, NY, Pennsylvania*, 41–64.

Seed, H. B. (1987). Design problems in soil liquefaction. *Journal of Geotechnical Engineering*, *113*(8), 827–845. https://doi.org/10.1061/(ASCE)0733-9410(1987)113:8(827)

Seed, H. B., & Idriss, I. M. (1967). Analysis of soil liquefaction: Niigata earthquake. *Journal of the Soil Mechanics and Foundations Division*, *93*(3), 83–108. https://doi.org/10.1061/JSFEAQ.0000981

Seed, H. B., & Idriss, I. M. (1971). Simplified procedure for evaluating soil liquefaction potential. *Journal of the Soil Mechanics and Foundations division*, *97*(9), 1249–1273. https://doi.org/10.1061/JSFEAQ.0001662

Seed, H. B., Idriss, I. M., & Arango, I. (1983). Evaluation of liquefaction potential using field performance data. *Journal of Geotechnical Engineering*, *109*(3), 458–482. https://doi.org/10.1061/(ASCE)0733-9410(1983)109:3(458)

Seid-Karbasi, M., & Byrne, P. M. (2007). Seismic liquefaction, lateral spreading, and flow slides: A numerical investigation into void redistribution. *Canadian Geotechnical Journal*, *44*(7), 873–890. https://doi.org/10.1139/t07-027

Shahir, H., Pak, A., Taiebat, M., & Jeremić, B. (2012). Evaluation of variation of permeability in liquefiable soil under earthquake loading. *Computers and Geotechnics*, *40*, 74–88. https://doi.org/10.1016/j.compgeo.2011.10.003

Sinha, S. K., Ziotopoulou, K., & Kutter, B. L. (2022). Centrifuge model tests of liquefaction-induced downdrag on piles in uniform liquefiable deposits. *Journal of Geotechnical and Geoenvironmental Engineering*, *148*(7), 04022048. https://doi.org/10.1061/(ASCE)GT.1943-5606.0002817

Sinha, S. K., Ziotopoulou, K., & Kutter, B. L. (2024). Effects of excess pore pressure redistribution in liquefiable layers. *Journal of Geotechnical and Geoenvironmental Engineering*, *150*(4), 04024014. https://doi.org/10.1061/JGGEFK.GTENG-11857

Sivathayalan, S., & Logeswaran, P. (2008). Experimental assessment of the response of sands under shear–volume coupled deformation. *Canadian Geotechnical Journal*, *45*(9), 1310–1323. https://doi.org/10.1139/T08-068

Sladen, J. A., D'hollander, R. D., & Krahn, J. (1985). The liquefaction of sands, a collapse surface approach. *Canadian Geotechnical Journal*, *22*(4), 564–578. https://doi.org/10.1139/t85-076

Suzuki, Y., Carotenuto, P., Dyvik, R., & Jostad, H. P. (2019). Experimental study of modeling partially drained dense sand behavior in monotonic triaxial compression loading tests. *Geotechnical Testing Journal*, *43*(5), 1174–1190. https://doi.org/10.1520/GTJ20190097

Taiebat, M., & Dafalias, Y. F. (2008). Sanisand: Simple anisotropic sand plasticity model. *International Journal for Numerical and Analytical Methods in Geomechanics*, *32*(8), 915–948. https://doi.org/10.1002/nag.651

Taiebat, M., Jeremić, B., Dafalias, Y. F., Kaynia, A. M., & Cheng, Z. (2010). Propagation of seismic waves through liquefied soils. *Soil Dynamics and Earthquake Engineering*, *30*(4), 236–257. https://doi.org/10.1016/j.soildyn.2009.11.003

Tasiopoulou, P., Taiebat, M., Tafazzoli, N., & Jeremic, B. (2015). Solution verification procedures for modeling and simulation of fully coupled porous media: Static and dynamic behavior. *Coupled Systems Mechanics*, *4*(1), 67–98. https://doi.org/10.12989/csm.2015.4.1.067

Theocharis, A. I., Vairaktaris, E., Dafalias, Y. F., & Papadimitriou, A. G. (2019). Necessary and sufficient conditions for reaching and maintaining critical state. *International Journal for Numerical and Analytical Methods in Geomechanics*, *43*(12), 2041–2055. https://doi.org/10.1002/nag.2943

Tobita, T., Kiyota, T., Torisu, S., Cinicioglu, O., Tonuk, G., Milev, N., Contreras, J., Contreras, O., & Shiga, M. (2024). Geotechnical damage survey report on february 6, 2023 turkey-syria earthquake, turkey. *Soils and Foundations*, *64*(3), 101463. https://doi.org/10.1016/j.sandf.2024.101463

Tokimatsu, K., & Yoshimi, Y. (1983). Empirical correlation of soil liquefaction based on spt n-value and fines content. *Soils and Foundations*, *23*(4), 56–74. https://doi.org/10.3208/sandf1972.23.4_56

Tsaparli, V., Kontoe, S., Taborda, D. M., & Potts, D. M. (2016). Vertical ground motion and its effects on liquefaction resistance of fully saturated sand deposits. *Proceedings of the Royal Society A: Mathematical, Physical and Engineering Sciences*, *472*(2192), 20160434. https://doi.org/10.1098/rspa.2016.0434

Tsaparli, V., Kontoe, S., Taborda, D. M., & Potts, D. M. (2020). A case study of liquefaction: Demonstrating the application of an advanced model and understanding the pitfalls of the simplified procedure. *Géotechnique*, *70*(6), 538–558. https://doi.org/10.1680/jgeot.18.P.263

Tuttle, M., & Seeber, L. (1991). Historic and prehistoric earthquake-induced liquefaction in newbury, massachusetts. *Geology*, *19*(6), 594–597. https://doi.org/10.1130/0091-7613(1991)019%3C0594:HAPEIL%3E2.3.CO;2

Vaid, Y. P., & Chern, J. C. (1983). Mechanism of deformation during cyclic undrained loading of saturated sands. *International Journal of Soil Dynamics and Earthquake Engineering*, *2*(3), 171–177. https://doi.org/10.1016/0261-7277(83)90014-1

Vaid, Y. P., & Chern, J. C. (1985). Cyclic and monotonic undrained response of saturated sands. *Advances in the Art of Testing Soils under Cyclic Conditions, ASCE Annual Convention*, 120–147.

Vaid, Y. P., & Eliadorani, A. (1998). Instability and liquefaction of granular soils under undrained and partially drained states. *Canadian Geotechnical Journal*, *35*(6), 1053–1062. https://doi.org/10.1139/t98-061

Vaid, Y. P., & Eliadorani, A. (2000). Undrained and drained (?) stress-strain response. *Canadian Geotechnical Journal*, *37*(5), 1126–1130. https://doi.org/10.1139/t00-036

Verdugo, R., & Ishihara, K. (1996). The steady state of sandy soils. *Soils and Foundations*, *36*(2), 81–91. https://doi.org/10.3208/sandf.36.2_81

Wakamatsu, K. (2000). Liquefaction history, 416–1997, japan. *Proceedings of 12th World Conference on Earthquake Engineering, Paper*, (2270), p8.

Wan, R. G., & Guo, P. J. (1998). A simple constitutive model for granular soils: Modified stress-dilatancy approach. *Computers and Geotechnics*, *22*(2), 109–133. https://doi.org/10.1016/S0266-352X(98)00004-4

Wanatowski, D., & Chu, J. (2011). Pre-failure instability behavior of sand in strain path testing under plane-strain conditions. *Soils and Foundations*, *51*(3), 423–435. https://doi.org/10.3208/sandf.51.423

Wanatowski, D., Chu, J., & Lo, R. S.-C. (2008). Strain-softening behaviour of sand in strain path testing under plane-strain conditions. *Acta Geotechnica*, *3*(2), 99–114. https://doi.org/10.1007/s11440-008-0064-1

Wang, R., Fu, P., Zhang, J. M., & Dafalias, Y. F. (2019). Fabric characteristics and processes influencing the liquefaction and re-liquefaction of sand. *Soil Dynamics and Earthquake Engineering*, *125*, 105720. https://doi.org/10.1016/j.soildyn.2019.105720

Wang, Z. L., Dafalias, Y. F., Li, X. S., & Makdisi, F. I. (2002). State pressure index for modeling sand behavior. *Journal of Geotechnical and Geoenvironmental Engineering*, *128*(6), 511–519. https://doi.org/10.1061/(ASCE)1090-0241(2002)128:6(511)

Widiyanto, W., Santoso, P. B., Hsiao, S.-C., & Imananta, R. T. (2019). Post-event field survey of 28 september 2018 sulawesi earthquake and tsunami. *Natural Hazards and Earth System Sciences*, *19*(12), 2781–2794. https://doi.org/10.5194/nhess-19-2781-2019

Yang, M., Taiebat, M., & Dafalias, Y. F. (2022). Sanisand-msf: A sand plasticity model with memory surface and semifluidised state. *Géotechnique*, *72*(3), 227–246. https://doi.org/10.1680/jgeot.19.P.363

Yang, Z. (2000). *Numerical modeling of earthquake site response including dilation and liquefaction*. Columbia University.

Yang, Z., & Elgamal, A. (2002). Influence of permeability on liquefaction-induced shear deformation. *Journal of Engineering Mechanics*, *128*(7), 720–729. https://doi.org/10.1061/(ASCE)0733-9399(2002)128:7(720)

Yang, Z. X., Li, X. S., & Yang, J. (2008). Quantifying and modelling fabric anisotropy of granular soils. *Géotechnique*, *58*(4), 237–248. https://doi.org/10.1680/geot.2008.58.4.237

Yao, Y. P., Liu, L., Luo, T., Tian, Y., & Zhang, J. M. (2019). Unified hardening (uh) model for clays and sands. *Computers and Geotechnics*, *110*, 326–343. https://doi.org/10.1016/j.compgeo.2019.02.024

Yimsiri, S., & Soga, K. (2001). Effects of soil fabric on undrained behavior of sands.

Yimsiri, S., & Soga, K. (2010). Dem analysis of soil fabric effects on behaviour of sand. *Géotechnique*, *60*(6), 483–495. https://doi.org/10.1680/geot.2010.60.6.483

Yu, H., Zeng, X., Li, B., & Ming, H. (2013). Effect of fabric anisotropy on liquefaction of sand. *Journal of Geotechnical and Geoenvironmental Engineering*, *139*(5), 765–774. https://doi.org/10.1061/(ASCE)GT.1943-5606.0000807

Zeng, S., Reyes, A., & Taiebat, M. (2024). Modeling cyclic liquefaction and system response of a sheet-pile supported liquefiable deposit: Insights from leap-2022. *Soil Dynamics and Earthquake Engineering*, *179*, 108548. https://doi.org/10.1016/j.soildyn.2024.108548

Zienkiewicz, O. C., & Shiomi, T. (1984). Dynamic behaviour of saturated porous media; the generalized biot formulation and its numerical solution. *International Journal for Numerical and Analytical Methods in Geomechanics*, *8*(1), 71–96. https://doi.org/10.1002/nag.1610080106